SPECTROSCOPIC METHODS FOR MEDICAL DIAGNOSIS AT TERAHERTZ WAVELENGTHS

CAROLINE REID

A thesis submitted to
University College London
for the degree of
DOCTOR OF PHILOSOPHY

Supervised by
Dr. Adam Gibson
Dr. Vincent Wallace

Department of Medical Physics and Bioengineering
University College London
2009

Declaration

I, Caroline Reid confirm that the work presented in this thesis is my own. Where information has been derived from other sources, I confirm that this has been indicated in the thesis.

Abstract

Terahertz (THz) radiation lies between the microwave and infrared regions of the electromagnetic spectrum. THz radiation excites intermolecular interactions and is non-ionising making it a viable tool for medical imaging. This thesis describes the development and validation of spectroscopic methods for diagnosis of tissue pathologies at THz wavelengths. Theoretical techniques were developed to determine the origin of the contrast seen in THz images of biological tissue. Specific biological tissues investigated in this thesis were colonic tissues with the aim of determining the origin of contrast between healthy and diseased tissue in THz images.

This thesis investigates the interaction of THz radiation with matter using simple tissue phantoms made from five biologically relevant materials: water, methanol, lipid, sucrose and gelatin. Phantoms are designed to imitate the spectroscopic properties of tissue at specific wavelengths where physical properties of the phantom, such as concentration and homogeneity, can be accurately controlled. The frequency-dependent absorption coefficients, refractive indices and Debye relaxation times of the pure compounds were measured and used as prior knowledge in the different theoretical methods for the determination of concentration. Three concentration analysis methods were investigated, a) linear spectral decomposition, b) spectrally averaged dielectric coefficient method and c) the Debye relaxation coefficient method. These methods were validated on phantoms by determining the concentrations of the phantom chromophores and comparing to the known composition. Two-component phantoms were made comprising water with methanol, lipid, sucrose or gelatin. Two different three-component phantoms were created; one with water, methanol and sucrose and a second with water, gelatin and lipid. The accuracy and resolution of each method was determined to assess the potential of each method as a tool for medical diagnosis at THz wavelengths. Finally, the spectroscopic methods were applied to measurements of *ex-vivo* colon tissues containing cancerous and dysplastic regions. Statistical analysis of the reflected time-domain waveforms demonstrated good distinction between healthy and diseased tissues with an estimated sensitivity of 89.2% and specificity of 78.3%.

Contents

List of Figures

List of Tables

List of Symbols

Symbol	Definition
A	light attenuation
T	light transmittance
I_o	intensity of incident electromagnetic wave
I_t	intensity of electromagnetic wave measured on transmission
I_r	intensity of electromagnetic wave measured on reflection
μ_a	absorption coefficient
α	specific absorption coefficient
μ_s	scattering coefficient
n	refractive index
$\widehat{\varepsilon}$	complex dielectric coefficient
ε'	real part of the complex dielectric coefficient
ε''	imaginary part of the complex dielectric coefficient
ε_∞	real part of the complex dielectric coefficient at high frequency
ε_S	real part of the complex dielectric coefficient at low frequency
$\widehat{n}$	complex refractive index
l	optical pathlength
N	number density of scattering particles
σ	scattering cross-section
c	speed of light
k_n	material specific wavevector
c_i	concentration of chromophore i
E	Electric field
H	Magnetic field
E_0	Incident electric field
H_0	Incident magnetic field
ω	angular frequency
t	time
x	propagation distance

Symbol	Definition
η	Intrinsic impedance of a material
μ	permeability
ε	permitivity
κ	extinction coefficient
ε	specific extinction coefficient
τ_j	relaxation time relating to the jth relaxation process
α_j	term accounting for the asymmetry of the dielectric dispersion curve
β_j	term accounting for the broadness of the dielectric dispersion curve

Acknowledgements

I would like to thank everybody who made it possible for me to produce this thesis. First of all I would like to thank my supervisors, Adam Gibson and Vince Wallace for all their help and suggestions. Many thanks also to Emma Pickwell-MacPhearson and Tony Fitzgerald for answering all my questions, no matter how daft, with patience and understanding. I would also like to thank Jan for putting up with this eternal thesis writing for such a long time, for the many fruitful discussions about the work, and also for proof reading. I would also like to thank George Reese and Dr. Goldin for their advice, help and company during the collection and analysis of the colon tissue data. Finally, many thanks to my family and chums for their patience and support while I finished this work.

This work would not have been possible without the financial support from TeraView Ltd and EPSRC who provided financial support for my PhD work.

Part I

Background

Chapter 1

Introduction and thesis overview

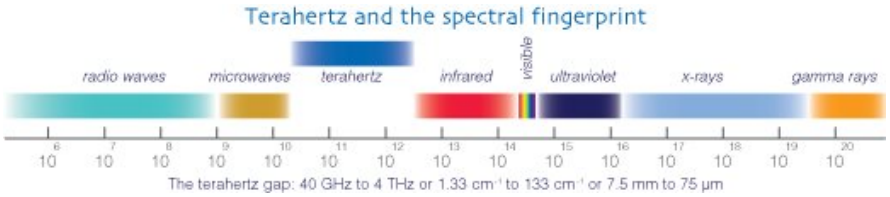

Figure 1.1: The Electromagnetic spectrum *(www.teraview.com)*.

The Terahertz (THz = 10^{12} Hz) range lies between microwave and infrared region of the electromagnetic spectrum, as seen in figure 1.1 with a wavelength and frequency range, typically, defined as 0.3mm to 3mm and 0.1 THz to 10 THz, respectively. It is commonly known as the 'THz gap' due to the historical difficulties in developing adequate sources and detectors to produce the THz radiation. Research into this spectral region was encouraged by the knowledge of an intermolecular vibration of water around 22 THz that had not been previously investigated. Work beginning in the 1890's sought to detect THz frequencies (Rubens and Nichols 1897, Rubens and Kurlbaum 1901, Nichols 1897), however, it was not until 1975 (Auston 1975) that the first THz emitter was developed. Rapid progress and development enabled progress in this field and in the 1990s, the first THz time domain spectroscopy and THz pulsed imaging systems were introduced based on the photoconductive emitter design (Hu and Nuss 1995).

Terahertz radiation is non-ionising and has the capability to penetrate a wide variety of non-conducting materials such as clothing, paper, cardboard, wood, masonry, plastic and ceramics, but is strongly absorbed by polar molecules, such as water, and reflected by metals. Currently, THz imaging and spectroscopy are being developed for use in three principal areas; chemical spectroscopy for the pharmaceutical industry, security measures for airports and screening, and medical imaging. As water is one of

the main constituents of tissue, penetration depths range from typically a few hundred microns in high water content tissues to several centimetres in tissues with a high fat content (Arnone et al. 1999, Fitzgerald et al. 2005). The first demonstration of THz imaging (Hu and Nuss 1995) concluded that a distinction could be made between the porcine muscle and fat with the hypothesis that the difference in water content of the two materials was responsible for the contrast. Since then, the number of reported biomedical studies using THz has increased greatly to include teeth and artificial skin models (Arnone et al. 1999), healthy skin and basal cell carcinoma in both vitro and in vivo (Woodward et al. 2002, Wallace et al. 2004), excised breast cancer (Fitzgerald et al. 2006) and cortical bone (Stringer et al. 2005).

The purpose of the work presented in this thesis was to investigate the potential of three different analytical methods; linear spectral decomposition, spectrally averaged dielectric coefficient method and the Debye relaxation coefficient method, to be used in the detection and specification of tissue pathologies at THz wavelengths. To be able to determine tissue pathologies in a real time system would have great implications for, for example, surgeons in ascertaining tissue pathology during surgery thus reducing the reliance on Moh's surgery procedures and reducing operation times. The three concentration analysis methods were validated through the analysis of measurements made on THz tissue-equivalent phantoms. The advantage of using phantoms is the accurate knowledge of their composition and the stability of the materials from which they are constructed. Phantoms have been used in previous THz studies where both solutions of naphthol green dye mixed with distilled water and TX151 gels were created with different concentrations and their THz spectra measured (Walker et al. 2004a). The phantoms provided similar absorption to tissue in the THz region, however, the use of these phantoms as biological tissue phantoms was limited as their refractive indices were very different to that of tissue. Another phantom has been used to simulate the dielectric properties of soft tissues over the microwave range between 500 MHz to 20 GHz (Lazebnik et al. 2005, Madsen et al. 2003). These phantoms were made using a mixture of lipid (oil), protein (gelatin) and water, the principle constituents of human tissue. The same phantoms and constituents are used here as the basis for the development of THz phantoms for the validation of the concentration analysis methods. The interaction of THz radiation with aqueous sucrose and methanol phantoms were also used to validate the three concentration analysis methods. The validated concentration analysis methods were then extended to measurements of excised healthy and diseased colonic tissues.

An introduction to the interaction of THz electromagnetic radiation with materials, the theories behind the experimental measurements and modelling techniques, and the physical and THz properties of materials measured for this work are described in Chapter 2. This includes details of the spectroscopic linear regression analysis used to determine concentrations from THz measurements. Dielectric relaxation analysis was used to provide information about the interactions between the materials. The application of dielectric relaxation analysis to mixtures can highlight the effect of solute molecules on the dielectric response of the mixtures, dependent on interactions between the solutes and free and bound water. The application of this analysis was used to identify underlying structural changes in the mixtures with changes in concentration. The imaging systems and spectrometer used for sample measurements and the measurement methods are described in Chapter 3. Then in Chapters 4 and 5 the methods outlined in Chapters 2 and 3 are applied to materials and mixtures that are components, or resemble components, of human tissue. Finally these methods were applied to measurements of *ex vivo* colon tissue to investigate the potential of THz imaging as an endoscopic tool, in Chapters 6 and 7, where the results of *ex vivo* imaging and spectroscopy of human colon tissue are presented.

Chapter 2

Background

2.1 Introduction

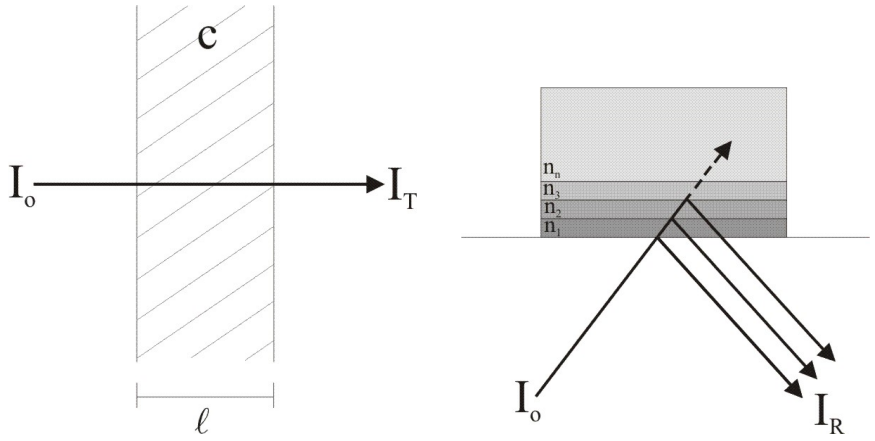

(a) Transmittance measurement (b) Reflection measurement

Figure 2.1: Diagram of the transmittance and reflectance of light as it travels through a material.

The aim of this project is to develop spectroscopic methods in the THz wavelength region for the determination of tissue composition and its application to the medical diagnosis of disease. Measurements can be made of the magnitude of either the transmitted, figure 2.1(a), or reflected, figure 2.1(b), pulses of THz radiation. As the THz pulse travels through tissue, the amplitude decreases and the waveform is delayed in the time domain, with respect to a reference measurement. Comparison of the measured waveforms with and without samples permitted the optical properties of the materials, specifically, the absorption coefficient, μ_a, refractive index, n, and the complex refractive index, $\widehat{\varepsilon}$, of the samples, to be estimated. Spectroscopic methods were then extended to multi-wavelength data which allowed concentrations to be extracted.

In this section we present the basic interactions of electromagnetic radiation radia-

tion with tissue followed by derivation of the transfer and propagation of electric fields at THz frequencies through dielectric media, section 2.3. The spectroscopic methods used to analyse the properties of the interrogated materials are presented in section 2.4. The structural and THz properties of the materials used in this study are detailed in section 2.5.

2.2 Interactions of electromagnetic radiation with tissue

2.2.1 Absorption

Absorption occurs when the energy of incident electromagnetic radiation is transferred to the electrons of the illuminated material.

The absorption of electromagnetic radiation by a medium results in a loss of transmitted intensity which is exponential with depth into a material. The absorption of photons in a non-scattering medium for an optical geometry shown in figure 2.1(a) is described by the Beer-Lambert law, equation 2.1. This law states that for a uniformly absorbing compound, the attenuation, A, measured in optical densities is equal to the $\log_{10}$ of the ratio of the light intensity incident on the medium, I_o, and the light intensity transmitted through the medium I_t. A is proportional to the concentration of the compound in the solution, c, the thickness of the solution, l, and the specific extinction coefficient of the absorbing compound, ε. The product $c.\varepsilon$ is known as the absorption coefficient of the medium, μ_a. The absorption coefficient has the units cm^{-1}.

$$A = \log_{10} \frac{I_o}{I_t} = \varepsilon.c.l = \mu_a.l \tag{2.1}$$

2.2.2 Scatter

Scatter is the change in direction of travel of a photon in a medium due to refractive index mismatches in a material. In tissue, this mismatch is usually due to cellular components. Scatter has the effect of significantly increasing the pathlength travelled by the photon. The direction of scatter is random and is dependent on the size of the scatterer, the wavelength of light and the refractive indices of the media through which it is travelling. The attenuation, A, due to a single scattering event is proportional to the number density of the scattering particles, N, the scattering cross section of the particles, σ, and the optical pathlength, d. The scattering coefficient μ_s is the probability

per unit length of a photon being scattered. Units are cm^{-1}.

$$A = \log \frac{I_o}{I_t} = N.\sigma.d = \mu_s.d \tag{2.2}$$

2.2.3 Refraction of light

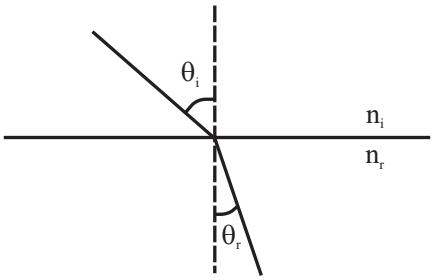

Figure 2.2: Behaviour of light at a boundary between two media with different refractive indices

Refraction occurs when light is incident at a non-normal angle, θ_i ,on a boundary of two media with different refractive indices, n_i and n_r. The light is refracted and will change direction to emerge at angle θ_r. The relationship between θ_i, θ_r, n_i and n_r is given by Snell's law, equation 2.3.

$$n_i \sin\theta_i = n_r \sin\theta_r \tag{2.3}$$

2.3 Theory of light transport in the THz wavelength region

This section broadly follows the description of the propagation of THz radiation through materials as previously outlined by Pickwell (2005). A summary is presented here.

2.3.1 Transfer and propagation matrices

Figure 2.3 illustrates the transfer of a wave of EM radiation incident on the interface of two semi-infinite layers of material with different refractive index and absorption coefficient, indicated by the material specific frequency wavevector, k, defined in equation 2.4 where n and μ_a are the frequency dependent refractive index and absorption coefficient, respectively, and c is the speed of light. The wavevector indicates the direction of propagation of the wave.

$$k = \frac{\omega}{c} n - \frac{i}{2}\mu_a \tag{2.4}$$

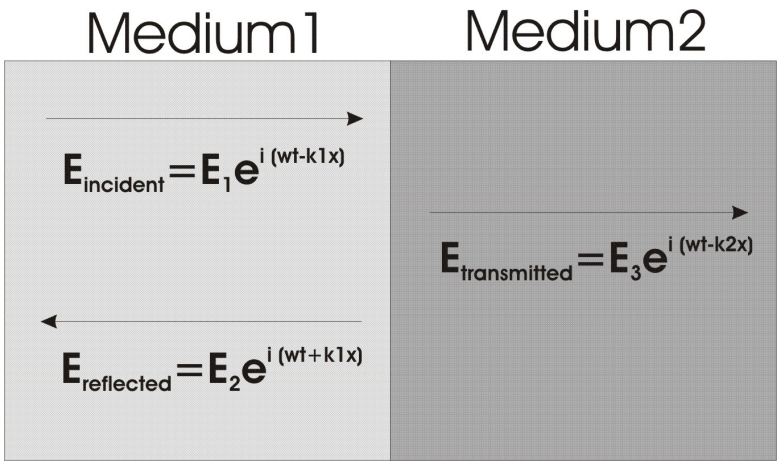

Figure 2.3: The electric field at an interface between two media with different optical properties.

The generic terms for an electromagnetic wave of angular frequency ω and propagation distance x are given in equations 2.5 and 2.6 for the E (electric) and H (magnetic) fields, respectively.

$$E(x,t) = E_0 e^{i(\omega t - kx)} \tag{2.5}$$

$$H(x,t) = H_0 e^{i(\omega t - kx)} \tag{2.6}$$

It is assumed that the wave is normally incident and that the materials are uniform in the $y-z$ plane. If we consider the incident wave to propagate through medium 1 towards the interface, the E and H fields are parallel to the x axis. A part of the incident energy will be reflected from the interface and a part will be transmitted into medium 2. If we consider the incident, reflected and transmitted waves to be represented, as in figure 2.3 by the subscripts $_1$, $_2$ and $_3$, respectively, the incident wave can be expressed in the form shown in equations 2.7 and 2.8.

$$E(x,t) = E_1 e^{i(\omega t - k_1 x)} \tag{2.7}$$

$$H(x,t) = H_1 e^{i(\omega t - k_1 x)} \tag{2.8}$$

Likewise, the reflected wave takes the form given by equations 2.9 and 2.10, the change of direction being indicated by the change of sign of k.

$$E(x,t) = E_2 e^{i(\omega t + k_1 x)} \tag{2.9}$$

$$H(x,t) = H_2 e^{i(\omega t + k_1 x)} \tag{2.10}$$

Finally, the transmitted wave is given by equations 2.11 and 2.12

$$E(x,t) = E_3 e^{i(\omega t - k_2 x)} \tag{2.11}$$

$$H(x,t) = H_3 e^{i(\omega t - k_2 x)} \tag{2.12}$$

We can now write the boundary conditions, equations 2.13 and 2.14, at the interface. The requirements of the boundary conditions are that the normally incident components of the E and H fields on either side of the interface are continuous.

$$E_1 + E_2 = E_3 \tag{2.13}$$

$$H_1 + H_2 = H_3 \tag{2.14}$$

The intrinsic impedance, η, of a material is the ratio of the electric to magnetic field amplitudes, equation 2.15, where μ is the permeability and ε is the permittivity of the medium. This relationship enables us to describe the boundary condition for the magnetic field strength in terms of, firstly the intrinsic impedance, equation 2.16, and, secondly, the material specific wavevector k, equation 2.17.

$$\eta = \frac{E}{H} = \sqrt{\frac{\mu}{\varepsilon}} = \frac{1}{k} \tag{2.15}$$

$$\frac{E_1}{\eta_1} + \frac{E_2}{\eta_1} = \frac{E_3}{\eta_2} \tag{2.16}$$

$$k_1 E_1 - k_1 E_2 = k_2 E_3 \tag{2.17}$$

In order to obtain expressions for the electric field strength of the incident and reflected radiation, we solve for E_1 and E_2 to obtain Equations 2.18 and 2.19.

$$E_1 = \frac{1}{2}\left(1 + \frac{k_2}{k_1}\right) E_3 \tag{2.18}$$

$$E_2 = \frac{1}{2}\left(1 - \frac{k_2}{k_1}\right) E_3 \tag{2.19}$$

Figure 2.4 depicts a wave propagating through a material of wavevector k_1, where $E_{reflected} = 0$. The propagation matrix, $\underline{P}$, describes the behaviour of the electric field as it travels through a material. For the propagation of a wave across a length Δx, the transmitted electric field is the incident field attenuated by a factor of $e^{-ik_n \Delta x}$, giving the propagation matrix for a material of wavevector k_1 and thickness Δx shown in

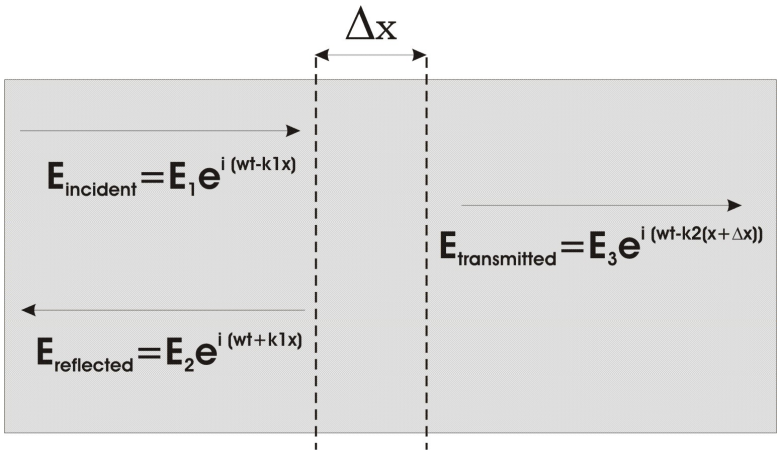

Figure 2.4: Electric Field Propagation

equation 2.20

$$\underline{P} = \begin{pmatrix} e^{-ik_n \Delta x} & 0 \\ 0 & e^{ik_n \Delta x} \end{pmatrix} \tag{2.20}$$

We now describe the light interactions in both transmission and reflection modes where the equations are shown for the single frequency case. The actual electric field is the sum of the components over all frequencies and the required frequency spectra are obtained by taking the Fourier transforms of the time domain waveforms. The temporal resolution of the waveform determines the frequency range and the highest frequency that can be detected without aliasing is half the sampling frequency.

2.3.1.1 Transmission mode measurements

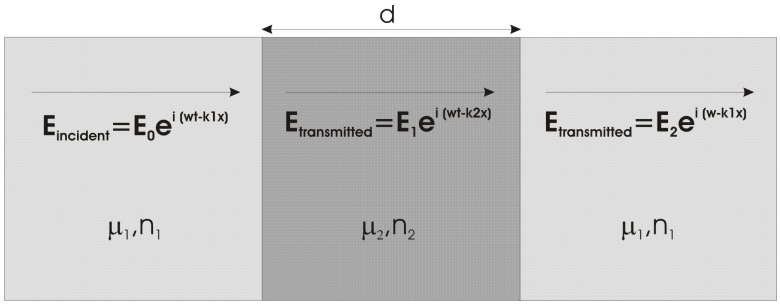

Figure 2.5: Electric Field Transmission

Figure 2.5 depicts the transmission set up for a sample of medium 2 between two layers of medium 1, where, in an experimental setup, medium 2 would be the sample under investigation and medium 1 would be the quartz windows containing the sample. The measured electric field is given by equation 2.21 and there are two interfaces and one propagation term to consider as the electric field is propagated through the materials. It

is important to ensure the thickness, and therefore absorption, of the sample material is sufficiently large to remove unwanted waves reflected at interfaces from the measured electric field. The first and third terms are the interfaces between material 1 and 2 and between materials 2 and 1 respectively. The second term is the propagation of the THz pulse through material 2. Equation 2.21 is simplified to achieve equation 2.22

$$E^{sample}_{transmitted} = \frac{1}{2}\left(1+\frac{k_2}{k_1}\right)e^{-ik_2d}\frac{1}{2}\left(1+\frac{k_1}{k_2}\right)E_o \tag{2.21}$$

$$= \frac{(k_1+k_2)^2}{4k_1k_2}e^{-k_2d}E_o \tag{2.22}$$

For the reference measurement the sample, medium 2, is effectively replaced by air, but the two windows, medium 1, are closed together to remove multiple reflections, as shown in equation 2.23.

$$E^{reference}_{transmitted} = e^{-ik_{air}d}E_o \tag{2.23}$$

The complex refractive index of the sample is calculated by dividing the reference E field by the sample E field:

$$\frac{E^{reference}_{transmitted}}{E^{sample}_{transmitted}} = \frac{4k_1k_2}{(k_1+k_2)^2}e^{-i(k_{air}-k_2)d} \tag{2.24}$$

$$= \frac{4k_1k_2}{(k_1+k_2)^2}e^{-i(\frac{w}{c}(n_{air}-n_2)-\frac{i}{2}(\mu_{a\ air}-\mu_{a\ 2}))d} \tag{2.25}$$

$n_{air} \simeq 1$ and $\mu_{a\ air} \simeq 0$, therefore:

$$ln\frac{E^{reference}_{transmitted}}{E^{sample}_{transmitted}} = ln\frac{4k_1k_2}{(k_1+k_2)^2} - i\{\frac{w}{c}(n_{air}-n_2) - \frac{i}{2}(\mu_{a\ air}-\mu_{a\ 2})\}d \tag{2.26}$$

$$= ln\frac{4k_1k_2}{(k_1+k_2)^2} + \frac{\mu_{a\ 2}d}{2} - i\frac{w}{c}(1-n_2) \tag{2.27}$$

The imaginary ($\Im m$) and real ($\Re e$) parts of equation 2.27 are taken to find the refractive index and the absorption coefficient respectively.

$$n_2 = 1 + \frac{c}{w}\Im m\left(ln\frac{E^{reference}_{transmitted}}{E^{sample}_{transmitted}}\right) \tag{2.28}$$

$$\mu_{a(2)} = \frac{2}{d}\left[\Re e\left(ln\frac{E^{reference}_{transmitted}}{E^{sample}_{transmitted}}\right) - ln\frac{4k_1k_2}{(k_1+k_2)^2}\right] \tag{2.29}$$

In order to approximate the term $\frac{4k_1k_2}{(k_1+k_2)^2}$, the Fresnel coefficient, it is assumed that the absorption coefficient is small compared to the refractive index, in equation 2.4, and so the term becomes $\frac{4n_1n_2}{(n_1+n_2)^2}$. Therefore the absorption coefficient can be calculated by

substituting the expression for n_2 in equation 2.29 into the expression for α_2.

$$\mu_{a(2)} \simeq \frac{2}{d}\left[\Re e\left(ln\frac{E^{reference}_{transmitted}}{E^{sample}_{transmitted}}\right) - ln\frac{4n_1n_2}{(n_1+n_2)^2}\right] \tag{2.30}$$

2.3.1.2 Reflection mode measurements

In figure 2.4, E_2, the reflectance signal, is measured experimentally. In a transfer matrix model of this case, there is only one interface and no propagation terms to consider. The dependance on the transmittance term, E_3, is removed by dividing equation 2.19 by equation 2.18 to give the complex reflectivity R, equation 2.31.

$$R = \frac{E_2}{E_1} = \frac{k-1-k_2}{k-1+k_2} \tag{2.31}$$

As the value of E_1 is unknown, in order to calculate k_2 for a material of unknown optical properties from the reflected measurements of E_2, a reference measurement of R using known materials of known refractive index and absorption must be taken. Typically this is a quartz/air interface as the optical properties of quartz and air are known. If we consider a quartz/air interface as a reference for the calculation of k_{sample} from a quartz/sample interface measurement, the reflectivity equations for the sample and reference measurements are given in equations 2.33 and 2.32, respectively.

$$R^{sample} = \frac{E^{sample}_2}{E^{sample}_1} \tag{2.32}$$

$$R^{ref} = \frac{E^{ref}_2}{E^{ref}_1} \tag{2.33}$$

The wave incident on the interface is the same for both measurements so $E^{ref}_1 = E^{sample}_1$ and therefore:

$$\frac{R^{sample}}{R^{ref}} = \frac{E^{sample}_2}{E^{ref}_2} \tag{2.34}$$

$$= \frac{(k_{quartz}-k_{sample})(k_{quartz}+k_{air})}{(k_{quartz}+k_{sample})(k_{quartz}-k_{air})} \tag{2.35}$$

$$= M \tag{2.36}$$

Where M is used to conveniently denote the ratio of the waveforms of the reflected sample and reference signals in the following equation. Equation 2.36 is rearranged to

extract k_{sample}:

$$k_{sample} = \frac{(1-M)\,k_{quartz}^2 + (1+M)\,k_{quartz}k_{air}}{(1-M)\,k_{air} + (1+M)\,k_{quartz}} \tag{2.37}$$

Again, k_{sample} is a frequency-dependant complex quantity from which the refractive index and absorption coefficient are found by taking the real and imaginary parts of k respectively, as in equation 2.4.

2.4 Spectroscopy at THz wavelengths

Spectroscopy is the study of molecular or atomic structure and composition of a material through the measurement of the electromagnetic radiation that is absorbed, emitted or scattered by the material as a function of wavelength. The manner in which the radiation interacts with material varies across the whole electromagnetic spectrum, as demonstrated in figure 2.6, from electronic interactions at the very small wavelength x-ray region to the larger molecular motions at the longer wavelength microwave region. The THz frequency range is between the microwave and infrared regions meaning THz spectroscopy probes molecular bonds, specifically vibrational and rotational modes. THz spectroscopy refers to techniques where one measures how much light at a given wavelength is absorbed by a sample.

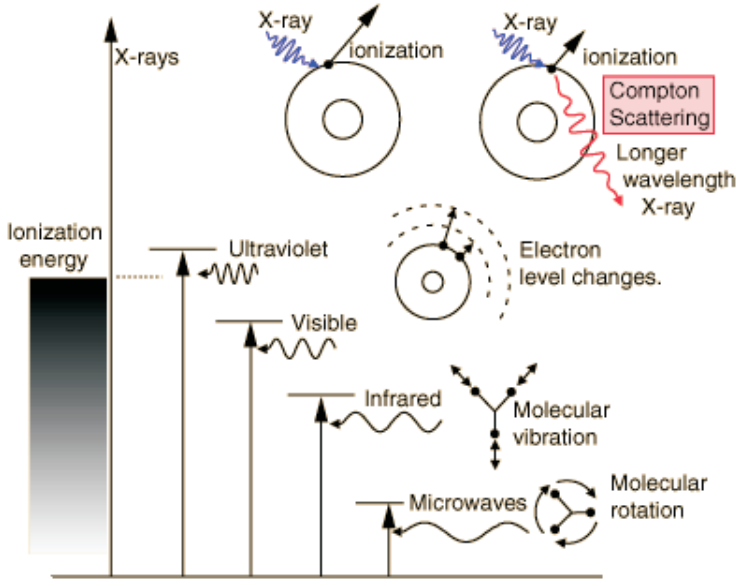

Figure 2.6: Molecular interaction across electromagnetic spectrum (Nave 2007)

Chemical bonds in molecules have specific frequencies at which they vibrate corresponding to energy levels within the molecule. The vibrational frequencies are related

to the strength of the bond and the mass of the atoms at either end of it, therefore, the vibrational frequency is associated with a particular bond type. The rotational spectrum describes the free rotation of a molecule, as illustrated in figure 2.7. A typical rotational spectrum consists of a series of peaks that correspond to energy levels within a molecule. Analysis of spectral lines of absorbed electromagnetic radiation from molecules provides information about bond lengths and bond angles of a molecule. This requires that the molecule must have a permanent dipole, that is, a difference between the centre of charge and the centre of mass or equivalently a separation between two unlike charges. The electric field of a pulse of electromagnetic radiation exerts a torque on the molecule causing it to rotate more quickly. After the pulse, the molecule decelerates and the associated change in molecular energy can be detected giving rise to a rotational spectrum. Pure rotational spectra can only be observed in the gaseous phase as in solids or liquids the rotational motion is usually hindered due to collisions. A non-polar molecule will not usually show a rotational spectrum. However, the exception to this is electronic excitation which can lead to a charge disturbance in some molecules, creating a net dipole moment to the molecule (Atkins 2002).

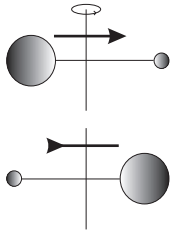

Figure 2.7: Rotating polar molecule (Atkins 2002)

2.4.1 Absorption spectroscopy

Absorption spectroscopy is based on the comparison of the intensity of a beam of radiation which is measured before and after interaction with a sample to provide both qualitative information, of the chemical composition of a sample, and quantitative information, of the relative concentrations of absorption compounds within the sample. Absorption spectroscopy is predominately performed in transmission mode, but can also be applied to reflection measurements, and can be applied to both pure, homogeneous samples or complex mixtures.

2.4.1.1 The Beer-Lambert law

The Beer-Lambert law is an empirical relationship that relates the measured absorption of light to the concentration of the absorbing chromophores in the sample and the

thickness of the sample through which the light is travelling. Therefore, if we know the shape of the spectrum of the absorbing chromophores in the sample, the optical path length travelled by the light and the amount of radiation absorbed by the sample, one can determine the concentrations of the absorbing chromophores. Multiple wavelengths are used because one wavelength is required for each chromophore under investigation. The law can break down at very high concentrations.

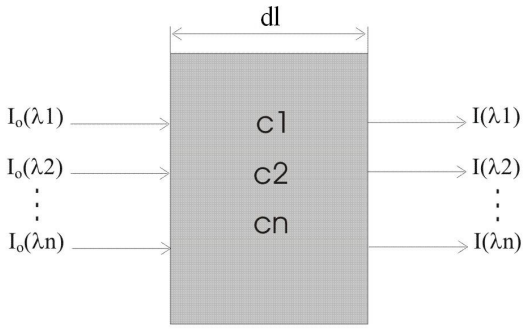

Figure 2.8: Diagram of Beer Lambert absorption of a beam of light as it travels through a cuvette of width dl.

The measurement principle of the Beer-Lambert law is shown in figure 2.8 where dl is the photon pathlength, I_o is the intensity of the incident interrogating radiation and I is the measured transmitted radiation. We will derive the Beer-Lambert law here for a single purely absorbing medium. The fraction of light absorbed by the medium is defined in equation 2.38. μ_a is the absorption coefficient of the absorbing chromophores in the sample (units cm^{-1}).

$$\frac{dI}{I_o} = -\mu_a dl \tag{2.38}$$

By integration, the transmitted intensity of the light, I, after travelling length l through the medium is then given by equation 2.39.

$$I = I_o e^{-\mu_a l} \tag{2.39}$$

The transmission of light, T, through the slab, is given by equation 2.40.

$$T = \frac{I}{I_0} = e^{-\mu_a l} \tag{2.40}$$

The absorption of light is equal to the log transmission of light and can be expressed in terms of both log_{10} and natural logarithms as shown in equations 2.41, typically used for gasses, and equations 2.42, typically used for liquids. α is the specific absorption coefficient (units typically $molar^{-1}cm^{-1}$), κ is the extinction coefficient (units

cm^{-1}) and ε is the frequency dependent specific extinction coefficient (units typically $molar^{-1}cm^{-1}$). The relation between μ_a and k is $\mu_a = kln10$.

$$\text{Natural Attenuation} = -ln(T) = -ln(\frac{I}{I_0}) = \mu_a l = \alpha lc \tag{2.41}$$

$$\text{Absorbance} = -log_{10}(T) = -log_{10}(\frac{I}{I_0}) = \kappa l = \varepsilon lc \tag{2.42}$$

Assumptions made in this derivation that each absorbing particle behaves independently with respect to the incident radiation and that no particle obstructs the optical path of another, can be sources of error, particularly at increased concentrations. In practice, however, the method provides a good approximation to the concentration of absorbing chromophores in a sample.

The absorbance of a sample containing n multiple absorbers with the concentrations c_1, c_2 to c_n and extinction coefficients ε_1, ε_2 to ε_n, is given by equation 2.43.

$$A(\lambda) = c_1\varepsilon_1 + c_2\varepsilon_2 + .. + c_n\varepsilon_n \tag{2.43}$$

2.4.2 Dielectric relaxation spectroscopy

Dielectric relaxation spectroscopy allows the study of the dynamics in a medium, from molecular vibrations and rotations to large-scale cooperative motions, by measuring its dielectric properties as a function of frequency. Particular molecular motions have characteristic relaxation frequencies and timescales and these relaxation times can range from several picoseconds in low-viscosity liquids, to several hours in glasses.

Dielectric relaxation spectroscopy is based on the decomposition of the complex dielectric coefficient of a material into the relaxation times of the underlying molecular motions. The complex dielectric coefficient of a material, $\widehat{\varepsilon}$, is simply related to the complex refractive index, $\widehat{n}$, as described by equation 2.44, where $\varepsilon^{'}(\omega)$ and $\varepsilon^{''}(\omega)$ are the real and imaginary parts of the complex dielectric coefficient. The relations for the real and imaginary parts of the dielectric function are given in equations 2.45 and 2.46, respectively.

$$\widehat{\varepsilon}(\omega) = \widehat{n}^2(\omega) = \varepsilon^{'}(\omega) + i\varepsilon^{''}(\omega) \tag{2.44}$$

$$\varepsilon^{'}(\omega) = n^2(\omega) - \mu_a^2(\omega) \tag{2.45}$$

$$\varepsilon^{''}(\omega) = 2n(\omega)\mu_a(\omega) \tag{2.46}$$

The complex dielectric coefficient of a material can, therefore, be determined simply from the measured values for absorption coefficient and refractive index. The index of refraction n and the absorption coefficient μ_a can be related to $\varepsilon^{'}(\omega)$ and $\varepsilon^{''}(\omega)$ as described in equations 2.47 and 2.48, respectively.

$$n(\omega) = \left(\frac{\sqrt{\varepsilon^{'2}(\omega) + \varepsilon^{''2}(\omega)} + \varepsilon^{'}(\omega)}{2} \right)^{1/2} \tag{2.47}$$

$$\mu_a(\omega) = \frac{2\omega}{c} \left(\frac{\sqrt{\varepsilon^{'2}(\omega) + \varepsilon^{''2}(\omega)} - \varepsilon^{'}(\omega)}{2} \right)^{1/2} \tag{2.48}$$

Dielectric relaxation spectroscopy is able to provide complementary information to other spectroscopy techniques, such as absorption spectroscopy which characterises the bulk properties of the sample by providing information on cooperative processes within a sample. In this work it is used to provide information on the molecular motions of samples to highlight the effect of solute molecules on the dielectric response of the mixtures, which can depend on interactions between the solutes and the free and bound water. These dynamics typically occurs on the picosecond time scales. The results of the application of this theory is used to identify underlying structural changes in the mixtures with the change in solute concentration.

2.4.2.1 The Debye Model

Debye theory (Debye 1929) describes the reorientation of molecules which could involve translational and rotational diffusion, hydrogen bond arrangement and structural rearrangement. The Debye relaxation time, the time constant τ, describes the time necessary for $\frac{1}{e}$ of the dipoles to relax to equilibrium after an impulse. For a pure material, multiple Debye type relaxation processes are possible where the complex dielectric function is described by equation 2.49.

$$\widehat{\varepsilon}(\omega) = \varepsilon_\infty + \sum_{j=1}^{n} \frac{\Delta\varepsilon}{[1 + (j\omega\tau_j)^{(1-\alpha_j)}]^{\beta_j}} \tag{2.49}$$

ε_∞ is the real part of the dielectric constant at the high frequency limit, $\Delta\varepsilon = \varepsilon_j - \varepsilon_{j+1}$, ε_j are intermediate values, occurring at different times, of the dielectric constant, τ_j is the relaxation time relating to the j^{th} relaxation process, ω is the angular frequency and α_j and β_j are two terms accounting for the asymmetry and broadness of the relaxation curve. The $\Delta\varepsilon$ term can be considered to be an 'amplitude', indicating the 'quantity' of that particular relaxation in the material under investigation. The Debye model accounts for purely exponential relaxations. Pure Debye relaxations are achieved when

$\alpha_j = 0$ and $\beta_j = 1$. Variants of the Debye model include the Cole-Cole equation, the Cole-Davidson equation and the Havriliak-Negami equation. The Cole-Cole equation (Cole and Cole 1941) is realised when $0 \leqslant \alpha_j < 1$ and $\beta_j = 1$ and relates to broadening of the dielectric dispersion curve. If $\alpha_j = 0$ and $0 \leqslant \beta_j < 1$, the Cole-Davidson equation is achieved (Davidson and Cole 1951) which indicates a skewed distribution of relaxation times. Finally, if both α_j and β_j are allowed to vary between 0 and 1, the Havriliak-Negami equation (Havriliak and Negami 1967) is achieved which accounts for asymmetry and broadness of the dielectric dispersion curve.

The frequency range 0.1-3 THz, the range investigated in this thesis, corresponds to a time range of relaxation times 0.15-10 ps. It is believed that the THz frequency range can probe three types of solvent relaxation; the main relaxation of the bulk solvent which occurs on a time scale of tens of picoseconds, the large-angle rotations of single or unbound molecules which occur on time scales of several picoseconds and the small molecular movements (distances smaller than a molecular diameter), small molecular rotations and hydrogen bond realignment which occur on time scales of hundreds of femtoseconds (Franks 1973).

2.5 Structural and THz properties of major tissue constituents

2.5.1 Water

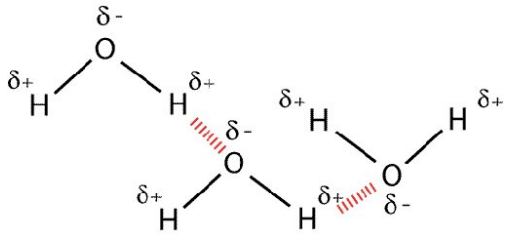

Figure 2.9: Illustration of the hydrogen bonding network in water where, on average, one water molecule bonds with four others *http://www.chemtools.chem.soton.ac.uk.*

Water is a polar molecule and is highly absorbing in the THz region. Water has a simple molecular structure; it comprises two hydrogen atoms covalently bonded to one oxygen, as illustrated in figure 2.9. The oxygen molecule has 4 electrons in its outer shell, two of which bond with the hydrogen atoms and two remain unshared making the oxygen atom ”electronegative” compared with hydrogen. This uneven distribution of electron density makes the water molecule polar. Water molecules in solution form

hydrogen bonds with three other surrounding molecules as illustrated in figure 2.9.

Individual water molecules are able to vibrate in a number of ways. In the gas state, the vibrations involve combinations of stretching and bending of the covalent bonds as shown in Figure 2.10. From the figure, 1) demonstrates symmetrical stretching where bonds stretch in unison, 2) asymmetrical stretching where bonds stretch in opposing directions 3) scissoring where there is simultaneous movement together and apart 4) rocking where there is asymmetrical movement forwards and backwards 5) wagging where there is symmetrical movement forwards and backwards and 6) twisting where there is symmetrical movement of the bonds side to side. Symmetrical and asymmetrical stretching and bending are molecular vibrations and rocking, wagging and twisting can be thought of as restricted molecular rotations. Water molecules in the liquid state, however, are hydrogen bonded together, resulting in a restriction in molecular motions. In free water, the exchange of the hydrogen bonds network can occur over the entire 4π solid angle and is fast, with a ps timescale (Franks 1973).

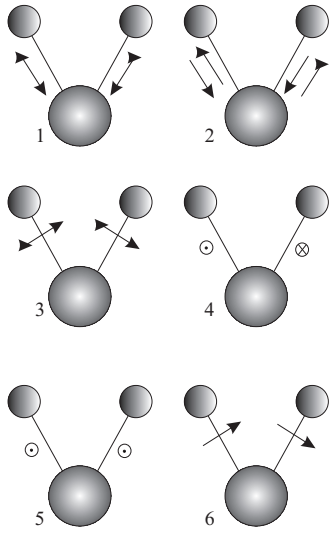

Figure 2.10: Vibrational modes within a water molecule

The absorption spectrum of water, figure 2.11, exhibits a broad peak centred at 5.6 THz attributed to resonant stretching of the hydrogen bond between water molecules and a stronger peak centred at 17 THz attributed to restricted oscillations within the molecules (Arnone et al. 1999). The effect of these absorption peaks, which extend down to the frequency range used in the THz imaging systems used for this work, makes this technique highly sensitive to water concentration. Much work has been carried out to identify and assign the mechanisms of absorption within water there is,

however, still much discussion on the subject regarding the rotational and combinational motions within the water molecules (Pickwell 2005). Two relaxation processes have been noted in the water response in the THz frequency range, using Debye theory, which have ascribed to the breaking of four hydrogen bonds between the tetrahedral molecular arrangement of water and the reorientation of the molecule. The breaking of the bonds is believed to be a slow process, described by a relaxation time of approximately 8.5ps, and the reorientation of the molecule is believed to be fast, described by a relaxation time of approximately 0.15ps (Kindt and Schmuttenmaer 1996, Ronne et al. 1997, Pickwell et al. 2004b).

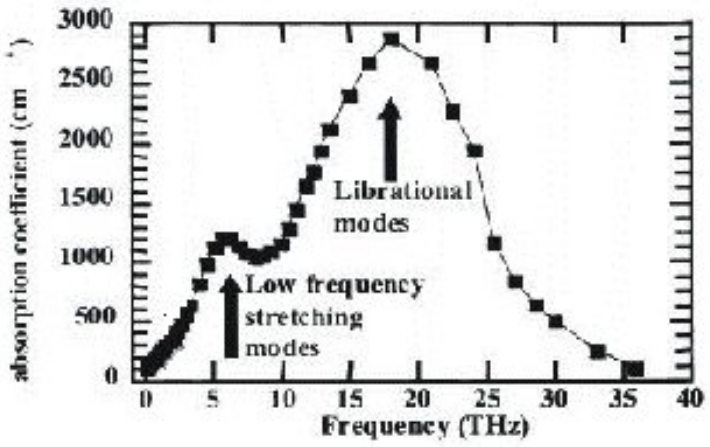

Figure 2.11: Absorption coefficient and refractive index of water in THz spectral range (Arnone et al. 1999)

2.5.2 Methanol

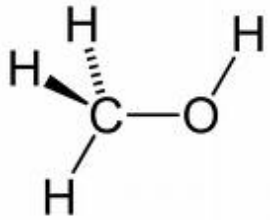

Figure 2.12: Methanol Molecule

Methanol, though not found in biological tissue, is used in this work for the purposes of experimental validation. Methanol is a very well studied molecule, particularly in its interactions with water. It is used here, therefore, to validate the proposed concentration analysis methods before they are applied to less well defined composites

and, eventually, tissues. Methanol is the simplest alcohol and consists of an OH group attached to a hydrocarbon chain to form CH_3OH, as shown in figure 2.12. The OH group is electronegative while the CH group is positive. This charge separation causes methanol to be a polar liquid, which results in significant absorption in the THz region. It is, however, less polar and, therefore, less absorbent than water. Methanol vibrates in much the same way as water and in the liquid phase the vibrations are damped by the effect of hydrogen bonding.

Alcohols have been investigated in the THz regime (Kindt and Schmuttenmaer 1996, Walker et al. 2004b), and some measurements made specifically of methanol, (Asaki et al. 2002, Kindt and Schmuttenmaer 1996, Barthel et al. 1990) where there is agreement that the complex dielectric coefficient of alcohols can be described using triple Debye theory. Workers have ascribed the three relaxation times observed in methanol to τ_1, the slowest relaxation to the flexing of chains of molecules, τ_2 to the rotation of a chain end molecule or a free molecule and τ_3, the fastest relaxation, to small motions of a methanol molecule between two hydrogen bond sites (Asaki et al. 2002). Studies of pure methanol have shown absorption maxima at frequencies of 4.5 and 20.6 THz, where first maximum has been suggested to be related to fast re-orientational processes while the second peak is associated with restricted oscillations of the hydrogen atoms (Skaf et al. 1993, Venables and Schmuttenmaer 2000a, Woods and Wiedemann 2005).

2.5.3 Lipid

Fats and oils are composed of fatty acids bonded to a glycerol molecule, as shown in figure 2.13. Fatty acids are long-chain hydrocarbon molecules with a carboxylic acid (COOH) group and are the major components of stored fat. The hydrocarbon chains in fatty acids are non-polar while the acid functional group is polar. The hydrocarbon chain affects the overall polarity of the molecule, due to charge cancelling effects, where molecules with very short carbon chains are more polar while longer chains have a non polar character. Glycerol ($C_3H_5(OH)_3$) is a sugar alcohol which has three hydrophilic hydroxyl (OH) groups causing the molecule to be polar. Three fatty acids and one glycerol molecule form a triglyceride via a bond between the OH groups of both the fatty acid and the glycerol, producing a water molecule in the process. Due to the removal of the polar OH groups of both the glycerol and the fatty acids, the resulting lipid molecule is non-polar.

Lipids can, nonetheless, become absorbent in the THz wavelength region. This is due to collision-induced dipole moments, where dipoles are induced following a shift

in electric charge distribution with respect to the centre of mass, which create short range transient ordering of the molecules (Pedersen and Keiding 1992). Lipids, however, attenuate THz radiation less strongly than polar molecules.

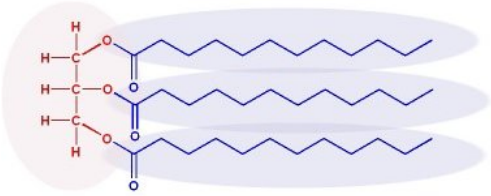

Figure 2.13: General structure of fats and oils where the structures to the left hand side are the positions of the fatty acids and the structure to the right hand side is the glycerol molecule.

Measurements of the THz properties of animal fats and plant oils (Hu et al. 2005, Gorenflo et al. 2006, Nazarov et al. 2008) show similarities between the measured absorption coefficients of the different oils and fats from 0.2 to 2.0 THz. A difference, however, between the measurements of refractive index of the animal and plant oil fats was shown. It was also observed in this study that the refractive index increased with temperature for the animal fats but the absorption coefficients were almost unchanged.

2.5.4 Macromolecules

2.5.4.1 Proteins

Proteins are large complex molecules made up of chains of amino acids, the structures of which are illustrated in figure 2.14. Proteins are characterised into two classes; globular and fibrous. Globular proteins such as enzymes, transport proteins and insulin are roughly spherical in shape while fibrous proteins such as keratin, collagen and elastin combine to form long cable-like structures. Globular proteins are generally soluble while fibrous proteins are insoluble.

Two different experimental approaches to the analysis of protein dynamics and function in the THz regime are noted from previous investigations; a) the analysis of pressed pellets of dry protein powders with differing thicknesses and b) the measurement of hydrated protein molecules. Analysis of dry pressed pellets such as polypeptides and cytochrome c (Kutteruf et al. 2003, Yamamoto et al. 2002) and horse heart myoglobin and hen egg white lysozyme (Markelz et al. 2002) present structural and vibrational mode information of protein molecules. These studies, however, do not account for the biologically relevant situation in which proteins are in a fully hydrated condition. A transmission study of bovine serum albumin (BSA) and collagen (Markelz et al. 2000)

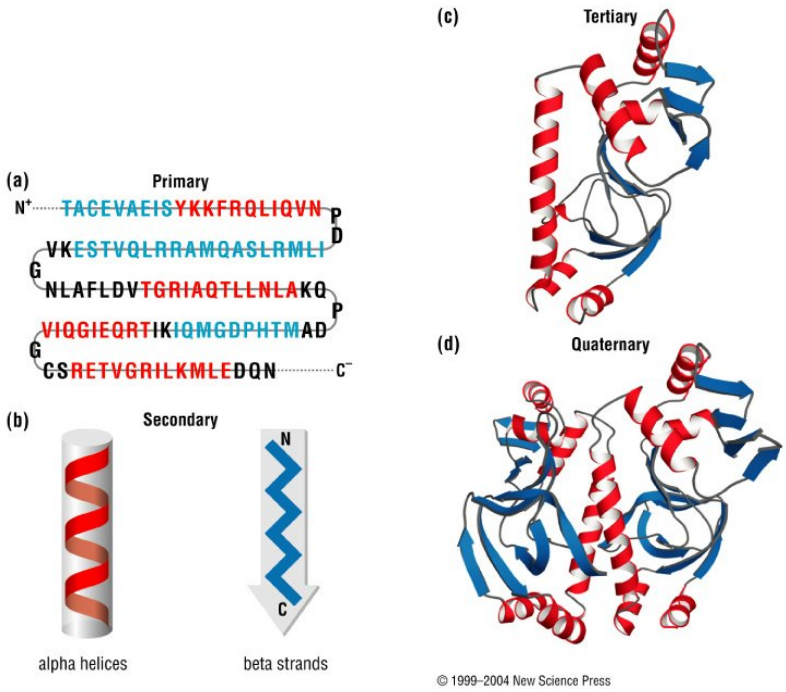

Figure 2.14: Protein Structure *www.new-science-press.com*. Proteins are large complex molecules made up of chains of amino acids. This is the primary structure of the protein as shown in figure 2.14a. The secondary structure is a highly regular sub-structure in either helix or sheet formation of local segments of a protein, as illustrated in figure 2.14b. A single protein molecule may contain many different secondary structures. The tertiary structure, figure 2.14c, is a three-dimensional structure made up of several of the secondary structures. This structure is a fully formed protein molecule. The quaternary structure, figure 2.14d, is made from several protein molecules which combine to form a larger protein complex.

investigated the absorption coefficients and refractive indices of both dry and hydrated powders and found an increase in refractive index with relative hydration. No increase in refractive index, however, was noted for BSA. This was attributed to the lower number of water molecules absorbed per unit surface area for the globular BSA structure compared to the strand-like collagen. Studies of hydrated myoglobin powders (Zhang and Durbin 2006) and protein gel films of α- and β-glycine (Shi and Wang 2005) and bacteriorhodopsin (Whitmire et al. 2003) present a more biologically relevant analysis of proteins than dried powders. However, these represent only partially hydrated samples and so cannot faithfully represent the true biological condition. Studies of proteins in solution such as lactose (Havenith et al. 2004) and BSA (Xu et al. 2006), therefore, present the most accurate view of biological protein dynamics and function in the THz regime.

The study of BSA extracted the absorption coefficient of the hydrated molecule and observed a broad, monotonic increase with frequency without any discrete spectral features apparent. The lactose study demonstrated the changes in the solvent structure in the layer around the lactose molecule. These changes affect the collective intermolecular modes of the lactose solutions which can be detected in the THz regime. It has, however, been suggested that there may ultimately be insufficient difference in the spectra of different proteins in the THz range to allow for protein identification (Markelz et al. 2002). However others believe that small differences in molecular bonding between proteins of the same type can cause a variation in the measured absorption and that a single mutation in a protein molecule can cause significant changes in its absorption spectrum (Yamamoto et al. 2002, Markelz et al. 2002).

The protein specifically considered in this work is gelatin, an extract of collagen, a structural protein and the main protein of connective tissue in mammals, making up about 25% of the whole-body protein content. Collagen is a long, fibrous structural protein and is not soluble in water. Gelatin, on the other hand, is a large molecular weight protein produced by partial hydrolysis of collagen and is soluble in most polar solvents. As gelatin is a mechanically and chemically extracted protein, the properties of the protein can vary between samples. Gelatin gels are formed when the gelatin strands are intertwined to form a giant, interconnected, three-dimensional structure (Bohidar et al. 1998, Vackier et al. 1999). Any increase in the degree of crosslinking, which can be achieved by adding formaldehyde, makes the network structure more condensed. 'Free' water can be compartmentalised in the spaces between the molecules, where difference between the bonding of the compartmentalised water to

bulk water is related to the space of the compartment; if the space is very small then the water has fewer hydrogen bonds than bulk water (Maeda and Kitano 1995). There is little water remaining which is unaffected by the gelatin and all water is bound to some extent (Grant et al. 1986).

No previous studies of the dielectric properties of gelatin have been made in the THz region, however, studies have been made in neighbouring frequency regions. These studies have noted a wider spread of relaxation times when compared to other proteins and lower values of relaxation time which is, in part, due to the smaller free water content of the gels to the protein solutions. The large displacement of the relaxation frequency of the gel relaxation time compared to that of free water, indicates that there is little water remaining which is unaffected by the gelatin and all water is bound to some extent (Grant et al. 1986). Nuclear magnetic resonance (NMR) studies have indicated that the surface topology of a gelatin molecule rather than hydrogen bonding between molecules is the main determinant of hydration dynamics. This study suggested the existence of a highly mobile hydration layer at the surface of the gelatin triple helix.

2.5.4.2 Sugars

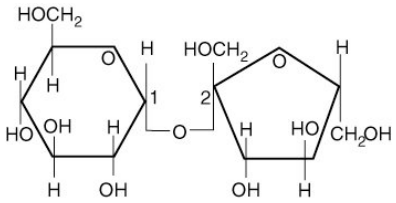

Figure 2.15: Sucrose molecule (Kelly and Keng 1975)

Sugar is a basic carbohydrate which consists of a class of crystalline substances including sucrose, lactose, glucose and fructose. The term *sugar* refers to any monosaccharide or disaccharide. Monosaccharides, such as glucose, store chemical energy which biological cells convert to other types of energy. Sucrose is a disaccharide and consists of two monosaccharides; glucose and fructose, joined by a glycosidic bond as illustrated in figure 2.15. Sugars are strongly polar compounds and are extensively hydrogen bonded to water where a single molecule can bind up to six water molecules (Kelly and Keng 1975, Engelsen and Perez 1996, Heugen et al. 2006). Intramolecular bonding between sucrose molecules increases, however, as the concentration of the solution increases (Molinero et al. 2003). As sucrose molecules are dissolved in water, the bonding structure of the free water is interrupted due to binding between the water and the sucrose molecules. High concentration sugar solutions form 'lattice' type

structures of bound sucrose molecules where water molecules, which retain a high degree of rotational and translational mobility, are trapped within the pores formed by the sucrose (Gulyi and Klimovich 1990, Molinero et al. 2003, Bordat et al. 2004, Lerbret et al. 2005). The water is, however, still constrained in comparison to free bulk water (Gulyi and Klimovich 1990). 30% sucrose concentration appears to be the value above which the sugars impose their own hydrogen bonding regime on the water. (Bordat et al. 2004, Lerbret et al. 2005).

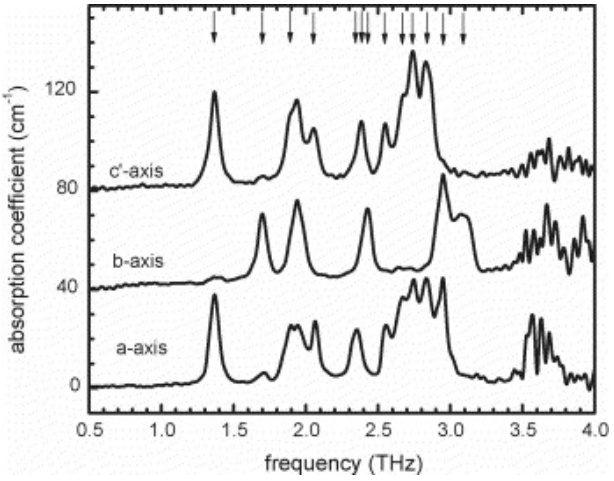

Figure 2.16: Dry sucrose molecule absorption coefficient measured using an electro-optic sensor unit, (Kroll et al. 2006), for three different axes of orientation of a sucrose crystal. The curves are vertically offset for clarity.

Spectroscopic measurements of dry sucrose crystals between 0.1 THz and 4 THz (Iwamoto et al. 2005, Kroll et al. 2006, Ueno and Ajito 2008) demonstrated a variation in absorption coefficient spectra with crystal orientation. All of these studies showed a flat linearly rising spectrum until 1.4 THz. Beyond 1.4 THz sucrose produces a series of peaks, as illustrated in figure 2.16. It is difficult to assign THz peaks as current theoretical models do not take into account molecular conditions, such as crystal orientation (Ueno and Ajito 2008). These peaks are not visible in measurements of sucrose solutions (Nagai et al. 2006, Jepsen et al. 2007). As is the case with proteins, measurements of dry crystals do not represent the more biologically relevant, fully hydrated molecular state, therefore measurements of sugar solutions is preferable. THz transmission measurements of lactose solutions (Heugen et al. 2006) sought to probe the dynamics of this hydration layer in the region 2.3 - 2.9 THz and observed that the water in the hydration layer absorbs more strongly than the bulk water in this frequency region.

2.5.4.3 Molecular Hydration

In biology, macromolecules, such as proteins and sugars, often occur in a *hydrated state*; the native or biologically active state which enables the molecule to engage in metabolic functions. The *hydration water* of a macromolecule consists of a hydrogen-bonded network of water molecules spanning the protein surface. The first hydration layer of strongly bound water molecules is surrounded by additional 'shells' of more weakly associated water molecules which have greater independence from the molecule but whose motions are still influenced by it. The ordering of the hydration water enables the extension of the electrostatic surfaces of the proteins away from their physical surfaces giving them far greater electrostatic influence to surrounding macromolecules (Jacobson 1953, Despa et al. 2004, Nakasako 2004, Hildebrandt et al. 2007). It is difficult to calculate the exact quantity of water contained in the hydration shell due to the difficulty in defining what constitutes hydration water as well as experimental difficulties in identifying this layer. The hydration shell has been shown, using THz spectroscopy, to extend out to at least 1-2 nm (Ebbinghaus et al. 2007).

The structure of water next to the macromolecule surface has a structure similar to that of ice with tightly bound, ordered water showing coherent hydrogen-bond patterns. This results in a distinct dielectric response in comparison to free water. Ice has a higher dielectric constant than liquid water, approximately 96.5 at 0.1^{o}C (http://skua.gps.caltech.edu/hermann/ice.table2.html), as a result of the ordered structure of ice reducing random reorientations of the water molecules. Water has a dielectric constant of 78.8 at room temperature (Kindt and Schmuttenmaer 1996). The degree of ordering in ice, however, is higher than that of hydration water, therefore the dielectric constant will be lower. The maximum reduction of the hydration water relaxation time from that of free water, occurs at the surface with the relaxation time increasing with distance from the surface (Despa et al. 2004, Yokomizo et al. 2005).

The calculation of the gelatin hydration layer is made difficult by the imprecise understanding of the properties of an individual gelatin molecule. One recent study has identified a highly mobile hydration layer on the surface of the gelatin triple helix along with a small number of trapped water molecules associated with structural defects and branch points in the gel (VacaChavez et al. 2006). This study suggested that the hydration layer consists of approximately five water molecules interacting with each amino acid in the gelatin molecule. On average, 2250 water molecules are adsorbed per gelatin molecule suggesting a hydration layer of 0.81 grammes of water per gramme

of gelatin. The hydration layer of sucrose decreases with solution concentration. For low concentration sucrose solutions the hydration layer is approximately seven water molecules per sucrose molecule while at concentrations of 60%, this is between 3.5 and 4.5 water molecules (Lerbret et al. 2005).

Chapter 3

Experimental Methods

3.1 Introduction

In this chapter, the techniques used for the generation and detection of of THz radiation are described in general terms in section 3.2. The specific systems used in this study are schematically illustrated and described in section 3.3, while alternate THz generation and detection methods are outlined in section 3.2.2. The design, manufacture, measurement and subsequent analysis of simple THz phantoms as well as tissue measurements are described in sections 3.4 and 3.5.

3.2 Terahertz generation and detection techniques

3.2.1 Photoconductive Systems

In this study, THz spectroscopy and imaging systems were used which are based on photoconductive generation and detection of THz radiation. This principle is based on the use of photoconductive switches excited by mode-locked femtosecond pulsed lasers. Femtosecond pulsed laser excitation of photoconductive switches cause rapid transients in the carrier density and conductance of the photoconductor. These are harnessed for the emission and detection of coherent THz electromagnetic radiation.

3.2.1.1 Photoconductive emission

THz radiation is generated using a photoconductive Hertzian dipole antenna, as shown in Figure 3.1(a), gated with an ultrashort optical pulse as illustrated in Figure 3.1(b). A photoconductive antenna consists of a small piece of semiconductor crystal (commonly gallium arsenide), on which two planar gold electrodes in a bowtie layout with a small gap in between support a large electric field across its surface. The bandgap of the GaAs substrate is 1.42 eV. THz pulses are generated by focusing ultrafast ($\sim$100 fs) pulses of near infrared light onto the gap between the electrodes at near infrared wavelengths (a Ti:Sapphire laser with a central wavelength of 800 nm). Since the pho-

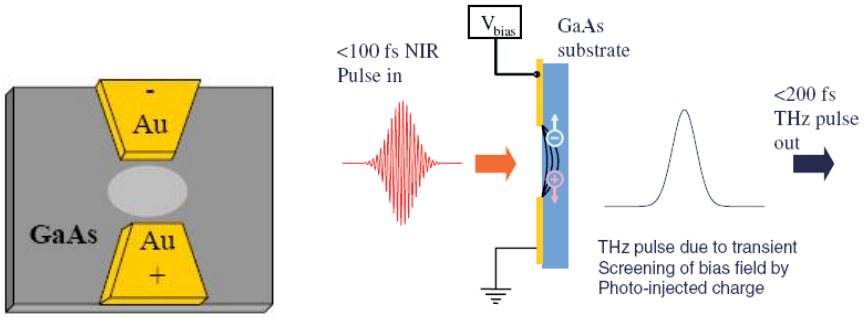

(a) (b)

Figure 3.1: a) Diagram of a bow tie photoconductive switch used to generate THz radiation pulses. The gold electrodes define a photoconductive gap on the GaAs substrate and the highlighted spot shows the conductive path between the electrodes when the device is illuminated. In the reflection and transmission systems used in this work, the photoconductive gaps were typically of the order of 10 μm. b) Schematic diagram of THz emission using a photoconductive switch. (Pickwell 2005)

ton energy of the 800 nm light is above that of the band gap of the gallium arsenide semiconductor, the photogenerated electron-hole pairs are excited at the surface of the substrate and subsequently separated by the electric field, in this case 50 V modulated at 30 kHz. This acceleration of the free carriers creates a transient photocurrent in the substrate which rapidly changes the conductance. If the lifetime of the photocurrent is sufficiently short, the fast, time varying current radiates pulses of coherent, broadband THz radiation from both the front and back surfaces of the device into free space. Subpicosecond pulse duration is required to achieve modulation on the THz timescale. The picosecond THz pulse is typically radiated from the back surface after passing through the substrate as this is the simplest configuration to implement. However, GaAs exhibits strong absorption at these frequencies resulting in the effective bandwidth of THz emission limited to about 10 GHz to 4 THz. The central frequency, bandwidth, and pulse duration of the emitted THz pulse is dependent on a number of factors, such as the pulse duration of the laser, the width of the antenna gap, the bandgap and lifetime of the semiconductor substrate, the bias voltage and the thickness of the substrate. The power of the THz radiation generated in the system used in this study is in the order of 100 nW.

3.2.1.2 Photoconductive detection

Coherent photoconductive detection is achieved using a similar photoconductive antenna to that used in emission. A second femtosecond laser beam, the so called probe beam which is derived from the same laser source used to generate the radiation, is irradiated onto the front surface of the detector. Again, electron-hole pairs are generated at

the surface of the substrate. Rather than applying a bias voltage between the electrodes, as is the case for the emitter, in the detector setup the incoming THz pulse accelerates the charge carriers. The transient current between the electrodes is measured via a low-noise current amplifier. The pulses in the optical beam synchronously, therefore, gate the receiver by driving the photocurrent switch. The current measured is the product of the induced THz voltage and the detector conductance. It is therefore proportional to the THz electric field and the detector carrier density. The signal can be measured and detected using lock-in techniques which are referenced against the 30 kHz modulation of the emitter bias voltage. The response time of the receiving antenna is determined by its gating time and the rise time of the transient photoconductivity. A signal-to-noise ratio (SNR) of around 4000:1 can be achieved, which is limited by the thermal noise in the antenna.

3.2.2 Alternative THz generation and detection methods

3.2.2.1 Quantum Cascade Lasers

A semiconductor-based THz source is the THz quantum cascade laser (QCL). QCL's emission is due to electron relaxation between subbands of quantum wells, typically between several GaAs layers (nm thick) separated by $Al_{0.15}Ga_{0.85}As$ barriers. The continuous wave emission power of these devices is tens of milliwatts when operating at crogenic temperatures. The first QCL, with a lasing frequency of $\sim$70 THz, was demonstrated in 1994. Continued research in the field has resulted in lasers emitting at 1.39 THz (Scalari et al. 2006). The emission of QCL's, however, rapidly deteriorates with increasing temperature posing significant challenges to their use at room temperature. Research into this field continues, specifically into the reduction of lasing frequencies, increase in operational temperatures and range of tuneable frequencies (Tonouchi 2007).

3.2.2.2 Photomixing Systems

Photomixing devices are THz sources based on the merging of beams of light from two different wavelength lasers to produce a 'beating' wave effect. The emerging beam modifies the conductance of a photoconductive switch to produce c.w. THz radiation. The emission frequency of the 'beating' wave is the difference between the two wavelengths and is typically tuneable up to 1.5 THz. Detection of THz radiation is possible using the reverse of this technique (Gregory et al. 2005; 2007). Maximum output powers of 20 mW and 10 μW have been achieved at 100 GHz and 1 THz, respectively (Ito et al. 2005). Photomixing, using inexpensive, compact and tuneable diode lasers, is a cost effective THz generation technique, however, their practical applicability is cur-

rently limited due to their single frequency output, a problem which could be addressed using multiple single frequency outputs from a tuneable system (Tonouchi 2007).

3.2.2.3 Electro-optic Sampling

A THz detection technique alternative to photoconductive detection, is electro-optic sampling. In this technique, both the THz pulse and a secondary, linearly polarised, optical laser pulse are focussed onto an electro-optic crystal. A change in the optical properties of the crystal is induced by the THz pulse. The changes in optical properties of the crystal create a polarisation change of the secondary optical laser pulse, which passes through the detection crystal, a quarter wave-plate and a polarising beam-splitter. When no THz pulse is present, the polarisation of the secondary beam is unchanged and the beam is circularly polarised by the quarter waveplate. The beam is then split into two orthogonally polarised components of equal intensity and are sampled by two photodiodes. When a THz pulse is present, the secondary beam is elliptically polarised, which remains unchanged through the quarter waveplate and is split into two components which are dependant on the polarisation (i.e. the retardation) experienced by the secondary beam. The detected change in current is directly proportional to the secondary beam polarisation which, in turn, is directly proportional to the THz electric field. In this method of detection, as in photoconductive detection, a rapid scan unit oscillates at up to 20 Hz to generate a ”real time” THz pulse (Wu et al. 1996, Wu and Zhang 1996, Nahata et al. 2002)

3.3 The TeraView THz imaging and spectroscopy systems

(a) Terahertz Pulsed Imaging (TPI) System

(b) Terahertz Pulsed Spectroscopy (TPS) System

Figure 3.2: TeraView THz imaging and spectroscopy systems

The systems used in this study were two stand-alone portable THz systems produced

by TeraView Ltd, Cambridge, the Terahertz Pulsed Imaging (TPI) system, figure 3.2(a) and the Terahertz Pulsed Spectroscopy (TPS) system, figure 3.2(b).

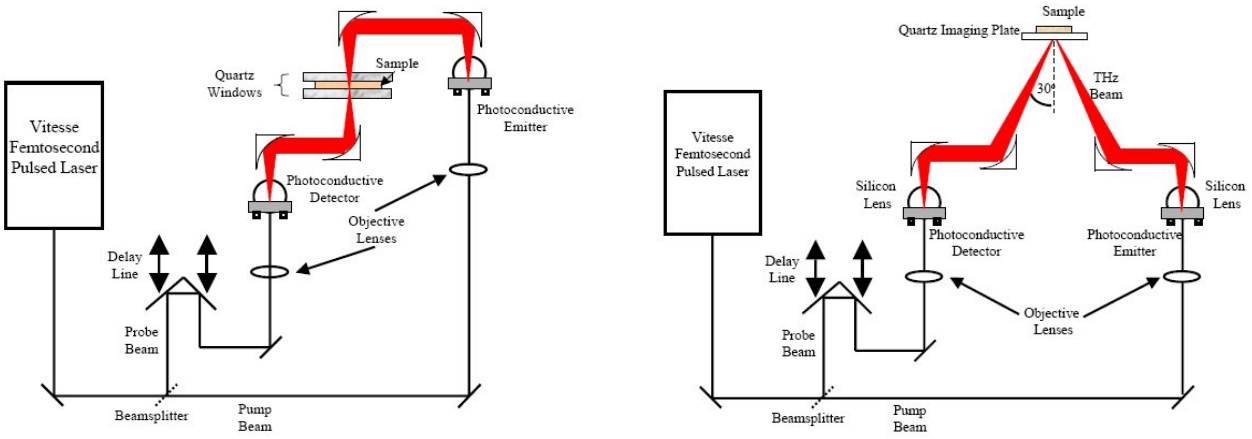

(a) Transmission

(b) Reflection

Figure 3.3: Schematic diagram of the photoconductive a) transmission and b) reflection systems (Pickwell 2005)

The general setup for the two THz systems used in this work is identical, as illustrated in figures 3.3(a) and 3.3(b). A 250 mW Vitesse 800 (Coherent Inc, Santa Clara, CA, USA) mode-locked Ti:Sapphire oscillator, is used to generate and detect THz radiation as outlined in section 3.2.1.1. The 100 fs laser pulses with 800 nm central wavelength at a repetition rate of 80 MHz are split by a beam splitter into a pump and a probe beam. The probe beam is passed through a delay line a mechanical translation stage which is moved at fixed intervals over a finite distance. The delay line is used to change the relative path length of the probe beam to the pump beam to facilitate the mapping of a whole THz pulse, as, if the path length of the pump and the probe beam are equal the THz electric field is essentially measured at only one instant in time. The delay line operates at a typical scan rate of 15 Hz, but as a pulse can be measured over both the up and the down sweep a pulse acquisition rate of 30 Hz is achieved. This rate was chosen as an optimum between acquisition time and signal-to-noise (SNR). By slowing the scan rate or by using signal averaging the SNR can be improved at the cost of a corresponding increase in data collection time and vice versa. The time resolution was approximately 200 fs which is limited by the width of the laser pulse. Following the delay line, the description of each system deviates.

3.3.1 Transmission and reflection mode measurements

The transmission spectroscopy and reflection imaging systems both consist of THz pulse generation and detection systems and computer control and differ in having a

spectroscopy unit for the transmission system and an imaging unit for the reflection system as illustrated in figures 3.3(a) and 3.3(b), respectively. The spectroscopy unit consists of a sealed sample chamber to enable measurements to be made in a nitrogen purged atmosphere. Following the delay line the transmission pulses are focused, using a pair of gold coated off-axis parabolic (OAP) mirrors onto a pair of z-cut quartz windows, between which a sample is held. The transmitted beam is focused by another pair of OPMs onto a photoconductive detection device.

Following the delay line the reflection pulses are focused onto the top of a 2mm thick z-cut quartz window. The beam is reflected from a reference or sample placed on the quartz window and is focused by another pair of OPMs onto a photoconductive detection device. The angle of reflection is 30^o to the normal. An entire THz waveform, approximately 35ps in length, is acquired at each x-y point. To create an image, the optics are raster-scanned in the x-y plane to collect a grid of data points.

3.4 THz imaging and spectroscopy sample holders

3.4.1 Liquid sample cell (transmission)

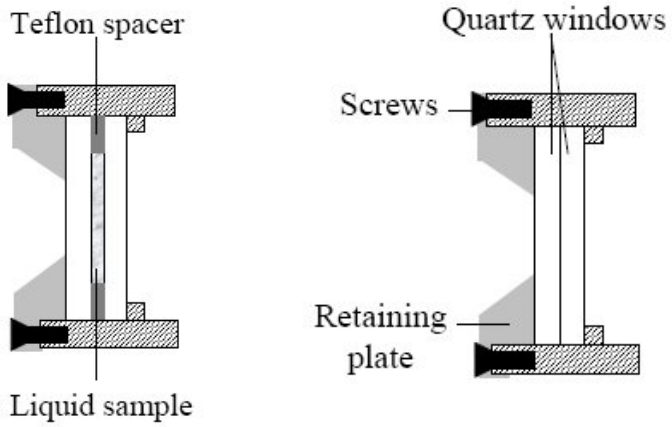

(a) Sample measurement (b) Reference measurement

Figure 3.4: Cross-section of liquid cell geometry for performing a) reference and b) sample measurements (Pickwell 2005)

The liquid sample transmission cell is designed to contain liquid samples of varying thicknesses. It consists of two quartz windows separated by a Teflon spacer which can be between 100μm to 1mm thick, as illustrated in figure 3.4(a). As the cell is designed to be used vertically in transmission mode, rubber rings are placed between the quartz windows and a retaining plate which is tightened to create a water-tight seal. Typical spacer thicknesses used in this work were 200μm for water rich samples and 500μm

for oil rich samples. A reference measurement was made in each instance using two pieces of quartz plate held together, as illustrated in figure 3.4(b).

3.4.2 Solid sample cell (transmission)

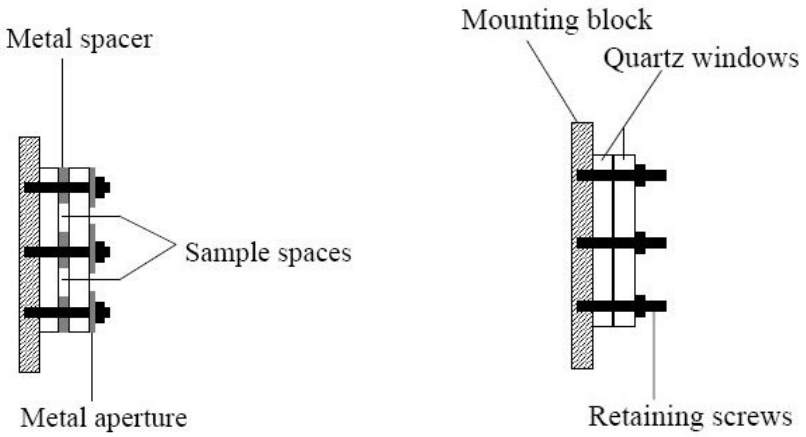

(a) Sample measurement (b) Reference measurement

Figure 3.5: Cross-section of solid sample cell geometry for performing a) reference and b) sample measurements (Pickwell 2005)

In order to ensure the uniform thickness of solid samples and that the measured thickness is accurately known, the solid sample transmission cell is used. In this cell, metal spacers were placed between two (z-cut) quartz windows, as illustrated in figure 3.5(a) to enable an accurate estimation of the uniform sample thickness to be achieved. This is achieved by through the selection of a spacer thickness which would allow the quartz windows to be gently pressed together, while a sample is in place, without deformation of the sample which would alter its optical density. A reference measurement was made in each instance using two pieces of quartz plate held together, as illustrated in figure 3.5(b).

3.4.3 Solid sample cell (reflection)

A tissue holder, a photo and schematic of which is shown in figures 3.6(a) and 3.6(b) respectively, was designed to control the orientation of the tissue samples throughout the complete tissue analysis process, from initial imaging through tissue fixing and histological examination. The tissue holder was designed to be easily removed from the imaging system to allow for the samples to be formalin fixed in the same position as they were imaged. The tissue samples were placed onto the quartz plate which had been positioned in the focal point of the reflected THz beam. The plastic lattice covering was placed over the sample and gently fixed into place with four screws to ensure the samples are securely positioned. The lattice covering is fixed gently to not overly

(a) Photo (b) Schematic

Figure 3.6: Tissue sample holder where a) shows a photograph of the tissue holder in place on the THz imaging system and b) shows the schematic drawing of the holder. The holder was designed and built at TeraView ltd, Cambridge.

compress the tissues which would affect their optical properties. Following sample imaging the whole tissue holder could be removed from the scanner and placed in formalin. The lattice covering allows for even fixing of the tissue sample and helps reduce the effect of uneven tissue shrinkage, which occurs during fixing and would impede accurate registration between histology and THz results. Gold markers on the quartz plate, which can be seen both in the THz images and the photographs aid registration of the samples.

3.5 Experimental materials and data analysis methods

Two and three component 'phantoms' were created by mixing the pure compounds, methanol, lipid, sucrose and gelatin, with water to provide increasingly complex test samples for the development of concentration analysis methods. A phantom is designed to imitate the absorption and scattering properties of a tissue at the appropriate THz wavelengths. A phantom is most often used when it is desirable to validate a technique as the physical properties of the phantom can be very accurately controlled. Descriptions of the phantoms are given in section 3.5.1, and of the measurement processes for the transmission, reflection and tissue measurements in section 3.5.2. The methods used to extract the data from the measured signals are outlined in section 3.5.3. Finally, in section 3.5.4, the three concentration analysis methods are detailed.

3.5.1 Materials

3.5.1.1 Pure compounds

The pure compounds used in this study were distilled water, methanol, lipids, intralipid, sucrose and gelatin. These materials were selected because they provide models for true tissue components allowing us to predict the eventual response of the validated concen-

tration analysis methods with tissue. Methanol, though not a 'biological' material was included for the purposes of experimental validation as the interactions of the molecule with water are very well studied. Methanol (99.9% pure) and gelatin were procured from Sigma-Aldrich while the sucrose was sugar available from the supermarkets. The gelatin and sucrose were bought as dry samples. The lipids measured were olive oil, cod liver oil, safflower oil, beef dripping and lard. The lipids were at least 99% pure with exception of the lard which had been manually purified. This was achieved by repeatedly melting the lard in boiling water to separate the pure oil, which floated on top of the water, from the impurities which sank to the bottom (vanVeen et al. 2004). Ancillary materials used in the manufacture of a solid water, lipid and gelatin phantom were formaldehyde, p-toulic acid and n-propanol.

3.5.1.2 Two component phantoms

Two component phantoms were produced as dilutions of distilled water with each of the pure compounds. Water and methanol solutions were produced in a series of '% by volume' dilutions from 0% to 100% methanol volume in 10% increments.

Water and lipid emulsions were made using a commercially available emulsion, Intralipid. This was due to inherent difficulties in producing stable oil-in-water or water-in-oil emulsions. Intralipid is a brand name nutritional supplement which is an oil-in-water emulsion of soyabean oil stabilised with 1.2% egg phospholipid with an average particle size of between 1μm and 40nm (Bryan et al. 1976, Ferezou et al. 2001). Dilutions of Intralipid with distilled water were produced in a series of '% by volume' dilutions beginning with 20% lipid volume, the concentration of the undiluted Intralipid, and decreasing to 4% lipid volume.

Water and sucrose solutions in a series of percent-by-weight (%wt) mixtures ranging from 5% and 33% sucrose content, in 3% increments. At the higher sucrose concentrations, it became increasingly difficult to dissolve the sucrose which limited the high end of the concentration range.

Water and gelatin gels were created in a series of percent-by-weight (%wt) mixtures ranging from 0% (distilled water) to approximately 30% gelatin.

Table 3.1: Percentage composition of 3-component tissue-mimicking phantom

%vol Oil	%wt Water	%wt Oil	%wt Gelatin	%wt p-toluic acid	%wt n-propanol	%wt formaldehyde
0	81.7	0.0	14.6	0.1	2.7	0.9
10	74.2	8.5	13.3	0.1	3.1	0.8
20	66.6	17.3	11.9	0.1	3.4	0.7
30	59.0	26.2	10.6	0.1	3.5	0.6
40	51.0	35.3	9.1	0.1	3.9	0.6
50	43.0	44.4	7.7	0.1	4.3	0.5
60	34.9	53.6	6.3	0.1	4.6	0.5

3.5.1.3 Three component phantoms

Two three-component phantoms were created. Two solutions of water, methanol and sucrose were created following the methods published by *Uhd Jepsen, et al*, the concentrations of which are given below,

- Solution A: 71.4% wt water, 20.4% wt sucrose, 8.2% wt methanol
- Solution B: 62.5% wt water, 20.8% wt sucrose, 16% wt methanol

Solid gels were made from gelatin, water and oil which had a volume per cent oil between 0 and 60%. These phantoms most closely resembled the composition of biological tissue than any of the other phantoms. The detailed procedure for producing these phantoms is described elsewhere, (Lazebnik et al. 2005), however, a brief outline is given here. A small amount of p-toluic acid and n-propanol were added to distilled water which was then heated and gelatin powder added. P-toluic acid, is a benzoic acid molecule with a methyl group substituted into the aromatic ring, and n-propanol which is a simple alcohol. These two compounds were added to the water solution to reduce the aggregation of gelatin particles and produce a uniform gel (Bohidar and Mohanty 2004, Usha and Ramasami 2004). A measure of oil was separately heated to 50^{o}C. The gelatin and water solution was added to the heated oil solution along with a surfactant and mixed vigorously to achieve a uniform suspension. A small measure of formaldehyde was added to the final solution to aid the crosslinking of the gelatin molecules, and the solution then allowed to set. The full composition of these phantoms is outlined in table 3.1.

3.5.1.4 Tissue samples

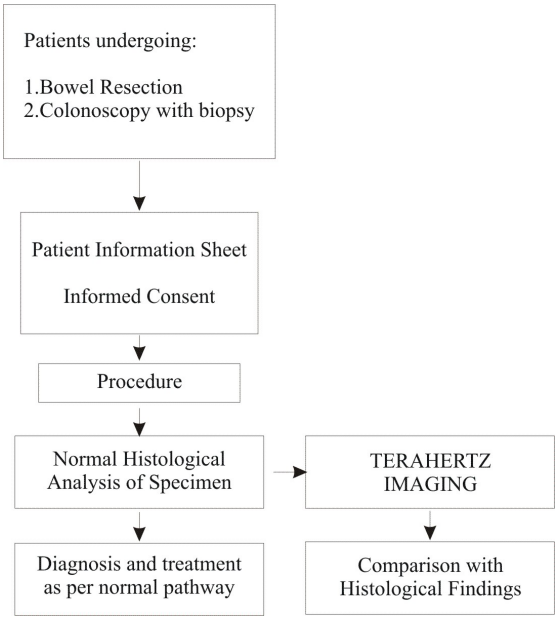

Figure 3.7: Procedure and study protocol followed during THz imaging of human colon tissue study

The procedure followed for the THz imaging of human colon tissue study is illustrated in figure 3.7. Suitable patients were selected in advance of undergoing surgery and gave informed consent to opt into the study after discussion with a surgeon (in accordance with the ethical approval and study protocol). Tissue was retrieved immediately following removal and taken to the pathology department. Pathological assessment was made of the removed tissue to identify sites of diseased and healthy tissue, from which tissues could be harvested for imaging. The number of tissue samples retrieved was decided by a consultant histopathologist and was dependent on a number of factors, with the primary aim being not to disrupt the normal pathological assessment of the specimen. Typically two samples of tissue were imaged from each excised colon. Healthy tissues were harvested well away from the diseased areas.

3.5.2 Measurements

3.5.2.1 Transmission Measurements

Transmission measurements are made using the TPS system, described in section 3.3.1. The refractive indices and absorption coefficients of the liquid samples were obtained using a transmission cell, section 3.4.1, with a quartz window separation of 200μm. For solid samples, the the solid sample cell was used, shown in section 3.4.2. The sample chamber in the TPS system was purged with nitrogen to remove water vapour.

A reference measurement was made in each instance using two pieces of quartz plate held together and all measurements were made at room temperature.

3.5.2.2 Reflection Measurements

Measurements in reflection mode were made in the flatbed geometry set-up of the imaging system, where samples are placed on top of the quartz plate. By raster scanning the sample in the x-y plane, a 3D image of the sample is generated where each pixel is the recorded THz time domain signal. To obtain the baseline for these measurements, a second quartz plate was placed on the quartz window to create the effect of an infinitely thick layer of quartz. There are no reflections, therefore, except for those from the lower surface of the fixed quartz window. A reference is created by focussing the beam onto the top surface of the quartz plate. An 'air reference', a measurement of the quartz/air interface at the empty surface of the quartz window, was used in the reflection measurements. All measurements were made at room temperature.

3.5.2.3 Tissue Measurements

The excised tissues were imaged in reflection mode using the TPI system. All measurements were made at room temperature. The time from tissue removal to tissue imaging was typically around 30 minutes and any tissue awaiting imaging was kept in an air-tight container. Two different approaches to positioning the tissue were used. The first ten patient samples were imaged by placing the tissue directly onto the quartz window. It was found, however, that the task of registering the terahertz images against histopathology results was difficult. The final 25 patients' samples were imaged using the tissue holding device, section 3.4.3, which was designed by TeraView, Ltd, which made tissue registration substantially easier. For the first ten samples, the tissue was photographed using a photographic camera inside the imaging system. The orientation of the tissue on the scan window was correlated to the photographic image and enabled easy correlation between regions of contrast in the THz image and features seen in the photographic image. The normal and tumour tissues were marked on the photo (later confirmed by histology). Once data collection had been completed, the tissue was pinned to a cork block to maintain the tissue size and shape, photographed and placed in a labelled formalin pot for fixation for 24hrs. Slight changes in tissue orientation, however, could occur during the pinning to the cork board which made accurate image registration difficult. The final 25 patients' samples were imaged using the tissue holding device. Following imaging the samples were placed in a labelled formalin pot while still positioned in the tissue holding device for fixation for 24hrs. To perform histology on the fixed tissue the whole sample was sequentially blocked or if the sample was too large to fit in a single block it was divided and processed in two

or more blocks. The sites of the histological blocks were marked on the digital image and sections were cut for histological examination to identify areas of normal mucosa, inflamed mucosa, dysplasia or invasive carcinoma and note the limit of the pathologies on the digital image.

Reference and baseline measurements were made in the same way as with the spectroscopic reflection measurements, section 3.5.2.2, except both quartz/air (typically used in tissue measurements) and quartz/water references were used for these measurements. References, used to normalise the measured data, are selected to closely match the normal properties of the material and thus improve image contrast by highlighting deviations within the material.

3.5.3 Data Extraction

The data extraction method for the transmission measurements has been outlined previously in section 2.3.1.1 whereby the ratio of the reference and water impulse functions will enable the refractive index and the absorption coefficient to be calculated. The analysis methods for the reflection image data is more complex. Images are collected as the optics are raster-scanned in the x-y plane. Each pixel represents a single point waveform. The acquired data represents the impulse function of the sample convolved with the reference data. Signal-processing is required to separate the components of the reflected THz waveforms due to properties of the measured sample from those resulting from instrumental and environmental effects. In order to remove any unwanted reflections purely from the quartz/air or quartz/sample interfaces, a baseline is subtracted from both the reference and sample waveforms. A baseline is not required in transmission measurements as no back reflections are measured. The measured reflection pulse is also sensitive to oscillations in the pulse shape due to atmospheric water. These can be removed by deconvolving the raw (-baseline) waveform with the reference (-baseline) waveform to extract the impulse function as shown by equation 3.1. This process, however, increases the noise of the impulse function. A Gaussian filter function is applied to remove both out-of-band noise and anomalies arising from deconvolution, equation 3.2 where t is time and u and l are upper and lower bandwidth time constants respectively. The Fourier transform of the time domain signal gives a frequency domain spectrum. Filtering is not required in transmission measurements as the measurements are performed in a nitrogen purged environment.

$$Pulse = FFT^{-1}\left[\frac{FFT\left(signal - baseline\right)}{FFT\left(ref - baseline\right)} \times FFT\left(filter\right)\right] \tag{3.1}$$

$$filter(t) = \frac{1}{u}\exp\left(-\left(\frac{t}{u}^2\right)\right) - \frac{1}{l}\exp\left(-\left(\frac{t}{l}^2\right)\right) \tag{3.2}$$

3.5.3.1 The THz pulse

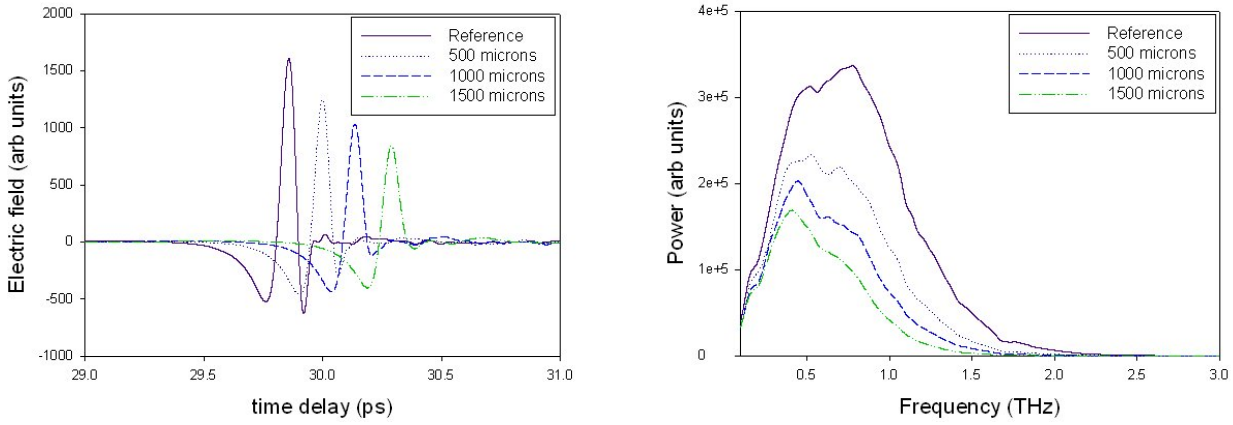

(a) Time Domain (b) Frequency Domain

Figure 3.8: Examples of delay, attenuation, and broadening seen in the terahertz pulse and frequency spectra through differing thicknesses of safflower oil.

As a pulse is transmitted through or reflected from a material it will experience delay, attenuation and broadening, with respect to the reference pulse, as the various component frequencies are phase shifted, absorbed, reflected, and scattered by the interrogated medium. Figure 3.8(a) shows example terahertz pulses transmitted through varying thicknesses of safflower oil, and the corresponding power spectra, figure 3.8(b). The pulses are increasingly delayed, attenuated, and broadened as the thickness of the oil increases. The power spectrum shows the frequency content of the pulses is centred around 0.5 THz, and there is an increasing attenuation of the higher frequency content as the thickness of the oil increases than is seen in the lower frequencies. This increased attenuation of high frequencies is also suggested in the time domain as the pulses through thicker oil samples are a lot smoother than the thinner samples, hence, they have less high frequency content. Plots in the time domain show changes in value in the electric field and describe the propagation of the THz pulse through media with differing thicknesses. A negative response (dip in the plot) indicates a reflection from a boundary between a medium with a lower refractive index and a higher refractive index medium. Similarly, a positive response (peak in the plot) indicates a boundary between a medium with a higher refractive index and a lower refractive index medium.

To extract information from the measured pulses and create images, parameters are identified which relate to the physical processes responsible for causing delay, atten-

uation and broadening of the pulses the raw data in both the time and the frequency domains. These images are referred to as 'parametric images'. Though the number of potential parameters which can be used in the creation of images is very large, some parameters are shown here as examples. Some example parameters used in the creation of time domain images are;

- The pulse amplitude which is the value of the signal pulse amplitude relative to the reference pulse amplitude representing the average transmitted power at each pixel.

- The pulse delay which is the time difference between the amplitudes of the reference and signal pulses and is dependant on the thickness and refractive index of the sample. The pulse delay and amplitude can refer to either the maximum amplitude of the pulses or the amplitude at a particular time in the waveform.

- The pulse width which is the full width at half maximum of the signal pulse and is dependent on the ratio of low and high frequency components of the pulses.

Example parameters typically used in the frequency domain are;

- The phase time delay of each frequency component of the signal pulses relative to the reference pulse which is due to the presence of the sample. This is proportional to the thickness and refractive index of the sample.

- The transmittance which is the ratio of transmitted to incident intensities at a given frequency and is determined by the sample thickness and absorption coefficient.

Previous studies have used the E_{max} and E_{min} time domain parameters to create tissue images (Fitzgerald et al. 2006). Some example parametric images are shown in figures 3.9(b), 3.10(b) and 3.11(b) which are based on the data parameters highlighted in figures 3.9(a), 3.10(a) and 3.11(a).

Although several physical properties of the interrogated materials can affect the values of the parameters, certain parameters have greater dependence on particular physical properties and so will be of most significance to the creation of images. As many parameters may be used in the creation of an image, each acquired dataset can lead to a 'set' of parametric images, the information from which should be combined in order to maximise the use of the measured data.

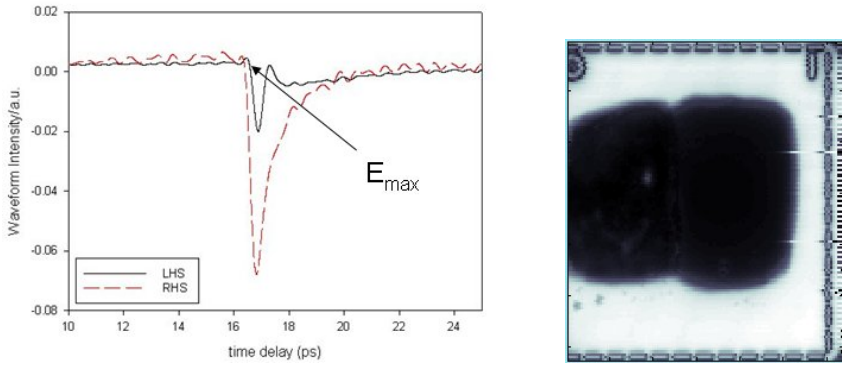

(a) Time Domain plot (b) THz image

Figure 3.9: THz image based on measured E_{max}

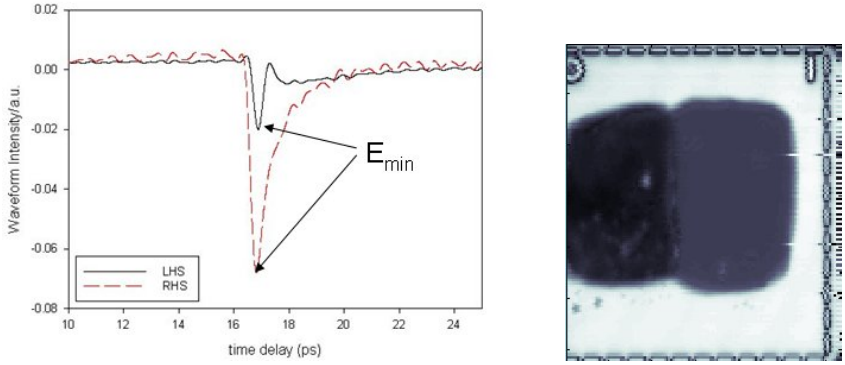

(a) Time Domain plot (b) THz image

Figure 3.10: THz image based on measured E_{min}

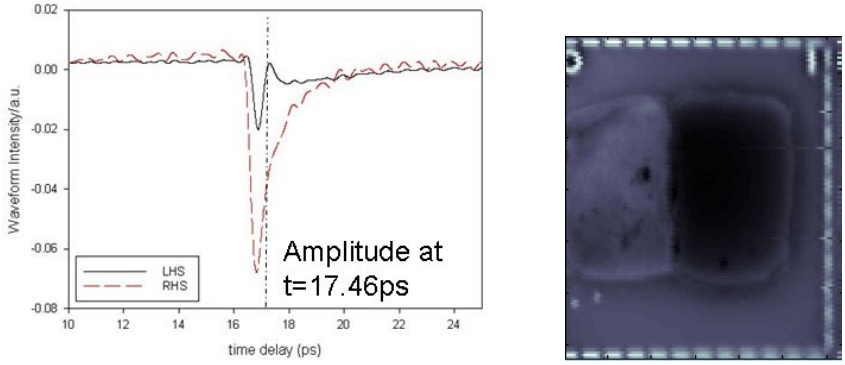

(a) Time Domain plot (b) THz image

Figure 3.11: THz image based on measured amplitude at t=17.46ps

The TPI system has a dedicated image reconstruction package, ScAnalyze, which allows for the production of images utilising parameters based on either the time or the frequency domain. At any position in the image, the software can display both the time and frequency domain waveforms. The user is able to select regions of interest (ROI) within an image to find the mean and standard deviation of the selected datapoints or an average of all the waveforms in the selected area.

3.5.4 Concentration determination techniques

Concentration analysis of the solute concentration, using both measurements of transmission and reflection data, was performed using three methods. Firstly, a method based on linear spectral decomposition of the absorption coefficient measurements of the samples, section 3.5.4.1, secondly an empirical analysis method based on the averaging of both the real and imaginary parts of the calculated dielectric coefficient of the samples, section 3.5.4.2, and, finally, an empirical analysis method based on the identified trends of the determined Debye relaxation parameters with concentration, section 3.5.4.3.

3.5.4.1 Method 1: Linear spectral decomposition

The linear spectral decomposition method for concentration determination is based on a linear forward model, the Beer-Lambert law, equation 2.43, which is typically used for conventional optical transmittance spectroscopy of non-scattering media containing different chromophores (Cope 1991). In this technique, the total absorption of the interrogated medium is considered to be the sum of the absorption contributions of each solute, where the contribution of each solute is linearly dependent upon its concentration as shown in equation 3.3. In the THz radiation region, the influence of scattering is assumed to be negligible in comparison to that of absorption meaning that the THz signal amplitude can be taken to be a linear function of μ_a (Smye et al. 2001, Zhang 2002). The concentration of each solute can be estimated directly using multilinear regression.

$$\mu_{a(phantom)} = \mu_{a(1)}.c_1 + \mu_{a(2)}.c_2 + .. + \mu_{a(n)}.c_n \tag{3.3}$$

To solve for concentration, prior information of the specific absorption coefficients of the absorbing chromophores is required. Measurements must be made at multiple wavelengths using a minimum of n wavelengths for a sample containing n absorbing

chromophores. This can be represented in matrix form, as illustrated in equation 3.4.

$$\begin{pmatrix} c_1 \\ c_2 \\ \vdots \\ c_n \end{pmatrix} = \begin{pmatrix} A_{\lambda_1} \\ A_{\lambda_2} \\ \vdots \\ A_{\lambda_n} \end{pmatrix}^{-1} \times \begin{pmatrix} \varepsilon_1(\lambda_1) & \varepsilon_1(\lambda_2) & \dots & \varepsilon_1(\lambda_n) \\ \varepsilon_2(\lambda_1) & \varepsilon_2(\lambda_2) & \dots & \varepsilon_2(\lambda_n) \\ \dots & \dots & \dots & \dots \\ \varepsilon_4(\lambda_1) & \varepsilon_4(\lambda_2) & \dots & \varepsilon_4(\lambda_n) \end{pmatrix} \tag{3.4}$$

The Beer-Lambert law is typically applied to transmission mode measurements, however, in this work we will also be applying the theory to reflection measurements. The reflection from THz reflection measurements is specular resulting from coherent incident light and, as the wavelength is larger than the scattering bodies in the samples and tissues studied, the reflected radiation is not diffused. This means that the use of the Beer-Lambert law is applicable to THz reflection measurements.

The technique relies on prior knowledge in the form of the absorption coefficient spectra of the solutes. For the water, methanol and lipids, these coefficients were determined easily from measurements of the pure compounds. For the determination of the absorption coefficients of the sucrose and gelatin molecules, it was assumed that the contribution from the solute and solvents of the aqueous sucrose and gelatin mixtures was linearly additive, that is, the contributions to the measured absorption coefficient of the mixtures follows equation 3.5. Previous studies of aqueous protein solutions have found this trend to be true (Xu et al. 2006). Equation 3.5 was, therefore, used to extraction of the absorption coefficients of the 'dry' sucrose and gelatin molecules where the absorption coefficient of water was multiplied by the % concentration of water in the solutions and then subtracted from the solution absorption coefficient. Following the same principle, determination of the hydrated molecules is achieved if the number of water molecules associated with the sucrose and gelatin molecules is subtracted, as detailed in section 2.5.4.3, from the total concentration of water in the solutions.

$$\mu_{a(dry)} = \mu_{a(solution)} - \mu_{a(H_2Obulk)} - \mu_{a(H_2Ohydrationlayer)} \tag{3.5}$$

3.5.4.2 Method 2: Dielectric averaging

The second method of concentration analysis was based on recent work, (Jepsen et al. 2007), which has suggested that empirical equations can be generated to relate the true concentration of a single solute to the averaged value of the real, ε', and imaginary, ε'', parts of the dielectric coefficients across a frequency range. These equations are then used as the basis for concentration analysis on future measurements of solutions

containing the same solutes. This method incorporates, through the use of both the real and imaginary parts of the dielectric coefficient, the measured absorption coefficient and refractive index which may improve the accuracy of the technique in comparison to the linear spectral decomposition method which uses only the absorption coefficient. This method will not, however, offer any explanations of the physics behind the concentration dependence of the materials.

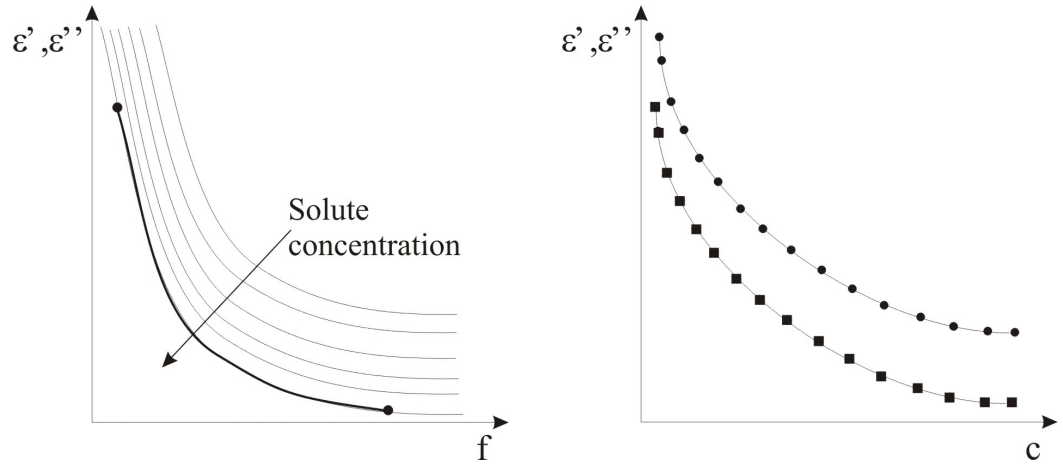

(a) Measured data (b) Averaged data

Figure 3.12: Diagram showing the implementation of the dielectric averaging method. a) Diagram representing the change in the real and imaginary dielectric coefficient spectra, as a function of frequency, as the solute concentrations of a generic phantom are varied. The spectra of each solution concentration is averaged over a given frequency range as shown. b) Diagram representing the variation with solute concentration of the averaged real and imaginary dielectric coefficients of a generic phantom. These trends with concentration are used to create empirical equations to be used in the determination of phantom concentrations.

The implementation of this method for a particular solution relies on establishing the variation with solute concentration of the calculated $\varepsilon^{'}$ and $\varepsilon^{''}$ over a frequency range, as shown in figure 3.12(a). The averaging was done over the frequency range 0.1-1 THz for both the transmission and reflection measurements. $\varepsilon^{'}$ and $\varepsilon^{''}$ are determined following equations 2.45 and 2.46 at each phantom concentration. The values of $\varepsilon^{'}$ and $\varepsilon^{''}$ are averaged and are plotted against solute concentration, as shown in figure 3.12(b). Empirical equations are then formed which describe the trend of both $\varepsilon^{'}$ and $\varepsilon^{''}$ with concentration. These take the form, in this work, of either an exponential (equation 3.6) or linear (equation 3.7) trend with concentration where x is the concentration of a single solute in the phantom, y is the measured $\varepsilon^{'}$ and $\varepsilon^{''}$ averaged over a frequency range and A, B and C are fitting coefficients. This is done for both transmission and reflection measurements. For the two component phantoms, the empirical equations

were created where x was the non-water solute concentration. To describe the concentration dependence of the three component phantoms, the empirical equations were generated by combining the equations for the two component mixtures. For example, for the sucrose, methanol and water solutions, the empirical equations for the sucrose and water solutions and the methanol and water solutions were combined. This is shown in equation 3.8, where x indicates the concentration of methanol, z indicates the concentration.

$$y = A + B\exp^{Cx} \tag{3.6}$$

$$y = A + Bx \tag{3.7}$$

$$y = A_{H_2O} + B_{H_2O}\exp^{C_{H_2O}x} + A_{methanol} + B_{methanol}z \tag{3.8}$$

The empirical equations form what can be considered a 'look-up-table' for the determination of phantom concentration. To determine the concentration of an unknown solution, the measured $\varepsilon^{'}$ and $\varepsilon^{''}$ values are averaged over the frequency range and substituted into the corresponding empirical equation, using the pre-determined fitting parameters. The two equations are inverted and solved for x (and y for the three component phantoms), resulting in an estimation of the solute concentration. An average of the two estimations is formed which provides the concentration estimate of the method.

3.5.4.3 Method 3: Inversion of Debye relaxation parameters

The third method of concentration analysis was based on determining a variation with solute concentration of the determined Debye relaxation coefficients. The complex dielectric coefficient for both the transmission and reflection measurements was determined, following equation 2.44, from the measured absorption coefficients and refractive indices of the mixtures. Debye theory, outlined in section 2.4.2.1, was then fitted to the complex refractive index of the phantoms. In this work both the double and triple Debye theories were used, where double Debye theory describes materials with two distinct relaxation processes and triple Debye theory describes materials with three distinct relaxation processes. The double and triple Debye equations were expanded from equation 2.49 to yield equations 3.9 and 3.10, respectively, where Δ_1, Δ_2, Δ_3, τ_1, τ_2, τ_3 and ε_∞ are the Debye relaxation coefficients. Δ_1, Δ_2 and Δ_3 are equal to $\varepsilon_S - \varepsilon_1$, $\varepsilon_1 - \varepsilon_2$ and $\varepsilon_2 - \varepsilon_3$, respectively, and describe the relative contributions to the complex dielectric coefficient from the relaxation modes, τ_1, τ_2 and τ_3. A non-linear least squares fitting routine (Matlab function *lsqnonneg*) was employed to fit the Debye coefficients to the measured complex dielectric coefficient. In all cases ε_S was held constant to improve the stability of the fitting procedure. As ε_S represents the static dielectric constant, a constant property for a given molecule, this approach is valid. All

fitting procedures were performed in the frequency range 0.15-2 THz.

$$\widehat{\varepsilon}(\omega) = \varepsilon_\infty + \frac{\Delta_1}{1 + (j\omega\tau_1)} + \frac{\Delta_2}{1 + (j\omega\tau_2)} \tag{3.9}$$

$$\widehat{\varepsilon}(\omega) = \varepsilon_\infty + \frac{\Delta_1}{1 + (j\omega\tau_1)} + \frac{\Delta_2}{1 + (j\omega\tau_2)} + \frac{\Delta_3}{1 + (j\omega\tau_3)} \tag{3.10}$$

Triple Debye theory was used to determine the Debye relaxation coefficients of the gelatin and water gels. The relaxation mechanisms observed in the dielectric spectra of the macromolecules are more numerous than those of less complex molecules and can include relaxations of bulk water, hydration waters of the molecules or water molecules trapped within the structure of the molecule or relaxations of the molecules themselves, such as amino acid side chains of a protein. This range of relaxation mechanisms can give rise to a broad spectrum of relaxation times in the dielectric relaxation response of macromolecular solutions and gels (Hasted 1973) which makes the detection of distinct relaxations within the gels difficult. Triple Debye theory has been used in previous studies of water-macromolecule studies to identify separate relaxation mechanisms within aqueous solutions of proteins (Grant 1966, Davies 1977, Pethig 1992, Yoshioka et al. 1995). Double Debye theory was used to determine the Debye relaxation coefficients of the methanol and water solutions despite triple Debye theory used to determine the Debye relaxation coefficients of pure methanol. When studying solutions of water and methanol the analysis procedure is simplified if a single modelling tool is used to extract the Debye relaxation coefficients of the solutions. As methanol is a simple alcohol with a chain length not much larger than that of water and forming only a few hydrogen bonds, double Debye theory can be used as a generalised model where the two relaxation terms can be considered as *effective* relaxation times of all possible relaxation process of the solution (Venables and Schmuttenmaer 2000b). Double Debye theory was used to determine the Debye relaxation coefficients of all other phantoms.

Values of the static dielectric coefficient, ε_S, were extrapolated between the ε_S values of pure water and pure methanol a technique verified by previously published studies (Venables and Schmuttenmaer 2000b, Koeberg et al. 2007). ε_S for the lipid and water emulsions were extrapolated between the ε_S values of pure water and pure lipid. ε_S for the sucrose and water solutions and water and gelatin gels were held constant at extrapolated values from previously reported data for aqueous sucrose and gelatin (ICT 1933, Gutman et al. 1992). ε_S for the three-phase phantoms were extrapolated, with respect to concentration, from previously reported values for their component parts and

held constant during the fitting routine.

The implementation of this method for concentration analysis relies on establishing the variation with solute concentration of each of the Debye relaxation parameters over a frequency range, as with the dielectric averaging method. As with the dielectric averaging method, empirical equations are created relating the variation of each of the Debye relaxation parameters, and ε_∞ to solute concentration, x. The empirical equations formed can be considered to be 'look-up-tables' for the determination of phantom concentration. To determine the concentration of an unknown solution, the calculated complex dielectric coefficient values of the phantom are substituted into equation 3.9, the double Debye equation, where the Δ_1, Δ_2, τ_1, τ_2 and ε_∞ coefficients have been replaced by their corresponding empirical equations. Equation 3.9 is then solved for x, solute concentration using a least squares fitting routine (Matlab function *fminsearch*).

3.5.4.4 Resolution and accuracy

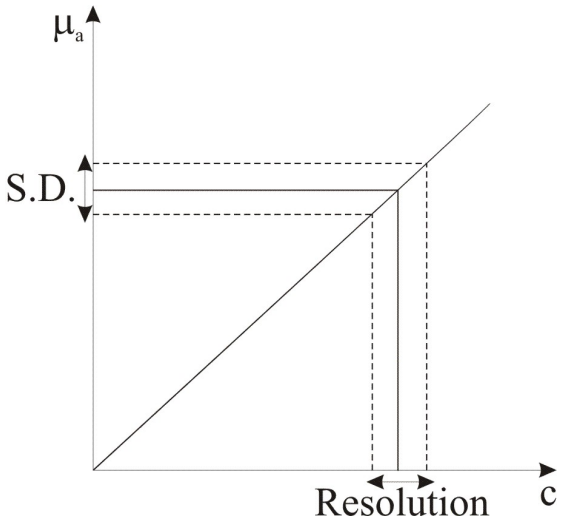

Figure 3.13: Representation of the calculation of resolution from an absorption coefficient measurement.

The resolution and accuracy of each of the concentration analysis methods were determined for each phantom analysed. The accuracy of a measurement is a gauge of the degree of closeness of a calculated quantity to its true value. For the three concentration analysis methods used here the accuracy at each discrete phantom concentration was determined by finding the difference between the calculated and the true concentration values. The discrete accuracies were then averaged over the concentration range of each phantom to give an estimation of accuracy for the application of each method to

Table 3.2: Standard Deviation of distilled water measured over a number of days and averaged over the frequency range 0.1-1.5 THz for the transmission measurements and 0.1-1 THz for the reflection measurements

	μ_a	n	ε'	ε''
Transmission	3.2	0.01	0.2	0.1
Reflection	8.6	0.1	0.4	0.2

the specific phantoms.

$$resolution = \sqrt{var(P)} = \sqrt{(XX')^{-1}\sigma^2} \tag{3.11}$$

The resolution in the determined parameters reflects the smallest detectable change in the determined parameters given the error in the measurement, as illustrated in figure 3.13, where concentrations within the resolution bracket have an equal statistical significance. The resolution in the determined parameters was calculated using equation 3.11, where P is an array of the variable input parameters, X is the design matrix of the model (X' is its conjugate transpose), which contains the derivative of the model with respect to the input parameters, and σ is the standard deviation of signal amplitude of the combined spectra, which was obtained from repeated measurements. The resolution is, therefore, a measure of the sensitivity of concentration resolution technique to noise on the data. For non-linear concentration variation, for example in the variation of the averaged dielectric coefficients or the Debye relaxation parameters which can be exponential or polynomial respectively, a linear gradient approximation was made at the points of maximum and minimum variation in the concentration trends.

The standard deviation was determined from multiple measured for each data set. However the standard deviation used in the determination of these resolutions was derived from measurements made over a number of days of a stable, constant material; distilled water. This was done for both transmission and reflection mode measurements, and are given in table 3.2. These standard deviations were used rather than standard deviations of the individually measured data sets, as variation in the system over a number of days is larger than the variation in a single day, meaning that the resolution determined in this way gives a more accurate representation of the limitations of spectroscopy and imaging in the THz electromagnetic region.

Part II

THz spectroscopy of tissue phantoms

Chapter 4

Optical properties and relaxation coefficients of pure components

The aim of the work presented in this thesis is to develop spectroscopic methods for diagnosis of tissue pathologies using THz radiation. This requires the ability of THz imaging and spectroscopy to distinguish different tissue types to be assessed. The development and validation of these spectroscopic methods was achieved through the use of phantoms. An optical phantom is designed to imitate the spectroscopic properties of a tissue at the appropriate optical wavelengths. A phantom is most often used when it is desirable to validate a technique as the physical properties of the phantom, such as concentrations and homogeneity, can be very accurately controlled.

Phantoms have been used in previous studies in the THz region where gels containing different concentrations of naphthol green dye, distilled water and TX151, a gelling agent, were created to recreate the optical properties of tissue (Walker et al. 2004a). The phantoms provided good similarities with the absorption of tissue in the THz region. The use of these phantoms to mimic tissue, however, was limited due to the significant difference between the refractive index of the phantoms and tissue.

In this study, a different approach to the design of phantoms is taken. As the main aim of the work is to develop and validate theoretical models for the determination of tissue composition, an ideal phantom would provide physical properties equivalent to tissue. Phantoms comprising the main constituents of tissue (water, lipids and protein) were created where the interaction between THz radiation and the phantom was similar to tissue. The validated theoretical methods were eventually tested on these phantoms to establish the sensitivity of THz spectroscopy in determining tissue composition, however, a series of simpler phantoms were also used to robustly test the THz spectroscopic sensitivity.

Firstly the absorption coefficients and refractive indices of individual materials were measured in the THz wavelength region. These materials were water, methanol, lipid, gelatin and sucrose. As water is strongly absorbing at THz frequencies, it is hypothesised that tissue water content is one of the main contrast mechanisms in THz images (Pickwell et al. 2004a, Fitzgerald et al. 2006). Methanol, though not of biological relevance, is a very well studied molecule, particularly in its interactions with water and is studied here for the purposes of experimental validation of THz spectroscopic techniques. Lipids, major components of adipose tissues, are composed of long, non polar, hydrocarbon chains, and so lipids are expected to be less absorbent of THz radiation but may nevertheless provide contrast. Gelatin, an extract of collagen, has been used here to investigate the bonding effects between macromolecules and their water environment. Sucrose is a biologically relevant molecule and presents a more regular and well defined macromolecular structure than gelatin.

Two-component phantoms were made comprising water with either methanol, lipid, sucrose or gelatin. These provided simple test materials. The study of the interactions between these molecules enabled the sensitivity of THz spectroscopy as determined by the spectroscopic methods under investigation to be validated and the methods developed.

Two three-component phantoms were created, one containing water, methanol and sucrose at two concentrations and a second containing water, gelatin and lipid at a number of concentrations. The first phantom was used to validate one of the methods developed as part of the work presented in this thesis, the spectrally averaged dielectric coefficient method, against published results from literature (Jepsen et al. 2007). The second phantom is based on a solid tissue mimicking phantom described by Lazebnik (2005) and is used to provide a tissue-like phantom.

In this chapter, the absorption coefficients, refractive indices and dielectric relaxations measured on the pure materials that were used in the preparation of tissue phantoms are presented. While the absorption coefficients of water, methanol and the lipids could be measured directly using transmittance spectroscopy, the absorption coefficients for sucrose and gelatin were obtained from measurements of aqueous solutions. This was necessary in order to obtain the absorption coefficients of the biologically more relevant 'hydrated' state of the molecules. The absorption spectra, refractive index and the dielectric spectra of the pure compounds were then used as prior information in

the determination of concentration from two-phase and three-phase mixtures. These measurements were all made in transmission mode.

4.1 Water and methanol

4.1.1 Absorption coefficient and refractive index

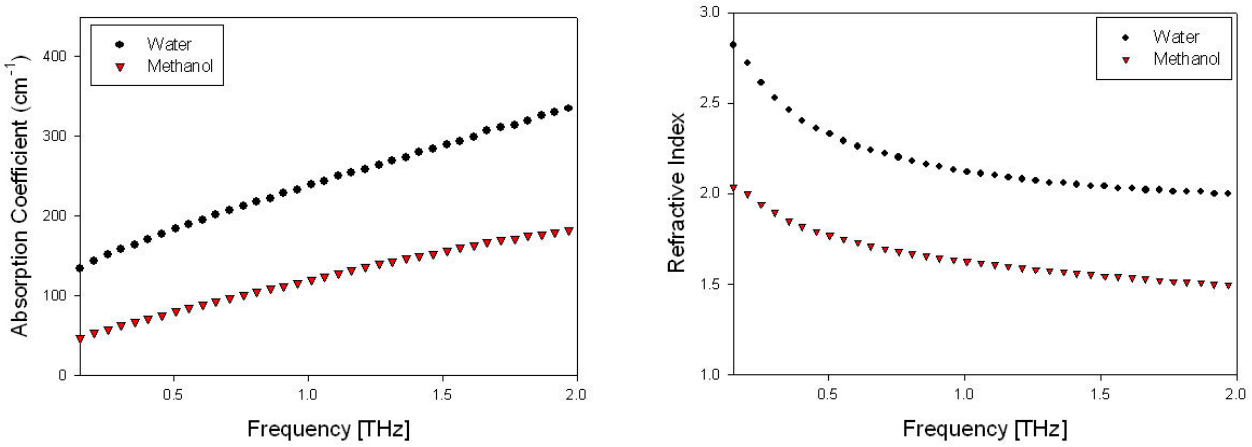

(a) Absorption Coefficient (b) Refractive Index

Figure 4.1: The a) absorption coefficient and b) index of refraction of methanol and water measured in transmission between 0.1 and 2.5 THz.

The absorption coefficients and refractive indices of methanol and water were measured in transmission mode and are shown in figure 4.1 for a frequency range of 0.1 to 2 THz. The average standard deviations of the absorption coefficient are ± 1.01 cm^{-1} for water and ± 1.72 cm^{-1} for methanol. The average standard deviations of the refractive index are ± 0.02 for both methanol and water. The absorption coefficients of both water and methanol increase with frequency. The absorption coefficients and reflective indices of water are larger than those of methanol which is due to the more polar nature of the water molecules compared to that of methanol, as described in section 2.5.2. The measured absorption coefficients and reflective indices of these compounds agree with previously presented measurements (Barthel et al. 1990, Kindt and Schmuttenmaer 1996, Asaki et al. 2002). The steadily increasing absorption spectra of water and methanol can be explained by the influence of the strong resonant absorption peak in water at 5.6 THz. This absorption peak has been attributed to resonant stretching of the hydrogen bonds between water molecules within a tetrahedral network, as described in section 2.5.1. In addition, methanol has absorption peaks at 4.5 THz and 20.6 THz due to re-orientational processes of the methanol chains, as described in section 2.5.2.

4.1.2 Debye relaxation coefficients

The complex dielectric coefficient of both water and methanol were calculated from the measured absorption coefficients and refractive indices according to equation 2.44 on page 32. From the complex dielectric coefficients, the Debye relaxation coefficients were determined, over the 0.1-2 THz frequency range. As Debye theory describes only rotational diffusion in molecules and the principal absorption bands at higher frequencies of both water and methanol are ascribed to restricted oscillations of the molecules, the validity of Debye theory is limited to the lower frequency range (Pickwell 2005). Double Debye theory, equation 3.9, was used to determine the water relaxation coefficients while triple Debye theory, equation 3.10, was used to determine the methanol relaxation coefficients. Due to the longer length of the methanol molecule, it has been found that triple Debye theory provides the most accurate description of the complex dielectric coefficient of methanol (Barthel et al. 1990, Kindt and Schmuttenmaer 1996, Asaki et al. 2002). The Debye relaxation coefficients were determined using a non-linear least squares fitting routine (Matlab function *lsqnonneg*). ε_S, the real part of the complex dielectric coefficient at low frequency, is a constant value and so was held constant to stabilise the fitting routines. ε_S was fixed at 32.72 for methanol (Wohlfarth 2008) and 78.8 for water, which was calculated using the temperature-dependent formula for water (Ronne et al. 1997) in line with published data (Pickwell et al. 2004b).

Figures 4.2(a) and 4.2(b) show a Cole-Cole plot (an Argand diagram of $\varepsilon^{'}$ against $\varepsilon^{''}$) which demonstrates good agreement between model and data. Figures 4.2(c) and 4.2(d) show the comparison between the refractive indices and absorption coefficients calculated from the Debye coefficient and the measured data. Good agreement is achieved between the calculated and measured refractive indices and absorption coefficients of water across the whole frequency range while the agreement between the calculated and measured refractive indices and absorption coefficients for the methanol data show a good agreement above 0.4 THz. The discrepancies at lower frequencies for methanol may be due to differences between the studies in the values of ε_S used, as this parameter represents low frequency behaviour.

The Debye relaxation coefficients determined for water and methanol are given in table 4.1 alongside previously published values from literature. The Δ_1, Δ_2 and Δ_3 terms describe the relative contributions from the relaxation modes, τ_1, τ_2 and τ_3, respectively. The relaxation times of methanol are much slower than those of water and can be ascribed to stronger methanol hydrogen bonds and their longer average lifetime

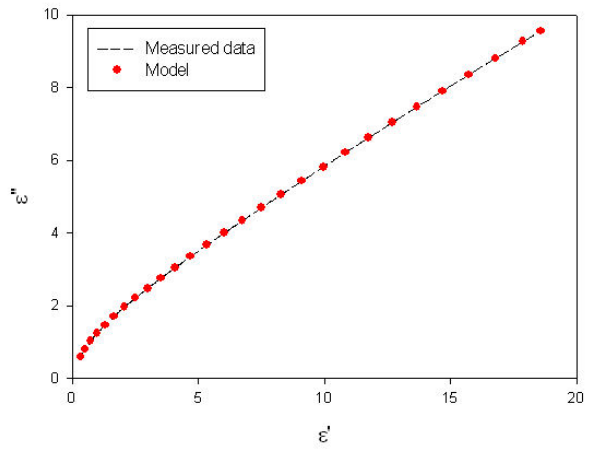

(a) Cole-Cole: Water

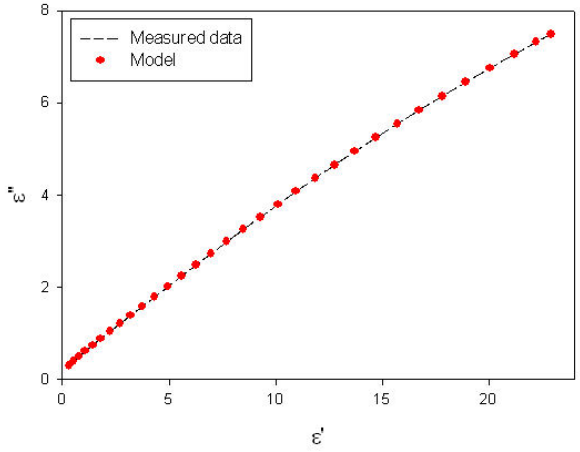

(b) Cole-Cole: Methanol

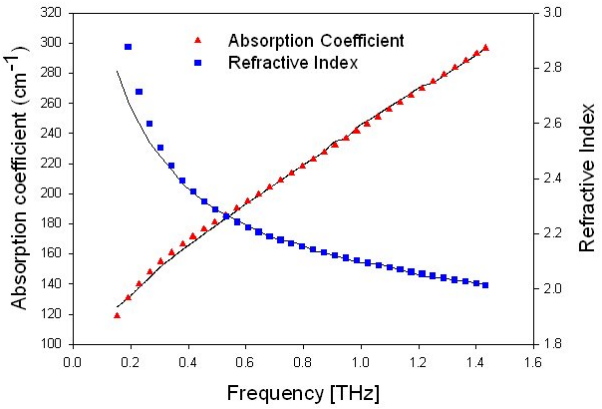

(c) Optical data comparison: Water

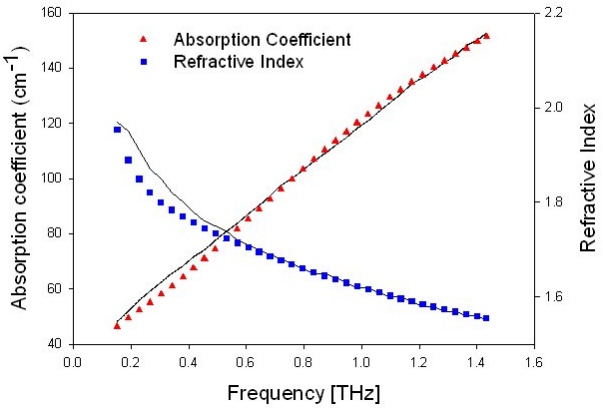

(d) Optical data comparison: Methanol

Figure 4.2: a) and b) show Cole-Cole plots of ε' vs ε'' of water and methanol. c) and d) show the refractive index and absorption coefficient as a function of frequency of water and methanol. In both graphs, the dots represent the measured data and the lines represent the fitted data.

Table 4.1: Triple Debye coefficients for pure methanol and Double Debye fitting coefficients for pure water

	Δ_1	Δ_2	Δ_3	τ_1(ps)	τ_2(ps)	τ_3(ps)	Frequency range (THz)
Methanol[a]	27.77	1.84	1	38.76	1.06	0.22	0.15-1.5
Methanol[b]	27.28	1.98	1.27	48	1.25	0.16	0.06-1.5
Methanol[c]	26.59	1.01	2.11	51.5	7.09	1.12	0.3-0.5
Methanol (this work)	**26.3**	**1.0**	**3.4**	**32.3**	**1.6**	**0.2**	0.1-2
Water[d]	75	1.9	-	8.5	0.17	-	0.1-2
Water[b]	73.87	1.45	-	8.24	0.18	-	0.06-1.02
Water[e]	74.0	1.8	-	8.5	0.15	-	0.1-2
Water (this work)	**74.2**	**1.4**	**-**	**8.4**	**0.1**	**-**	0.1-2

[a] (Asaki et al. 2002)
[b] (Kindt and Schmuttenmaer 1996)
[c] (Barthel et al. 1990)
[d] (Ronne et al. 1997)
[e] (Pickwell et al. 2004b)

compared to water (Matsumoto and Gubbins 1990, Suresh and Naik 2002).

Slight differences exist between the Debye relaxation coefficients determined by each separate study given in table 4.1. Temperature-dependent studies of water and heavy water (Ronne et al. 1997) have shown there is no dependence on the measured properties over the small temperature ranges seen in these studies. Temperature differences are, therefore, unlikely to be the source of the differences in the determined values by the different groups. Other differences between parameters are may arise from differences in experimental conditions and fitting methods. Different systems have led to different determined coefficients the earlier work due to systematic errors causing differences between measured absorption coefficients and refractive indices (Pickwell et al. 2004b). The complex refractive indices calculated using the method described in this work are only accurate if it can be assumed that the incident radiation, at each frequency, can be approximated by a normal incidence plane-wave. The beams in a THz spectrometer, however, are not appropriately modelled by a normal incidence plane wave as they suffer diffractive spreading. This will result in an error in the derived optical properties (Bowen et al. 2004). Experimental errors may include the purity of the materials used. The critical frequency for a Debye process with relaxation time τ is given by $\omega_{crit} = \tau^{-1}$ (Kindt and Schmuttenmaer 1996). For example, to be able to detect a time constant of 0.1 ps, the critical frequency is 10x10^{12} rad/s or 1.6 THz. If ω_{crit} is greater than the maximum probe frequency then it will be difficult to accurately determine the relaxation time. Therefore, the frequency ranges used in the determination of each set of Debye coefficients, as given in table 4.1, affect the extent of the range of Debye relaxation times each study is able to accurately determine. Differences in the values chosen for the ε_S of methanol between the studies may account for the differences in relaxation coefficients identified for methanol.

4.2 Lipids

4.2.1 Absorption coefficient and refractive index

The frequency dependence of the absorption coefficient and refractive index of pure lipids were measured in transmission, the measurement procedure of which is described in section 3.5.2.1. The results are presented in figure 4.3. The average standard deviations of these measurements are $\pm$0.04cm^{-1} for the absorption coefficient and $\pm$0.002 for the refractive index. These measurements agree with previously presented measurements made on plant, animal and synthetic oil samples (Hu et al. 2005, Gorenflo et al. 2006, Nazarov et al. 2008). The absorption coefficient and refractive index of

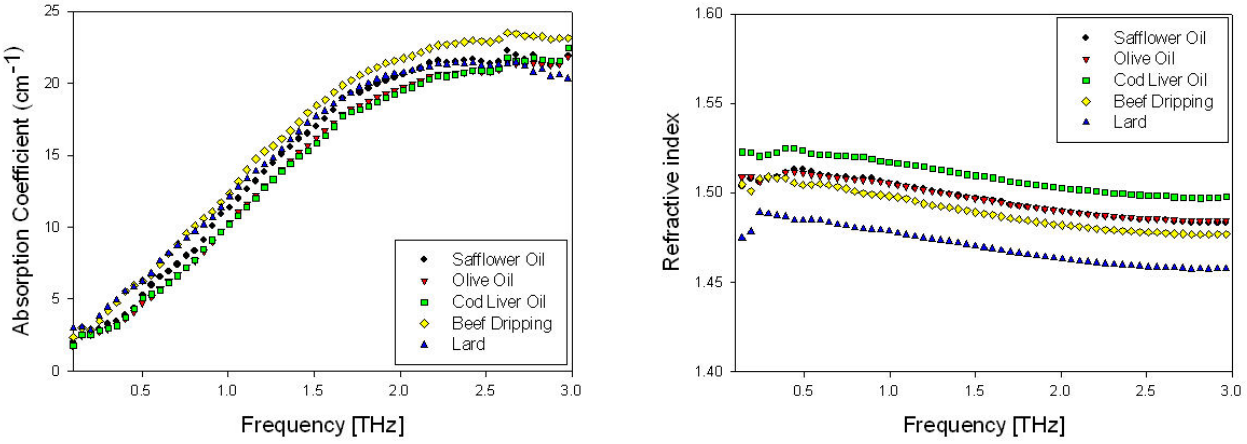

(a) Absorption Coefficient (b) Refractive Index

Figure 4.3: The THz a) absorption coefficient and b) index of refraction of pure lipids measured in transmission

lipids are smaller than those for water (μ_a=220 cm^{-1}, f=1 THz) and methanol (μ_a=120 cm^{-1}, f=1 THz) which results in high signal-to-noise ratios allowing measurements to be made up to a frequency of 3 THz. The absorption coefficient for all lipids increases with frequency and plateaus around 2 THz.

4.2.2 Debye relaxation coefficients

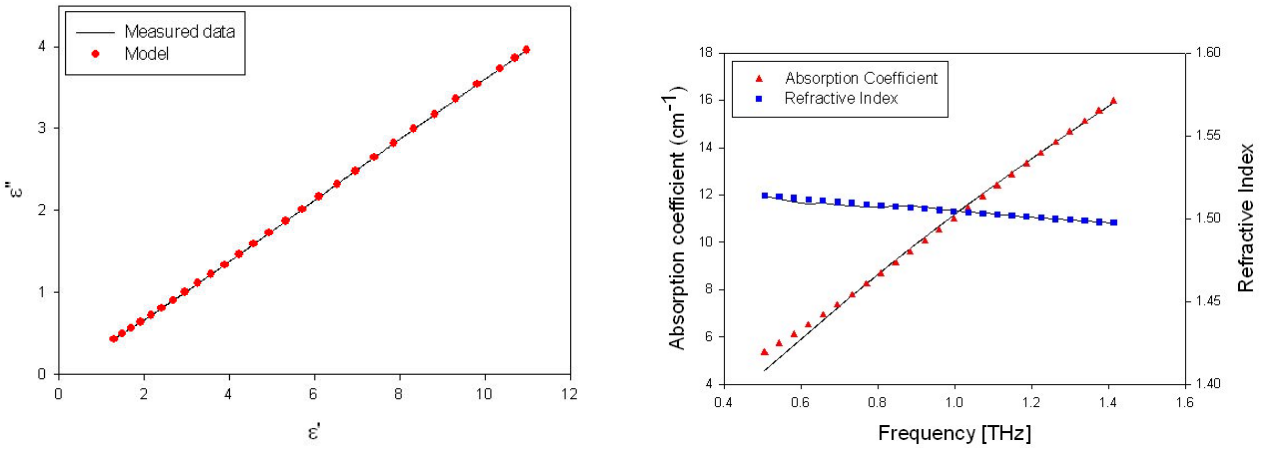

(a) (b)

Figure 4.4: a) shows the Cole-Cole plot of ε' vs ε'' of lipid. b) show the refractive index and absorption coefficient as a function of frequency of lipid. In both graphs, the dots represent the measured data and the lines represent the fitted data.

The complex dielectric coefficient of the different lipids were determined from the measured absorption coefficients and refractive indices according to equation 2.44. By fitting double Debye theory, equation 3.9, to the complex dielectric coefficients over

the 0.1-2 THz frequency range, the Debye relaxation coefficients were determined. The Debye relaxation coefficients were determined using a non-linear least squares fitting routine (Matlab function *lsqnonneg*). ε_s, a constant, was held constant at 2.5 (Thompson 2005). Figure 4.4(a) shows the Cole-Cole plots of ε' vs ε'' for both the measured and fitted data and for lipid which demonstrates good agreement between model and data. Figure 4.4(b) shows a comparison between the refractive indices and absorption coefficients calculated from the Debye coefficient and the measured data for lipid, calculated from double Debye theory. A good agreement is achieved between the measured and calculated refractive indices and absorption coefficients of lipid above 0.6 THz.

Table 4.2: Double Debye fitting coefficients for lipids

Lipid	Δ_1	Δ_2	τ_1(ps)	τ_2(ps)
Safflower Oil	0.2	0.1	1.6	0.1
Olive Oil	0.2	0.1	1.9	0.1
Cod Liver Oil	0.2	0.1	1.2	0.1
Beef Dripping	0.2	0.1	1.0	0.1
Lard	0.3	0.1	1.4	0.1

The Debye coefficients are given in table 4.2 for the five oil types examined. Δ_1 and Δ_2 are the relative contributions from the relaxation modes, described by relaxation times τ_1 and τ_2, respectively. Though lipids are non-polar materials, and hence have no permanent dipole moment, NMR studies have confirmed a relaxation effect in pure lipids (Todt et al. 2006, Hornak et al. 1990, Opstad et al. 2008). The absorption coefficient spectra of the lipids in the THz region are the results of transient collision-induced dipole moments which create short-range temporary ordering in the molecules (Pedersen and Keiding 1992).

The application of Debye theory to lipid data has little merit unless the molecular properties of the lipids can be related to the determined relaxation coefficients. If a lipid is considered to be a liquid containing discrete molecules with a spread of molecular radii, as is the case with the variation in carbon chain length of the component fatty acids of each lipid, shown in table 4.3, then one or more of the fitting coefficients could be related to the average chain length of the lipids. In figure 4.5, the Debye fitting coef-

Table 4.3: Average carbon chain length of the fatty acids making up commercially available lipids (Gunstone 1996)

Lipid	Olive Oil	Safflower Oil	Cod Liver Oil	Beef Dripping	Lard
Av. number of carbon atoms	17.4	17.7	17.1	16.8	17.1

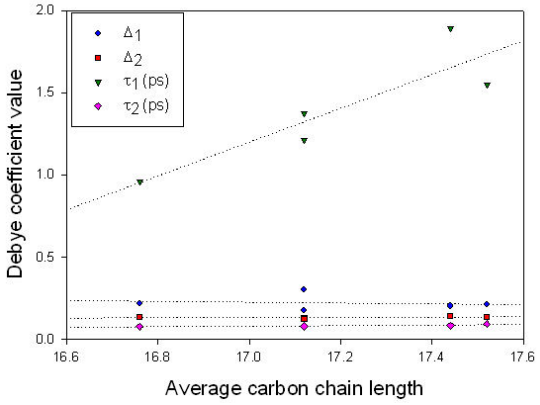

Figure 4.5: The Debye coefficients for five pure lipids shown in comparison to the average carbon chain length of the fatty acids contained within the lipids

ficients are compared to the molecular chain length in each lipid. For the case of τ_1, it can be noted that there is a trend towards an increase in relaxation time with increasing average carbon chain length. Comparisons with the other fitting coefficients yielded no obvious trend. Figure 4.5, therefore, suggests that the carbon chain length of lipids could be determined from the relaxation time τ_1 obtained by fitting double Debye theory to the measured data. The τ_1 relaxation time is much smaller than that noted for polar liquids, indicating a faster relaxation trend, which has been confirmed in nuclear magnetic resonance (NMR) studies of lipids (Godefroy et al. 2001).

4.3 Hydrated sucrose and gelatin molecules

When measuring the optical properties of macromolecules, it is essential to consider their hydrated state (the native or biologically active state which enables the molecule to engage in metabolic functions) rather than to measure them as dry powders. In this study, the optical properties of both the 'dry' and 'hydrated' molecules were determined from measurements of sucrose and gelatin in solution, as outlined in section 3.5.4.1, where the 'hydrated' molecules were assumed to comprise the 'dry' molecule plus the number of water molecules that are bound to the molecule. Estimates from

literature of the number of water molecules in the hydration layers for both sucrose and gelatin are given in section 2.5.4.3. Calculations for the 'dry' and 'hydrated' absorption coefficients and refractive indices were made from transmission measurements of each individual concentration of macromolecular solution or gel. These calculated absorption coefficients and refractive indices were then averaged to produce the absorption coefficients and refractive for the 'dry' and 'hydrated' states of both sucrose and gelatin indices given in the following sections.

4.3.1 Absorption coefficient and refractive index

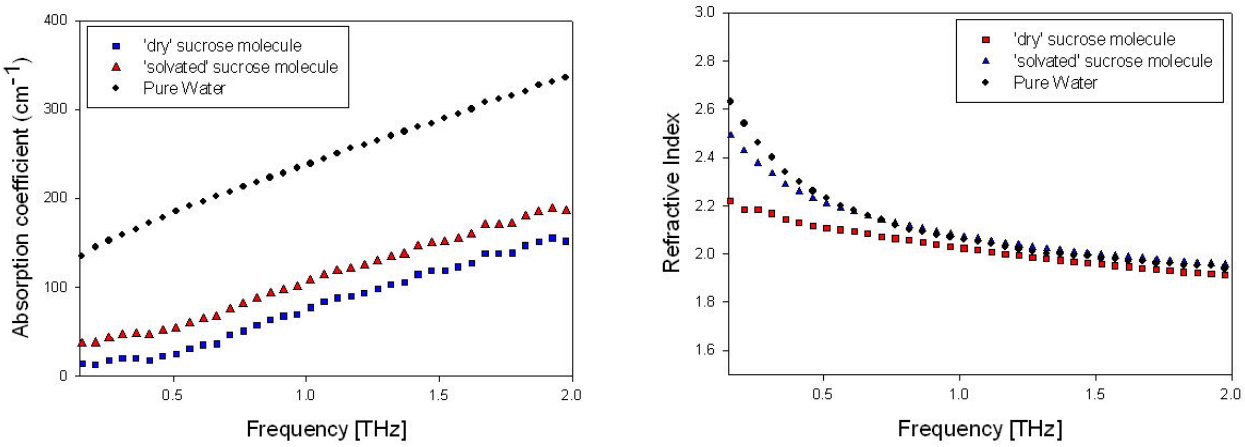

(a) Absorption Coefficient (b) Refractive Index

Figure 4.6: The THz absorption coefficient and index of refraction spectra of dry and hydrated sucrose, determined from measured absorption coefficient and index of refraction spectra of sucrose and water solutions, measured in transmission mode.

The absorption coefficients and refractive indices of the dry and hydrated sucrose and dry and hydrated gelatin molecules are shown in figures 4.6 and 4.7. The absorption coefficient and refractive index spectra of water are shown for comparison. The absorption coefficient and the refractive index of the dry molecules are lower than those of the hydrated molecules. The THz absorption coefficient of the hydrated molecules is larger than that of the dry molecules due to the contribution from the bound water. The overall shape of the spectrum of the dry and hydrated molecules is not significantly altered. Gelatin shows a larger difference in absorption coefficient between the dry and hydrated states than sucrose due to the larger number of water molecules that are bound to gelatin compared to sucrose, as discussed in section 2.5.4.3. A source of uncertainty in the calculated absorption coefficients and refractive indices of the hydrated molecules in the estimation of the hydration shell size. It is possible, therefore, that the true absorption coefficients and refractive indices of these molecules are between those

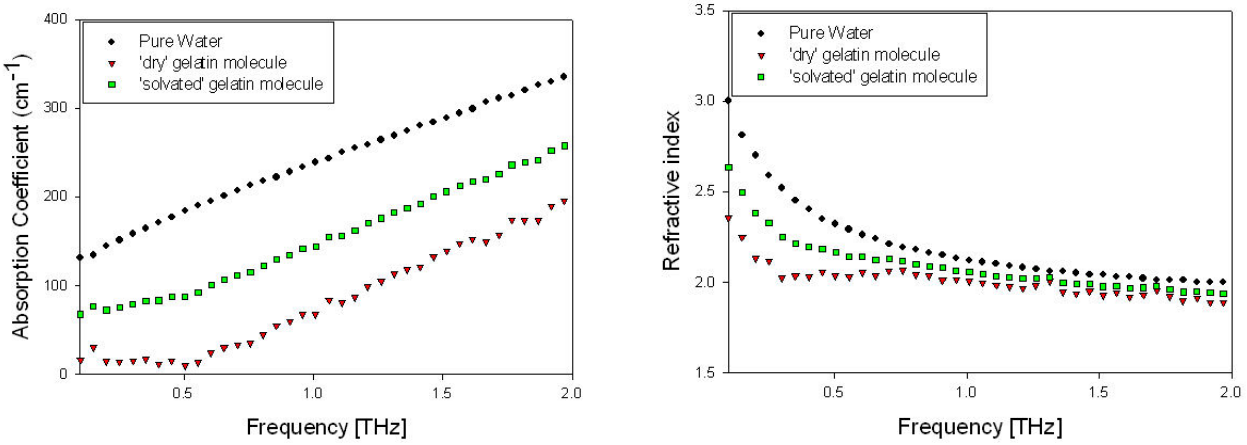

(a) Absorption Coefficient (b) Refractive Index

Figure 4.7: The THz absorption coefficient and index of refraction spectra of dry and hydrated gelatin, determined from measured absorption coefficient and index of refraction spectra of gelatin and water gels, measured in transmission mode.

given here for the 'dry' and 'hydrated' states. In this study the two extreme absorption coefficients (i.e. those of 'dry' and 'hydrated' gelatin and sucrose) are used.

Previous studies of dry protein and sucrose samples in the THz region have described a monotonic frequency dependent increase below 2 THz for dry samples of DNA, BSA, cytochrome c, polypeptides, myoglobin, DNA and collagen (Markelz et al. 2000; 2002, Yamamoto et al. 2002, Globus et al. 2002, Kutteruf et al. 2003, Zhang and Durbin 2006) and 1.45 THz for sucrose (Nagai et al. 2006, Upadhya et al. 2003). It has been suggested that this is due to a dense collection of overlapping vibrational modes in macromolecules. These result in a rapid rise with frequency in the density of vibrational modes followed by a plateau or saturation at higher frequencies. This has been recreated in molecular dynamics simulation studies of several small proteins (Brooks and Karplus 1983, Go et al. 1983, Hinsen 1998, Markelz et al. 2002, Whitmire et al. 2003). At 1.45 THz, dry samples of sucrose display distinct resonance (Walther et al. 2003, Jepsen and Clark 2007). These features, however, are not apparent in the measured absorption coefficient spectra determined during this study. Studies of hydrated sucrose have also shown the 1.45 THz resonance to be absent from the hydrated spectra (Nagai et al. 2006, Upadhya et al. 2003). For both the gelatin and sucrose samples, the spectra measured in this study show a strong monotonic frequency-dependent increase up to at least 2.5 THz without any apparent resonances. The monotonic increase with frequency observed in the absorption of sucrose and gelatin is consistent with a the proposed theory of a dense collection of overlapping vibrational modes. However, no

plateau is observed in the data from this study. Recent THz studies have also shown that this plateau, if reached, may be at much higher frequencies than predicted (Xu et al. 2006) which is may explain the results presented here.

4.3.2 Debye relaxation coefficients

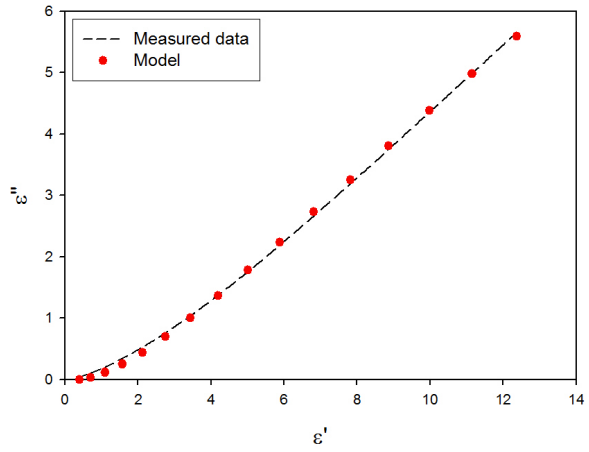

(a) Cole-Cole: Hydrated sucrose

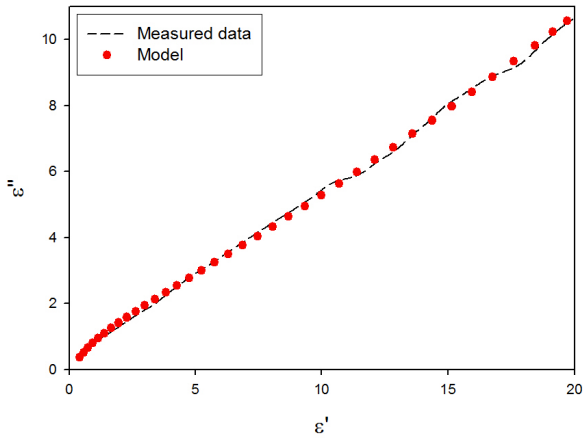

(b) Cole-Cole: Hydrated gelatin

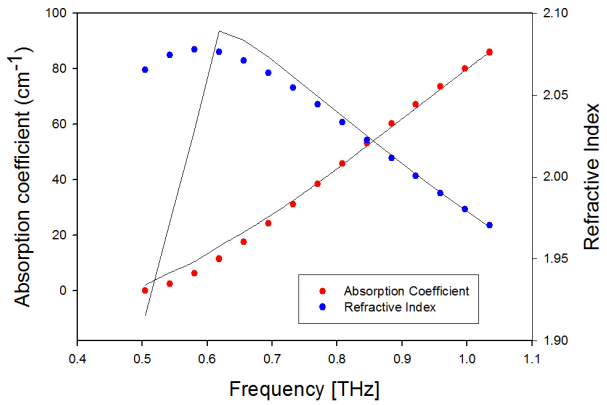

(c) Optical data comparison: Hydrated sucrose

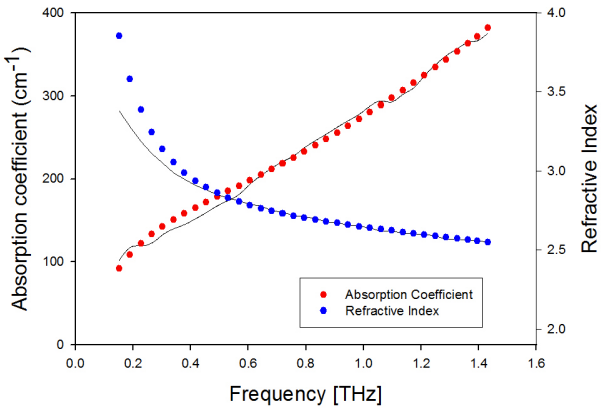

(d) Optical data comparison: Hydrated gelatin

Figure 4.8: a) and b) show Cole-Cole plots of ε' vs ε'' of hydrated sucrose and gelatin. c) and d) show the refractive index and absorption coefficient as a function of frequency of hydrated sucrose and gelatin. In both graphs, the dots represent the measured data and the lines represent the fitted data.

The complex refractive indices of the hydrated sucrose and gelatin molecules were determined from the measured absorption coefficients and refractive indices according to equation 2.44. By fitting double Debye theory, equation 3.9, to the complex dielectric coefficients over the 0.1-2 THz frequency range, the Debye relaxation coefficients were determined. The Debye relaxation coefficients were determined using a non-linear least squares fitting routine (Matlab function *lsqnonneg*). ε_s, a constant, was held constant

at values from previously reported data for sucrose and gelatin (ICT 1933). The determined Debye coefficients are given in table 4.4. The hydrogen bonding between the gelatin or sucrose molecules and water molecules is stronger than the hydrogen bonding between water molecules in free solution. This would suggest that the relaxation times of hydrated water would be slower in comparison to the free water which, from this study, has relaxation times of τ_1= 8.4ps and τ_2= 0.1ps. Studies of confined water in micelles have already shown a slowing in it's relaxation times in comparison to free water (Mittleman et al. 1997, Maeda and Kitano 1995). Studies have suggested that relaxation times of hydration water should be a factor of 10^1-10^4 slower than those of free water (Baumgartner et al. 2003, Bordat et al. 2004, Heugen et al. 2006). This would yield, assuming a principle relaxation time of 8.4ps as determined in this work, a relaxation of between 84ps and 84ns, which is not apparent from the results presented in table 4.4 which appear, instead, to be slightly faster than the relaxation times of free water determined in this study. As previously stated, the critical frequency for a Debye process with relaxation time τ is given by $\omega_{crit} = \tau^{-1}$ (Kindt and Schmuttenmaer 1996). In order to detect a time constant within the range of 84ps and 84ns, the critical frequency range is 11.9 MHz and 11.9 GHz, beyond the scope of the frequencies used in this work. Further experimental and modelling work could investigate the origin of these relaxation times in macromolecules.

Table 4.4: Debye coefficients for hydrated sucrose and gelatin molecules

	Δ_1	Δ_2	$\tau_1(ps)$	$\tau_2(ps)$
Gelatin	71.6	4.1	5.7	0.1
Sucrose	74.3	1.3	7.7	0.1

4.4 Optical properties of ancillary phantom manufacture materials

Additional compounds used in the manufacture of the water, gelatin and lipid phantoms are p-toulic acid, n-propanol and formaldehyde, as outlined in section 3.5.1.3. The concentrations of these materials in the phantoms are very low, as given in table 3.1, and the addition of these compounds is, therefore, not expected to affect the optical properties of the phantoms significantly. For completeness, the measured optical properties are

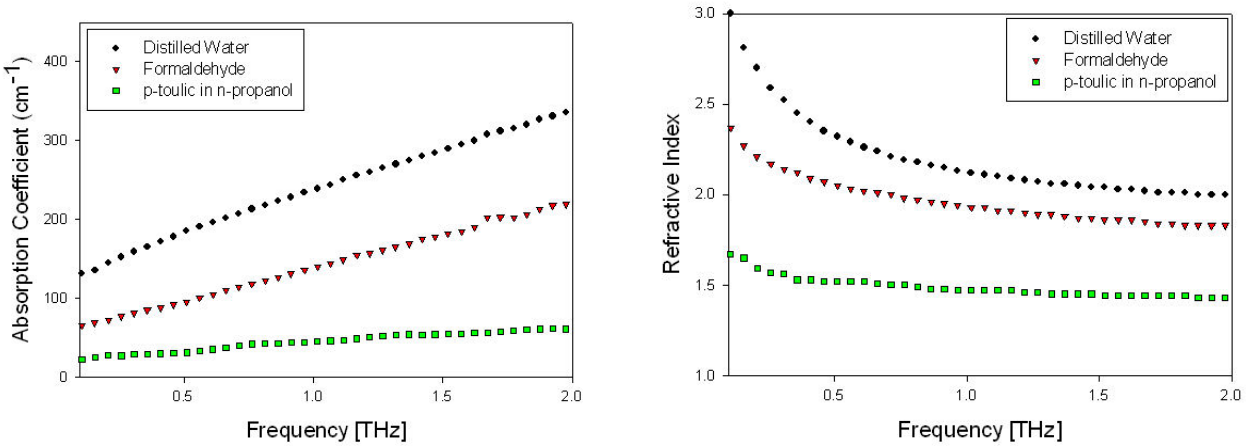

(a) Absorption Coefficient (b) Refractive Index

Figure 4.9: Spectra of the a) absorption coefficient and b) the refractive index of ancillary ingredients used in the manufacture of 3-phase phantoms, measured using transmission THz spectroscopy

given here. Figure 4.9 shows the measured absorption coefficient and refractive index spectra. The optical properties are shown for the p-toulic acid, a powder, dissolved in n-propanol, an alcohol, at the concentrations used in the manufacture of the phantoms. The absorption coefficients and the refractive indices for both the formaldehyde and the p-toulic acid and n-propanol dilution are smaller than that for distilled water. Given that these compounds as they are expected to have very little influence on the overall optical properties of the water, gelatin and lipid phantoms, their Debye relaxation coefficients were not determined.

Chapter 5

Determination of the composition of tissue phantoms

5.1 Introduction

In this chapter, three methods of determining the composition of optical tissue phantoms using THz spectroscopy are evaluated.

1. Linear spectral decomposition: This method employs a linear forward model, based on those used for conventional optical transmittance spectroscopy of non-scattering media containing different chromophores (Cope 1991), which has been outlined in section 3.5.4.1. In this technique, the total absorption coefficient of the medium is considered to be equal to the sum of the absorption contributions of each chromophore, where the contribution of each chromophore is considered linearly dependent upon its concentration, equation 3.3. It is usually assumed that the measured medium is non-scattering. Since optical scattering at THz wavelengths is negligible, the THz signal amplitude can be considered linearly proportional to μ_a (Smye et al. 2001, Zhang 2002). The concentration of each chromophore can be estimated from the wavelength dependent total attenuation of the material using linear matrix inversion, equation 3.4. The technique relies on prior knowledge in the form of the absorption coefficient spectra of each of the chromophores in the THz wavelength region. These were measured as part of this study and were presented in chapter 4.

2. Spectrally averaged dielectric coefficient method: This method is an empirical method based on recent work by *Jepsen et al* where the real and imaginary dielectric coefficients are averaged over a specific frequency range (Jepsen et al. 2007). By repeating this process for a number of measurements made on samples with different concentrations, empirical equations can be obtained that relate the

averaged dielectric coefficients to chromophore concentration. This is described in section 3.5.4.2. Although this technique does not provide a theoretical model of the physical processes responsible for the concentration dependence of the measured THz signals, it nevertheless incorporates empirical knowledge of the concentration dependence of the absorption coefficient *and* the refractive index through the use of the complex dielectric coefficient.

3. Debye relaxation coefficient method: Debye theory relates relaxation processes within a material to an alternating external electric field where the material is considered a noninteracting population of dipoles. The method used in this work is empirical and is based on determining the concentration dependence of Debye coefficients from measurements made in phantoms of different composition. By determining the Debye relaxation coefficients for a number of measurements made on samples with different concentrations, empirical equations can be obtained that relate the Debye relaxation coefficients to chromophore concentration. This approach is described in section 3.5.4.3. Previous work has used Debye coefficients in creating a forward model for the propagation of a THz pulse through a material (Pickwell et al. 2004b; 2005). The work presented in this thesis explores the possibility of using this technique for the determination of material composition.

All three techniques of composition analysis were applied to different tissue phantoms and are presented in sections 5.2, 5.3 and 5.4, respectively. The specific phantoms investigated were the following two-phase phantoms:

- Water and methanol solutions
- Water and lipid emulsions
- Water and sucrose solutions
- Water and gelatin gels

and three-phase phantoms:

- Water, methanol and sucrose solutions
- Water, gelatin and lipid emulsions

The three concentration analysis techniques were validated sequentially on the phantoms in the order presented in this list. The results in this chapter are also presented in the same order.

In assessing the capability of THz imaging and spectroscopy for medical applications, it is the measurements made in reflection mode which are of greatest relevance. Though transmission measurements offer advantageous measurement conditions in terms of relatively high SNR, transmission measurements of biological tissue samples cannot typically be made. The results of the linear spectral decomposition concentration analysis made on transmission measurements can nevertheless be used to gain an appreciation of the best possible performance of THz spectroscopy.

5.2 Method 1: Determination of phantom composition using linear spectral decomposition

For the successful implementation of the linear spectral decomposition technique, it is necessary for the wavelength dependence of the absorption coefficient of each chromophore to be distinct over the measured frequency range. The differences between the shape of the absorption coefficient spectra of all chromophores used in the phantoms are illustrated in figure 5.1. For the solutions of methanol and water, sufficient difference exists between the chromophore spectra in the frequency range 0.1-1 THz. For the solutions of lipid and water, sufficient differences exist between the chromophore spectra in the frequency range 0.1-2 THz. For all other phantom compositions, sufficient difference exists between the chromophore spectra in the frequency range 0.1-1.5 THz.

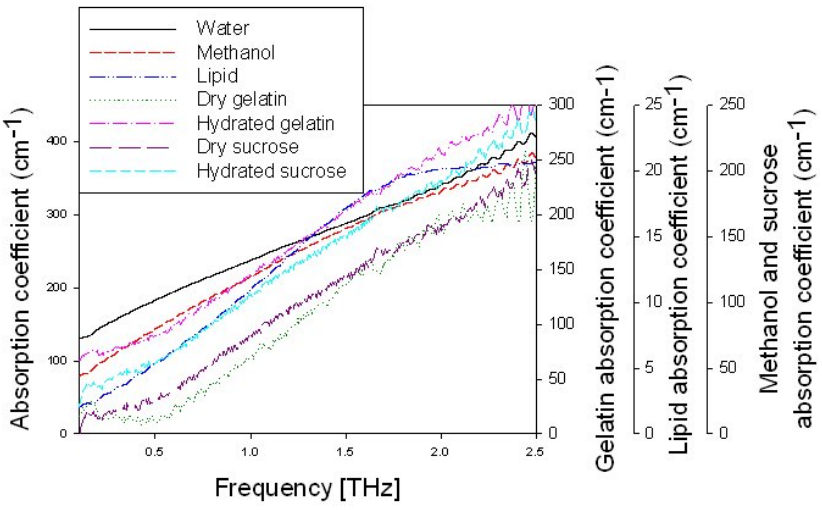

Figure 5.1: Absorption coefficients of all phantom chromophores over the frequency range 0.1-2.5 THz.

The linear spectral decomposition technique was described in section 3.5.4.1. The implementation and results of this method are presented in six sections, one for each phantom composition investigated. Each section presents the absorption coefficients and refractive indices followed by the results of the concentration analysis. The concentration of each phantom component was estimated from the measured absorption coefficient spectrum using multilinear regression. The absorption coefficient spectra of the pure components (see chapter 4) formed the prior knowledge.

The results are presented, where applicable, for both transmission and reflection mode measurements. As the absorption coefficients and refractive indices of the sucrose and gelatin were determined from transmission mode measurements of aqueous sucrose and gelatin, concentrations can only be determined from reflection mode measurements using linear spectral decomposition. The absorption coefficients and refractive indices of water, methanol and lipid were determined from the pure chromophores so linear spectral decomposition can be used to determine concentrations from both transmission and reflection mode measurements.

The accuracy of the method, described in section 3.5.4.4, was calculated from the difference between the calculated and the true concentration values. The individual accuracies were then averaged over all measurements of each phantom to give an estimation of the average accuracy.

The resolutions, which represent the smallest detectable change in the determined concentrations given the standard deviation of the measurement, were determined using equation 3.11. The standard deviations used for the calculation of the resolution of both the transmission and reflection mode measurements was the standard deviation calculated from water measurements repeated over several days and using different THz imaging and spectroscopy systems.

5.2.1 Water and methanol solutions

The absorption coefficient and refractive index of water and methanol solutions with different concentrations, measured in transmission and reflection, are illustrated in figure 5.2. There is an increase in both the absorption coefficient and refractive index of the solutions, with increasing water concentration. The results obtained from transmission measurements have a higher SNR than those obtained from reflection measurements. Though it would be expected that the transmission and reflection spectra are identical, measurements of absorption coefficient made in reflection mode are

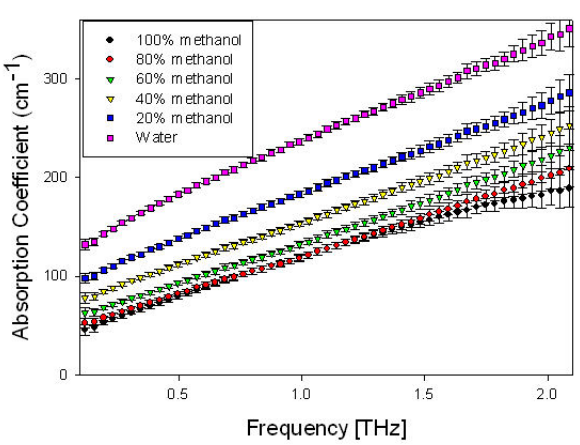

(a) Transmission

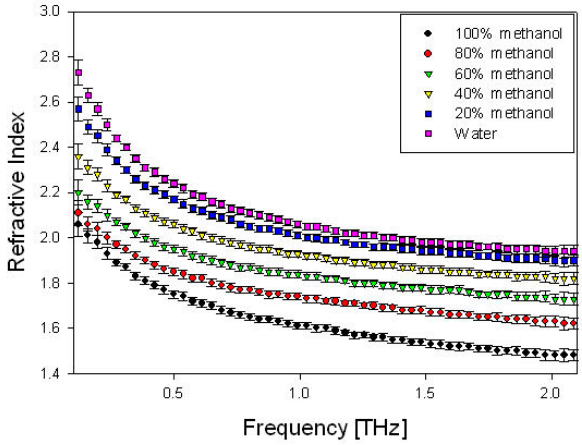

(b) Transmission

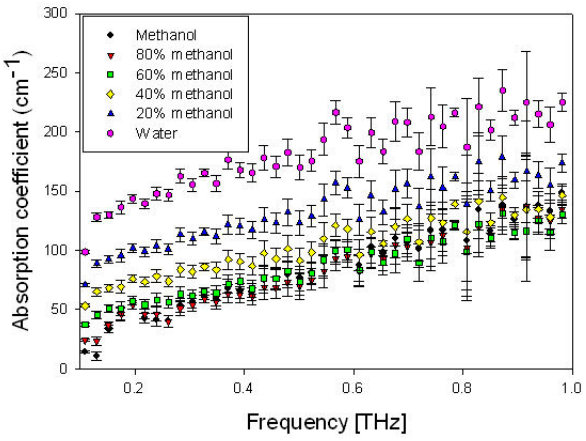

(c) Reflection

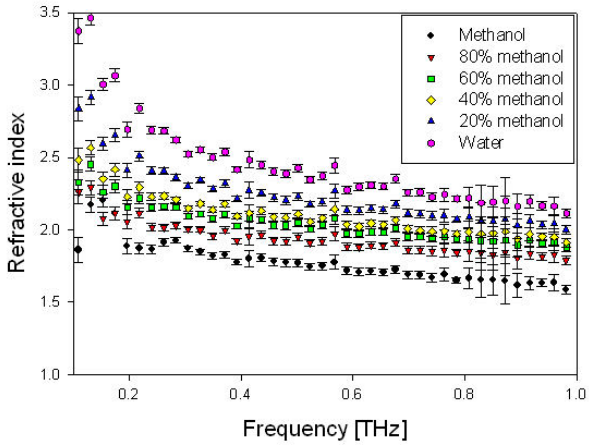

(d) Reflection

Figure 5.2: The THz absorption coefficient and index of refraction for different concentrations of methanol in water measured in a) and b) transmission and c) and d) reflection.

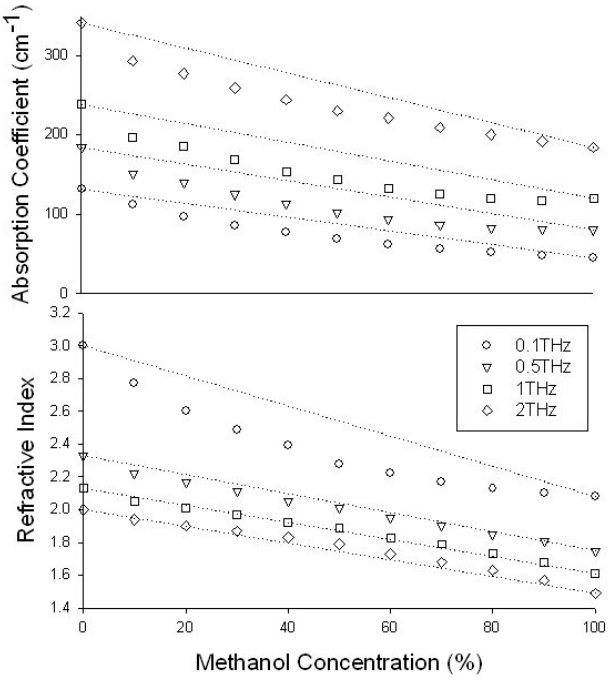

Figure 5.3: The concentration dependence of the measured absorption coefficient and refractive index for methanol and water solutions. The data are presented for discrete frequency values. The symbols represent the measured data and the dotted lines represent the absorption coefficient and refractive index as predicted by linear volumetric mixing of the two chromophores.

inherently noisier than those made in transmission. In transmission mode, the absorption coefficient is calculated from the amplitude of the waveforms whereas in reflection mode they are derived from the phase components of the imaginary data. If the phase of the pulse changes between the reference and the raw data measurement, errors can be produced in the determined absorption coefficients.

The variation of the measured absorption coefficients and refractive indices as a function of concentration for different frequencies, figure 5.3, shows that they do not follow a linear relationship with concentration. This has also been seen in other studies (Venables and Schmuttenmaer 2000b) and is a result of the entropy and bonding within the solutions. The entropy of a system is a measure of how much energy is not available to do work and is also a measure of the disorder of a system. Entropy increases with disorder, a lower entropy indicating a more ordered system. The entropy of aqueous methanol solutions is lower than would be expected for an ideal solution where the molecules of methanol and water are randomly mixed. Molecular modelling of the hydrogen bond mechanisms in methanol and water solutions (Venables and Schmuttenmaer 2000b) has shown the bonding mechanisms to be non-random. This indicates a more ordered structure within the solutions which is thought to be due to the retention of a bulk water structure by the water molecules, where 87% of water molecules in aqueous methanol solutions are thought to be part of a chain of water molecules that can be 2-20 molecules long (Dixit et al. 2002, Markovitch and Agmon 2007). The bonding mechanisms for these solutions causes the solutions to become less polar in comparison to the randomly mixed solutions of pure water and methanol (Lees and Burawoy 1963, Zhong et al. 2007), resulting in a lower absorption coefficient and refractive index than what would be predicted from ideal volumetric mixing of the pure liquids (Franks and Ives 1966, Guo et al. 2003). The non linearity of absorption coefficient and refractive index as a function of concentrations of water and methanol indicates that the application of the linear spectral decomposition technique will be inappropriate as a concentration analysis tool. However, the technique is nonetheless applied here for completeness.

Figure 5.4 shows the concentrations determined from absorption coefficient spectra measured in solutions of water and methanol using linear spectral decomposition. Figure 5.4(a) shows results for transmission measurements and figure 5.4(b) shows results for reflection measurements where the triangular and circular dots are the determined concentrations and the dotted lines are the true concentrations. The accuracy and the resolution of the technique are given in table 5.1.

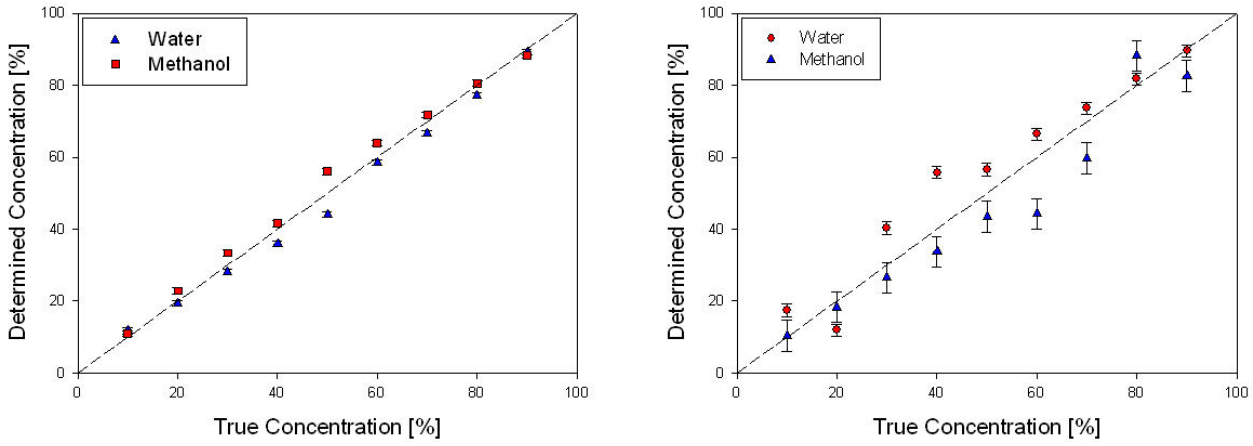

(a) Transmission (b) Reflection

Figure 5.4: Concentrations of methanol and water determined from the absorption coefficient spectra of methanol and water solutions measured in a) transmission mode and b) reflection mode using the linear spectral decomposition technique plotted against their known concentrations. The line represents the line of unity while the symbols represent the determined values. The error bars represent the calculated resolutions of the measurements.

Table 5.1: Accuracy and resolution of concentrations determined using linear spectral decomposition for methanol and water solutions

Measurement mode	Water resolution	Methanol resolution	Water accuracy	Methanol accuracy
Transmission	±0.8%	±1.7%	-2.1%	+2.1%
Reflection	±1.7%	±4.3%	+4.8%	-4.8%

It is interesting to note from figures 5.4(a) and 5.4(b) that the accuracy of the determined concentrations for the methanol and water phantoms appears to correlate with the non-linearity observed in the absorption coefficients, illustrated in figure 5.3. The accuracies of the calculated concentrations are worse for solutions around 50% concentration in both the transmission and reflection measurements in comparison to the extreme ends of the concentration ranges. This result indicates that the validity of the linear spectral decomposition technique is limited due to non-linear changes in absorption coefficient with respect to concentration.

From table 5.1, it can be noted that the resolution of the technique is better for the

water component of the solutions in both the transmission and reflection modes, in comparison to the methanol. This is due to the stronger absorption coefficient of water compared to methanol which means that this technique can detect smaller changes in the concentration of water than in methanol. In comparing the resolutions for both chromophores in the transmission and reflection modes, a better resolution, and therefore smaller change in concentration, has been determined for the transmission measurements. This is due to the smaller standard deviation of the measured signal in transmission mode in comparison to the measured reflection mode signal, as given in table 3.2.

5.2.2 Water and lipid emulsions

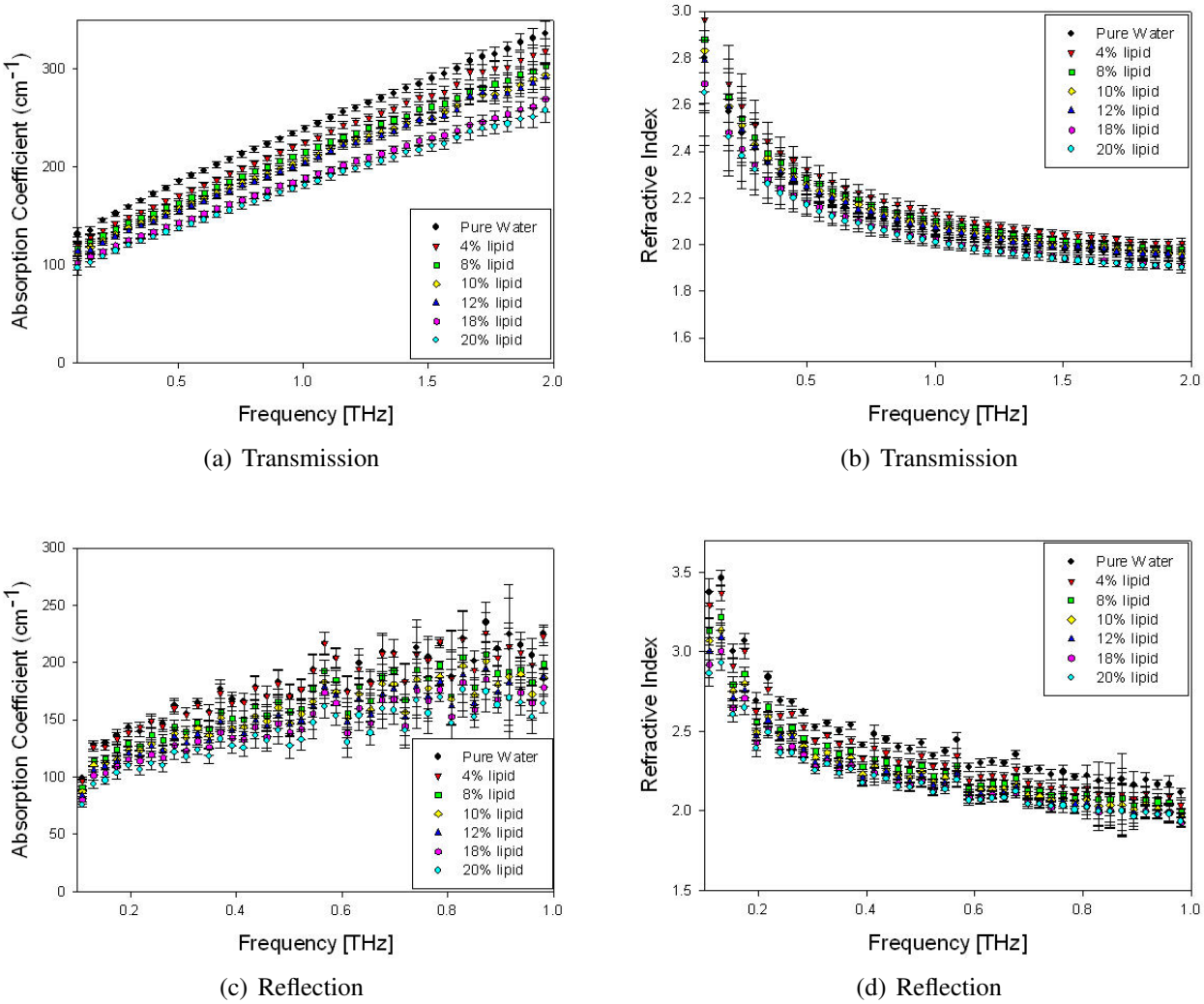

(a) Transmission

(b) Transmission

(c) Reflection

(d) Reflection

Figure 5.5: The THz absorption coefficient and index of refraction for different concentrations of lipid in water measured in a) and b) transmission and c) and d) reflection.

The absorption coefficients and refractive indices of lipid and water emulsions mea-

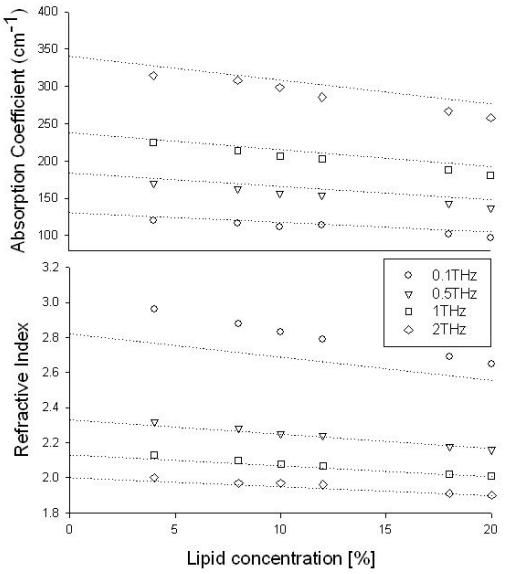

Figure 5.6: The concentration dependence of the absorption coefficient and refractive index for lipid and water emulsions. The data were extracted at discrete frequencies and are represented by symbols. The dotted lines represent the absorption coefficient and refractive index as predicted by linear volumetric mixing of the two chromophores.

sured in transmission are illustrated in figure 5.5 where an increase in both the absorption coefficient and the refractive index with increasing water content of the emulsions is observed. The variations in the absorption coefficient and refractive index as a function of concentration are well correlated to values predicted by linear volumetric mixing using the absorption coefficient and refractive index of the pure components, as illustrated in figure 5.6. The good agreement between the measured and predicted values suggests that there is little interaction between the lipid and the water molecules. This implies lipid and water act as independent absorbers.

Figure 5.7 shows the concentrations determined from absorption coefficient spectra measured in water and lipid emulsions in transmission, figure 5.7(a), and reflection, figure 5.7(b) modes. The triangular and circular dots are the determined concentrations and the dotted lines are the true concentrations. The accuracy and the resolution of this technique are given in table 5.2. The determined concentration accuracies are worse for reflection mode measurements than for the transmission mode measurements, and the determined concentration accuracies are worse than those determined from the methanol and water solutions, in both measurement modes. The highest resolution is the water component of the emulsions which is small in comparison to the resolution of the lipid component. This is due to the large difference in the absorption coefficients

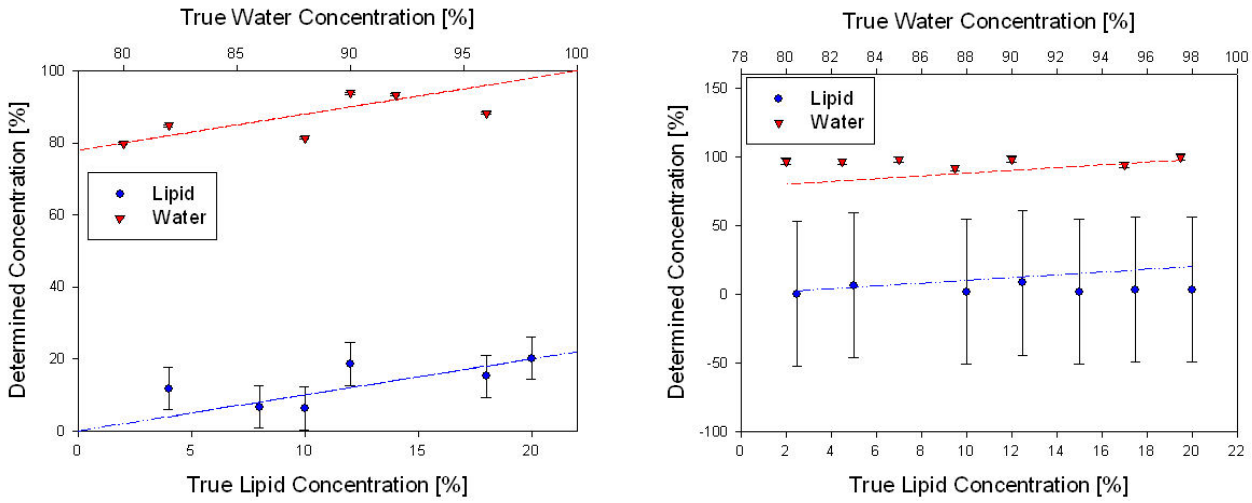

(a) Transmission (b) Reflection

Figure 5.7: Concentrations of lipid and water determined from measurements of the absorption coefficients of lipid and water emulsions captured in a) transmission mode and b) reflection mode using the linear spectral decomposition technique. The determined concentrations are plotted against the known concentrations of lipid and water. The line represents the line of unity while the symbols represent the determined concentrations. The error bars represent the calculated resolutions of the measurements.

which is approximately 20 times greater in water than in lipid at 1 THz. This suggests that, though the accuracy of the linear spectral decomposition is good when applied to emulsions of lipid and water, it is primarily the water content of the emulsion that THz spectroscopy is sensitive to.

Table 5.2: Accuracy and resolution of concentrations determined using linear spectral decomposition for lipid and water solutions

Measurement mode	Water resolution	Lipid resolution	Water accuracy	Lipid accuracy
Transmission	±0.3%	±5.9%	-1.1%	+1.1%
Reflection	±2.1%	±52.8%	+3.7%	-3.7%

5.2.3 Water and sucrose solutions

The absorption coefficients and refractive indices of the sucrose and water solutions are shown in figure 5.8. Both quantities decrease with increasing sucrose content.

Figure 5.9 shows the concentrations determined from absorption coefficient spectra

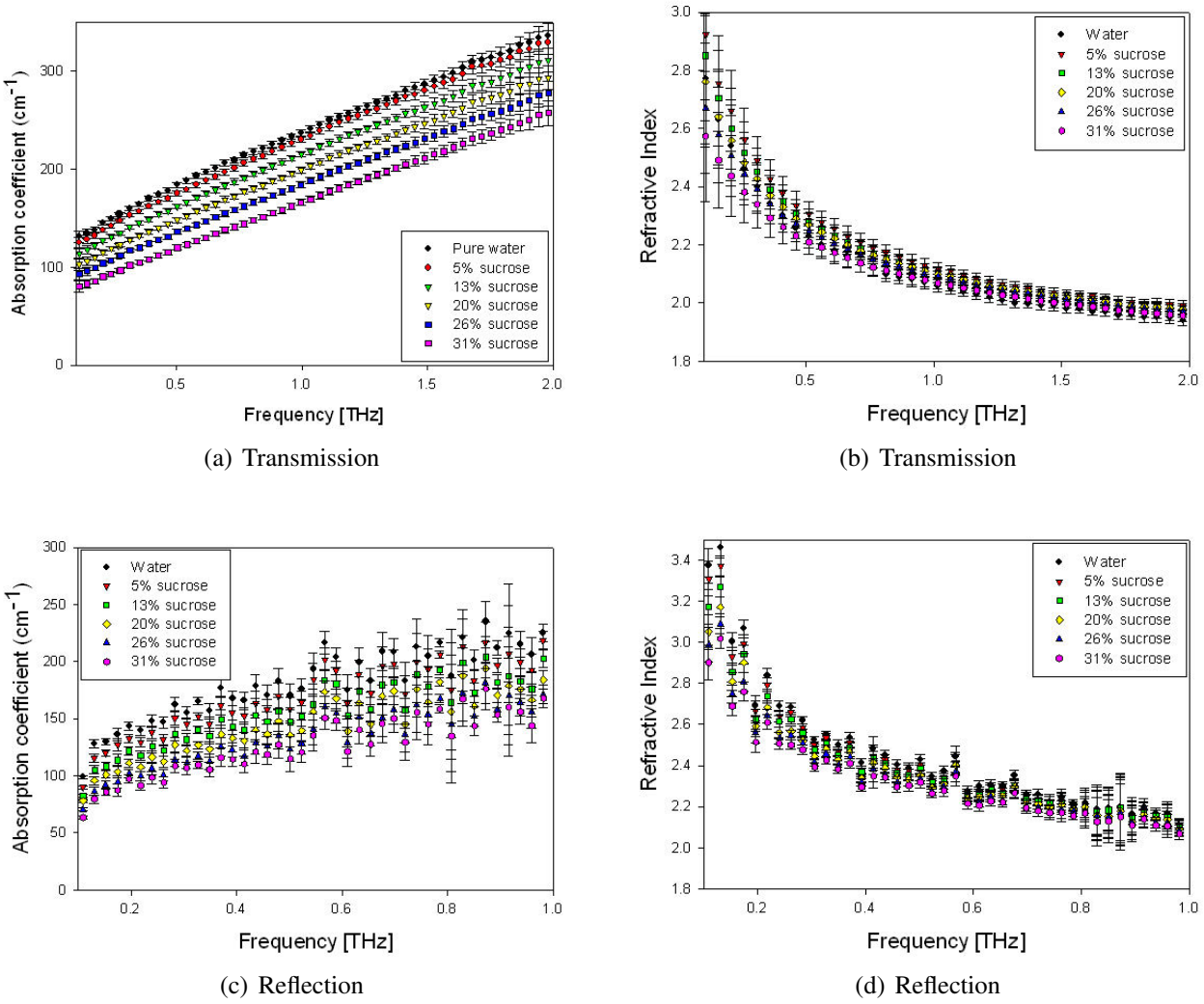

(a) Transmission

(b) Transmission

(c) Reflection

(d) Reflection

Figure 5.8: The THz absorption coefficient and index of refraction for different concentrations of sucrose in water measured in a) and b) transmission and c) and d) reflection.

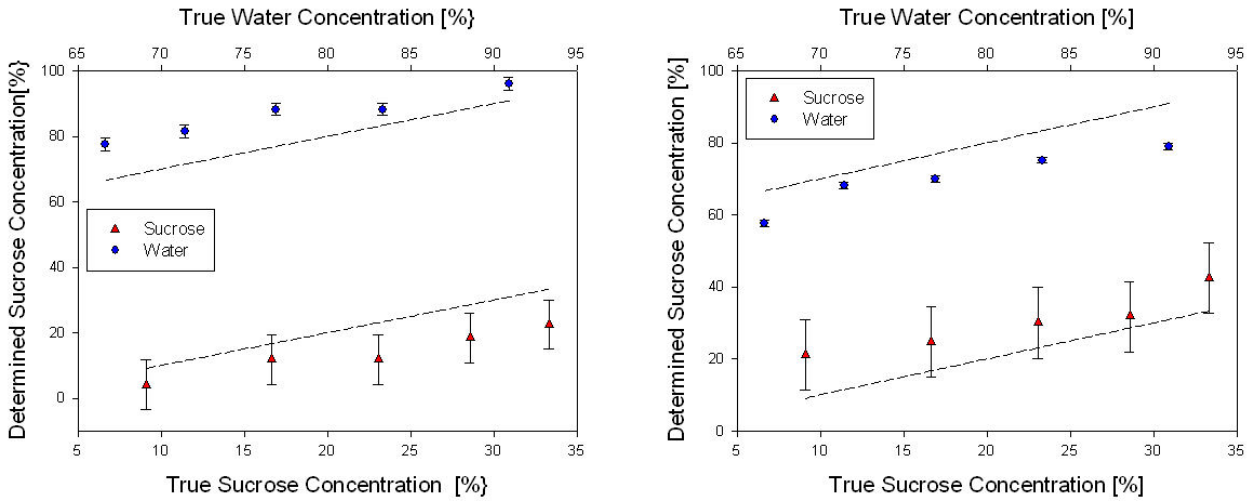

(a) Dry sucrose molecule and water

(b) Hydrated sucrose molecule and water

Figure 5.9: The concentrations of water and sucrose determined from the spectra of absorption coefficient and refractive index of aqueous sucrose solutions measured in reflection mode, plotted against known concentrations. The results in a) were obtained using the absorption spectrum of 'dry' sucrose as prior information in the linear spectral decomposition. The results in b) were obtained using the absorption spectrum of 'hydrated' sucrose as prior information in the linear spectral decomposition. The dashed line represents the true concentrations while the symbols represent the calculated concentrations. Error bars represent the calculated resolutions of the measurements.

measured in reflection mode of solutions of water and sucrose. Analysis was performed only on reflection mode data, as the transmission mode measurements had been used to calculate the absorption coefficient of sucrose, as described in section 3.5.4.1. The concentrations of water and 'dry' sucrose were determined, figure 5.9(a), and also the concentrations of water and 'hydrated' sucrose were determined, figure 5.9(b). The accuracy and the resolution of this technique are given in table 5.3 from which it can be noted that the accuracy of the determined concentrations is slightly better for hydrated sucrose than for the dry state. There is an underestimation in the determined concentrations of sucrose when the absorption coefficient for dry sucrose was used and an overestimation in the determined concentrations of sucrose when the absorption coefficient for hydrated sucrose was used. While an error must be assumed in the determination of the absorption coefficients of the hydration layer of each macromolecule due to difficulties in defining the true extent of the hydration layer and, thus, knowing the number of water molecules contained in that layer, it has been previously suggested that the true absorption coefficient of the macromolecules could lie in between the 'dry' and 'hydrated' extremes presented here (Xu et al. 2006). That the determined concentrations follow the trends of the true concentrations but are either overestimated or underestimated depending on the which sucrose absorption

coefficient was used as prior knowledge, suggests that the true absorbtion coefficient of the hydrated sucrose molecules does indeed lie between the two used in this work.

From table 5.3, it can be seen that the resolution is better for the water component than for either the 'dry' and 'hydrated' sucrose. This is due to the stronger absorption coefficient of water compared to the 'dry' and 'hydrated' sucrose, as shown in figure 4.6(a).

Table 5.3: Accuracy and resolution of concentrations determined using linear spectral decomposition for water and sucrose solutions

Prior information used for sucrose spectrum	Water resolution	Sucrose resolution	Water accuracy	Sucrose accuracy
Dry	±1.9%	±7.6%	+8.5%	-8.5%
Hydrated	±0.9%	±9.8%	-5.6%	+5.6%

5.2.4 Water and gelatin gels

The absorption coefficients and refractive indices of gelatin and water gels at different gelatin concentrations are illustrated in figure 5.10 where a decrease in both the absorption coefficient and refractive index with increasing gelatin content of the solutions is observed.

Figure 5.11 shows the concentrations determined using linear spectral decomposition from absorption coefficient spectra of gels of water and gelatin measured in reflection mode. Analysis was performed only on the reflection mode data, as the transmission mode measurements had been used to calculate the absorption coefficient of gelatin, as described in section 3.5.4.1. The concentrations were determined for the water component of the gels as well as 'dry' gelatin molecules, figure 5.11(a), and 'hydrated' gelatin molecules, figure 5.11(b).

The accuracy and the resolution of this technique are given in table 5.4. While the determined concentrations of gelatin and water follow the trend of the true concentrations when the absorption coefficient for 'dry' gelatin was used as prior information, the concentrations determined using the 'hydrated' gelatin absorption coefficient as prior knowledge fluctuate around the true concentration values. Supposing that, as hy-

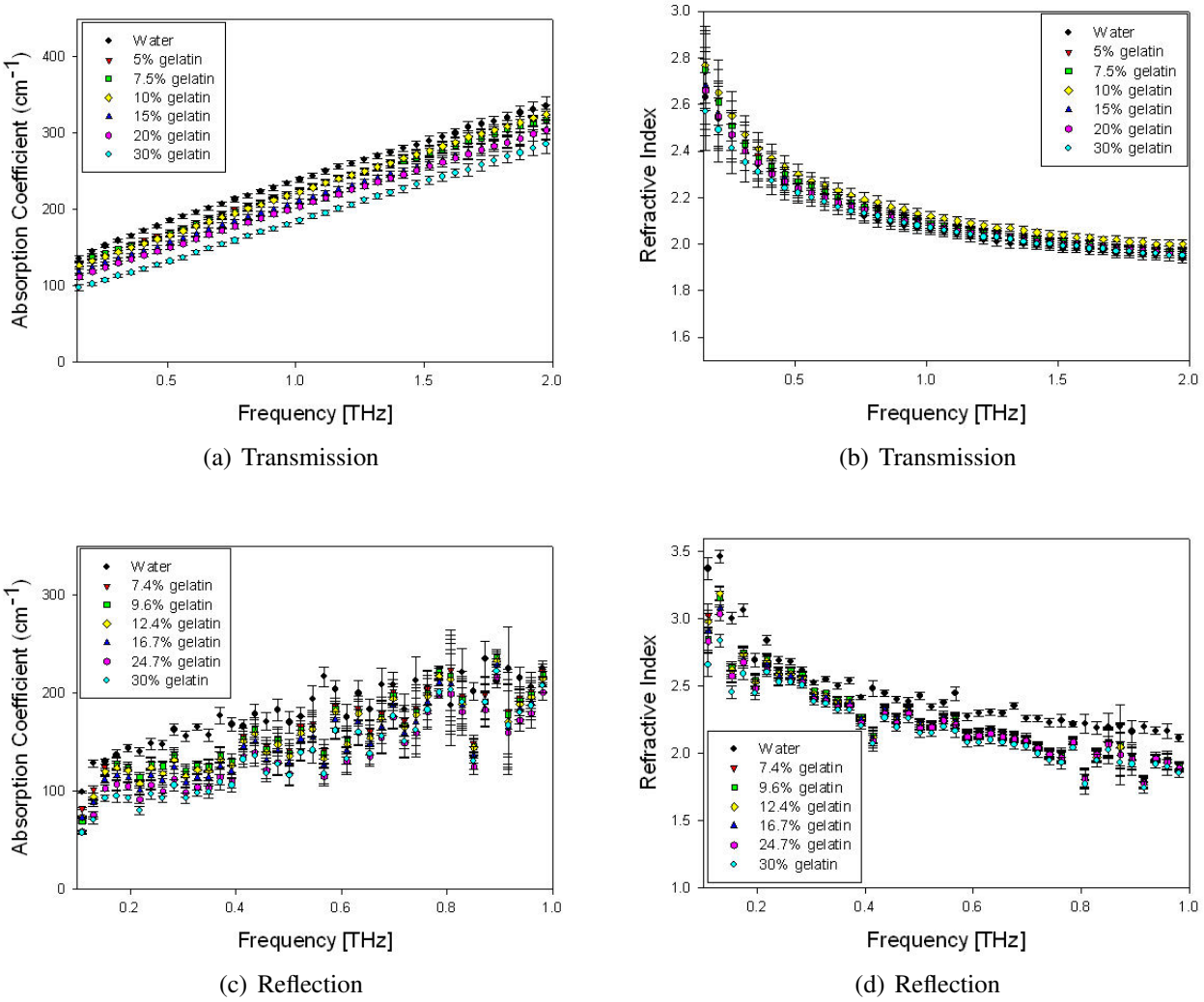

(a) Transmission

(b) Transmission

(c) Reflection

(d) Reflection

Figure 5.10: The THz absorption coefficient and index of refraction for different concentrations of gelatin in water measured in a) and b) transmission and c) and d) reflection.

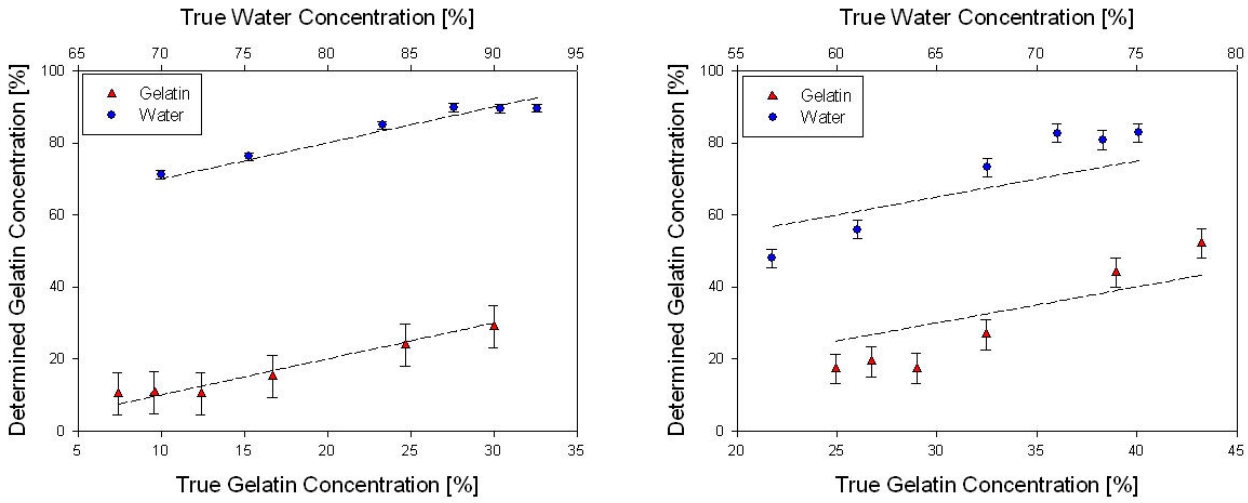

(a) Dry gelatin molecule and water

(b) Hydrated gelatin molecule and water

Figure 5.11: The concentrations of water and gelatin determined from the spectra of absorption coefficient and refractive index of water and gelatin gels measured in reflection mode, plotted against known concentrations. The results in a) were obtained using the absorption spectrum of 'dry' gelatin as prior information in the linear spectral decomposition. The results in b) were obtained using the absorption spectrum of 'hydrated' gelatin as prior information in the linear spectral decomposition. The dashed line represents the true concentrations while the symbols represent the calculated concentrations. Error bars represent the calculated uncertainties of the measurements.

pothesised from the sucrose and water solution results, the true absorption coefficient of the macromolecule lies between the determined 'dry' and 'hydrated' absorption coefficients, we may conclude that the true absorbtion coefficient of the hydrated gelatin molecule is closer to the 'dry' absorption coefficient. The concentrations determined using the 'hydrated' absorption coefficient as prior knowledge fluctuate around the true concentrations rather than being offset as seen with the 'hydrated' sucrose and water solutions. The calculation of the hydration layer of the sucrose molecule incorporated a variation with respect to concentration where the number of water molecules in the hydration layer decreases as the sucrose concentration in solution increases. This was not accounted for in the calculation of the hydration layer of gelatin as no supporting literature was available. However, if the hydration layer of gelatin molecules is variable with respect to concentration, this could account for the underestimation of the gelatin concentration at low concentrations and the overestimation at higher concentrations. Further work is needed to investigate this hypothesis.

The resolutions determined for water and gelatin are slightly better for the gelatin component but similar for the water component when compared to those determined for the water and sucrose solutions. This is as a result of the larger absorption coeffi-

Table 5.4: Accuracy and resolution of concentrations determined using linear spectral decomposition for gelatin and water gels

Prior information used for gelatin spectrum	Water resolution	Gelatin resolution	Water accuracy	Gelatin accuracy
Dry	±1.1%	±5.9%	+0.3%	-0.3%
Hydrated	±2.6%	±4.1%	+3.1%	-3.1%

cients of gelatin in comparison to sucrose.

5.2.5 Water, methanol and sucrose solutions

Having used linear spectral decomposition methods to determine the composition of two component phantoms, phantoms made from three components were also used to assess the accuracy of of the technique when applied to more complex systems. In the linear spectral decomposition analysis of the three-phase phantoms, the absorption coefficient of 'dry' sucrose and gelatin will be used as the prior knowledge spectra.

Two solutions of water, methanol and sucrose were created following the methods published by *Uhd Jepsen, et al*, the concentrations of which are given below,

- Solution A: 71.4% wt water, 20.4% wt sucrose, 8.2% wt methanol
- Solution B: 62.5% wt water, 20.8% wt sucrose, 16% wt methanol

The absorption coefficients and refractive indices of the solutions are illustrated in figure 5.12. The absorption coefficient and refractive index of solution 'A' is greater than those of solution 'B' across the measured spectrum, which could also be predicted from the absorption coefficients and refractive indices of the pure components.

The accuracy and the resolution of this technique are given in table 5.5. The accuracies are equivalent to those determined for the corresponding two-component phantoms; water and methanol, and water and sucrose, for both measurement modes. The resolutions are slightly larger than those determined for the individual solution components from both the transmission and reflection mode measurements, where the resolutions determined for the transmission mode measurements are better than those determined for the reflection mode measurements. The lower resolutions are a result of a greater number of variables being determined from the standard deviation measurements of the system, which inherently leads in poorer results.

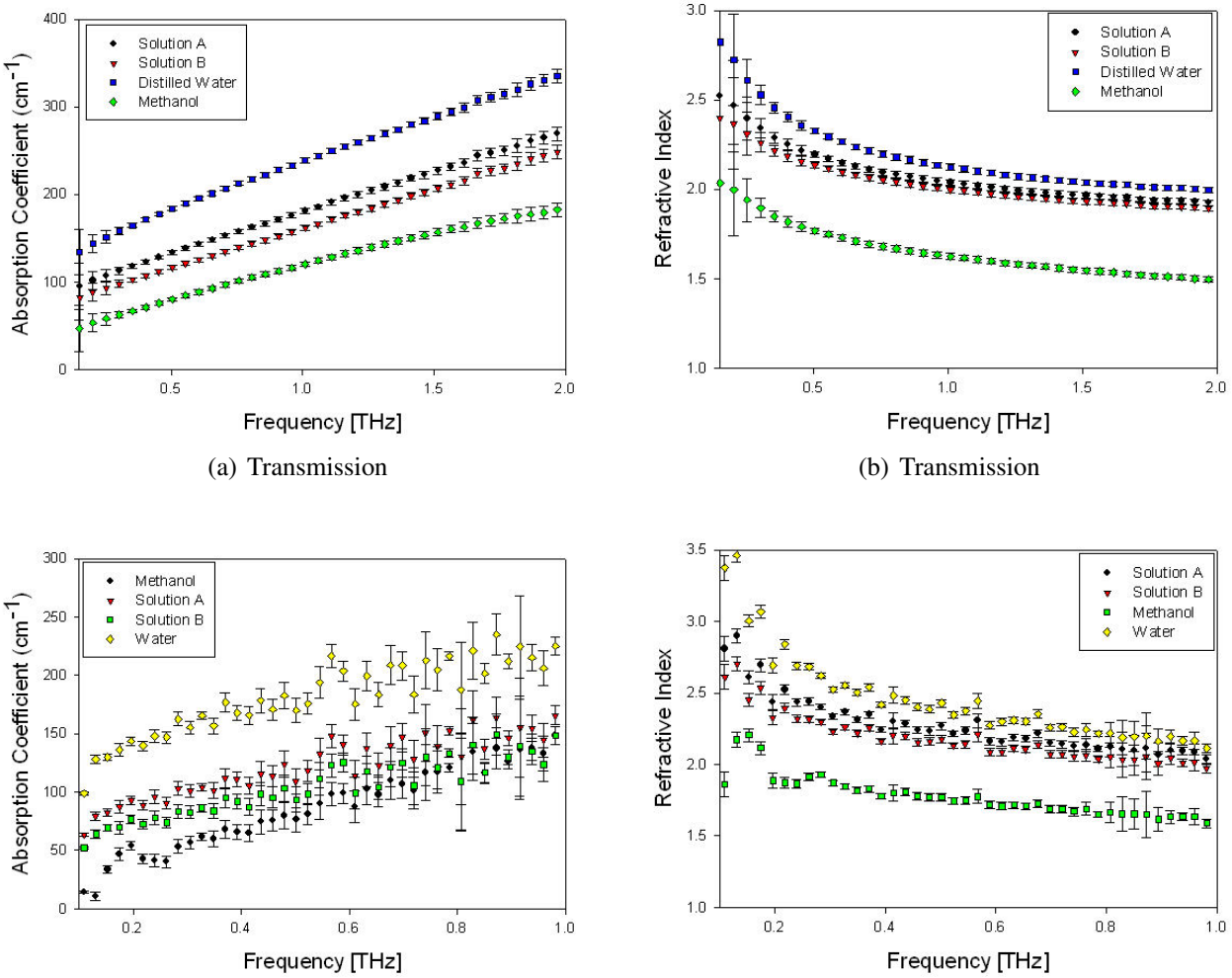

(a) Transmission

(b) Transmission

(c) Reflection

(d) Reflection

Figure 5.12: The THz absorption coefficient and index of refraction for different concentrations of two different methanol, sucrose and water solutions measured in a) and b) transmission and c) and d) reflection. Solution 'A' was a solution of 60% water, 20% methanol and 20% sucrose while solution 'B' was a solution of 70% water, 20% methanol and 10% sucrose.

Table 5.5: Accuracy and resolution of water methanol and sucrose concentrations determined using linear spectral decomposition method

	Resolution Transmission	Resolution Reflection	Accuracy Transmission	Accuracy Reflection
Water	±1.7%	±2.2%	-0.9%	-2.5%
Methanol	±4.9%	±6.8%	+0.8%	+0.2%
Sucrose	±3.3%	±5.0%	+0.5%	+2.7%

5.2.6 Water, gelatin and lipid phantoms

The absorption coefficients and refractive indices of gelatin, lipid and water phantoms, with respect to frequency, are illustrated in figure 5.13 where a decrease in both the absorption coefficient and refractive index with increasing lipid content is observed.

The concentrations determined from measurements made in both transmission and reflection mode of these phantoms are are illustrated in figure 5.14. The accuracy and the resolution of this technique are given in table 5.6. As with previous calculations of concentration using this technique, the accuracy of the resolved concentrations is better for the transmission measurements than for those determined from reflection measurements. However, the accuracy of the determined concentrations of all the phantom components is worse in comparison to those determined for the transmission and reflection modes measurements of the corresponding two-component phantoms. This decrease in accuracy could be due to more complex bonding within the phantoms which is not accounted for in the model. The success of this method is reliant on the linear additivity of the individual absorption coefficient of the phantom chromophores. However, if the physical structure of the phantoms is more complex, such as is the case with formaldehyde strengthened gelatin networks of these phantoms, then the optical properties may be altered and the validity of this technique may be compromised. Uncertainty in defining, with confidence, the true absorption coefficient of hydrated gelatin, as has been discussed previously, contributes to inaccuracies in the determined concentrations. Calculation of the resolutions of water, gelatin and lipid were slightly lower than those determined for the corresponding two component phantoms. As stated for the water, methanol and sucrose solutions, the lower resolutions are a result of a greater number of variables being determined from the standard deviation measurements of the system, which inherently leads in poorer results.

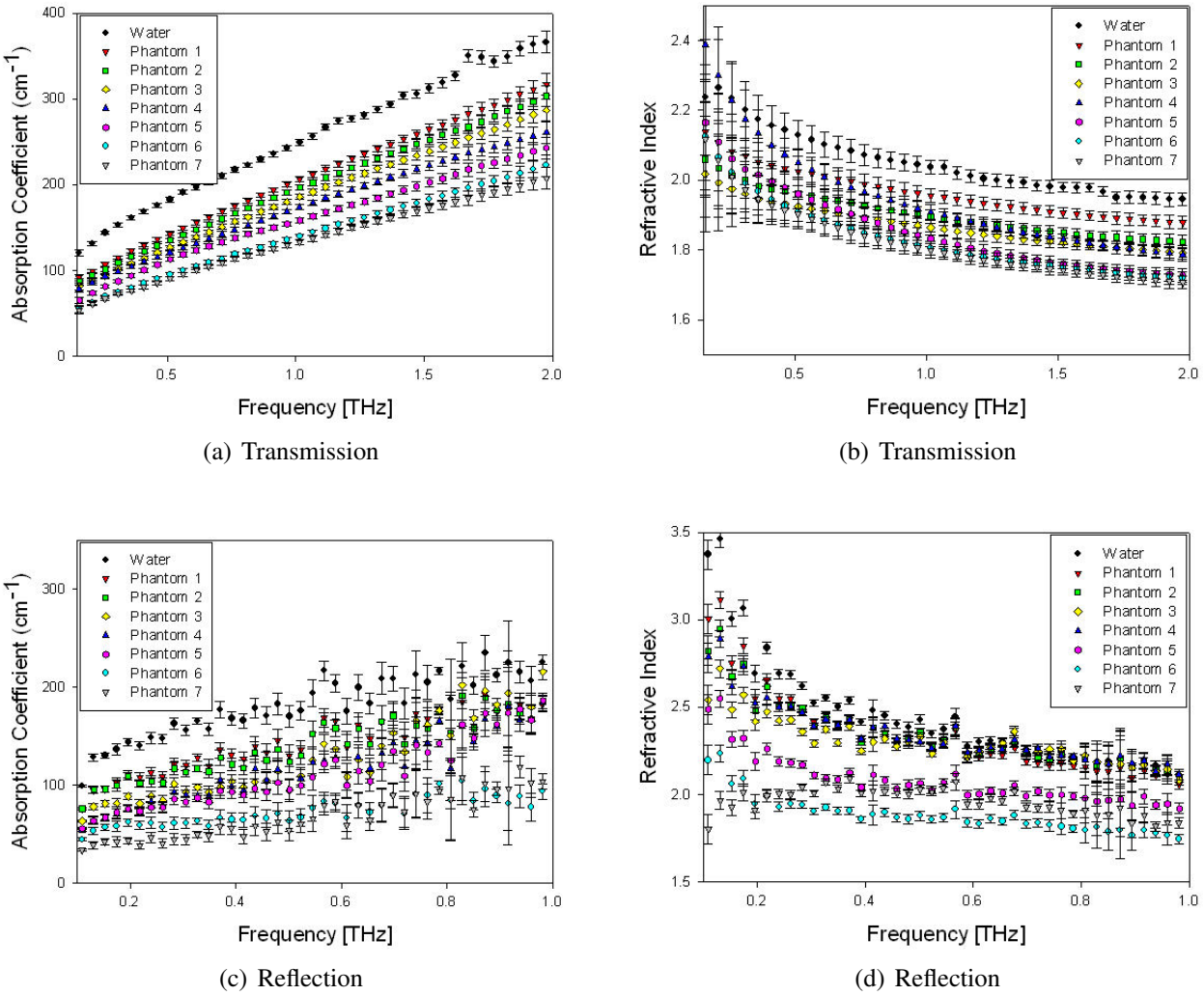

(a) Transmission

(b) Transmission

(c) Reflection

(d) Reflection

Figure 5.13: The THz absorption coefficient and index of refraction for different concentrations of water, gelatin and lipid measured in a) and b) transmission and c) and d) reflection.

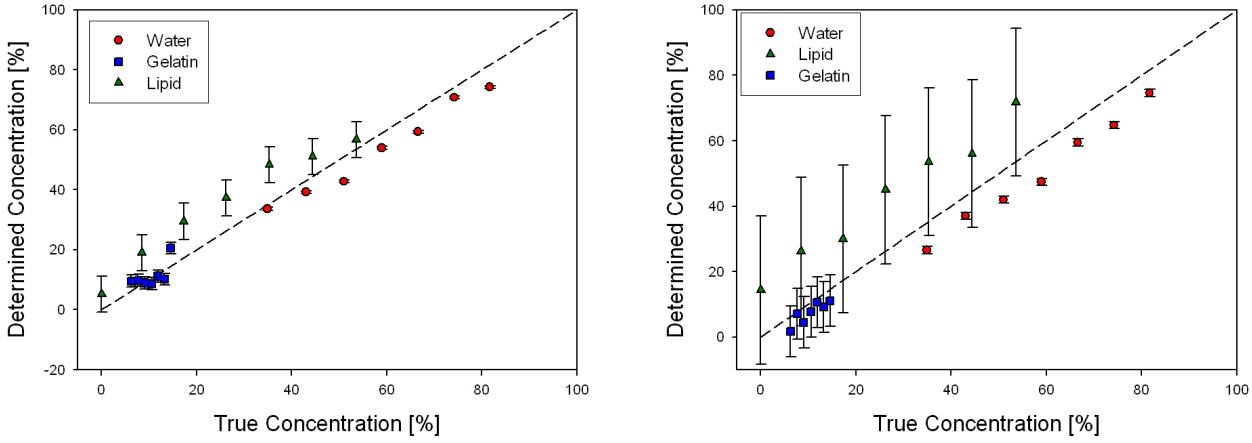

(a) (b)

Figure 5.14: Concentrations of water, gelatin and lipid determined from measurements of the a) transmitted and b) reflected intensity of water, gelatin and lipid phantoms using the linear spectral decomposition technique. Concentrations are plotted against the known concentrations of water, gelatin and lipid. The dashed line represents the line of unity while the symbols represent the calculated concentrations. Error bars represent the calculated resolutions of the measurements.

Table 5.6: Accuracy and resolution of concentrations determined using linear spectral decomposition for gelatin lipid and water phantoms

	Resolution Transmission	Resolution Reflection	Accuracy Transmission	Accuracy Reflection
Water	±0.5%	±1.1%	-4.9%	-8.1%
Gelatin	±2.0%	±7.8%	+1.1%	-2.8%
Lipid	±6.0%	±52.6%	+7.4%	+14.5%

5.2.7 Summary

For all phantoms, the concentrations determined from transmission measurements were more accurate than those obtained from reflection measurements. There is difficulty in accurately determining the absorption coefficient from reflection mode measurements which results in an increased error in comparison to the transmission mode measurements. Measurements in reflection mode for all phantoms were made at single point locations at the centre of the imaging window to reduce the influence of an uneven imaging window. In the measurements of the liquid phantoms, as in the mixtures of water with methanol, lipid and sucrose, physical effects such as bending of the imaging window and non uniform contact of the samples are unlikely to affect the derived

absorption coefficients. However, measurements of the solid phantoms did require a slight pressure to be applied to the sample to ensure good contact with the imaging window which may account for error in these measurements.

The resolutions determined using this technique were better for the water component of each phantom. This is due to the absorption coefficient of water being much larger than any of the other phantom components, leading to the largest value of $\frac{\Delta\mu_a}{\Delta c}$ for water. As the calculation of resolution takes into account the $\frac{\Delta\mu_a}{\Delta c}$ values for each phantom component, a comparatively large $\frac{\Delta\mu_a}{\Delta c}$ results in an increased sensitivity. This is most apparent in the resolutions determined for the lipid and water emulsions, where lipid has a small absorption coefficient in comparison to water. This produces a large difference in $\frac{\Delta\mu_a}{\Delta c}$ between the two components and results in a poor resolution for lipid.

5.3 Method 2: Determination of phantom composition from spectrally averaged dielectric coefficients

This method, described in section 3.5.4.2, was based on recent work, (Jepsen et al. 2007), in which it was suggested that the dependence of $\varepsilon^{'}$ and $\varepsilon^{''}$ on concentration may enable concentrations to be determined. Empirical equations were used to relate the concentration of a single solute to the averaged value of $\varepsilon^{'}$ and $\varepsilon^{''}$ across a frequency range. By comparing the averaged $\varepsilon^{'}$ and $\varepsilon^{''}$ of unknown samples to the empirical equations, an estimate of concentration may then be determined. This method incorporates, through the use of both $\varepsilon^{'}$ and $\varepsilon^{''}$, the measured absorption coefficient and refractive index. This approach has been demonstrated previously, (Jepsen et al. 2007), in solutions of water and methanol, water and sucrose and water, sucrose and methanol. Here we have validated these measurements and methods of analysis to ensure their correct implementation, before expanding the method to water and lipid, water and gelatin and, finally, the more complex phantom consisting of water, gelatin and lipid.

The results of this method are presented in six sections, one for each phantom composition investigated. Each section presents $\varepsilon^{'}$ and $\varepsilon^{''}$ of each phantom followed by the results of the concentration analysis using the spectrally averaged dielectric coefficient method. In the implementation of this method, transmission mode measurements of $\varepsilon^{'}$ and $\varepsilon^{''}$ were used to determine the coefficients of the empirical equations. The implementation involved the following steps.

Firstly, the variation of the calculated ε' and ε'' with solute concentration was established for transmission mode measurements. These were then averaged over a frequency range of 0.1-1 THz. ε' and ε'' were calculated using equations 2.45 and 2.46 from the measured absorption coefficients and refractive indices.

For two-phase phantoms, the second step was the plotting of the averaged ε' and ε'' values with respect to the concentration of the non-water component of the phantom, i.e., methanol, lipid, sucrose or gelatin. Empirical equations were then formulated from these plots, the coefficients of which described the trend of ε' and ε'' with non-water component concentration. Linear functions, equation 3.7, were sufficient to describe these trends for the water and lipid, water and sucrose, and water and gelatin phantoms. The empirical functions that most closely resembled the variation in averaged ε' and ε'' of the water and methanol solutions were exponential functions, equation 3.6. For the three-phase phantoms the empirical equations for the corresponding two component phantoms were combined to create a single empirical equation, as demonstrated in equation 3.8. The empirical equations for the two-phase phantoms were created for the %wt of the relative solutes in the phantoms to enable them to be commutable to the concentration analysis of the three-phase phantoms, the concentrations of which are defined as %wt of the relative solutes. These combined empirical equations describe the variation in the averaged ε' and ε'' of the three phase phantoms with respect to its two non-water components. The foundation for this approach is that the variations of ε' and ε'' of a material can be described as the sum of the individual variations arising from its component parts.

The final step was to determine the concentrations of the components in 'unknown' aqueous phantoms, using the empirical equations that form the prior knowledge. Reflection mode measurements of ε' and ε'' were used as 'unknown' data from which concentrations were determined. The empirical equations were solved for concentration using the averaged values of ε' and ε'' determined from reflection mode measurements. It is only the concentrations of the non-water components which are directly determined from the measured data. As the phantoms measured as part of this study contain only the components resolved for and water, with the exception of the water, gelatin and lipid phantoms, we can infer that the 'remaining' concentration of the phantoms is the concentration of water. In this section, the accuracy and resolutions will be quoted for only the directly determined component concentrations. However in the figures both the directly determined component concentrations and the inferred water

component concentrations are given.

The accuracy of the technique was calculated from the difference between the calculated and the true concentration values. The individual accuracies were then averaged over all measurements made in a particular phantom to give an estimation of the average accuracy.

The resolutions were determined using equation 3.11. The standard deviation used in these calculations was obtained from reflection mode measurements of distilled water made over a number of days, given in table 3.2. The change in $\varepsilon^{'}$ and $\varepsilon^{''}$ with respect to a change in concentration, $\frac{\Delta\varepsilon'}{\Delta c}$ and $\frac{\Delta\varepsilon''}{\Delta c}$, as defined by the empirical equations, formed the design matrix of the method. As previously mentioned, linear functions were used as the basis of the empirical equations for most phantoms, while exponential functions were used as the basis of the empirical equations for only the water and methanol solutions. The use of linear empirical functions results in the same value for $\frac{\Delta\varepsilon'}{\Delta c}$ and $\frac{\Delta\varepsilon''}{\Delta c}$ for all concentrations, and therefore constant resolution. By contrast, the water and methanol solutions have a variable sensitivity to concentration change across the investigated concentration range, which results in a variable resolution.

5.3.1 Water and methanol solutions

The real and imaginary parts of complex dielectric coefficient of water and methanol solutions are shown in figure 5.15 for both transmission and reflection mode measurements over the frequency range 0.1-1 THz. There is an increase in ε' and ε'' with increasing water concentration. The increase is greatest at lower frequencies for the transmission mode. While the transmission and reflection data follow the same general trends, the dielectric coefficients of the transmission mode measurements are much smoother than those for the reflection mode. As described in section 5.2.1, there is difficulty in achieving an accurate measurement of the absorption coefficient in reflection mode which may account for the noise in the reflection data. The influence of absorption coefficient and refractive index on ε' and ε'' is given by equations 2.45 and 2.46. It can be seen from these equations that ε' is most sensitive to changes in the absorption coefficient while ε'' is influenced equally by changes in the refractive index and absorption coefficient.

The agreement between the empirical functions and the measured data are illustrated in figure 5.16(a) where the coefficients for the empirical equations are also given. The non-linearity in the variation of the averaged dielectric coefficients as a function of

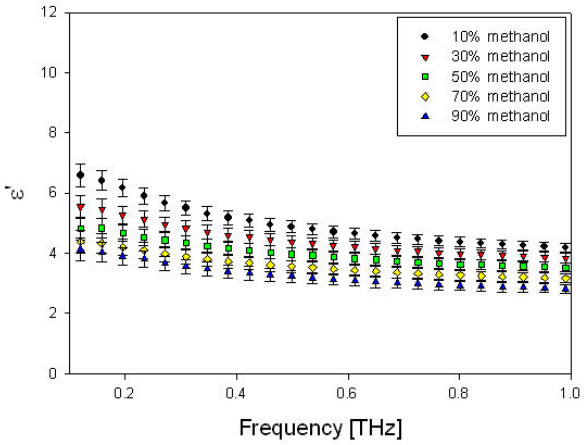

(a) Transmission mode

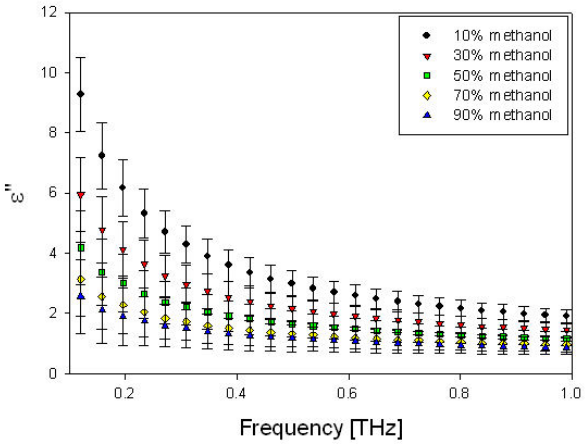

(b) Transmission mode

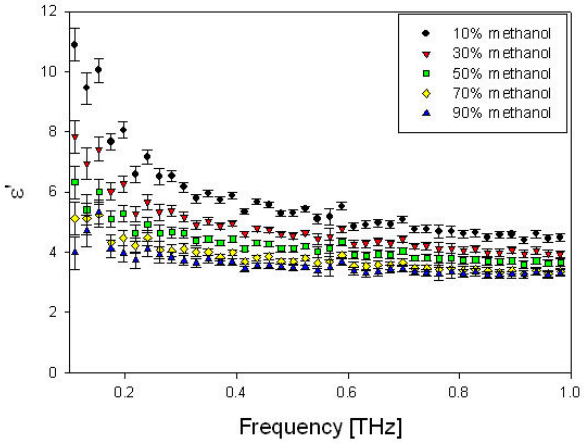

(c) Reflection mode

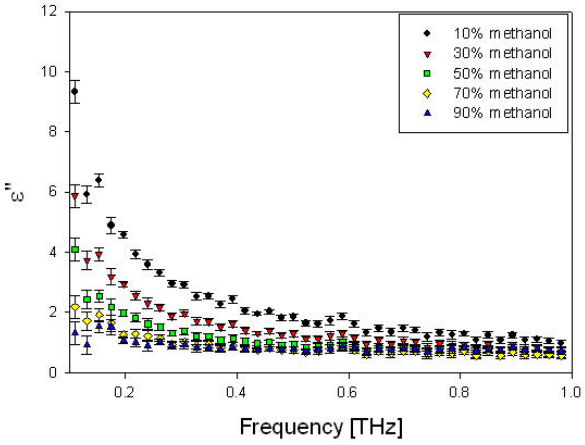

(d) Reflection mode

Figure 5.15: The real and imaginary dielectric coefficients of water and methanol solutions plotted for different concentrations of methanol as a function of frequency for a) and b) transmission and c) and d) reflection mode measurements.

concentration mimics the non-linear relationship with concentration noted in the absorption coefficients and refractive indices of the water and methanol solutions, section 5.2.1.

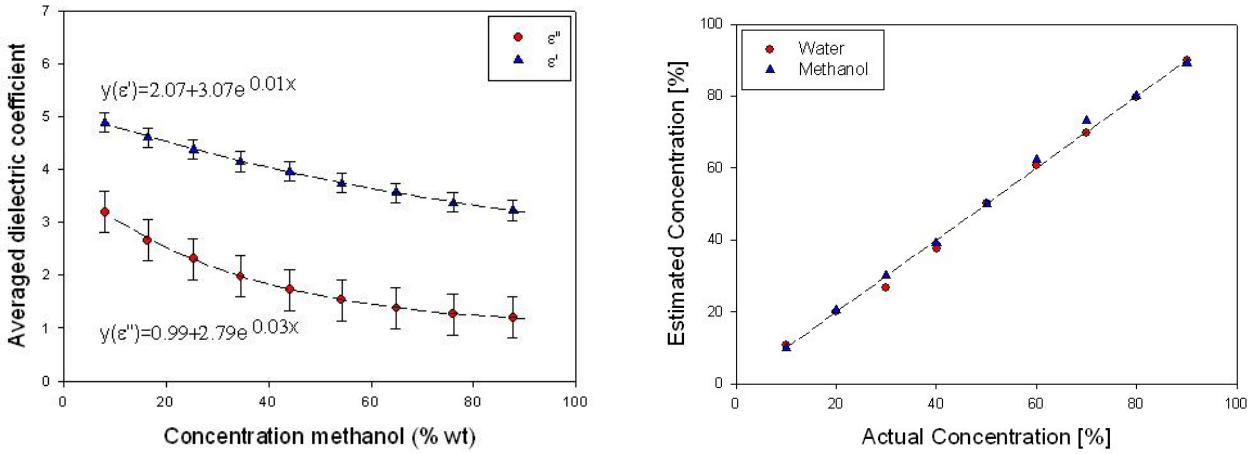

(a) (b)

Figure 5.16: Plot showing a) the average value of ε' and ε'' in water and methanol solutions as a function of methanol concentration. The symbols are the averaged dielectric coefficients determined from the experimental data and the dashed lines represent the best fit of the empirical functions to the data measured in transmission mode. b) shows the concentrations of water and methanol determined from measurements of ε' and ε'' in water and methanol solutions using spectrally averaged dielectric coefficient method. The calculated concentrations are plotted against the known concentrations of water and methanol. The line represents the line of unity while the symbols represent the calculated concentrations.

The concentrations determined from measurements of ε' and ε'' made in reflection mode are shown in figure 5.16(b). The accuracy and resolution of the concentrations obtained using this technique are given in table 5.7. As the empirical equations, which describe the variation in ε' and ε'' with methanol concentration are non linear, $\frac{\Delta\varepsilon'}{\Delta c}$ and $\frac{\Delta\varepsilon''}{\Delta c}$ are dependent on concentration and are largest at high methanol concentrations. This results in a variable resolution, ranging from $\pm 3.1\%$ at 10% methanol concentration to $\pm 26.5\%$ at 90% methanol concentration. The average resolution is given in table 5.7.

5.3.2 Water and lipid emulsions

ε' and ε'' measured on water and lipid emulsions are shown in figure 5.17 for the transmission and reflection modes over the frequency range 0.1-1 THz. There is an increase in both ε' and ε'' with increasing water concentration in both measurement modes and

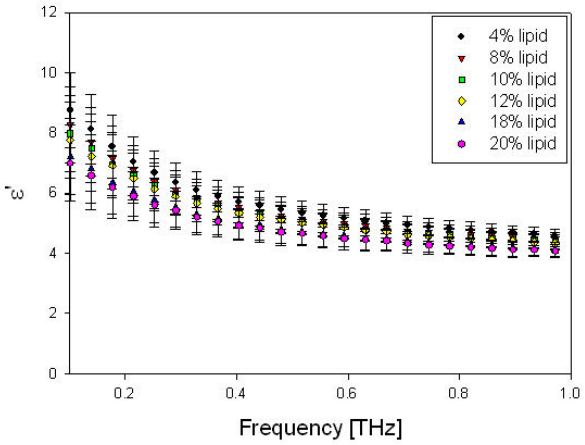

(a) Transmission mode

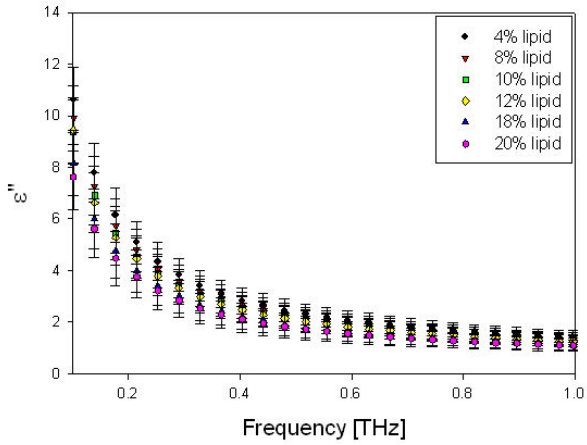

(b) Transmission mode

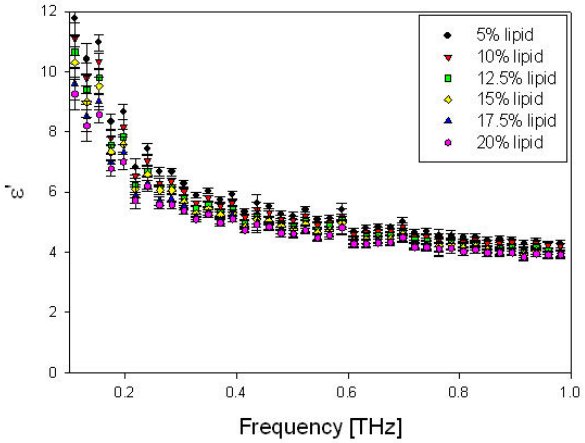

(c) Reflection mode

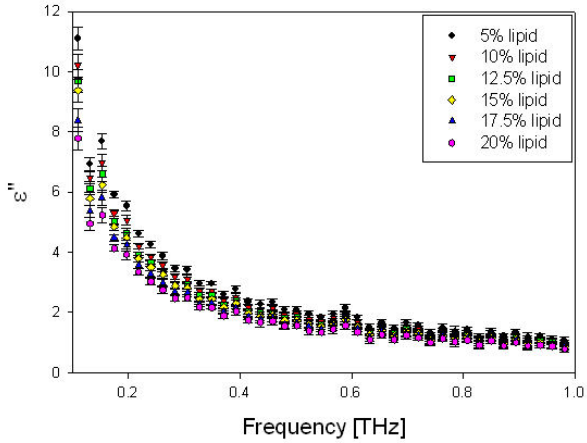

(d) Reflection mode

Figure 5.17: The real and imaginary dielectric coefficients of water and lipid solutions plotted for different concentrations of lipid as a function of frequency for a) and b) transmission and c) and d) reflection mode measurements.

Table 5.7: Accuracy and resolution of methanol concentration determined using the spectrally averaged dielectric coefficient method

	Resolution	Accuracy
Methanol	±11.6%	+0.5%

the dielectric coefficients of the transmission mode measurements are much smoother than those for the reflection mode.

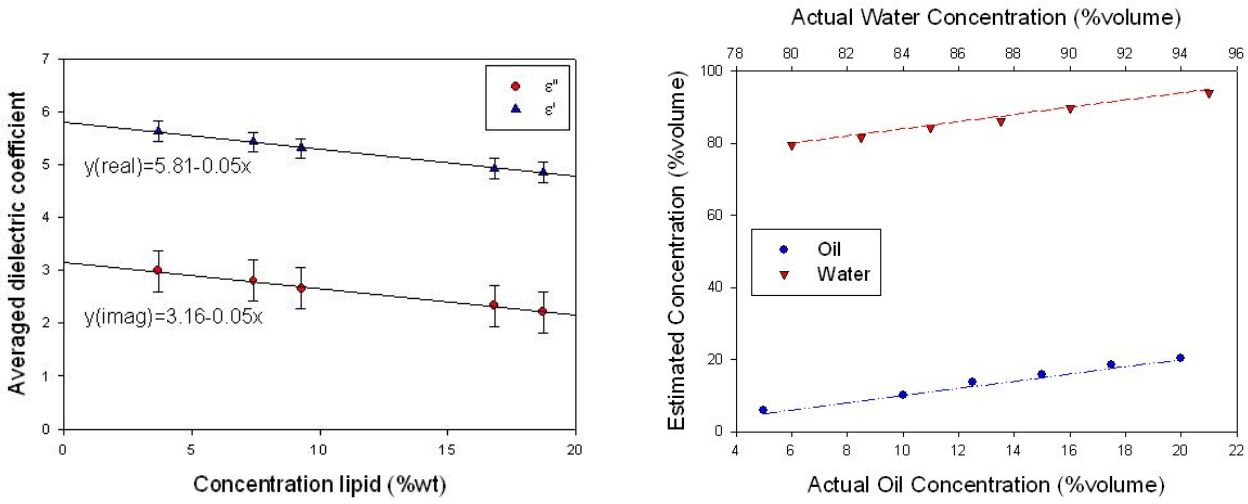

(a) (b)

Figure 5.18: Plot showing a) the average value of ε' and ε'' in water and lipid emulsions as a function of lipid concentration. The symbols are the averaged dielectric coefficients determined from the data and the dotted lines represent the best fit of the empirical functions. b) shows the concentrations of water and lipid determined from measurements of ε' and ε'' in water and lipid emulsions using spectrally averaged dielectric coefficient method. These calculated concentrations are plotted against the known concentrations of water and lipid. The line represents the line of unity while the symbols represent the calculated concentrations.

The agreement between the empirical functions and the measured data is illustrated in figure 5.18(a) where the coefficients for the empirical equations are also given. The concentrations determined from measurements of ε' and ε'' made in reflection mode are shown in figure 5.18(b). The accuracy and the resolution of this technique are given in table 5.8. From figure 5.18(a), it can be noted that the gradient of the magnitude of ε' and ε'' with respect to concentration is relatively low. Given the magnitude of the standard deviations of ε' and ε'' used to determine the resolution of the method, the low gradient results in a poor resolution. For example, the maximum concentration of

lipids is 20% which compares to a resolution of 31.5%, table 5.8.

Table 5.8: Accuracy and resolution of lipid concentration determined using the spectrally averaged dielectric coefficient method

	Resolution	Accuracy
Lipid	±31.5%	+0.8%

5.3.3 Water and sucrose solutions

ε' and ε'' of water and sucrose solutions obtained from transmission and reflection mode measurements are shown in figure 5.19. There is an increase in both ε' and ε'' with increasing water concentration in both measurement modes. There appears to be a stronger dependence of ε'' on sucrose concentration than ε'.

The agreement between the empirical functions and the measured data is illustrated in figure 5.20(a) where the coefficients for the empirical equations are also given. The concentrations determined from measurements of ε' and ε'' made in reflection mode are shown in figure 5.20(b). The accuracy and the resolution of this technique are given in table 5.9. From figure 5.20(a), it can be seen that the gradient of ε' and ε'' with respect to, and hence it's sensitivity to, concentration is low. Given the magnitude of the standard deviations of ε' and ε'' used to determine the resolution of the method, the low gradient results in a poor resolution. For example, the maximum concentration of sucrose is 33.3% which compares to a resolution of 42%.

Table 5.9: Accuracy and resolution of sucrose concentration determined using the spectrally averaged dielectric coefficient method

	Resolution	Accuracy
Sucrose	±42.0%	+1.9%

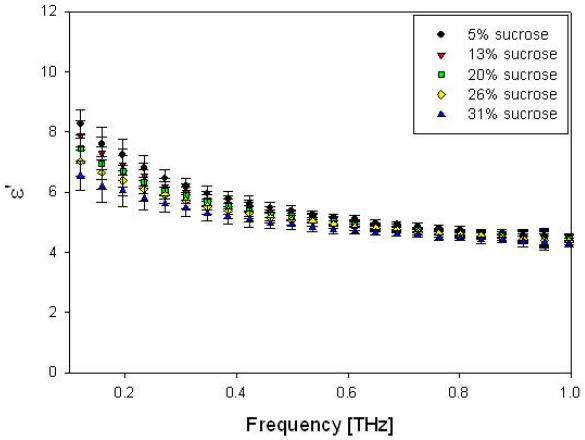

(a) Transmission mode

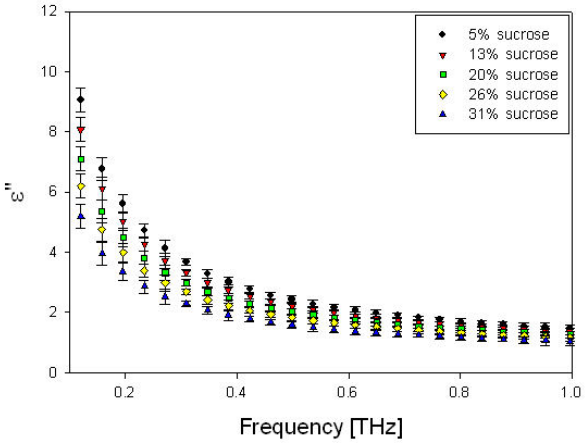

(b) Transmission mode

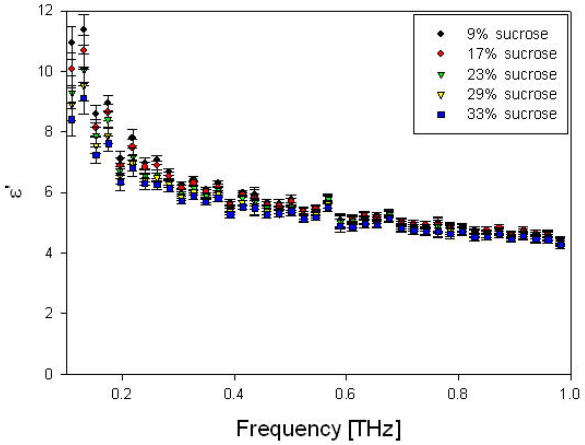

(c) Reflection mode

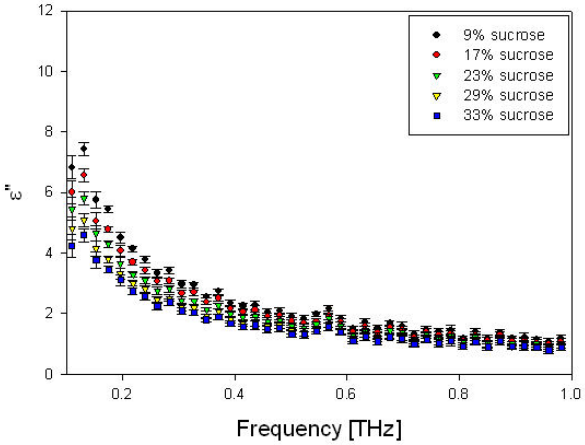

(d) Reflection mode

Figure 5.19: The real and imaginary dielectric coefficients of water and sucrose solutions plotted for different concentrations of sucrose as a function of frequency for a) and b) transmission and c) and d) reflection mode measurements.

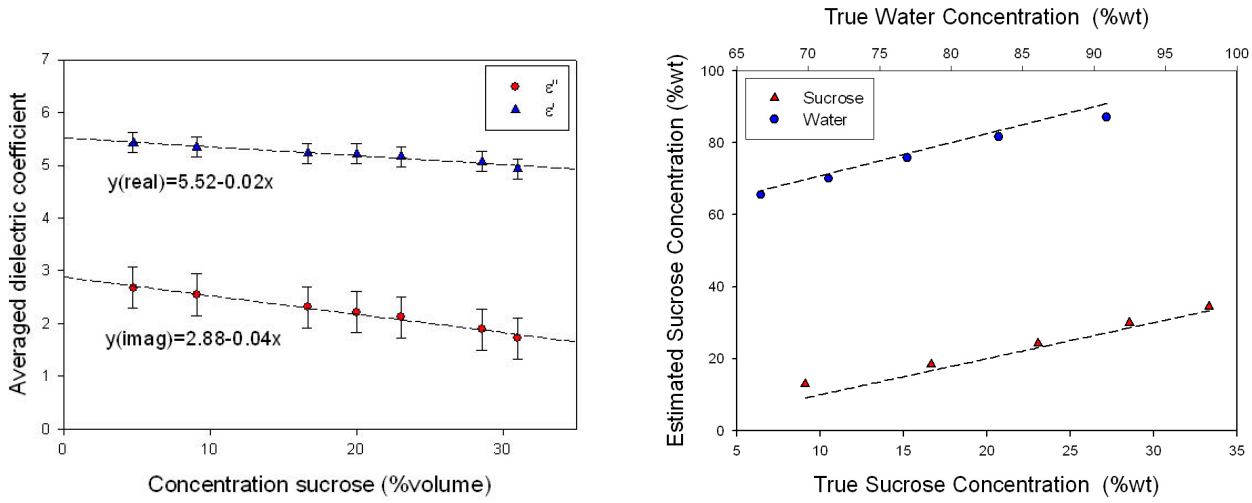

Figure 5.20: Plot showing a) the average value of ε' and ε'' in water and sucrose solutions as a function of sucrose concentration. The symbols are the averaged dielectric coefficients determined from the experimental data and the dotted lines represent the best fit of the empirical functions to the data measured in transmission mode. b) shows the concentrations of water and sucrose determined from measurements of ε' and ε'' using spectrally averaged dielectric coefficient method. The calculated concentrations are plotted against the known concentrations of water and sucrose. The line represents the line of unity while the symbols represent the calculated concentrations.

5.3.4 Water and gelatin gels

ε' and ε'' obtained from transmission and reflection mode measurements are shown in figure 5.21. There is an increase in both ε' and ε'' with increasing water concentration in both measurement modes. However, the concentration dependence of the dielectric coefficient is not as strong as observed on, for example, methanol and water solutions. The agreement between the empirical functions and the measured data is illustrated in figure 5.22(a) where the coefficients for the empirical equations are also given. The concentrations determined from measurements of ε' and ε'' made in reflection mode are shown in figure 5.22(b). Their accuracy and resolution are given in table 5.10. From figure 5.22, it can be seen that the gradient of ε' and ε'' with respect to concentration is low which results in a poor resolution. For example, the maximum concentration of gelatin is 30% which compares to a resolution of 55%.

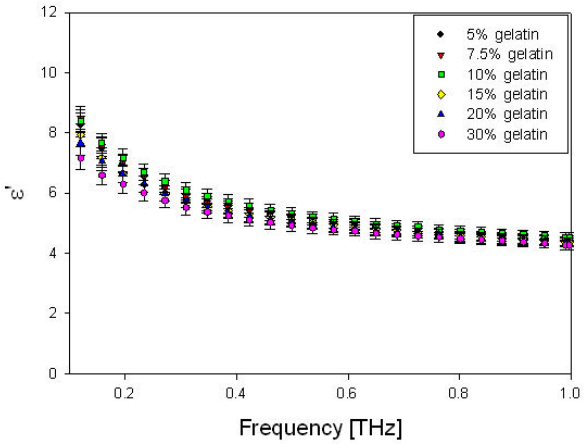

(a) Transmission mode

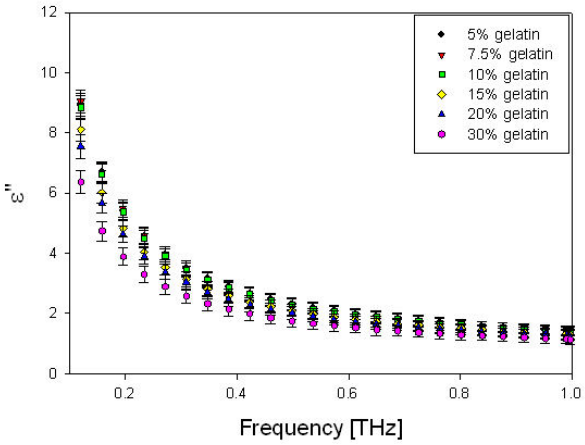

(b) Transmission mode

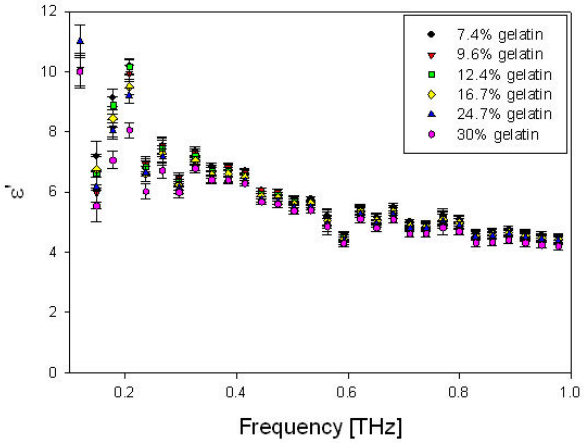

(c) Reflection mode

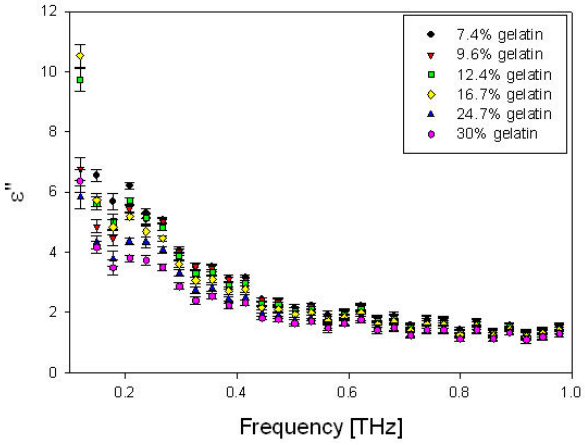

(d) Reflection mode

Figure 5.21: The real and imaginary dielectric coefficients of aqueous gelatin gels plotted for different concentrations of gelatin as a function of frequency for a) and b) transmission and c) and d) reflection mode measurements.

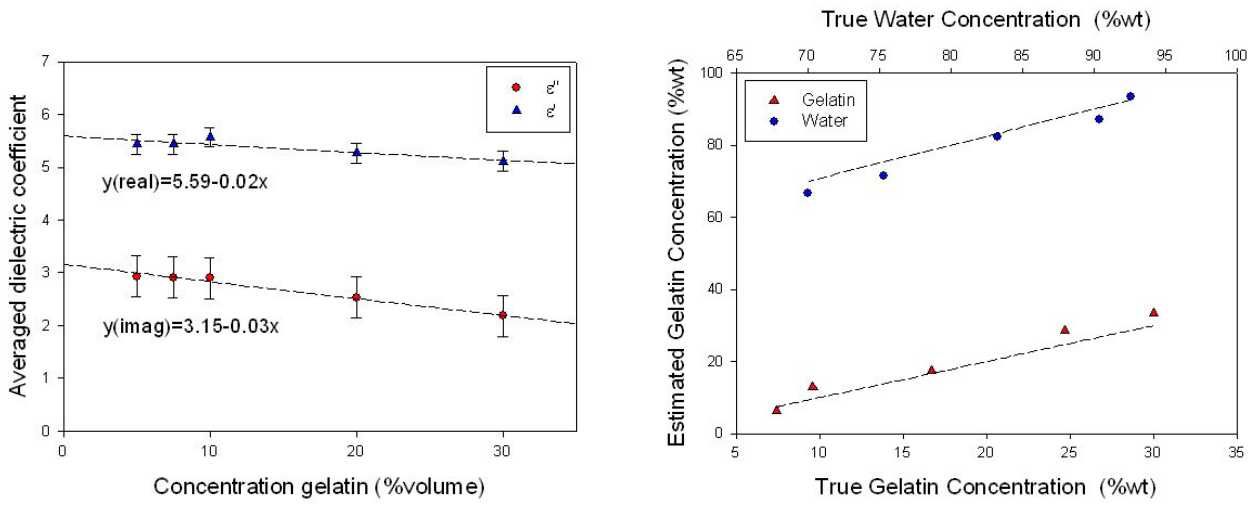

Figure 5.22: Plot showing a) the average value of the real and imaginary parts of the dielectric coefficient in aqueous gelatin gels as a function of gelatin concentration. The symbols are the averaged dielectric coefficients determined from the experimental data and the dotted lines represent the best fit of the empirical functions to the data measured on transmission mode. b) shows the concentrations of water and gelatin calculated from measurements of the real and imaginary parts of the dielectric coefficient in aqueous gelatin gels using spectrally averaged dielectric coefficient method. The line represents the line of unity while the symbols represent the calculated concentrations.

Table 5.10: Accuracy and resolution of gelatin concentration determined using the spectrally averaged dielectric coefficient method

	Resolution	Accuracy
Gelatin	±55.0%	+2.1%

5.3.5 Water, methanol and sucrose solutions

Having determined the empirical relationships between the concentration of a single solute and the real and imaginary parts of the dielectric coefficient of the solutions, the technique is now applied to the simultaneous determination of solute concentrations in three component phantoms. It is assumed that the changes in the dielectric coefficient are a combination of all phantom constituents. Only two chromophores can be directly quantified with this method.

Firstly water, methanol and sucrose solutions are investigated. Figure 5.23 illustrates ε' and ε'' for aqueous solutions of methanol and sucrose measured in both transmission and reflection modes. Both ε' and ε'' are larger for solution A than solution B which is

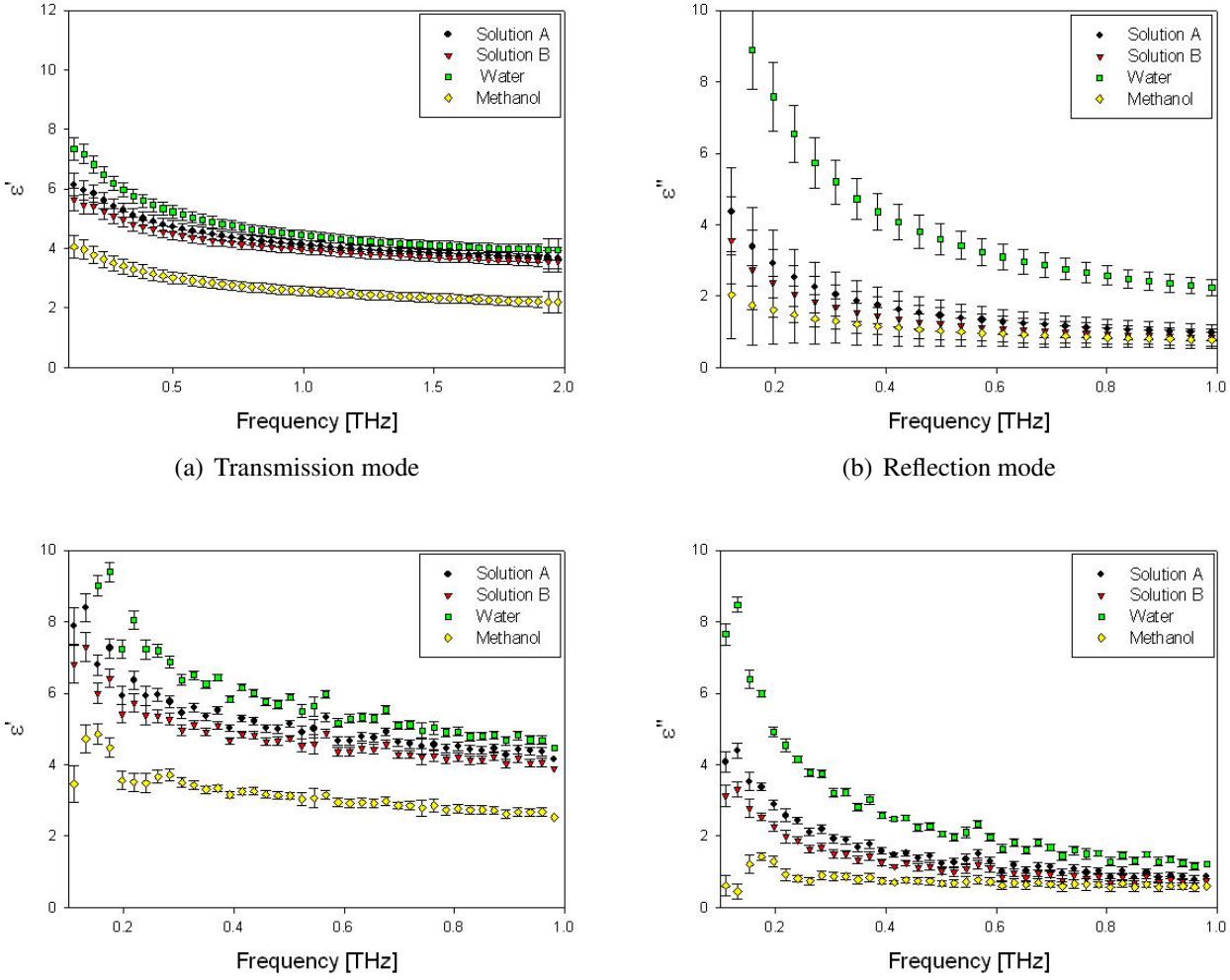

(a) Transmission mode

(b) Reflection mode

(c) Reflection mode

(d) Reflection mode

Figure 5.23: The real and imaginary dielectric coefficients of water, methanol and sucrose solutions plotted for different concentrations of water, methanol and sucrose as a function of frequency for a) and b) transmission and c) and d) reflection reflection mode measurements.

most likely due to the higher water of content solution A.

The determination of concentrations of solutions containing more than two compounds was achieved by combining the empirical equations for both ε' and ε'' that were obtained for the individual solutes (methanol and sucrose, shown in figures 5.16(a) and 5.20(a), respectively). The combined equations have two unknowns, the methanol concentration and the sucrose concentration. This method was applied to measurements made in both transmission and reflection mode.

Table 5.11: Accuracy and resolution of methanol and sucrose concentrations determined using spectrally averaged dielectric coefficient method

	Resolution Transmission	Resolution Reflection	Accuracy Transmission	Accuracy Reflection
Methanol	$\pm$26.9%	$\pm$41.3%	-0.5%	-0.1%
Sucrose	$\pm$29.9%	$\pm$42.0%	+2.1%	+2.3%

The accuracy and resolution of the concentrations determined using the spectrally averaged dielectric coefficient are given in table 5.11. The accuracy of the determined concentrations from both measurement modes are comparable to those determined from the methanol and water solutions and the sucrose and water solutions. The results reported by the original publication of this method gave an accuracy of $+1.5\%$ for the determined sucrose concentration and -1% for the determined methanol concentration (Jepsen et al. 2007). The suitability of the technique for use in the simultaneous concentration determination of two solutes in an aqueous solution is limited by the resolutions, which are poor in relation to the magnitude of the concentrations to be resolved. The transmission mode resolutions are better than those for the reflection mode measurements. This is due to the smaller standard deviations of these measurements.

The successful application of this concentration analysis method to three component mixtures requires that changes of the complex dielectric coefficient be described as the sum of the individual complex dielectric coefficients of the two components. Next this concentration analysis method is applied to the more complex gelatin, lipid and water phantoms.

5.3.6 Water, gelatin and lipid phantoms

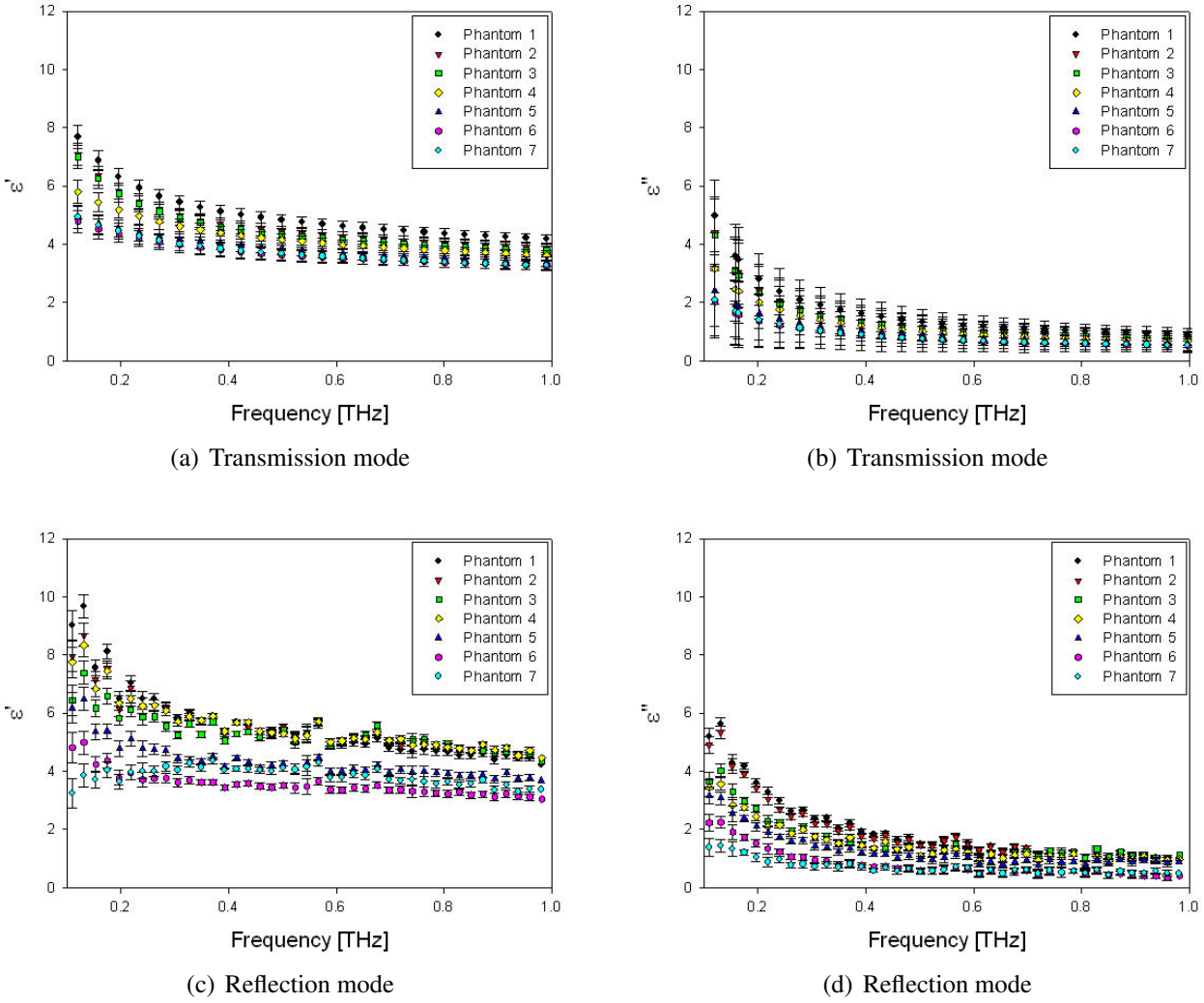

(a) Transmission mode

(b) Transmission mode

(c) Reflection mode

(d) Reflection mode

Figure 5.24: The real and imaginary dielectric coefficients of water, gelatin and lipid phantoms plotted for different concentrations of water, gelatin and lipid as a function of frequency for a) and b) transmission and c) and d) reflection mode measurements.

The spectrally averaged dielectric coefficient method was used to determine the concentrations of lipid and gelatin in the three component solid phantoms. ε' and ε'' of these phantoms are shown in figure 5.24 for both the transmission and reflection modes over the frequency range 0.1-1 THz. There is a decrease in both ε' and ε'' of the phantoms, with decreasing lipid concentration which can be observed in both measurement modes, where the decrease is greatest at lower frequencies.

The concentrations determined from measurements of ε' and ε'' made in transmission and reflection mode are shown in figure 5.25. Their accuracy and resolution are given in table 5.12. It can be noted that the accuracy is much worse than the accuracies de-

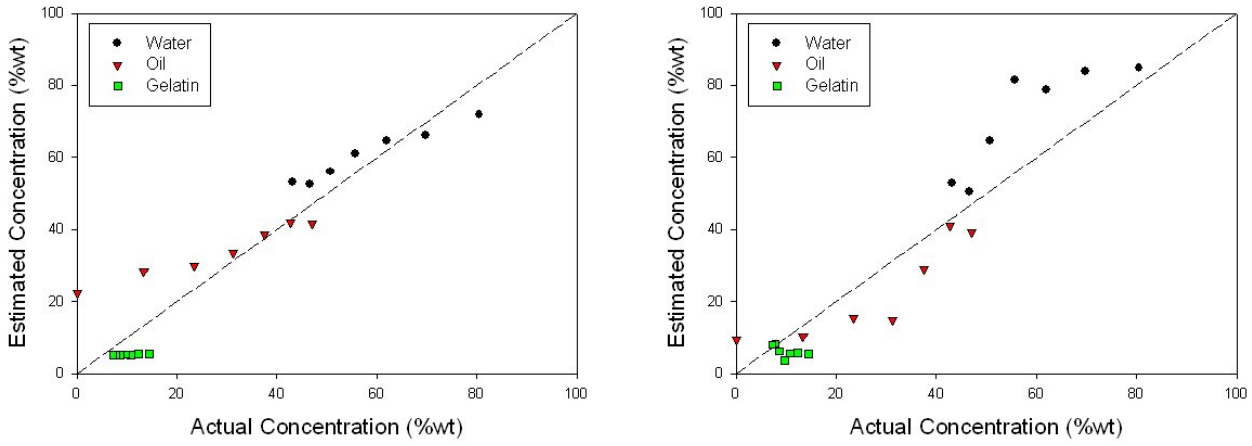

(a) Transmission (b) Reflection

Figure 5.25: The concentrations of water, gelatin and lipid determined from the averaged ε' and ε'' of 3 phase phantoms measured in a) transmission and b) reflectance measurement mode. The determined concentrations are plotted against the true concentration where the symbols represent the calculated values and the dotted line represents the true concentrations.

Table 5.12: Accuracy and resolution of gelatin and lipid concentrations determined using spectrally averaged dielectric coefficient method

	Resolution Transmission	Resolution Reflection	Accuracy Transmission	Accuracy Reflection
Gelatin	±57.3%	±80.3%	-4.8%	-4.8%
Lipid	±51.8%	±73.3%	+7.7%	-4.7%

termined for the corresponding two component solutions and gels. This was also noted from the concentrations determined from the linear spectral decomposition method in section 5.2.6 and, again, could be an indication of more complex bonding within the phantoms and its effect on ε' and ε'' which are not accounted for in the model. As with all phantoms analysed using this technique, the resolutions for this phantom are poor in comparison to the magnitude of the concentrations to be resolved, limiting the potential of this concentration analysis technique as a tissue spectroscopy tool.

5.3.7 Summary

For all phantoms, the determined concentrations have an improved accuracy when compared to those determined using the linear spectral decomposition technique. The resolutions of this technique, however, were poor. This is due to the small $\frac{\Delta\varepsilon'}{\Delta c}$ and $\frac{\Delta\varepsilon'}{\Delta c}$ as can be seen from the shallow gradients of the empirical equations. The resolutions

were larger, in some instances, than the concentrations of the phantoms under investigation. In addition, as only a maximum of two components could be resolved using this technique, its future use as a tissue spectroscopy tool is limited.

5.4 Method 3: Determination of phantom composition from Debye relaxation coefficients

This method, which is described in section 3.5.4.3, is an empirical technique based on Debye theory. Debye theory models the dynamical behaviour and interactions of molecules within a material when irradiated by electromagnetic radiation and is employed in this method to determine the composition of tissue phantoms. Empirical equations were created to describe the dependence of Debye relaxation coefficients determined from measurements of $\varepsilon^{'}$ and $\varepsilon^{''}$ across a frequency range, on concentration. By comparing the Debye relaxation coefficients determined from $\varepsilon^{'}$ and $\varepsilon^{''}$ of unknown samples to these empirical equations, an estimate of concentration may be obtained. This method incorporates the measured absorption coefficient and refractive index through the use of both $\varepsilon^{'}$ and $\varepsilon^{''}$.

The results of this method are presented in five sections, four sections for each two-phase phantom and one section for the three-phase phantoms. Each section presents Debye relaxation coefficients determined from measurements of $\varepsilon^{'}$ and $\varepsilon^{''}$ across a frequency range of each phantom. This is followed by the results of the concentration analysis. In the implementation of this method, transmission mode measurements of $\varepsilon^{'}$ and $\varepsilon^{''}$ were used to determine the coefficients of the empirical equations. Reflection mode measurements of $\varepsilon^{'}$ and $\varepsilon^{''}$ were used as 'unknown' data from which concentrations were determined. The implementation involved the following steps.

Firstly, Debye relaxation coefficients were determined from transmission mode measurements of ε' and ε'', section 2.4.2.1, for each phantom composition over the 0.1-2 THz frequency range. Double Debye theory, equation 3.9, was used to determine the Debye relaxation coefficients of the phantoms as a function of concentration. The exception was triple Debye theory, equation 3.10, which was used to investigate more complex of relaxation mechanisms within the gelatin and water gels. This is described in section 3.5.4.3.

Secondly, the variation with concentration of the determined Debye relaxation coefficients was established. Empirical equations were formulated for each Debye re-

laxation coefficient to describe its concentration dependence. This was done for a single solute in each of the phantoms: the concentration of the non-water component of the phantom, i.e., methanol, lipid, sucrose or gelatin. Empirical equations were formulated from these plots, the coefficients of which described the trend of the Debye relaxation coefficients with non-water component concentration. These took the form of polynomial functions and all functions are presented in appendix A. The empirical equations for the two-phase phantoms were created for the %wt of the relative solutes in the phantoms to enable them to be commutable to the concentration analysis of the three-phase phantoms, the concentrations of which are defined as %wt of the relative solutes.

The final step was to determine the concentrations of the components in 'unknown' aqueous phantoms, where the derived empirical equations using the pre-determined fitting parameters formed the prior knowledge. The empirical equations were solved, using a least squares fitting routine, for concentration using the Debye relaxation coefficients determined from reflection mode measurements.

As with the spectrally averaged dielectric coefficient method, it is only the concentrations of the non-water components which are directly determined from the measured data. The 'remaining' concentration of the phantoms is considered to be that of water. In this section, the accuracy and resolutions will be quoted for only the directly determined component concentrations. However, in the figures both the directly determined component concentrations and the inferred water component concentrations are given.

The accuracy of the technique was calculated from the difference between the calculated and the true concentration values. The individual accuracies were then averaged over all measurements made in a particular phantom to give an estimation of the average accuracy.

The calculation of the resolutions for the Debye coefficients method was a two-part process to ensure the correct propagation of the error in the measured data through to the quoted resolutions. Firstly the resolution in each of the determined Debye coefficients was calculated. This was determined from the calculation of uncertainty, equation 3.11, where the design matrix of the model is the change in ε' and ε'' with a small change in each of the Debye coefficients determined for a particular phantom concentration ie, $\frac{\Delta\varepsilon'}{\Delta\Delta_1}$, $\frac{\Delta\varepsilon''}{\Delta\tau_1}$, etc. The standard deviation of the real and imaginary parts of the measured dielectric coefficient was used, table 3.2. This yielded the uncertainties

in each of the determined Debye coefficients. These resolutions were then used as the standard deviation in equation 3.11 in the second step of the process to calculate the overall resolution of the Debye coefficients method. In this second step, the design matrix of the model, was the change in Debye relaxation coefficients with a small change in concentration, ie, $\frac{\Delta\Delta_1}{\Delta c}$, $\frac{\Delta\tau_1}{\Delta c}$, etc. The value calculated by equation 3.11 following this second implementation is the overall resolution of the Debye coefficients method at a particular phantom concentration.

As polynomial functions were used as the basis of the empirical equations there is a variation in sensitivity to concentration change across the concentration range. The resolutions quoted in this section are the resolutions averaged over the concentration range of each phantom.

5.4.1 Water and methanol solutions

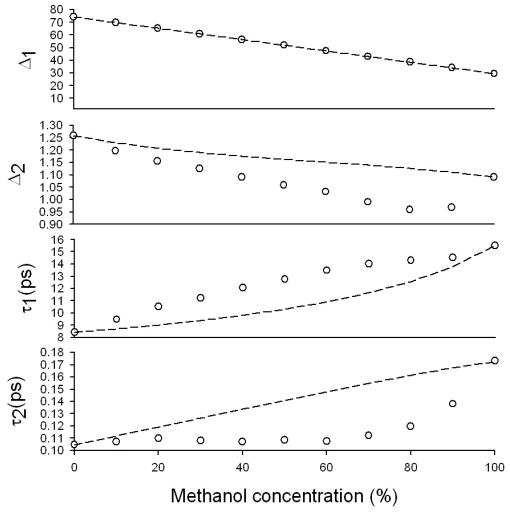

Figure 5.26: The measured Debye coefficients of the methanol and water solutions, as a function of methanol concentration. The circles represent the Debye coefficients obtained from the measured data while the dotted line shows those extracted from the complex dielectric coefficients of linear volumetric mixing of methanol and water where the contribution by both solutes to the absorption coefficient and refractive index is linear.

The variation in the determined Debye relaxation coefficients with methanol concentration are illustrated in figure 5.26. A significant deviation from the Debye coefficients predicted by linear volumetric mixing can be observed which has been previously reported (Venables and Schmuttenmaer 2000b, Koeberg et al. 2007). τ_1 is believed to represent the reorientation of molecular species while τ_2 is generally ascribed to hydrogen bonding and the relaxation of single molecules (Venables and Schmuttenmaer

2000b). The variation in the τ_1 and τ_2 relaxation times are understood to result from 'incomplete mixing' of the water and methanol molecules, as previously suggested from section 5.2.1. Previous studies have suggested that the viscosity and rigidity of clusters of pure methanol and pure water molecules could produce an anti-cooperative effect on reorientation between molecules (Ladanyi and Skaf 1996, Borin and Skaf 1998, Skaf 1999, Nieto-Draghi et al. 2005) which could increase the hydrogen bond lifetime with increasing methanol concentration resulting in the slowed τ_1 relaxation time. The fraction of water molecules bonded to both water and methanol molecules has a maximum at a higher methanol concentration than would be expected for a randomly dispersed solution of the pure solutes. Water molecules are more likely to bond with each other than with molecules of other species while methanol in high water content solutions is thought to become similar to water in its bonding characteristics (Palinkas et al. 1991, Laaksonen et al. 1997, Venables and Schmuttenmaer 2000b). Variations in the τ_2 relaxation time, therefore, could be an indication of the dominance of water-like hydrogen bond activity. This is confirmed in the results shown in figure 5.26, where the value of τ_2 is similar to that of pure water up to concentrations of methanol up to approximately 60%.

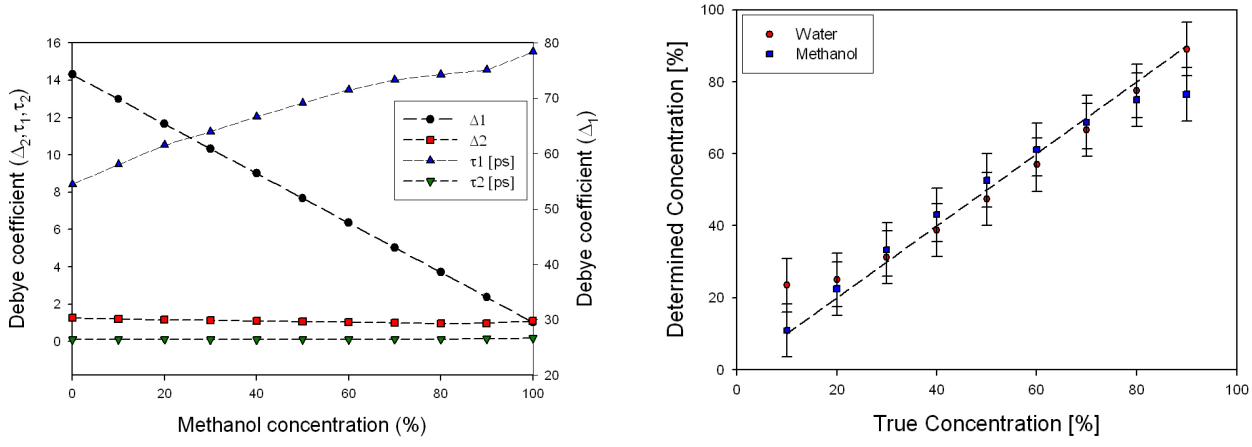

(a) Transmission empirical equation

(b) Concentration Analysis

Figure 5.27: a) The Debye coefficients measured in transmission in water and methanol solutions, plotted as a function of methanol concentration. The symbols are the Debye relaxation coefficients determined from the experimental data and the dotted lines represent the best fit of empirical functions to the data measured on transmission mode. b) The concentrations of water and methanol calculated using the Debye coefficient trends method analysing the complex dielectric coefficient measured in reflection on water and methanol solutions. The line represents the line of unity while the symbols represent the calculated concentrations.

The empirical functions describing the variation in Debye relaxation coefficients and concentration are illustrated in figure 5.27(a). The concentrations determined on measurements of water and methanol solution made in reflection mode are shown in figure 5.27. The accuracy and the resolution of the concentrations are given in table 5.13.

Table 5.13: Accuracy and resolution of methanol concentration determined using Debye relaxation coefficients

	Resolution	Accuracy
Methanol	$\pm$7.4%	-0.7%

5.4.2 Water and lipid emulsions

The variation in the determined Debye relaxation coefficients with respect to lipid concentration are illustrated in figure 5.28(a). The τ_1 relaxation time of the lipid and water emulsions remains almost constant and is consistent with the Debye coefficients predicted by linear volumetric mixing, while τ_2 shows a slight tendency towards slowing with increasing concentration but is faster than the predicted Debye coefficients. Possible influences on the relaxation processes within the emulsions include the relaxations of the individual molecules of water and lipid, reorientation of lipid micelles, inter-micelle interactions and interactions between the micelle and the solution. To describe the relaxation of a spherical molecule of radius r rotating in a medium with viscosity η, Debye proposed equation 5.1, where k is Boltzmann's constant and T is temperature in kelvin. The rotation of a molecule is, therefore, dependent on the volume of the rotating molecule and the viscosity of the surrounding solution.

$$\tau = \frac{4\pi r^3 \eta}{kT} \tag{5.1}$$

If a lipid micelle is considered as a molecule with a radius of 5nm within the emulsion (Flock et al. 1992), equation 5.1 predicts the relaxation time to be 3.8 ms corresponding to a frequency of 0.26 kHz, well outside the measured frequency range. Inter-micelle interactions and aggregation of suspended particles increase in significance when the volume fraction of micelles approaches 10% (Mittleman et al. 1997, Fricke and Curtis 1937). However, τ_1 is approximately constant and the change in τ_2 appears to be fairly linear across the concentration range with no indication of increased effect following the 10% micelle volume. A study of suspensions of polar solutes in a non polar solution using the THz frequency range, (Oka and Tominaga 2006), observed relaxations which were attributed to collision induced dipole moments between the non polar solvent and the polar solute micelles in the solution which would occur on a scale of, typically, a few hundreds of femtosecond. This could be responsible for the change in τ_2 measured in this study as these collisions would increase with increased micellular concentration. However, the most plausible conclusion is that it is the water content of the emulsions that give rise to the change in Debye relaxation coefficients. The values of the τ_1 and τ_2 relaxation times are similar to those determined for pure water, shown in table 4.1. Both the Δ_1 and Δ_2 values, which give an indication of the volume of contributors to a relaxation process, decrease with decreasing water volume. This suggests that there is little interaction between the water and the lipid, as suggested from figure 5.6 when emulsions were examined using the linear spectral decomposition method.

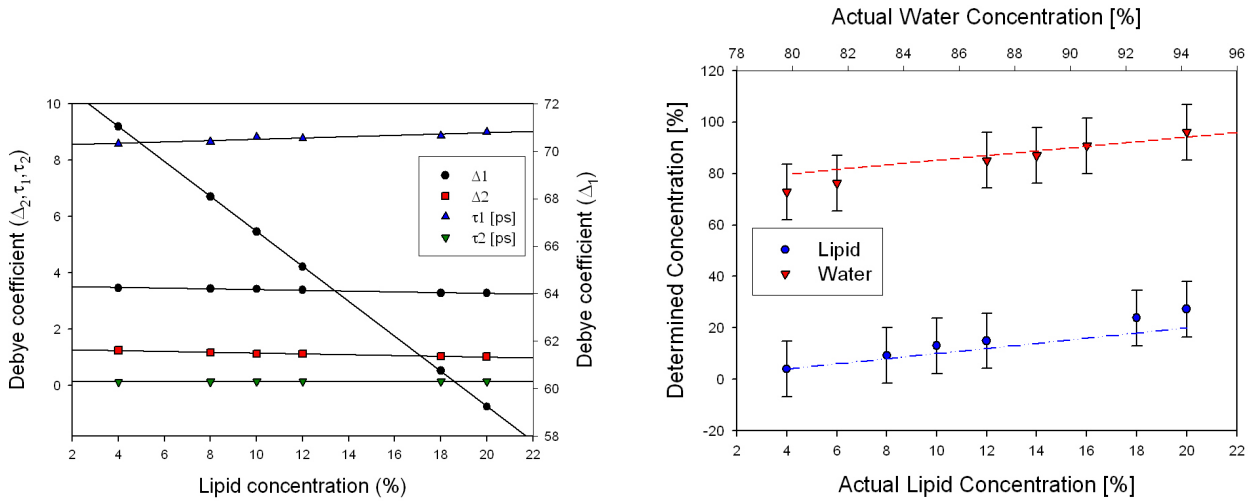

(a) (b)

Figure 5.28: a) The Debye coefficients measured in transmission in water and lipid emulsions, plotted as a function of lipid concentration. The symbols are the Debye relaxation coefficients determined from the experimental data and the dotted lines represent the best fit of empirical functions to the data measured on transmission mode. b) The concentrations of water and lipid calculated using the Debye coefficient trends method analysing the complex dielectric coefficient measured in reflection on water and lipid emulsions. The line represents the line of unity while the symbols represent the calculated concentrations.

While τ_1 remains fairly constant with concentration, the other coefficients display subtle changes. The empirical functions describing the variation in Debye relaxation coefficients and concentration are illustrated in figure 5.28(a). The concentrations determined on measurements of water and methanol solution made in reflection mode are shown in figure 5.28(b). The accuracy and the resolution of the concentrations are given in table 5.14. The average resolution of this method is still low in comparison to the concentrations of the phantoms under investigation, for example, the maximum concentration of lipids is 20% which compares to a resolution of 10.8%, 50% of the concentration value.

Table 5.14: Accuracy and resolution of lipid concentration determined using Debye relaxation coefficients

	Resolution	Accuracy
Lipid	±10.8%	+2.0%

5.4.3 Water and sucrose solutions

The dependence of the determined Debye relaxation coefficients on sucrose concentration is illustrated in figure 5.29(a) for the double Debye theory. The Debye relaxation coefficients determined using double Debye theory show an increase in τ_1 with increasing sucrose concentration. τ_2 appears to remain constant with increasing sucrose concentration.

Previous studies of the interaction of sugars with water in the 100kHz to 35GHz frequency range concluded that τ_2 reflects the relaxation of bulk water while the longer relaxation, τ_1, is attributed to the relaxation of the sugar and the water contained in the hydration layer (Suggett 1976, Tait et al. 1972). Relaxation times of water molecules in the presence of sugars are 1.2 to 10 times slower than those of pure water, (Bordat et al. 2004, Heugen et al. 2006). As the sucrose concentration increases, therefore, a larger proportion of water becomes associated with sugar molecules resulting in slowing of water relaxations, seen in both τ_1 and τ_2 relaxations (Maeda and Kitano 1995, Molinero et al. 2003). This is evidence of the extended hydrodynamic shell which surrounds a macromolecule where the relaxations of the bound water are slowed as the sucrose concentration increases.

The empirical functions describing the variation in Debye relaxation coefficients and concentration are illustrated in figure 5.29(a). The concentrations determined on measurements of water and methanol solution made in reflection mode are shown in figure 5.29(b). The accuracy and the resolution of the concentrations are given in table 5.15. The average resolution of this method is not large in comparison to the concentrations of the phantoms under investigation, for example, the maximum concentration of sucrose is 33.3% which compares to a resolution of 3.9%, 10% of the concentration value.

Table 5.15: Accuracy and resolution of sucrose concentration determined using Debye relaxation coefficients

	Resolution	Accuracy
Sucrose	$\pm$3.9%	-1.9%

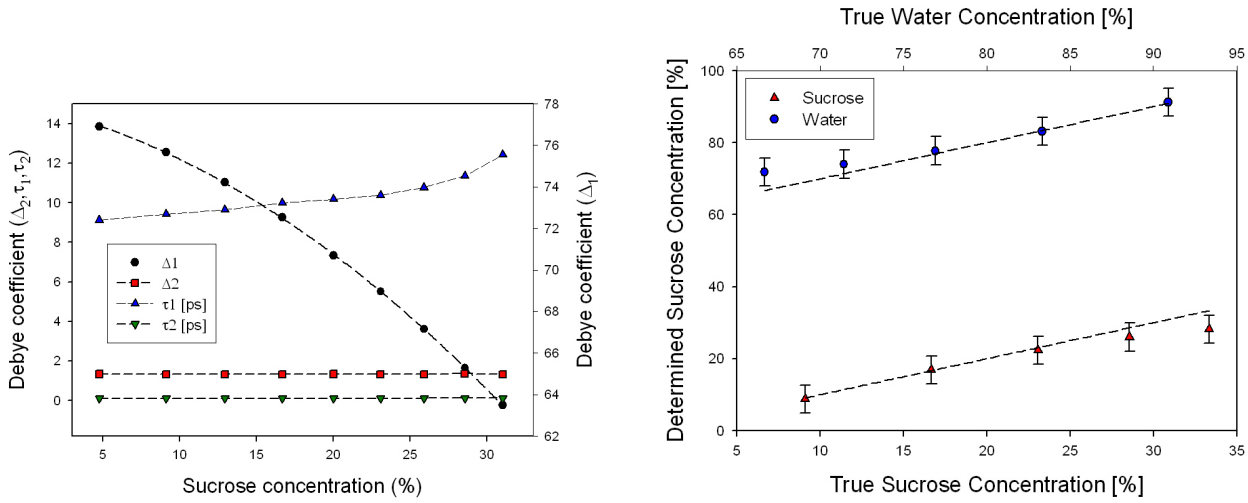

(a) (b)

Figure 5.29: a) The Debye coefficients measured in transmission in water and sucrose solutions, plotted as a function of sucrose concentration. The symbols are the Debye relaxation coefficients determined from the experimental data and the dotted lines represent the best fit of empirical functions to the data measured on transmission mode. b) The concentrations of water and sucrose calculated using the Debye coefficient trends method analysing the complex dielectric coefficient measured in reflection on water and sucrose solutions. The line represents the line of unity while the symbols represent the calculated concentrations.

5.4.4 Water and gelatin gels

The dependence of the Debye relaxation coefficients determined using double and triple Debye theory are shown in figures 5.30(a) and 5.30(b), respectively, as a function of gelatin concentration. The Debye relaxation coefficients determined using double and triple Debye theory do not display a significant trend with gelatin concentration. There may be some relationship, however, it is obscured by noise on the data. In both Debye fitting routines, Δ_1, which represents the contribution by the τ_1 relaxation coefficient to the overall signal, decreases with increasing gelatin concentration. The value of the τ_1 relaxation coefficient fluctuates around 5.5ps, the same value reported in the analysis if the hydrated gelatin molecule, section 4.3.2.

A more systematic change in Debye coefficients with gelatin concentration is observed when double Debye theory is applied where the ε_s value is held constant at 78.8, i.e. that of pure water. The empirical functions describing the variation in Debye relaxation coefficients and concentration are illustrated in figure 5.31(a). An increase is observed in the values of both the τ_1 and τ_2 relaxation times with the τ_1 relaxation appearing to exponentially increase as the gelatin concentration increases. This trend is similar to that observed in trends shown by the Debye relaxation coefficients of the sucrose and

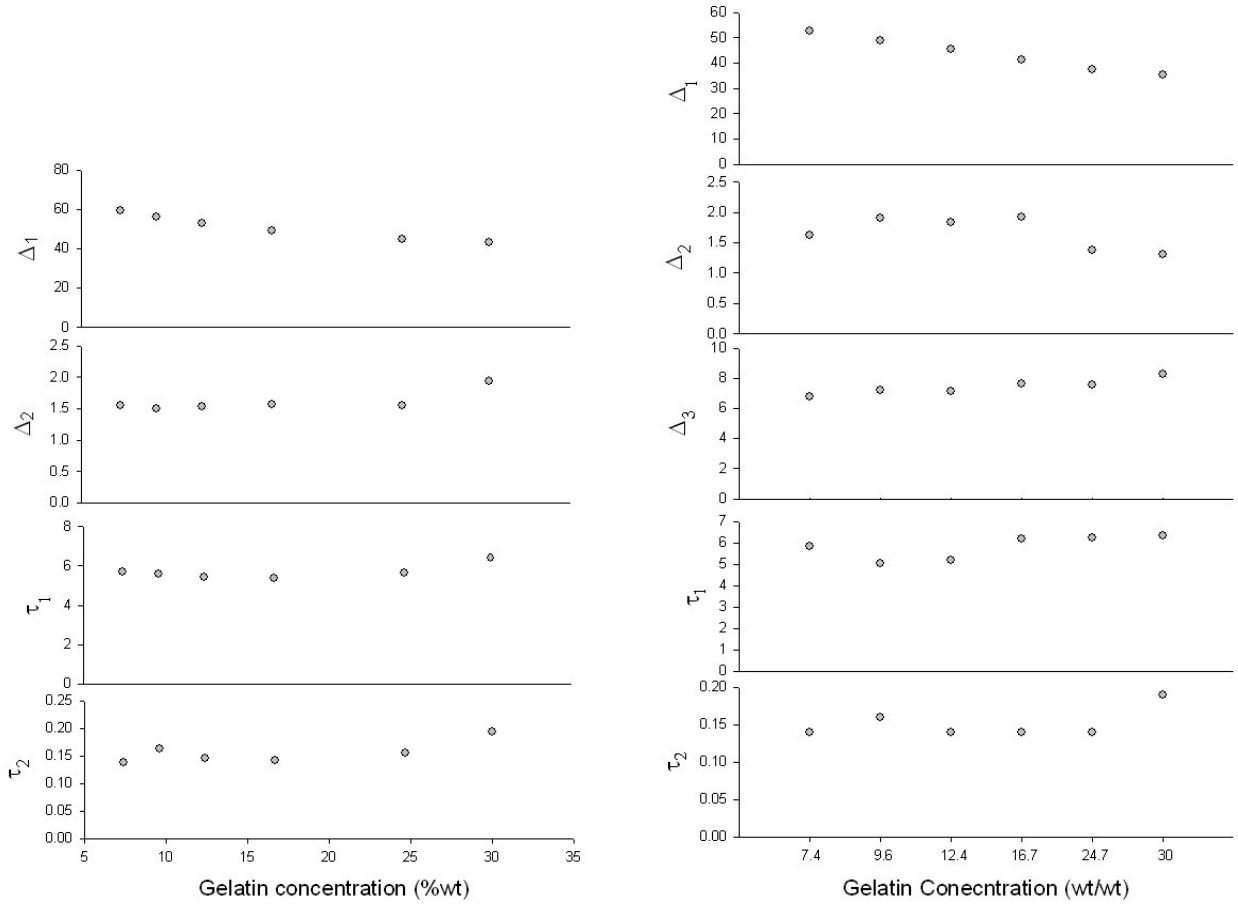

(a) Double Debye (b) Triple Debye

Figure 5.30: The Debye coefficients of gelatin and water gels, as a function of gelatin concentration.

water solutions.

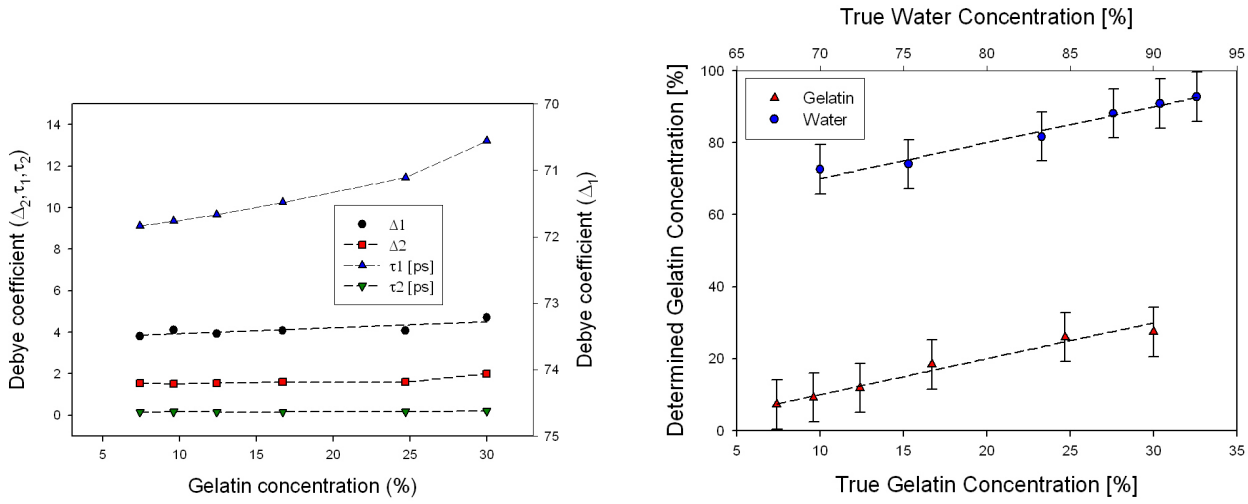

(a) (b)

Figure 5.31: a) The Debye coefficients measured in transmission in water and gelatin gels, plotted as a function of gelatin concentration. The symbols are the Debye relaxation coefficients determined from the experimental data and the dotted lines represent the best fit of empirical functions to the data measured on transmission mode. b) The concentrations of water and gelatin calculated using the Debye coefficient trends method analysing the complex dielectric coefficient measured in reflection on water and gelatin gels. The line represents the line of unity while the symbols represent the calculated concentrations.

Table 5.16: Accuracy and resolution of gelatin concentration determined using Debye relaxation coefficients

	Resolution	Accuracy
Gelatin	±6.8%	+0.2%

The concentrations determined on measurements of water and gelatin gels made in reflection mode are shown in figure 5.31(b). The accuracy and the resolution of the concentrations are given in table 5.16. The average resolution of this method is still quite large in comparison to the concentrations of the phantoms under investigation, for example, the maximum concentration of gelatin is 30% which compares to a resolution of 6.8%, ∼22% of the concentration value.

5.4.5 Three component phantoms

The suitability of the Debye relaxation coefficient method to determined the concentrations of three component mixtures is now considered. The Debye relaxation coeffi-

cients for the water, sucrose and methanol solutions are given in table 5.17. A reminder of the concentrations of these solutions is given below:

- Solution A: 71.4% wt water, 20.4% wt sucrose, 8.2% wt methanol
- Solution B: 62.5% wt water, 20.8% wt sucrose, 16% wt methanol

It can be seen that there is a greater Δ_1 value for the higher water content solution A, while the τ_1 values appear to be steady around 12ps.

Table 5.17: Double Debye coefficients determined from the complex dielectric coefficients of methanol sucrose and water solutions

	Solution A	Solution B
Δ_1	50.7	46.4
Δ_2	4.7	4.4
τ_1(ps)	4.3	4.6
τ_2(ps)	0.1	0.1

Alcohols and carbohydrates are known to be highly miscible with water and are able to form intermolecular hydrogen bonds with each other and neighbouring water molecules whilst in solution. Studies of the dielectric relaxation times of aqueous alcohol and carbohydrate solutions highlighted an average decrease of relaxation times in aqueous carbohydrate solutions, around 12ps for low concentration solutions (Bateman and Gabriel 1987, Gabriel et al. 1998), suggesting that the addition of both solutes to the aqueous solutions will contribute to a greater structure breaking effect on the H_2O lattice than if only a single solute was added.

The overall relaxation times for three component solutions are lower than the relaxation times determined in equivalent concentrations of two component solutions of water and methanol (where $\tau_1 \sim$ 9ps and 8.5ps respectively) and water and sucrose (where $\tau_1 \sim$ 9ps). This indicates that the method followed when applying the spectrally averaged dielectric coefficient method to three component phantoms where the empirical equations for the two-phase phantoms were combined to create empirical equations for the three-phase phantoms would not be suitable. This is most likely because this method links physical properties of the measured materials, in the form of molecular relaxation times, to chromophore concentration which are more complex than the bulk

interactions probed by the spectrally averaged dielectric coefficient and linear spectral decomposition methods.

In order to extend this analysis technique to the determination of the concentrations of phantoms containing more than two components, more detailed analysis of the variation in Debye relaxation coefficients with concentrations is required. It would be necessary to detail the variation in Debye relaxation coefficients with the variation of each individual solute in turn to create a multi-dimensional 'look-up-table' of Debye relaxation coefficients. From this table it may then be possible to correlate, with concentration, the variation in the determined Debye relaxation coefficients for multiple chromophores. However, this was beyond the scope of the work presented in this thesis.

5.4.6 Summary

For all phantoms, the determined concentrations have a similar accuracy when compared to those determined using the spectrally averaged dielectric coefficient method. The resolutions of this technique, however, were better than those determined using the spectrally averaged dielectric coefficient method. This is due to the larger value of $\frac{\Delta Debye}{\Delta c}$ as can be seen from the empirical functions. This technique was only validated here on two-phase phantoms, however, further investigation of the variations in determined Debye coefficients with tissue or phantom concentration should indicate its potential in use as a tissue spectroscopy tool.

5.5 Discussion

The relative accuracies and resolutions produced by the three different concentration analysis methods and presented in this chapter will now be discussed. Table 5.18 presents the accuracies of the concentrations determined using the three validated analysis methods. Only the results derived from reflection mode measurements are compared and discussed here. In assessing the capability of THz imaging and spectroscopy for medical applications, it is the measurements made in reflection mode which are of greatest relevance.

The accuracies of the techniques will first be discussed. From table 5.18 it is apparent that the order of best accuracies, from best to worst, the three methods may be listed as below:

1. Method 2: Spectrally averaged dielectric coefficient method
2. Method 3: Debye relaxation coefficient method

Table 5.18: Accuracy of concentrations in %wt determined using the linear spectral decomposition method (method 1), the spectrally averaged dielectric method (method 2) and the Debye relaxation coefficient method (method 3) for all water-based phantoms determined from reflection mode measurements

		Method 1			Method 2		Method 3
Solute 1	Solute 2	Water	Solute 1	Solute 2	Solute 1	Solute 2	Solute 1
Methanol		+4.8	-4.8	-	+0.5	-	-0.7
Lipid		+3.7	-3.7	-	+0.8	-	+2.0
Sucrose[a]		+8.5	-8.5	-	+1.9	-	-1.9
Sucrose[b]		-5.6	+5.6	-	-	-	-
Gelatin[a]		+0.3	-0.3	-	+2.1	-	+0.2
Gelatin[b]		+3.1	-3.1	-	-	-	-
Methanol	Sucrose	-2.5	+0.2	+2.7	+2.1	+2.3	-
Gelatin	Lipid	-8.1	-2.8	+14.5	-4.8	-4.7	-

[a] Absorption coefficient of 'dry' molecule used as prior knowledge

[b] Absorption coefficient of 'hydrated' molecule used as prior knowledge

3. Method 1: Linear spectral decomposition

Spectral decomposition approaches, such as method 1, should be a standard method for the determination of concentrations of these phantoms. Method 1 is reliant on only the absorption coefficient in its assessment of concentration and utilises the absorption coefficients of pure components measured in transmission mode in the analysis of the reflection signals. Small deviations between absorption coefficients measured in transmission and reflection modes can cause systematic differences. For example, measurements of the absorption coefficient made in reflection mode are inherently noisier than those made in transmission. In transmission mode, the absorption coefficient is calculated from the amplitude of the waveforms whereas in reflection mode they are derived from the phase components of the measured data and are only accurate if it can be assumed that the incident radiation, at each frequency, can be approximated by a normal incidence plane-wave. In the spectrometer used in this study, beams are incident at an angle of 30^o. This is not appropriately modelled by assuming a normal incidence plane wave. An EM wave incident at an angle suffers diffractive spreading. This may result in an error in the absolute value of the measured absorption coefficients and, hence, in the determined concentrations (Bowen et al. 2004). In addition, the inherently noisier signals detected in reflection mode may also reduce the accuracy of the method.

Methods 2 and 3, make use of a wider range of the measured data to determine concentrations compared to than method 1, by also incorporating the measured refractive indices of the phantoms through use of ε' and ε''. The use of twice as many measured data points by these two methods than used by method 1 results in methods 2 and 3 being inherently less sensitive to error and, therefore, more accurate. Method 3 is currently limited as the empirical functions only allow the analysis of data measured in two-phase phantoms. In order to build a detailed description of the variation in the Debye coefficients with each individual chromophore of the three component phantoms, it is necessary to measure the full variation of the Debye relaxation coefficients as a function of the concentrations of all compounds. While this is feasible, it would have required time-intensive measurements which were beyond the scope of this work.

The relative resolutions of the techniques will now be discussed. Table 5.19 presents the resolutions from the three validated analysis methods from which it is apparent that the order of the resolutions provided by the three methods may be listed as given below, from best to worst:

1. Method 1: Linear spectral decomposition
2. Method 3: Debye relaxation coefficient method
3. Method 2: Spectrally averaged dielectric coefficient method

Resolution is determined by the sensitivity of the measured data to changes with concentration, $\frac{\delta Data}{\delta Conc}$, and the standard deviation of the measurement. Since the same standard deviation was used for all calculations of the resolution in this work, it is then primarily dependent upon sensitivity, where a large sensitivity value results in a small resolution.

The resolutions determined for the linear spectral decomposition method are smaller for water compared to the other chromophores. This is because the absorption coefficient of water is greater over the whole frequency range than the absorption coefficients of the other chromophores, resulting in a larger sensitivity to water concentration. This is most apparent in the case of the aqueous lipid emulsion where the resolution of water is much higher than that of lipid, which is explained by an absorption coefficient of lipid that is much smaller than that of water.

In method 2, the sensitivity is small for all phantoms which produces low resolutions.

Table 5.19: Resolution of concentrations in %wt determined using the linear spectral decomposition method (method 1), the spectrally averaged dielectric method (method 2) and the Debye relaxation coefficient method (method 3) for all phantoms determined from reflection mode measurements

		Method 1			Method 2		Method 3
Solute 1	Solute 2	Water	Solute 1	Solute 2	Solute 1	Solute 2	Solute 1
Methanol		±1.7	±4.3	-	±11.6	-	±11.6
Lipid		±2.1	±52.8	-	±31.5	-	±10.8
Sucrose[a]		±1.9	±7.6	-	±42.0	-	±3.9
Sucrose[b]		±0.9	±9.8	-	-	-	-
Gelatin[a]		±1.1	±5.9	-	±55.0	-	±6.8
Gelatin[b]		±2.6	±4.1	-	-	-	-
Methanol	Sucrose	±2.2	±6.8	±5.0	±41.3	±42.0	-
Gelatin	Lipid	±1.1	±7.8	±52.6	±80.3	±73.3	-

[a] Absorption coefficient of 'dry' molecule used as prior knowledge

[b] Absorption coefficient of 'hydrated' molecule used as prior knowledge

This is explained by the shallow gradients of the empirical equations with respect to concentration. The best resolution, was obtained from measurements on methanol and water solutions where the non-linear relationship between ε' and ε'' and concentration produces large sensitivity at low methanol concentration resulting in a relatively high averaged resolution. The dependence of ε' and ε'' with concentration was smallest for the gelatin and water gels in the two-phase phantoms, resulting in a low resolution. The resolutions for the three-phase phantoms using method 2 are lower than those determined for the corresponding two-phase phantoms. This is the result of a greater number of variables being determined, which inherently reduces the sensitivity. The resolutions produced by method 2 are in general larger than the actual concentrations. Since any value within the resolution limits has equal statistical significance, it means that the determined concentrations are not uniquely determined. This makes method 2 unviable as a THz technique for determining tissue composition. The resolutions for method 3 are better than those of method 2. This is due to the gradients of the empirical equations of method 3 being less shallow that those of method 2 with respect to concentration. The resolutions determined using this particular method, therefore, are higher in comparison to method 2. The resolutions for method 3 are equivalent to those determined using method 1 with the exception of the resolutions for the lipid chromophore in the emulsions, which is better using method 3.

Despite enabling the determination of relatively accurate concentrations, the resolutions obtained from method 2 were the poorest of all the validated methods. The two methods which display the strongest sensitivity, methods 1 and 3, therefore return the best resolutions in the THz region investigated here.

In summary, the differences displayed in the absorption spectra made it possible to distinguish between different solutes using method 1. Method 1 is applicable only to materials in which the frequency dependence of absorption coefficient can be considered to be a linear combination of the component parts. This method is limited, however, due to the reliance on the absorption coefficients of the phantom chromophores as prior knowledge, which are difficult to measure accurately for more complex chromophores with hydration layers measured as part of this work, such as sucrose and gelatin. Method 2 enables accurate determination of concentrations despite the absence of spectral features in the measured dielectric coefficients. If specific signatures could be identified in the dielectric spectrum, then linear decomposition approaches such as those employed in method 1 may become efficient and enable more complex materials to be analysed. Method 2 is also limited to the analysis of materials containing up to three absorbing solutes. In addition it returns low resolutions, limiting its potential as a tool for tissue spectroscopy. In comparison to methods 1 and 2, both the accuracy of the determined concentrations and the calculated resolutions for method 3 were reasonable. When the resolutions of the validated methods are compared, those returned for method 3 are better than those returned for the other two methods. The resolutions determined for method 1 are good in general, except for cases when absorption coefficient of one chromophore is much smaller than the absorption coefficients of the others, such as is the case in the water and lipid emulsions. If method 3 can be extended to encompass three-phase phantoms, then the application of this concentration method to tissues may prove to be the most promising of all those validated in this work.

Part III

Colon imaging

Chapter 6

Colon imaging and spectroscopy background

6.1 Introduction

Having used well-defined biological systems in previous chapters to test experimental and theoretical methods, the following chapters apply these methods to excised human colon tissue samples. Values for the optical properties of colon tissue in the THz regime need to be determined in order to be able to use in vivo reflection images to diagnose colonic pathologies. In Chapter 7, results from reflection imaging of colon tissues are presented. Healthy tissues were imaged next to diseased tissues, including cancers, dysplastic tissues and inflamed tissues. THz spectroscopy is used to extract the optical properties of excised tissue from the reflection images. This chapter presents background information on the structure and properties of colonic tissue, detains of the most common tissue pathologies to affect colonic tissues and descriptions of some of the current and novel endoscopic techniques used in identifying colonic tissue pathologies.

6.2 Structure of the gastrointestinal tract

The gastrointestinal (GI) tract is a layered tissue that is approximately 6.5 metres long and consists of the upper (mouth, pharynx, oesophagus, and stomach) and lower (bowel, small intestine, large intestine, anus) GI tracts, figure 6.1. The histology of the GI tract is generally uniform allowing for differences which reflect tissue specialisations. The basic structure of the GI tract, figure 6.2, comprises a mucosal layer, submucosa, muscular layers and the serosa/adventitia.

6.2.1 Mucosa

The mucosa is the innermost layer of the GI tract, surrounding the lumen (space within the tube). The mucosal membrane, made mostly of flattened cells and covered in ep-

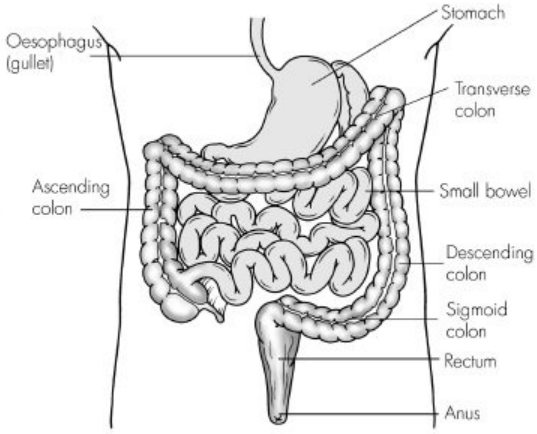

Figure 6.1: Diagram of the gastrointestinal tract (GI). The GI tract is divided into two parts, the small bowel and the large bowel. The large bowel is made up of the colon and rectum. This figure was adapted from www.cancerbackup.org.uk

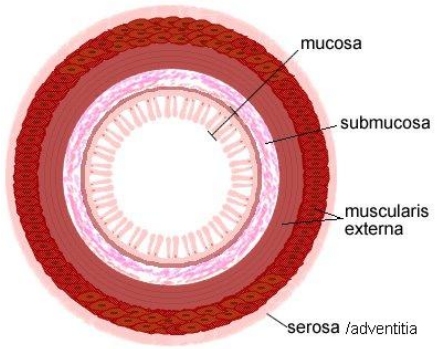

Figure 6.2: A cross sectional view of the colon. The colon consists of four distinct layers: the mucosal layer, the submucosa, muscular layers and the serosa. This illustration was adapted from www.coloncancer.about.com

ithelium, and glands along the mucosa absorb and secrete a thick fluid called mucus. The mucosa consists of the epithelium (tissue composed of layers of cells which line the cavities and surfaces of structures throughout the body), lamina propria (a thin layer of loose connective tissue which lies beneath the epithelium) and muscularis mucosae (a thin layer of smooth muscle separating the mucosal layer from the submucosa) (Smith and Morton 2001).

6.2.2 Submucosa

The submucosa consists of a dense irregular layer of connective tissue with large blood vessels, lymphatics and nerves branching into the mucosa and muscularis. The layer supports the mucosa while connecting it to the muscularis externa (Smith and Morton 2001).

6.2.3 Muscularis externa

The muscularis externa is a region of muscle adjacent to the mucous membrane and consists of a circular inner muscular layer and a longitudinal outer muscular layer. It is responsible for gut movement such as peristalsis; the circular muscle layer prevents the food from going backwards and the longitudinal layer shortens the tract (Smith and Morton 2001).

6.2.4 Serosa and adventitia

The serous membrane (serosa) is a smooth membrane consisting of a thin layer of cells which excrete a fluid, known as serous fluid. Serous membranes line and enclose several body cavities, known as serous cavities. The secreted fluid lubricates tissue, reducing friction from muscle movement. Adventitia is a connective tissue layer which binds together structures rather than reducing friction between them. Whether an organ is covered in adventitia or serosa depends upon the function of the tissue being covered. In the GI tract, the muscularis externa is bounded in most cases by serosa. However, at the thoracic esophagus, ascending colon, descending colon and the rectum, the muscularis externa is bounded by adventitia. The muscularis externa of the duodenum is bounded by both tissue types (Smith and Morton 2001).

6.3 Disorders of the gastrointestinal tract

In the following section we present an outline of the most common tissue pathologies to affect colonic tissues. We focus particularly on tissues investigated during the course of this work; predominantly cancerous and dysplastic tissues. Colorectal cancer is the third most common cancer in men and women in the UK with approximately 35,000 new cases per year, and it is the second most common cause of cancer-related death. It

is the fourth most common cancer across the world. The disease is slow to develop; the risk of invasive cancer developing within an adenoma, a benign collection of growths, is approximately 2% per year. Early diagnosis and removal of these growths is an effective method of reducing cancer risk. Survival depends on the stage of disease at time of presentation, and early detection of dysplastic lesions and treatment while the disease remains confined to the mucosa improves survival (Kerr et al. 2001, Taylor et al. 2007).

6.3.1 Neoplastic diseases

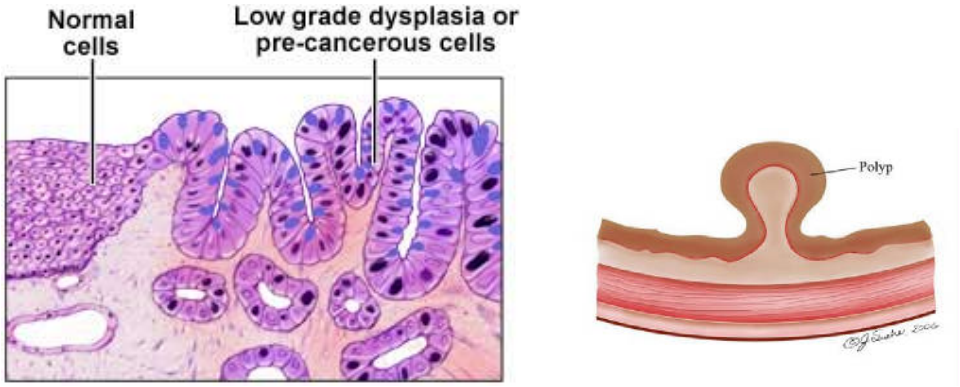

(a) Dysplasia (b) Polyp Adenoma

Figure 6.3: An illustration of a) the expansion of immature cells resulting in an abnormality of cells within a tissue, referred to as dysplastic tissue and b) a protruding growth from the colon surface, called a polyp. Most polyps are benign, however, there is a there is a risk cancer development in polyps over time. Images adapted from www.mayoclinic.org and www.surgeryinfo.org.

Neoplastic disorders are characterised by the presence of abnormal and uncontrolled cellular growth generally resulting in the development of a growth, referred to as a neoplasm. A neoplasm can be benign (non cancerous), potentially malignant (pre-cancer), or malignant (cancerous). The term 'dysplasia' describes an abnormality of cells within a tissue, typically an expansion of immature cells resulting in a decrease in the number of mature cells in the tissue, illustrated in figure 6.3(a). Dysplasia is often an indicator of neoplastic formation as it is the earliest form of pre-cancerous lesion recognisable in a smear or biopsy. Dysplasia can be termed 'low grade' or 'high grade'. Dysplasia can transform into a cancerous mass if the cells do not develop and mature, essentially loosing their tissue identity, reverting to a basic cell form that grows rapidly and without regulation. There is a low risk associated with low grade dysplasia, however, once the cells are classed as 'high grade' then they are in a more advanced progression towards cancer development. Metaplasia, in contrast to dysplasia, results from mature cells of one species being replaced by mature cells of another. An adenoma

is a benign collection of dysplastic growths which, over time, may progress to become malignant (adenocarcinomas). Colonic adenomas are initially flat though they can grow to protrude from the colonic surface, at which point they are called polyps, illustrated in figure 6.3(b). A polyp is an abnormal growth of tissue projecting from a mucous membrane. There are few symptoms associated with polyps and they are usually only discovered at the time of colon cancer screening. Non-neoplastic polyps make up the vast majority of epithelial polyps found in the large intestine (approximately 90%), they increase in frequency with age and are mostly found in the large bowel. Though the majority of polyps are non-neoplastic, there is a risk of non-neoplastic colon polyps transforming over time into colon cancer and so all polyps found during screening are removed to reduce the future likelihood of cancer development. Invasive carcinoma is a cancer which has invaded beyond the original tissue layer and may be able to spread to other parts of the body. Local symptoms of colon cancer do not typically appear until the tumour has grown to a large size. More than 70% of colorectal cancers stem from adenomas developed in polyps (Jones 1999, Kerr et al. 2001). It is also possible, however, for a malignancy to develop from a flat adenoma. These are more difficult to detect using endoscopy and are believed to result in a more aggressive cancer with a higher rate of change from benign to malignant. Causes of colorectal cancer are believed to involve trends in dietary and nutritional practices; the intake of animal fats and a lack of dietary fibre have been shown to be positively related to the risk of colorectal cancer (Jones 1999, Kerr et al. 2001).

6.3.2 Inflammatory and vascular disorders

6.3.2.1 Enterocolitis

Enterocolitis is an inflammation of both the small and large intestines, where enteritis is specifically the inflammation of the small intestine and colitis is inflammation of the large intestine, especially the colon. Infectious enterocolitis is the cause of approximately 12,000 child deaths each day in the developing world and more than 50% of all deaths before the age of 5 worldwide. Specific types of enterocolitis include bacterial enterocolitis (results from ingestion of a bacterial organism or a preformed toxin), viral gastroenteritis and necrotising enterocolitis (most common in premature infants) (Jones 1999).

6.3.2.2 Crohn's disease

Crohn's disease is a chronic, episodic, inflammatory condition of the gastrointestinal tract. Damage to the gastrointestinal tract can affect the entire wall of the involved bowel or it can be patchy, called skip lesions, where the intestine is affected in segmen-

tal fashion, the intervening segments being normal. The changes present in the tissue vary with the intensity and stage of disease. The cause of Crohn's disease is not known, however, it is believed to be an autoimmune disease that is genetically linked. The condition occurs when the immune system contributes to damage of the gastrointestinal tract by causing inflammation. Crohn's disease increases the risk of cancer in the area of inflammation (Jones 1999).

6.3.2.3 Ulcerative colitis

Ulcerative colitis (UC) is a chronic, relapsing inflammatory disorder of the gastrointestinal tract presenting, in contrast with Crohn's disease, as continuous lesions with no normal tissue between affected sites. Mild cases may show only inflammation with increasing severity demonstrated by swelling, mucosal granularity, the tenancy to easily crumble, bleeding and ulceration. The ulcers may show extensive erosion of the mucosa in severe cases, leaving projecting islands of regenerating inflamed mucosa forming "pseudopolyps". UC involves the mucosa and submucosa almost exclusively, rarely involving the muscle layer, so that thickening of the bowel wall is not seen. During periods of inactivity the colon may appear relatively normal. There exists a higher risk of cancer in patients with ulcerative colitis than with Crohn's disease, as this condition is premalignant. The carcinoma associated with ulcerative colitis occurs in flat mucosa as opposed to the usual colorectal carcinoma which is a raised lesion (polyp) (Jones 1999).

6.3.2.4 Ischemic colitis

Ischemic bowel disease (IBD) results from inadequate flow of oxygenated blood to the intestines; the disorder occurs when an artery that supplies blood becomes blocked or narrowed. There are several possible causes of IBD; blockage in the arteries due to a tumour or blood clot, narrowing of the arteries supplying blood and obstruction of the blood supply. Mild cases of IBD are most commonly followed by complete regeneration of the mucosal layer following treatment, however, the most severe extent of the disease can lead to perforation of the bowl, gangrene and can be fatal if left untreated (Jones 1999).

6.4 Screening of colon disorders

Descriptions of some of the current and novel endoscopic techniques used in identifying colonic tissue pathologies are presented in this section.

6.4.1 Current methods

6.4.1.1 Colonoscopy and sigmoidoscopy

Colonoscopy and sigmoidoscopy are a medical examination of the large intestine from the rectum through to the sigmoid or descending colon. The procedures require the insertion of a short, flexible, lit tube into the rectum which transmits an image of the inside of the rectum and colon to select suitable areas for biopsy. Colonoscopy allows an examination of the whole of the large bowel, which measures four to five feet in length, while sigmoidoscopy is an examination of only the final two feet of the colon. A sigmoidoscopy is often used as a screening procedure for a full colonoscopy. Bleeding and puncture of the colon are possible, but uncommon, complications of these procedures. Colonoscopy is the gold standard technique for the examination of the colon and rectum, however, it is an expensive technique, and there is a need for full bowel preparation (Jones 1999).

6.4.1.2 Barium enema/meal

A barium enema is a rectal injection of barium sulphate to coat the lining of the colon and rectum. Barium sulphate absorbs x-rays more strongly than tissue, thus providing a high-contrast outline of the colon and rectum allowing examination of the structure of the lower intestinal tract. The principle applies, also, with a barium meal, which is taken orally to examine the upper intestinal tract. The barium enema procedure may additionally use air in the large bowel to give a double contrast technique. A barium enema is cheaper and has a lower complication rate than colonoscopy, however, it is an invasive technique, requires full bowel preparation and does not allow for the biopsy of GI tissues (Jones 1999).

6.4.1.3 Faecal blood tests

The test identifies partly digested blood in the stool as bleeding is often an early sign of a bowel cancer. Faecal blood tests have been rolled out as a national bowel cancer screening programme in the UK where all people in the UK aged 60-69 are be invited to do a test every two years with the aim of detecting the early stages of bowel cancer (Jones 1999).

6.4.1.4 Virtual colonoscopy

Virtual colonoscopy, which uses 2D and 3D images reconstructed from computed tomography (CT) scans or from nuclear magnetic resonance (MR) scans, is also possible, as a totally non-invasive medical test, although it is not standard and still under investigation regarding its diagnostic abilities. Furthermore, virtual colonoscopy does not allow for therapeutic maneuvers such as polyp/tumor removal or biopsy and cannot

identify lesions smaller than 5 millimetres. If a growth or polyp is detected using CT colonography, a standard colonoscopy would still need to be performed (Kay et al. 2000).

6.4.2 Novel methods

A number of recent developments in colonic screening have shown potential, and a brief description is each is given in the following sections. A brief outline of some of the advantages and disadvantages of these methods are given in table 6.1.

6.4.2.1 Chromoendoscopy

Chromoendoscopy is a relatively simple and inexpensive method for enhancing differences and irregularities in mucosal topography and vasculature. This is achieved by using a variety of coloured contrast or absorptive agents which accumulate in crevices and pits in the mucosa. They may be sprayed on to the mucosal surface, ingested orally or given as an enema before endoscopy (Eisen et al. 2002, Kiesslich et al. 2004b, Kiesslich and Neurath 2005). The stain effect can be visualised either by conventional white light endoscopy or by high-power magnification endoscopy. Chromoendoscopy is useful in determining the boundary of lesions, and it may improve the detection of flat and depressed adenomas/carcinomas and allow the identification of the subtle changes associated with the development of aberrant crypt foci (Bird 1987, Kudo et al. 1996, Eisen et al. 2002). Chromoendoscopy has demonstrated its ability in differentiating neoplastic from non-neoplastic lesions with a sensitivity of 93% and specificity of 70-88% (Kudo et al. 1994, Axelrad et al. 1996, Tung et al. 2001, Kiesslich and Neurath 2005, Hurlstone et al. 2005, Apel et al. 2006).

6.4.2.2 Optical coherence tomography

Optical coherence tomography (OCT) is a novel imaging technique where the images are formed by detecting light that is reflected from subsurface tissue microstructures, providing real-time, high spatial resolution (4-20μm) cross-sectional imaging (Tearney et al. 1997, Kobayashi et al. 1998, Yang et al. 2004). OCT can be performed through air, but has a limited imaging depth of about 1-2mm owing to the scattering of light by tissues (Zysk et al. 2007). OCT is usually performed using NIR light delivered via standard endoscopes and colonoscopes. OCT can be used to survey regions of mucosa to locate regions likely to harbour pathology and guide biopsy (Sivak et al. 2000). The technique may be used to assess the depth of tumour invasion through the muscularis mucosa, and this may help preoperative staging of local disease and the selection of patients for endoscopic treatment (Das et al. 2001). Doppler OCT allows the assessment of local blood flow velocities in vivo in addition to providing tissue

Table 6.1: Summary of the advantages and disadvantages of current novel methods of colonoscopic techniques (Taylor et al. 2007)

Technique	Advantages	Disadvantages
Chromoendoscopy	Simple, safe and inexpensive	Unable to determine polyp histology
	Uses currently available colonoscopes	Operator dependent
	Improves detection of adenomas and dysplasia	
Fluorescence spectroscopy	Differentiates normal from neoplastic tissues	False positives in patients with
	Surveys large mucosal area in real time	inflammatory bowel disease
	Improves identification of flat adenomas	Artefact caused by mucosal folds
Light-scattering spectroscopy	Inexpensive, uses white light	Small volume of tissue sampled
	Differentiates normal from neoplastic tissues	Poor reproducibility of signal
	Strong signal generated	
Raman spectroscopy	Objective, molecular specific technique	Small volume of tissue sampled
	Differentiates between a wide range of pathologies	Time consuming
		Expensive equipment needed
Optical coherence tomography	High spatial resolution	Subjectivity of image interpretation
	Identifies superficial tumour invasion	Artefact caused by peristalsis
Confocal fluorescence microscopy	Yields three dimensional images	Requires topical/systemic fluorescence agents
	Comparable diagnostic accuracy to histology	Unable to survey wide areas of mucosa
		Artefact from peristalsis

microstructural information (Rollins et al. 2002).

6.4.2.3 Raman Spectroscopy

Raman spectroscopy is an optical technique that uses the inelastic scattering of light photons to interrogate biological tissues. Upon interaction with tissue molecules, the change in energy of a scattered photon results in a different wavelength than that of an illuminating photon, known as the Raman shift, which is specific to the species of molecule responsible for the scattering. When all the shifted wavelengths from photons scattered by the different molecules present in a tissue are combined, they form a Raman spectrum specific to that tissue (Taylor et al. 2007). The Raman spectrum is a direct function of the molecular composition of the substance being studied and, because the onset of neoplastic change is accompanied by changes in chemical composition, it has the potential to be a powerful diagnostic measurement (Dacosta et al. 2002, Stone et al. 2002; 2004).

6.4.2.4 Fluorescence spectroscopy

The absorption of light by molecules in tissue can lead to fluorescence. The ratio of fluorescence intensity to wavelength of incident light can be used to differentiate between tissues exhibiting different absorption/fluorescence characteristics. Different excitation wavelengths activate different groups of fluorophores and fluorescence can be used to differentiate nonneoplastic from neoplastic colonic lesions, depending on altered quantities and distributions of tissue fluorophores owing to changes in tissue architecture and devascularisation (Cothren et al. 1996, Crow et al. 2003, Dacosta et al. 2003a;b). In addition to autofluorescence, it is also possible to add molecules which can be administered systemically or topically, to increase the production of the fluorophores within neoplastic lesions. These molecules can be coupled to tumour-specific antigens or antibodies targeted against these tumour-specific antigens in order specifically to enhance the contrast between normal and abnormal tissues (Wang et al. 1999).

6.4.2.5 Light scattering spectroscopy

Light-scattering spectroscopy (or diffuse reflectance spectroscopy) is based on white light reflectance where photons incident on tissue are backscattered off tissue molecules without any change in their energy (Zonios et al. 1999, Wang et al. 1999). The greatest scattering occurs at boundaries between high and low refractive index and so changes in the distribution of scattering boundaries change the tissue scattering properties. An elastic scatter spectrum of scattered light intensity against wavelength contains quantitative information about changes in tissue composition and structure (Backman et al. 2000). The light scattering of various colonic tissues have been characterised, and have

suggested that it may be possible to differentiate colonic mucosa into normal, metaplastic, adenomatous and carcinomatous groups (Mourant et al. 1996b;a, Ge et al. 1998).

6.4.2.6 Confocal fluorescence microscopy

Recent advances in confocal fluorescence microscopy have led to the development of clinically applicable tools for both in vitro and in vivo endoscopic tissue analysis (Inoue et al. 2003, Kiesslich et al. 2004a). Confocal fluorescence microscopy can be used to image fluorescence from fluorophores in tissues and reflected light. The image is formed point-by-point by a scanning laser beam, resulting in high-resolution fluorescent optical slices through the sample. By varying the focal point through the specimen, a stack of optical sections can be collected without physical sectioning of the specimen. Three dimensional fluorescence images can be created, yielding sufficient cellular details for diagnostic interpretation (MacAulay et al. 2004). Differences in fluorescent features between normal, dysplastic and neoplastic mucosa can be exploited to aid diagnostic classification. Results have shown the technique to have a sensitivity of 97% and a specificity of 99% with an accuracy of 99% when compared with conventional histology (Inoue et al. 2003, Kiesslich et al. 2004a).

6.4.3 Potential of THz imaging as a colonic screening technique

The potential of THz imaging as an endoscopic tool for the detection of colonic tissue pathologies is encouraged by positive results in discriminating healthy tissues from diseased in THz imaging of skin (Woodward et al. 2002, Wallace et al. 2004) and breast (Fitzgerald et al. 2004; 2006) tissue studies. Although the sensitivities and specificities have not just been defined for these studies, THz imaging of both skin and breast cancers have shown that the contrast is sufficient to identify tumour margins when compared with histology. However, these tissues differ from the composition of colonic tissues as they have a higher fat and lower water content. PET, MRI and NIR studies have all offered evidence that tumours have an increased water content in comparison to healthy tissues (Rofstad et al. 1994, Tromberg et al. 2000, Bruehlmeier et al. 2003, Clothier and Bourne 2003). As water has such a strong absorption across the THz range, a likely source of image contrast is changes in water content of the imaged tissues. Studies of protein dynamics with THz radiation, however, have presented differing spectra amongst the proteins suggesting that THz may be a useful tool in protein analysis and identification, and confirm that the contrast observed in THz imaging is due to more complex mechanisms than simply water absorption. Proteins studied to date include, bovine serum albumin (BSA), cytochrome c, collagen, glycine, lysozyme, myoglobin and polypeptides (Markelz et al. 2000; 2002, Mickan et al. 2002, Yamamoto et al. 2002, Shi and Wang 2005, Zhang and Durbin 2006). Other biological molecules

such as DNA (Globus et al. 2002; 2003) and sugars (lactose and glucose) (Havenith et al. 2004) have been studied, a suggest these molecules also display a differentiable absorption trend in the THz region. An increase in tumour water content in comparison to the healthy tissue would suggest the possibility of distinguishing between the two tissue pathologies.

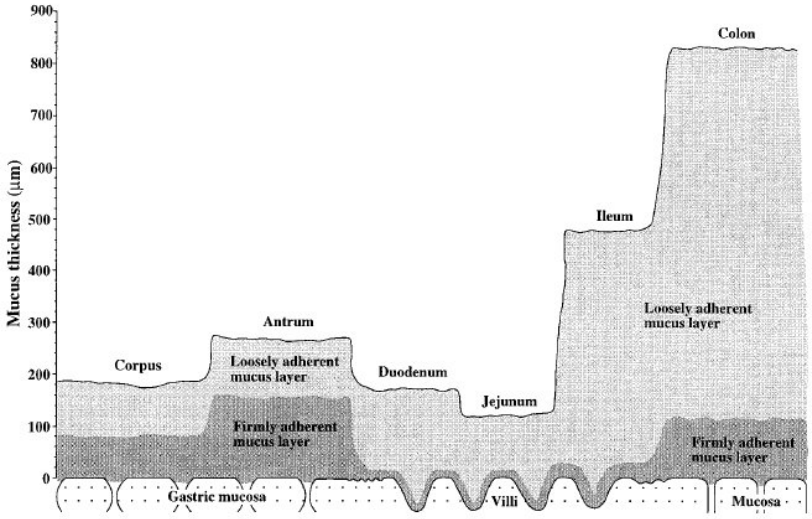

Figure 6.4: Average mucosal layer thickness (Atuma et al. 2001)

THz radiation is non-ionising so THz imaging is suitable for medical applications, however, the use of THz imaging as an endoscopic tool might be limited by the optical properties of ancillary substances in the colon, such as mucus linings of the mucosal layer. Figure 6.4 illustrates the average thickness of this lining which is 0.8mm thick in the colon, however, this is loosely adhered and the strongly adhered is approximately 0.1mm thick. As the penetration depth of THz radiation into tissues is typically a few hundred microns in high water content tissues to several centimetres in tissues with a high fat content (Arnone et al. 1999, Fitzgerald et al. 2005), the absorption of THz radiation due to the strongly adhered mucus linings of the mucosal layer should not impede the penetration of THz radiation into sub mucosa tissues. The thickness of colonic tissue layers in healthy tissues is approximately 2-3mm (Fisher 1982, Haber and Stern 2000) increasing by up to 3mm in inflamed tissues (Price and Morson 1975). THz should, therefore, be able to penetrate sufficiently deeply into tissue to enable THz endoscopy. Current work towards the development of a handheld probe (Wallace et al. 2005) and significant recent work in the area of THz remote delivery (Mendis and Grischkowsky 2001, Wang and Mittleman 2004, Walther et al. 2005, Kerby and Bernhard 2007, Mendis 2007, Bowden et al. 2008) indicates that it should be possible,

in time, to deliver THz radiation successfully, endoscopically. The distinct advantage of developing a terahertz endoscopic imaging system, in comparison to other existing endoscopic techniques, would be the use of a computer algorithm driven diagnosis. Current endoscopic techniques are dependent on operator experience which requires a skilled endoscopist to operate the systems. A terahertz system, where tissue classification is based on the interpretation of the terahertz signals by computer would enable a relatively unskilled endoscopist to guide biopsies.

Chapter 7

Spectroscopy and Imaging of *ex vivo* colon tissues

7.1 Introduction

Following the development of spectroscopic methods for the analysis of tissue chromophore concentrations in chapter 5, the application of these techniques to the diagnosis of tissue pathologies, specifically colonic tissues is considered. The aim of colonic screening is to detect bowel cancer at an early developmental stage, when treatment is more likely to be effective. Early stage cancers are dysplastic tissues, described in chapter 6.3.1. The advantages and disadvantages of current screening techniques are outlined in section 6.4.1, where there is a clear clinical need for the development of techniques to distinguish healthy tissues from diseased and pre-cancerous states. Several techniques are currently being developed for this purpose, as outlined in table 6.1. However, as stated in section 6.4.3, one advantage of a terahertz endoscopic technique would be the use of computer driven diagnosis which would reduce diagnostic dependence on operator experience. The purpose of this study, therefore, was to investigate the ability of terahertz pulsed imaging to map regions of diseased tissues from healthy tissues in freshly excised human colon tissue and determine areas of healthy from dysplastic tissues.

In this chapter both spectroscopy and imaging results are reported. The results from an imaging study where cancerous, dysplastic and normal colonic samples were imaged from 35 patients are presented in section 7.2.3. Twelve of these cases were further analysed through slide staining to explore likely contrast mechanisms in the THz images, the results of which are presented in section 7.2.2. The optical properties of excised normal and diseased tissues are presented in section 7.2.5, from which the complex refractive indices of the tissues are derived. Spectroscopic methods for the analysis

of tissue chromophore concentrations were then applied to the tissue measurements. Finally, spectroscopic properties of three ancillary colonic substances, mucus, faeces and blood are presented in section 7.3.

7.2 THz Imaging and spectroscopy of *ex vivo* colon tissues

7.2.1 Methods

7.2.1.1 Patients and Specimen Preparation

The tissue samples investigated in this study were from 35 patients (20 male, 15 female, mean age: 63 years, range: 19-87 years) undergoing colonic resection surgery at St. Mary's Hospital, London, UK. Ethical approval for the study was granted by the Local Research Ethics Committee and all patients had given their informed, signed consent for the excised tissues to be used for research, as outlined in section 3.5.1.4. The samples included cancer, dysplasia, metaplasia and inflamed tissues, as well as normal tissue samples. The majority of these samples were from the lower gastrointestinal (GI) tract (the colon), with 4 cases examining upper GI cancer.

Measurements of ancillary colonic materials, which were blood and mucus, were made. Blood samples were obtained from a single healthy member of the research team and split into three separate samples. One sample was centrifuged for 10 minutes to separate the sample into blood serum and blood cells and one was set to one side for a few hours and allowed to clot. The final sample was measured as whole blood. No Heparin was used in the preparation of any of the blood samples. Mucin from porcine stomach (Aldrich, UK) was used to create aqueous gels at physiological concentrations of 90% and 95% water volume by weight. This was used to mimic the composition of biological mucus which has a typical mucin content of 90-95% (Bansil et al. 1995). The aqueous mucin gels were gently heating in an ultrasonic bath helped break up protein aggregates and displace air bubbles to produce a homogenous sample.

7.2.1.2 Data acquisition and data analysis

The Terahertz Pulsed Imaging (TPI) system, illustrated in figure 3.3(b), was used to measure the excised tissue samples. As described in section 3.5.1.4, suitable patients were selected in advance of undergoing surgery and gave informed consent to opt into the study after discussion with a surgeon (in accordance with the ethical approval and study protocol). Tissue was retrieved immediately following removal and taken to the pathology department. Pathological assessment was made of the removed tissue to

identify sites of diseased and healthy tissue, from which tissues could be sampled for imaging. The number of tissue samples retrieved was decided by a consultant histopathologist and was dependent on a number of factors, with the primary aim being not to disrupt the normal pathological assessment of the specimen. Typically two samples of tissue were imaged from each excised colon. Healthy tissues were harvested well away from the diseased areas. The measurement procedure and histology analysis for the tissue samples is described in section 3.5.2.3. Single samples of healthy tissues were placed next to individual samples of diseased tissues on the imaging window for each imaging procedure. Additional measurements were made on ancillary healthy tissues; adipose tissue, muscle and mucosa, following the procedures outlined in section 3.5.2.2. The tissue samples were measured less than 1hr following excision. All measurements were made at room temperature. Transmission measurements were made using the terahertz transmission system, illustrated in figure 3.3(a), of mucus and blood. The measurement procedure is described in section 3.5.2.1. The tissue cell, figure 3.4.2 was used to obtain the refractive index and absorption coefficients for the blood clot and blood cells while the liquid cell, figure 3.4.1 used to retrieve the optical properties of the whole blood, blood serum and mucus. All measurements were averaged over the collected data sets and all measurements were made at room temperature. A separation distance of 200μm was used in all transmission measurements.

7.2.1.3 Data analysis

The results of the histopathologic examination of the imaged tissues were used to identify the size and shape of tissue pathology regions on the terahertz images. Regions of interest (ROI) were marked out in the terahertz images, as outlined in section 3.5.3.1, and were selected from areas identified by pathology results. The waveforms from the ROI were averaged to generate a single waveform describing the reflected THz wave. An example of the imaging results is shown in figure 7.1.

7.2.2 Slide staining

To investigate other potential sources of contrast in the samples, staining of the slides was undertaken to identify a physical property of the tissue correlating to differences in terahertz measurements between pathologies. The results of this slide staining are kindly allowed for reproduction by Mr. George Reese. Twelve samples were identified for staining using imunohistochemical stains. A list of the stains used are shown in table 7.1.

Masson's trichrome and sirius red are two stains used to identify the collagen content

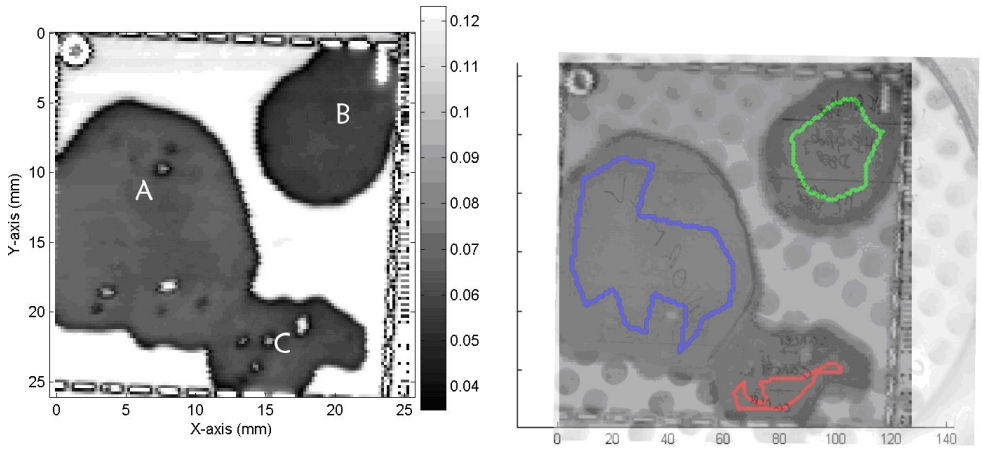

(a) Example THz image: generated from the E_{min} THz signal

(b) Histology results overlaid on the THz image

Figure 7.1: Illustration of the imaging procedures for this study. a) is an example THz image of a healthy tissue sample next to a sample of cancer, in this particular case the THz image generated from the E_{min} signal is shown. b) shows the histology results (drawn onto a photographic image of the tissue samples) overlaid on the THz image from which regions of interest can be selected. Impulse functions for the respective tissue types are extracted from the regions of interest. In this example, region *a* is normal tissue, *b* is dysplastic tissue and *c* is cancerous tissue.

Table 7.1: Stains used in colon histology analysis

Stain	Identifies
Masson's trichrome (MT)	Collagen
Sirius red (SR)	Collagen
Diastase periodic acid-Schiff (DPAS)	Antitrypsin phenotype (AAT)
CD31	Endothelium of small vessels
CAM 5.2	Cytokeratin protein
D240	Lymphatic marker

of the samples. Diastase resistant periodic acid Schiff (DPAS) was used to identify α_1 antitrypsin content, a protein made in the liver which neutralises protein-destroying enzymes. Human colorectal carcinoma cells synthesise α_1 antitrypsin and its incidence is higher in advanced adenocarcinomas than in early ones (Tahara et al. 1984, Karashima et al. 1990, Zelvyte et al. 2004). Platelet Endothelial Cell Adhesion Molecule (CD31) was used to locate the endothelium of small vessels and identify regions of increased vascularisation. Vascularisation, when blood vessels from the surrounding host tissues are stimulated into supplying the tumour, establishes a capillary network from which nutrients and oxygen are provided to the tumour (Alarcon et al. 2005). Anti-Cytokeratin (CAM 5.2) stains most epithelial-derived tissue but does not react with some squamous cell carcinomas, therefore, it is used to identify the presence of these cells (Moll et al. 1982, Makin et al. 1984). Hematoxylin counterstain (D240) is used to identify the extent of the lymphatic systems in the samples.

The slides were manually examined using a microscope and regions of pathology were identified from histology. An increase in the vascularity of the tissue samples from normal through dysplasia to cancer was identified from the CD31 stain which could suggest an increase with disease progression in liquid content of the tissues which might be a source of image contrast. The D240 stain, a lymphatic marker, also showed a more pronounced difference between tissue pathologies where 14% cancer, 12% dysplasia but fell to 3.5% for normal. The other stains did not reveal any uniform differences between the pathology groups. Some conclusions can be drawn from these results, which suggest that the physical differences between the diseased samples and healthy samples may be due to increases in localised densities of lymphatic and vascular cells in the dysplastic and cancerous tissues.

7.2.3 Imaging and histology results

From figure 7.1 it can be seen that that the cancerous and dysplastic tissue regions are slightly darker than those from the region of healthy tissue which indicates differences in the reflected waveforms. Absorption coefficients and refractive indices were calculated, as in section 2.3.1.2, from the reflected waveforms for cancerous, dysplastic and healthy tissues. In figure 7.2.3, plots showing the difference between the refractive index and the absorption coefficient of cancer and dysplasia compared to that of the normal tissue are presented for a single patient. In general, the diseased tissues display higher refractive indices and absorption coefficients than the healthy tissue. If cancerous tissue has an increased water content in comparison to normal tissue (Rofstad et al. 1994, Tromberg et al. 2000, Bruehlmeier et al. 2003, Clothier and Bourne 2003),

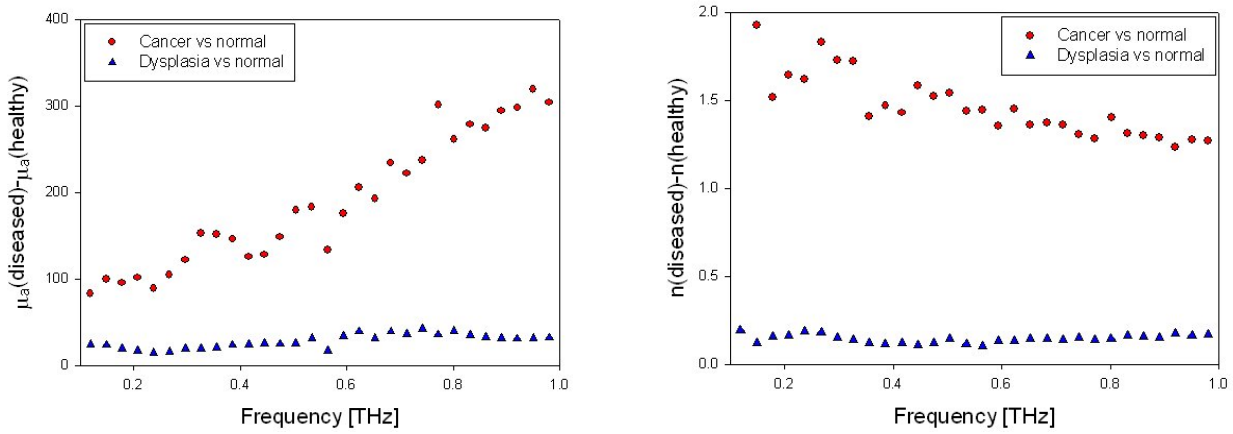

(a) Absorption Coefficient (b) Refractive Index

Figure 7.2: Difference between diseased and healthy tissues for cancerous and dysplastic tissue from a single patient. a) shows the difference between differences in absorption coefficient and b) shows the differences in refractive indices.

it would would be expected that the absorption coefficients of the diseased tissues would be greater than healthy tissues. However, difference plots illustrated in figure 7.3 highlight the spread of measurements and the large variation between samples. The accuracy of the measurements may be affected by difficulties in accurately determining the optical properties of a material in reflection mode. As discussed previously with the phantom results, the optical properties determined from reflection mode measurements of the THz imaging system, section 3.3, are derived from the phase components of the imaginary data. The phase is highly sensitive to sample position meaning any difference between the reference and the raw data measurement will result in errors in the measured optical properties. Furthermore, the reference signals were made at the centre point of the imaging window and, as the reference was applied across the whole image regardless of location, this could lead to errors in the measured phase at the non-central points in the image. Other potential sources of error in the measurements could be the imaging window not being entirely flat causing the phase to change across the window, the sample not being in close contact across the scanned surface or pressure on the sample creating a bend in the supporting metallic structure of the quartz window which would change the phase at across the surface. The most likely source of error is pressure on the sample caused by the top surface of the tissue holding device, section 3.4.3, though effort was made to reduce this risk. Single point measurements may not suffer from these effects of phase changes.

It would be difficult, therefore, to suggest that a definite distinction may be made

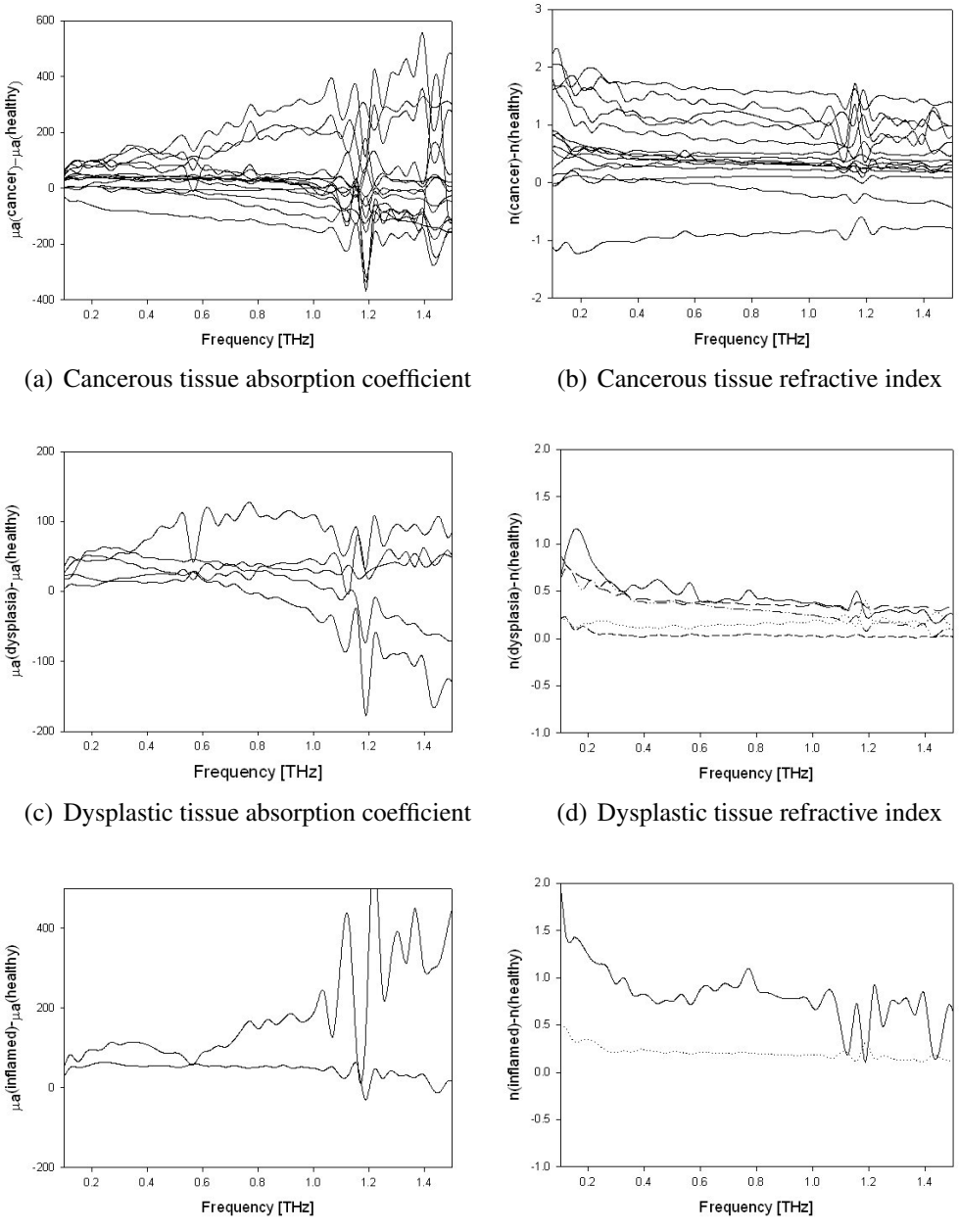

(a) Cancerous tissue absorption coefficient

(b) Cancerous tissue refractive index

(c) Dysplastic tissue absorption coefficient

(d) Dysplastic tissue refractive index

(e) Inflamed tissue absorption coefficient

(f) Inflamed tissue refractive index

Figure 7.3: Spectra of the difference in absorption coefficient and refractive index of diseased tissues and their 'comparative' healthy samples for a-b) cancerous, c-d) dysplastic and e-f) inflamed colon tissue.

between the tissue types when considered as a group. However, if analysis is performed within an individual case, it may be possible to identify differences between the tissue pathologies.

7.2.4 Statistical analysis

The averaged waveforms extracted from the ROIs identified on the THz images of the tissue sample were analysed by a bio-statistician from Imperial College London using STATA (Version 10) and SPSS (Version 15). This work has not yet been published and some of the results are reproduced here for completeness. The aim of the analysis was to construct a statistical model for classification of normal, dysplasia or cancer using a series of terahertz parameters. A number of parameters for both air and water referenced data were identified. As discussed in section 3.5.3.1, particular parameters have a more pronounced dependence on particular physical properties than others and so will be of most significance to the creation of images. The parameters identified for use in this study include those that have been used previously to distinguish tumours and healthy tissue for a number of cancers (Woodward et al. 2003, Fitzgerald et al. 2004). For the air referenced data these were:

1. Emin: Minimum value of THz pulse
2. -Emin/Emax
3. A(t)/Emin: Normalised amplitude at t = 0.33 ps prior to Emin time.
4. A(t)/Emin: Normalised amplitude at t = 2 ps after Emin time
5. Integral of values in THz pulse from 0.33 ps before Emin time to 2 ps after.
6. P(f): Power in spectrum at f = 0.6 THz
7. Integral of power spectrum over freq range 0.44 - 0.60 THz.
8. Full width half maximum (FWHM)
9. Emax - Emin

For the water referenced data these were:

1. Emax: Maximum value of THz pulse
2. A(t): Amplitude of pulse at time t = 0.26 ps prior to Emax time.
3. A(t): Amplitude of pulse at time t = 0.26 ps after Emax time

4. Integral in THz pulse from 0.26 ps before Emax time to 0.26 ps after.
5. P(f): Power in spectrum at f = 0.6 THz
6. Integral of power spectrum over freq range 0.44 - 0.60 THz
7. Log of Integrated power
8. Full width half maximum (FWHM)

Firstly a comparison was made between the averaged waveforms from all regions identified as healthy, cancerous and dysplastic in the tissue samples. Values of the parameters listed above were collated for all the samples. A multinomial logistic regression analysis was used to compare ”benign” and ”neoplastic” tissues within patients. The averaged waveforms were grouped into benign (normal and reactive pathology) and neoplastic pathology (cancer and dysplasia) (in keeping with similar studies reporting data on narrowband imaging and chromoendoscopy). Six parameters were identified as statistically significant. However, the model gave best classification when 9 of the 17 parameters were considered. The model estimated a sensitivity of 82% and a specificity of 77%.

Secondly a comparison was made between the averaged waveforms from regions identified as healthy and dysplastic in the tissue samples. Again, values of the parameters listed above were collated for all the relevant samples. Individually most parameters showed a statistically significant difference between normal and dysplasia and binary logistic regression analysis was used to build a model for classification of data as dysplastic or normal. The model suggested an 89.2% sensitivity and a 71.4% specificity. The model suggested that the data for the 2 groups was significantly different with a p value of 0.021.

7.2.5 Concentration analysis of ex-vivo colonic tissue samples

These results are the average of the data from the 35 samples. The average refractive index and absorption coefficients were calculated from the measured impulse functions for all represented tissue types. The absorption coefficients and refractive indices of healthy tissues, adipose tissue, muscle and the mucosal layer are shown in figure 7.4. The absorption coefficient and refractive index of pure water is included for comparison.

The absorption coefficients and refractive indices of cancerous, dysplastic, inflamed and healthy mucosa (included for comparison) tissue are illustrated in figure 7.5. The

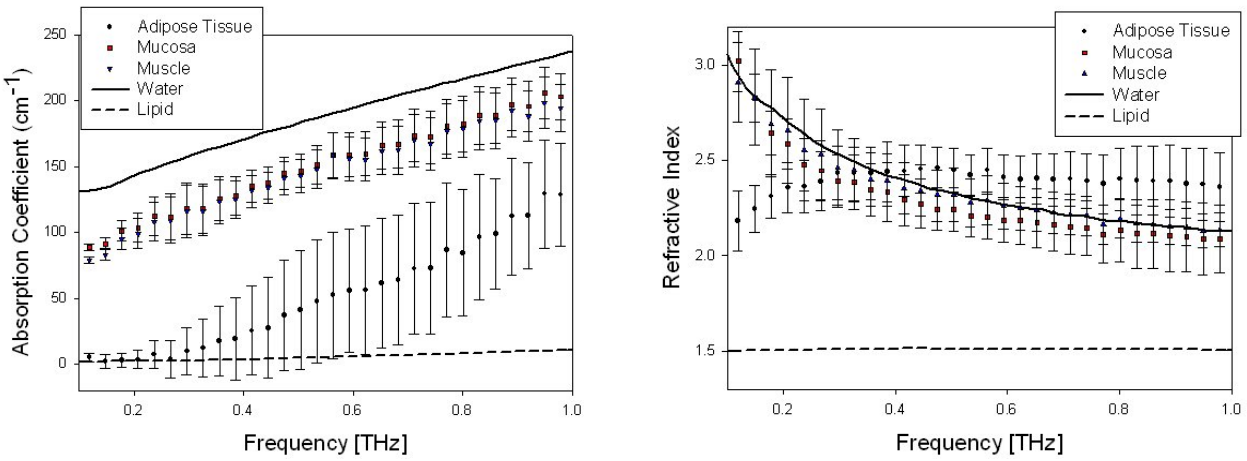

(a) Absorption Coefficient (b) Refractive Index

Figure 7.4: Absorption coefficients and refractive indices of three healthy colon tissue examples: muscle, mucosa and adipose tissue, averaged over a number of excised tissue samples.

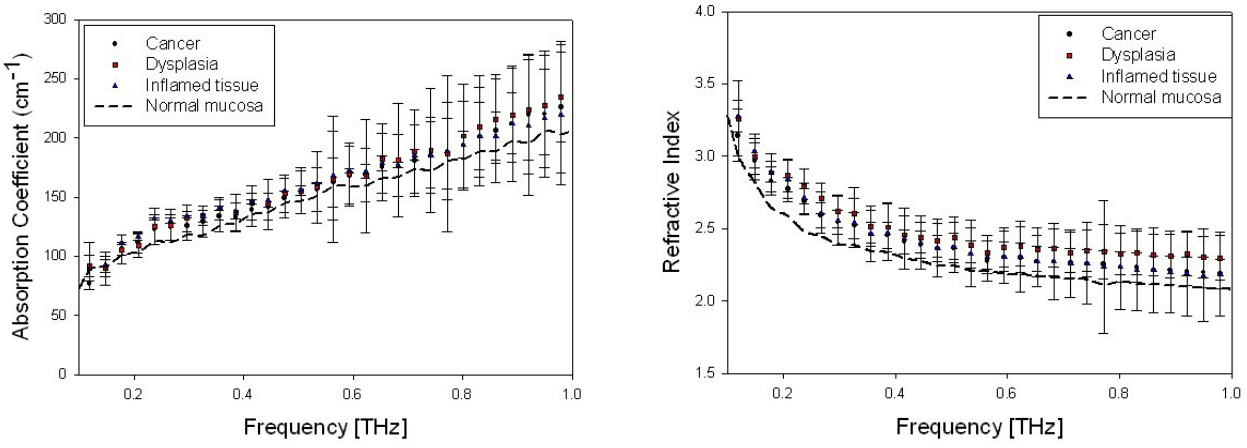

(a) Absorption Coefficient (b) Refractive Index

Figure 7.5: Absorption coefficients and refractive indices of three diseased colon tissue examples: cancer, dysplasia and inflamed tissue, averaged over a number of excised tissue samples.

absorption coefficients of all the tissues increase with frequency, with the absorption coefficients of the muscle and mucosal layers appearing very similar and the absorption coefficient of these tissues is lower than healthy tissues. This agrees with previous studies (Thueler et al. 2003, Zonios et al. 1996, Hornung et al. 1999). The composition of these tissues is illustrated in figure 7.6, where skin is used as a guide to the properties of the mucosal layer as they are both epithelial tissues. The water content of these two tissues is very similar. The absorption coefficient of the adipose tissue is lower than the mucosa and muscle tissues. From figure 7.5, it can be noted that n and μ_a of the diseased tissues are consistently higher than of healthy tissue. This is consistent with the tumourous tissues having a higher water content than normal tissue as their refractive index and absorption coefficient are closer to those of water. The error bars for the determined optical properties are relatively large.

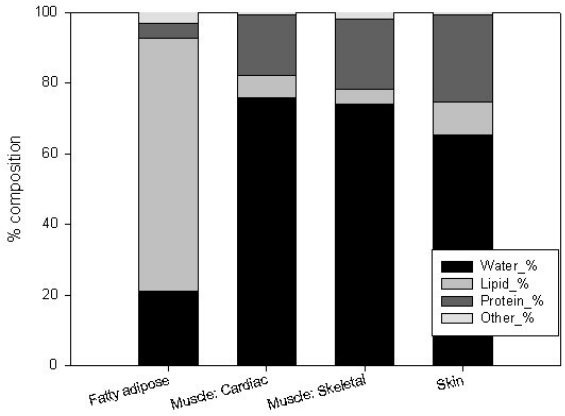

Figure 7.6: Typical water, fat and protein composition of four examples of healthy human tissue types, adipose, muscle (cardiac and muscular) and skin, an endothelial tissue (Duck 1990)

The tissues were assumed to consist of only three compounds: water, lipid and protein. The concentration analysis methods applied to the tissues were, as with the measurements made of phantom materials, linear spectral decomposition, dielectric averaging, and the determined trends with concentration of the Debye relaxation coefficients. The optical properties of these compounds required as prior knowledge for implementation of these techniques were the absorption coefficients from transmission measurements (chapter 4) for the linear spectral decomposition method. The empirical equations relating the variation of the real and imaginary parts of the averaged dielectric coefficient to lipid and gelatin concentration were used to determine the concentration of the

tissues.

7.2.5.1 Linear spectral decomposition

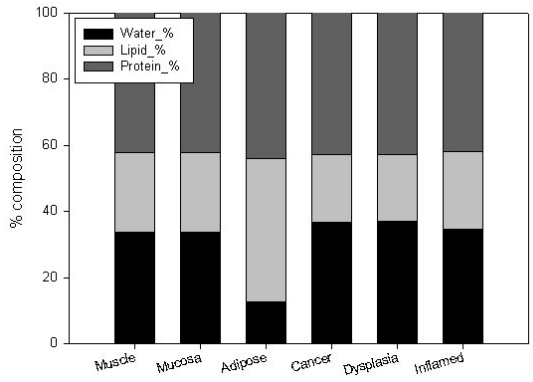

Figure 7.7: Water, lipid and gelatin concentrations of three diseased tissue examples; cancerous, dysplastic, inflamed, and three healthy tissue examples; adipose, muscle and mucosa determined using the linear spectral decomposition.

The linear spectral decomposition technique was applied to absorption coefficient measurements of the healthy and diseased tissues in reflection mode, using the absorption coefficients of water, lipid and gelatin as prior knowledge. The results of this spectral decomposition are shown in table 7.7. The determination of the true concentrations of water, lipid and protein in the tissues would have required histological analysis of each individual sample, however, figure 7.6 can act as a guide where the water content of muscle is $\sim$75%, for epithelial tissues $\sim$65% and for adipose tissue $\sim$20%. The broad differences in tissue chromophore concentrations are identified. Linear spectral decomposition appears to underestimate the water content and overestimate the protein and lipid content of the tissue, when compared to the general values given in figure 7.6. However, the general trend in the variation of the composition of the tissues is preserved by the method, where the water content of adipose tissue is determined to be much lower than all others, and the diseased tissues are determined to have slightly higher water content than the healthy samples.

7.2.5.2 Spectrally averaged dielectric coefficient method

The dielectric averaging method utilises spectral information from both the absorption coefficient and refractive index of the measured samples, through the relationships of ε' and ε'', given by equations 2.45 and 2.46, respectively. ε' and ε'' were calculated, therefore, from the averaged measured absorption coefficients and refractive indices of the tissue samples. The empirical equations describing the variation in ε' and ε'' with gelatin and lipid concentration, as described in section 5.3.6, were solved, using the

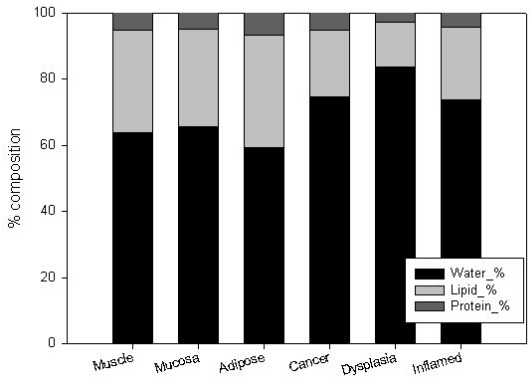

Figure 7.8: Water, lipid and gelatin concentrations of three diseased tissue examples; cancerous, dysplastic, inflamed, and three healthy tissue examples; adipose, muscle and mucosa determined using the spectrally averaged dielectric coefficient method

averaged tissue ε' and ε'' values, for two unknowns: protein (gelatin) and lipid over the frequency range 0.1-1 THz. The solute concentration estimations are illustrated in figure 7.8. The dielectric averaging method provides a more accurate estimation of the water content, with reference to the values given in figure 7.6. There is an underestimation of the protein content and an overestimation of the lipid content, however, the results are a significant improvement on those yielded by the linear spectral decomposition method. This averaging technique is based on empirical relationships between pure substances and, as tissue is likely to contain other components which would contribute to changes in the dielectric coefficients, inaccuracies are to be expected. The results, nevertheless, demonstrate that it is possible to analyse the concentration trends in tissue.

7.2.5.3 Debye relaxation coefficients method

The Debye relaxation coefficients method was only validated on two-phase phantoms, however, further investigation of the variations in determined Debye coefficients with tissue concentration should indicate its potential in use as a tissue spectroscopy tool. This method links physical properties of the measured materials, in the form of molecular relaxation times, to the chromophore concentration which may provide more sophisticated information than the previous two methods. The Debye relaxation coefficients of the tissue samples are presented here with the aim of highlighting any variations in the coefficients which may indicate the potential of the technique.

To determine the Debye relaxation coefficients for the tissues, double Debye theory, section 2.4.2.1, was applied to the complex dielectric coefficient of the *ex vivo* tissue, determined from ε' and ε'' as described in section 3.5.4.3 between 0.1 and 2 THz. In

Table 7.2: Debye coefficients for healthy and diseased excised colonic tissues

Tissue	Δ_1	Δ_2	τ_1	τ_2
Muscle	52.4	1.8	8.0	0.2
Mucosa	52.9	1.4	8.4	0.2
Adipose	3.8	3.7	24.7	0.1
Cancer	52.6	1.6	8.8	0.2
Dysplasia	52.6	1.6	7.6	0.1
Inflamed	52.2	2.0	7.4	0.1
Water	*74.2*	*1.3*	*8.43*	*0.1*

fitting the model to the data, ε_S was held constant at 54.7, except in the determination of the adipose tissue coefficient, when it was held at 10, in keeping with values for biological tissues determined by previous studies (Gabriel et al. 1996). The determined Debye relaxation coefficients for the tissues are given in table 7.2. Both the τ_1 and τ_2 relaxation times for both the healthy and cancerous tissues are similar to those for the pure water. The τ_1 value for the adipose tissue is much larger than for the other tissues. Differences are expected due to the increased lipid content of the adipose tissue. However, the τ_1 value of the pure lipid is very low. In considering the trend of the Debye relaxation coefficients of the intralipid, section 5.4.2, it can be seen that the τ_1 relaxation time increases with increasing lipid content. The average fat content of the adipose tissue is $\sim$65% so one could expect the τ_1 value to be larger compared to pure water.

7.3 Spectroscopy of ancillary colonic substances

The optical properties of substances which appear in the gastrointestinal system and which may bear some influence on THz measurements, mucus, whole blood and blood components, are presented here.

7.3.1 Mucus

Mucus is a viscous secretion of the mucous membranes (such as the colonic mucosa) and provide a protective and lubricating function due to the ability to form a gel layer adhered to the underlying epithelium. Mucus is the principle lubrication method for transport through the gastrointestinal system, as it prevents trauma to the tissues from the materials passing through, which become progressively more solid as water is ex-

tracted. Mucus is composed of salts, immunoglobins, mucin and water (Bansil et al. 1995). The typical thickness of the mucus layer in the human colon, as discussed in section 6.4.3, is 0.8mm of loosely adhered mucus and approximately 0.1mm of strongly adhered mucus.

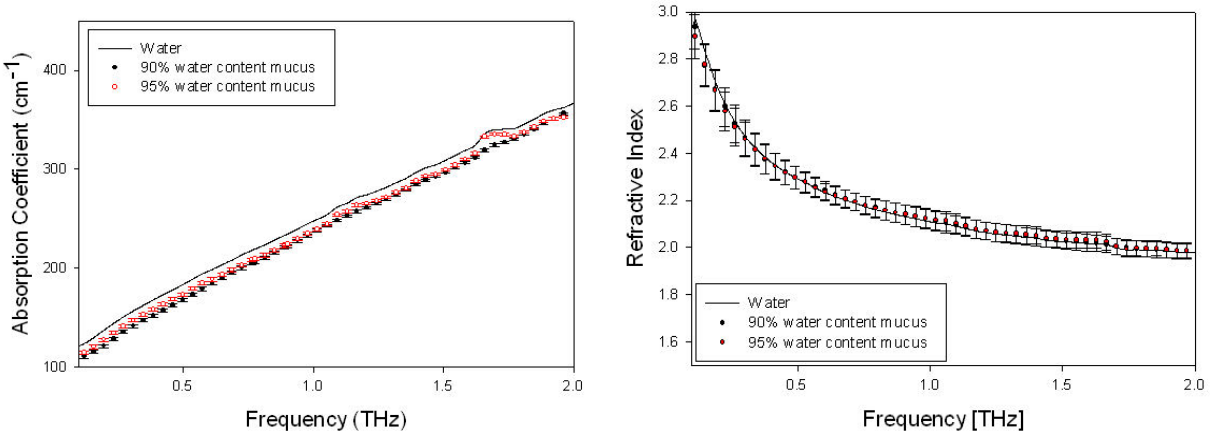

(a) Absorption Coefficient (b) Refractive Index

Figure 7.9: Absorption coefficient and refractive index for mucus in comparison to water.

The measured absorption coefficients and refractive indices for the two mucus concentrations are illustrated in figure 7.9. The absorption coefficients of the aqueous mucin mixtures are marginally lower than that of water and display a concentration dependence, with the absorption of the '90%' sample being slightly lower than that of the '95%' sample over the frequency range 0.1-2 THz. The refractive indices of the two mucus concentrations are not concentration dependent and are very similar to that of pure water. This is very similar to results that will be presented for gelatin gels in section 5.2.4, suggesting that the structure of the mucus is similar to the bound protein structure found in gelatin. The formation of this bound structure is due to the mucin protein, a large coil like protein which forms a gel matrix in a similar fashion to gelatin (Bansil et al. 1995).

Considering the impact of the mucus lining on colon imaging, these results indicate that there will be similar reflections from interfaces as water, which is determined by the refractive index. However, there will be slightly less absorption of the pulse so it will be able to penetrate further through a layer of mucus in comparison to water.

7.3.2 Whole Blood and Blood Components

Blood is composed of cells suspended within a plasma. The cells present in whole blood are red blood cells, white blood cells and platelets. Blood is, by volume, typically 45% red blood cells, 55% plasma and a very small amount of white blood cells. Plasma is composed predominantly of water ($\sim 92\%$) and dissolved proteins and salts ($\sim 8\%$). Plasma circulates nutrients, removes waste products and circulates hormones around the body. Red blood cells contain haemoglobin, a molecule which transports oxygen by reversibly binding to the gas. The haemoglobin molecule consists of four protein subunits. Each subunit is composed of a protein chain and a non-protein heme which consists of an iron atom surrounded by an organic compound ring. White blood cells are cells of the immune system and defend the body against both infectious disease and foreign materials. Platelets are involved in the formation of blood clots. A blood clot, or thrombus, is formed through a process called coagulation where a solid mass is formed containing platelets and fibrin; platelets group together to form an plug, quite simply a group of cells clustered together, while proteins in the blood plasma form fibrin strands which form covalent bonds and strengthen the platelet plug (Mosesson 2005).

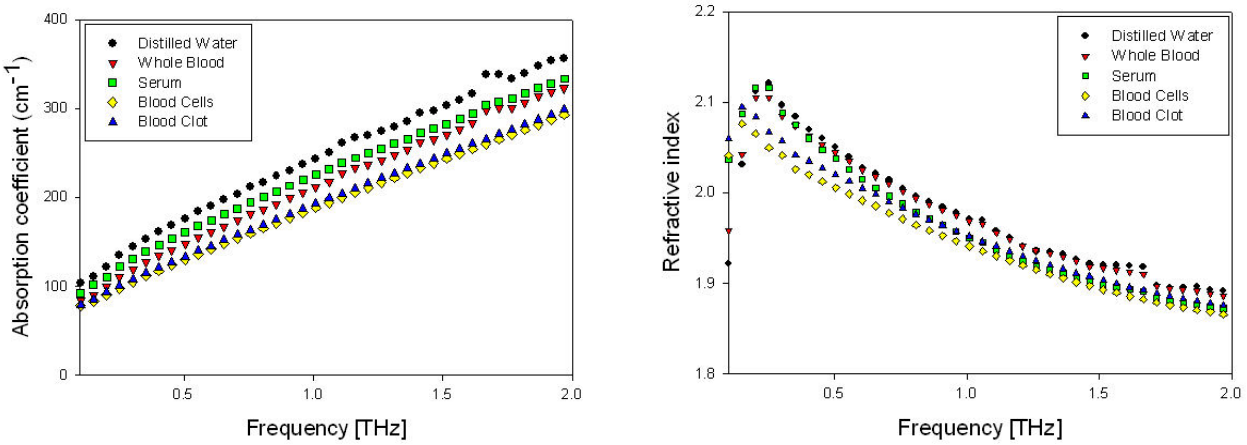

(a) Absorption Coefficient (b) Refractive Index

Figure 7.10: Absorption coefficient and refractive index for whole blood, blood cells, serum and a blood clot and its components.

Transmission spectroscopy measurements were made of whole blood, blood plasma, blood cells and a blood clot, from which the absorption coefficients and refractive indices of each component was determined. The preparation and measurement of these samples are described in section 7.2.1.1. The absorption coefficients and refractive indices of the blood components are illustrated in figures 7.10(a) and 7.10(b) and are

Table 7.3: Double Debye coefficients for whole blood and blood components

	E_∞	E_S	E_2	τ_1(ps)	τ_2(ps)
Whole Blood	2.1	130[a]	3.8	14.4	0.1
Blood Serum	1.7	78.8	3.6	8.0	0.1
Blood Cells	3.4	2.5[b]	23.8	410.8	1.8
Blood Clot	2.2	130[a]	3.7	16.1	0.1
Water	*3.3*	*78.8*	*4.5*	*8.4*	*0.1*

[a] (Schwan 1983)
[b] (ICT 1933)

shown in comparison to pure water. From the graph of the absorption coefficient, figure 7.10(a), it is evident that the absorption of pure water is greater than whole blood or any of its components. It is apparent that there is a decrease in overall absorption coefficient as the water content of the blood components is reduced; serum (92% water), whole blood (50.6% water) and blood cells (residual water remaining after centrifuging). The exception, however, is the blood clot which has the same water content as whole blood where, clearly, the effect of coagulation and the formation of a thrombus has an effect on the absorption coefficient. It is likely that the formation of a thrombus, a protein/fibrin covalently bonded structure, encapsulates much of the water present impeding its ability to attenuate THz radiation. The refractive index, figure 7.10(b), of whole blood and blood components, in comparison to pure water show, overall, that the refractive index of water is greater than the whole blood and components. It would be expected that components with high water content would have refractive indices very similar to pure water and, while this is true of the whole blood sample, this does not appear to be the case with the serum sample. The refractive index of the serum at low frequency (0.1-0.5 THz) is consistent with water and whole blood, however, begins to diverge at higher frequencies. The refractive indices of the blood clot and blood cells appear to be consistently 0.05 below that of pure water.

To further investigate if the relaxation mechanisms present in the whole blood and blood components from which these differences in optical properties arise can be determined, the Debye parameters of the samples are considered. The complex dielectric coefficients were calculated from the measured absorption coefficient and refractive indices following equation 2.44 for all the samples, and double Debye theory was applied

where the ε_S values were held constant. The determined Debye relaxation coefficients are given in table 7.3. The τ_1 relaxation for the whole blood, at 14.37ps, is significantly higher than that of the pure water. If this is compared to those that will be presented for sucrose solutions, section 5.4.3, which can be considered a solutions of molecules in water, the relaxation times for both solutions are comparable suggesting that the red blood cells have a similar retardation effect on the water relaxations. In considering the τ_1 relaxation for the blood clot, there an increased slowing of the relaxation mechanisms can be seen, suggesting that the coagulation of the blood results in a greater impedance of the free water present. Interestingly, the τ_1 relaxation for the blood cells is very large. While this is unlikely to correspond to a relaxation of the cell itself or of haemoglobin molecules within the cells as these would be much slower processes, this relaxation may well be due to the slowed relaxation of the associated water surrounding the molecule, which is, approximately, 10^1-10^4 slower than the free water (Baumgartner et al. 2003, Bordat et al. 2004, Heugen et al. 2006).

7.4 Summary

THz imaging has been shown to be sensitive to differences in colon tissue composition under controlled conditions. Tissue staining has identified increases in lymphatic systems and vasculature of the diseased tissue in comparison to the normal mucosa, which may indicate physical differences between the tissue pathologies useful in determining underlying contrast mechanisms in terahertz imaging. Investigation into the spectroscopic properties of the *ex vivo* tissues showed a reduction in both the absorption coefficient and refractive indices of the diseased tissues in comparison to healthy tissues which is an indicator of increased tissue water content. Statistical analysis has determined a sensitivity of 82% and a specificity of 77% when using a multinomial logistic regression analysis to compare parameters extracted from the averaged waveforms of regions identified as healthy, cancerous and dysplastic in the tissue samples. Six parameters were identified as statistically significant, however, the model gave best classification when 9 of the 17 parameters were considered. A second statistical analysis using binary logistic regression analysis to compare averaged waveforms from regions identified as healthy and dysplastic in the tissue samples determined a sensitivity of 89.2% and a specificity of 71.4%. This analysis suggested that the data for the 2 groups was significantly different with a p value of 0.021.

Part IV

Conclusions and future work

Chapter 8

Conclusions and future work

8.1 Conclusions

The purpose of the work presented in this thesis was to investigate the potential of three different analytical methods; linear spectral decomposition, spectrally averaged dielectric coefficient method and the Debye relaxation coefficient method, to detect and specify tissue pathologies at THz wavelengths. The questions this thesis aimed to answer were: does THz spectroscopy allow the measurement of tissue composition; and is it sufficiently accurate and sensitive to make a diagnosis of pathologies?

While accuracy of the determined concentrations was found to be strongly dependent on the method of analysis used, it was nevertheless shown for all analysis methods that THz spectroscopy is in principle capable of recovering material composition. The most precise accuracies were determined by the spectrally averaged dielectric coefficient and Debye relaxation coefficient methods as these methods being less susceptible to systematic differences between measurements. Nonetheless, the concentrations determined by the linear spectral decomposition method still reflected the general changes in the concentration of the phantoms. This demonstrates significant sensitivity in the measured THz signal to the composition of the phantoms and establishes that, in principle, terahertz spectroscopy has the potential to analyse tissue composition and specify tissue pathologies.

Although the accuracies resolved for each of the three concentration analysis technique demonstrated the ability of THz spectroscopy to resolve composition, the resolutions produced by the three concentration analysis methods were varied. The linear spectral decomposition method has demonstrated an average resolution of $\pm 1.7\%$ for the water component of all the phantoms measured. This method is most sensitive to chromophores with large absorption coefficients in the THz wavelength region, such as

polar molecules like water and methanol. For non-polar chromophores with relatively low absorption, such as lipid, the sensitivity is significantly smaller. The resolutions provided by the Debye relaxation method are more consistent across all the measured phantoms and are not as sensitive to the polarity of the chromophores. The sensitivity to concentration of all three concentration analysis methods determined using this method is fixed. In order to improve resolution, therefore, only the standard deviation of the measurement systems may be improved which may be achieved by increasing the signal to noise ratio (SNR) of the system. Systems such as Quantum Cascade Lasers (QCLs) (Williams 2007, Sirtori 2009) and higher power systems (Tachiki 2008) are being developed with the aim of delivering increased power thus increasing the SNR. The SNR may also be improved through the development of more sensitive detectors (Stillman and Shur 2007)

From the results presented in this thesis the answer to the question of whether THz spectroscopy can determine tissue composition is mixed. From the accuracies of the three concentration analysis methods, THz spectroscopy has been shown to be sensitive to concentration and capable of recovering material composition. However, from the determined resolutions, it can be concluded that THz spectroscopy is not yet capable of accurately resolving small enough changes in concentration to enable confident tissue diagnosis. The resolutions are limited by the specifications of the systems used in this study, but ongoing technological advances in the field which increase the SNR of the systems may enable smaller resolutions to be resolved in the future.

In Chapter 7 we presented spectroscopy results for ex vivo samples of both normal and diseased colonic tissues. The results from the study of colon cancer and adjacent normal tissue revealed, using binary logistic regression analysis of time-domain reflected signals, a sensitivity of 89.2% and a specificity of 71.4% between regions identified as healthy and dysplastic in the tissue samples. Although this study did not fully model the physical interaction of THz radiation with the tissue, the analysis of specific parts of the reflected time-domain waveform nevertheless indicated that THz spectroscopy is sensitive to differences between tissue types. These results provide further encouragement that THz spectroscopy may allow tissue diagnosis provided suitable theoretical models are developed.

The analysis of THz data measured in sucrose solutions also presented an interesting potential application. This thesis has shown that THz spectroscopy is sensitivity to sucrose concentration indicating a potential application of THz spectroscopy to mon-

itoring glucose levels non-invasively in tissue. Debye modelling of aqueous sucrose solutions as part of this study has suggested the ability of the THz spectroscopy in probing macromolecular dynamics in solution, such as distinguishing hydration waters of sucrose and bulk water. This has been suggested from previous studies (Ebbinghaus et al. 2007). For THz spectroscopy to be a viable glucose monitoring tool would require much greater sensitivity than that provided by the current system as the concentrations of glucose in the blood are very small. The physiological range is typically between 4-6mM. This corresponds to a glucose concentration range of 0.06-0.13% wt of blood. The best resolutions of the aqueous sucrose solutions determined as part of this study were ± 3.9 for the Debye relaxation coefficient method. As stated previously, the resolutions are limited by the SNR of the measurements and so the current limitations on THz systems used in this study inhibit the expansion of THz spectroscopy into this dynamic biomedical field at this present time. However, the development of high power THz spectroscopy systems may enable the SNR of the systems to be increased sufficiently to enable THz tissue glucose monitoring in the future.

Biomedical THz imaging is still in its early stages of development but, as this thesis has shown, has great potential to be a valuable imaging technique in the future. Current imaging systems have a relatively low SNR, which limits both the resolution of the concentration analysis methods and the penetration depth through materials. The development of high power systems (Williams 2007, Tachiki 2008, Sirtori 2009) which deliver increased power and so increase the SNR would hopefully enable greater sensitivity to concentration changes and greater depth penetration enabling THz spectroscopy studies of biological tissues at depth. TeraView is currently developing a hand-held probe and is assessing the accuracy of the probe as an intra-operative tool for the diagnosis of breast cancer (Ashworth et al. 2008). It is conceivable that the diagnostic scope of this hand-held probe may be extended to other tissue types, specifically where disorders are present near the surface, such as cancers and dysplasia of the skin and mucosal layers (colon, oral tissue, etc).

8.2 Future Work

The work presented in this thesis has shown that THz spectroscopy has the potential to distinguish biological tissue types. However, the technique is not yet a clinical diagnostic tool. For this to become possible, more detailed studies of the interaction of THz radiation with tissues and tissue phantoms must be undertaken in order to understand the physical principles that give rise to the detected signals. Studies have shown that there is a statistical difference in the THz time-domain reflection signal of a selection of

healthy human tissues, including liver, kidney, heart muscle, leg muscle, pancreas and abdominal fat (Huang et al. 2009). Work presented in this thesis has established that the reflected THz time-domain waveform from excised colonic tissues can be classified into dysplastic, cancerous or healthy tissues using a set of parameters extracted from the waveform. Future developments extending from this work, therefore, are focused on improvement of the tissue classification of biological tissues through analysis of the time-domain reflection signal.

In order to develop and improve mathematical models for analysing tissue composition in the THz time-domain from measurements made in reflection mode, a number of issues must be addressed in future work.

- Measurements must be made to establish the response of individual tissue chromophores such as tissue specific proteins. This is in itself a non trivial task because the importance of water in protein dynamics means that some difficultly is involved in separating the response of the protein and the water molecules that are bound to it from the background water solution. Developments in biomolecular analysis techniques, promise a more controlled and precise method of molecular study (Arikawa et al. 2008, Heyden et al. 2008).

- The Finite Difference Time-Domain (FDTD) model should be built incorporating the THz response of an increasing number of chromophores. Each step in the development could then be validated using phantoms composed of the chromophores included in the model. In this way a reliable analytical method can be developed in a controlled manner. This may then used to analyse measurements of ex vivo and in vivo tissue. The results of this analysis may then be compared to histological results to assess the accuracy of the model in identifying tissue types and tissue pathologies.

Part V

Appendices

Appendix A

Empirical equations relating Debye relaxation coefficients to phantom concentration

A.1 Water and methanol

x=methanol concentration

$$\Delta_1 = -0.2291x^2 - 44.503x + 74.266$$
$$\Delta_2 = 4.5433x^5 - 8.0298x^4 + 4.1526x^3 - 0.2621x^2 - 0.5705x + 1.2566$$
$$\tau_1 = -3.5613x^2 + 10.294x + 8.4958$$
$$\tau_2 = 0.3176x^4 - 0.3336x^3 + 0.0694x^2 + 0.0141x + 0.1051$$

A.2 Water and lipid

x=lipid concentration

$$\Delta_1 = -0.7363x + 73.982$$
$$\Delta_2 = 0.0003x^2 - 0.0213x + 1.3237$$
$$\tau_1 = 0.0234x + 8.5018$$
$$\tau_2 = 0.001x + 0.1243$$

A.3 Water and sucrose

x=sucrose concentration

$$\Delta_1 = -0.0097x^2 - 0.1647x + 77.95$$
$$\Delta_2 = 0.0003x + 1.3208$$
$$\tau_1 = 0.0004x^3 - 0.0172x^2 + 0.2839x + 8.062$$
$$\tau_2 = -6E - 07x^3 + 2E - 05x^2 + 0.0002x + 0.1049$$

A.4 Water and gelatin

x=gelatin concentration

$$\Delta_1 = -0.0089x + 73.549$$
$$\Delta_2 = 0.0165x + 1.3582$$
$$\tau_1 = 0.0004x^3 - 0.0162x^2 + 0.3287x + 7.3822$$
$$\tau_2 = 2E - 05x^3 - 0.0011x^2 + 0.017x + 0.0791$$

Bibliography

T. Alarcon, H. M. Byrne, and P. K. Maini. A multiple scale model for tumor growth. *Multiscale Model Simulation*, 3(2):440–475, 2005.

D. Apel, R. Jakobs, D. Schilling, U. Weickert, J. Teichmann, M. H. Bohrer, and J. F. Riemann. Accuracy of high-resolution chromoendoscopy in prediction of histologic findings in diminutive lesions of the rectosigmoid. *Gastrointestinal Endoscopy*, 63 (6):824–828, 2006.

T. Arikawa, M. Nagai, and K. Tanaka. Characterizing hydration state in solution using terahertz time-domain attenuated total reflection spectroscopy. *Chemical Physics Letters*, In Press, Accepted Manuscript, 2008.

D. D. Arnone, C. M. Ciesla, A. Corchia, S. Egusa, M. Pepper, J. M. Chamberlain, C. Bezant, E. H. Linfield, R. Clothier, and N. Khammo. Applications of terahertz (thz) technology to medical imaging. *Proceedings of SPIE*, 3828(1):209–219, 1999.

M. L. T. Asaki, A. Redondo, T. A. Zawodzinski, and A. J. Taylor. Dielectric relaxation of electrolyte solutions using terahertz transmission spectroscopy. *J. Chem. Phys.*, 116(19):8469–8482, 2002.

P. C. Ashworth, P. O'Kelly, A. D. Purushotham, S. E. Pinder, M. Kontos, M. Pepper, and V. P. Wallace. An intra-operative thz probe for use during the surgical removal of breast tumors. *Infrared, Millimeter and Terahertz Waves, 2008. IRMMW-THz 2008. 33rd International Conference on*, pages 1–3, 2008.

P. Atkins. *Atkins' Physical Chemistry*. Oxford University Press, 8 edition, 2002.

C. Atuma, V. Strugala, A. Allen, and L. Holm. The adherent gastrointestinal mucus gel layer: thickness and physical state in vivo. *Am J Physiol Gastrointest Liver Physiol*, 280(5):G922–G929, 2001.

D. H. Auston. Picosecond optoelectronic switching and gating in silicon. *Applied PhysicsLetters*, 26(3):101–103, 1975.

A. M. Axelrad, D. E. Fleischer, A. J. Geller, C. C. Nguyen, J. H. Lewis, F. H. Al Kawas, M. I. Avigan, E. A. Montgomery, and S. B. Benjamin. High-resolution chromoendoscopy for the diagnosis of diminutive colon polyps: Implications for colon cancer screening. *Gastroenterology*, 110(4):1253–1258, 1996.

V. Backman, M. B. Wallace, L. T. Perelman, J. T. Arendt, R. Gurjar, M. G. Muller, Q. Zhang, G. Zonios, E. Kline, T. McGillican, S. Shapshay, T. Valdez, K. Badizadegan, J. M. Crawford, M. Fitzmaurice, S. Kabani, H. S. Levin, M. Seiler, R. R. Dasari,

I. Itzkan, J. Van Dam, and M. S. Feld. Detection of preinvasive cancer cells. *Nature*, 406(6791):35–36, 2000.

R. Bansil, E. Stanley, and J. T. Lamont. Mucin biophysics. *Annual Review of Physiology*, 57(1):635–657, 1995.

J. Barthel, K. Bachhuber, R. Buchner, and H. Hetzenauer. Dielectric spectra of some common solvents in the microwave region. water and lower alcohols. *Chemical Physics Letters*, 165(4):369–373, 1990.

J. B. Bateman and C. Gabriel. Dielectric properties of aqueous glycerol and a model relating these to the properties of water. *J. Chem. Soc. , Faraday Trans. 2*, 83:355–369, 1987.

S. Baumgartner, G. Lahajnar, A. Sepe, and J. Kristl. Investigation of the state and dynamics of water in hydrogels of cellulose ethers by 1 h nmr spectroscopy. *AAPS PharmSciTech*, 3(4):1–8, 2003.

R. P. Bird. Observation and quantification of aberrant crypts in the murine colon treated with a colon carcinogen: Preliminary findings. *Cancer Letters*, 37(2):147–151, 1987.

H. B. Bohidar and B. Mohanty. Anomalous self-assembly of gelatin in ethanol-water marginal solvent. *Phys. Rev. E*, 69(2):021902, 2004.

H. B. Bohidar, S. S. Jena, S. Maity, A. Saxena, and S. Jena. Dielectric behaviour of gelatin solutions and gels. *Colloid and polymer science*, 276(1):81–86, 1998.

P. Bordat, A. Lerbret, J. P. Demaret, F. Affouard, and M. Descamps. Comparative study of trehalose, sucrose and maltose in water solutions by molecular modelling. *Europhys. Lett.*, 65(1):41–47, 2004.

I. A. Borin and M. S. Skaf. Molecular association between water and dimethyl sulfoxide in solution: the librational dynamics of water. *Chemical Physics Letters*, 296 (1-2):125–130, 1998.

B. Bowden, J. A. Harrington, and O. Mitrofanov. Low-loss modes in hollow metallic terahertz waveguides with dielectric coatings. *Appl. Phys. Lett.*, 93(18):181104–3, 2008.

J. W. Bowen, G. C. Walker, S. Hadjiloucas, and E. Berry. The consequences of diffractively spreading beams in ultrafast thz spectroscopy. *Infrared and Millimeter Waves, 2004 and 12th International Conference on Terahertz Electronics, 2004. Conference Digest of the 2004 Joint 29th International Conference on*, pages 551–552, 2004.

B. Brooks and M. Karplus. Harmonic dynamics of proteins: Normal modes and fluctuations in bovine pancreatic trypsin inhibitor. *Proceedings of the National Academy of Sciences of the United States of America*, 80(21):6571–6575, 1983.

M. Bruehlmeier, U. Roelcke, P. Blauenstein, J. Missimer, P. A. Schubiger, J. T. Locher, R. Pellikka, and S. M. Ametamey. Measurement of the extracellular space in brain tumors using 76br-bromide and pet. *J Nucl Med*, 44(8):1210–1218, 2003.

H. Bryan, A. Shennan, E. Griffin, and A. Angel. Intralipid-its rational use in parenteral nutrition of the newborn. *Pediatrics*, 58(6):787–790, 1976.

R. H. Clothier and N. Bourne. Effects of thz exposure on human primary keratinocyte differentiation and viability. *Journal of Biological Physics*, 29(2):179–185, 2003.

K. S. Cole and R. H. Cole. Dispersion and absorption in dielectrics i. alternating current characteristics. *J. Chem. Phys.*, 9(4):341–351, 1941.

M. Cope. *The application of near infrared spectroscopy to non invasive monitoring of cerebral oxygenation in the newborn infant*. Phd, University College London, 1991.

R. M. Cothren, M. J. Sivak, J. Van Dam, R. E. Petras, M. Fitzmaurice, J. M. Crawford, J. Wu, J. F. Brennan, R. P. Rava, R. Manoharan, and M. S. Feld. Detection of dysplasia at colonoscopy using laser-induced fluorescence : a blinded study. *Gastrointestinal Endoscopy*, 44(2):168–176, 1996.

P. Crow, N. Stone, C. A. Kendall, R. A. Persad, and M. P. J. Wright. Optical diagnostics in urology: current applications and future prospects. *BJU International*, 92(4):400–407, 2003.

R. S. Dacosta, B. C. Wilson, and N. E. Marcon. New optical technologies for earlier endoscopic diagnosis of premalignant gastrointestinal lesions. *Journal of Gastroenterology and Hepatology*, 17(1s):85–105, 2002.

R. S. Dacosta, H. Andersson, and B. C. Wilson. Molecular fluorescence excitationemission matrices relevant to tissue spectroscopy. *Photochemistry and Photobiology*, 78(4):384–392, 2003a.

R. S. Dacosta, B. C. Wilson, and N. E. Marcon. Photodiagnostic techniques for the endoscopic detection of premalignant gastrointestinal lesions. *Digestive Endoscopy*, 15(3):153–173, 2003b.

A. Das, M. J. Sivak, A. Chak, R. C. K. Wong, V. Westphal, A. M. Rollins, J. Willis, G. A. Isenberg, and J. A. Izatt. High-resolution endoscopic imaging of the gi tract: A comparative study of optical coherence tomography versus high-frequency catheter probe eus. *Gastrointestinal Endoscopy*, 54(2):219–224, 2001.

D. W. Davidson and R. H. Cole. Dielectric relaxation in glycerol, propylene glycol, and n-propanol. *J. Chem. Phys.*, 19(12):1484–1490, 1951.

M. Davies. *Dielectric and Related Molecular Processes*, volume 3. The Chemical Society, London, 1977.

P. Debye. *Polar Molecules*. The Chemical Catalog Company, New York, 1929.

F. Despa, A. Ferndendez, and R. S. Berry. Dielectric modulation of biological water. *Physical review letters*, 93(22):228104, 2004.

S. Dixit, J. Crain, W. C. K. Poon, J. L. Finney, and A. K. Soper. Molecular segregation observed in a concentrated alcohol-water solution. *Nature*, 416(6883):829–832, 2002.

F. Duck. *Physical Properties of Tissue*. Academic Press, London, 1990.

S. Ebbinghaus, S. J. Kim, M. Heyden, X. Yu, U. Eugen, M. Gruebele, D. M. Leitner, and M. Havenith. An extended dynamical hydration shell around proteins. *PNAS*, 104(52):20749–20752, 2007.

G. M. Eisen, C. Y. Kim, D. E. Fleischer, R. A. Kozarek, D. L. Carr-Locke, T. C. M. Li, C. J. Gostout, S. J. Heller, E. A. Montgomery, F. H. Al Kawas, J. H. Lewis, and S. B. Benjamin. High-resolution chromoendoscopy for classifying colonic polyps: A multicenter study. *Gastrointestinal Endoscopy*, 55(6):687–694, 2002.

S. B. Engelsen and S. Perez. The hydration of sucrose. *Carbohydrate Research*, 292: 21–38, 1996.

J. Ferezou, A. Gulik, N. Domingo, F. Milliat, J. C. Dedieu, S. Dunel-Erb, C. Chevalier, and A. C. Bach. Intralipid 10 percent: physicochemical characterization. *Nutrition*, 17(11-12):930–933, 2001.

J. K. Fisher. Normal colon wall thickness on ct. *Radiology*, 145(2):415–418, 1982.

A. J. Fitzgerald, V. P. Wallace, R. Pye, M. Jimenez-Linan, L. Bobrow, A. D. Purushotham, and D. D. Arnone. Terahertz imaging of breast cancer, a feasibility study. pages 823–824, 2004.

A. J. Fitzgerald, E. Pickwell, V. P. Wallace, A. Purushotham, S. Pinder, M. Linan, R. Pye, and T. Ha. Medical applications of broadband terahertz pulsed radiation. *Lasers and Electro-Optics Society, 2005. LEOS 2005. The 18th Annual Meeting of the IEEE*, pages 120–121, 2005.

A. J. Fitzgerald, V. P. Wallace, M. Jimenez-Linan, L. Bobrow, R. J. Pye, A. D. Purushotham, and D. D. Arnone. Terahertz pulsed imaging of human breast tumors. *Radiology*, 239(2):533–540, 2006.

S. T. Flock, S. L. Jacques, B. C. Wilson, W. M. Star, and M. J. Gemert. Optical properties of intralipid: a phantom medium for light propagation studies. *Lasers in Surgery and Medicine*, 12(5):510–519, 1992.

F. Franks. *Water : a comprehensive treatise. Volume 3 Aqueous solutions of simple electrolytes*. Plenum, New York, 1973.

F. Franks and D. J. G. Ives. The structural properties of alcoholwater mixtures. *Quarterly reviews - Chemical Society*, 20(1):1–44, 1966.

H. Fricke and H. J. Curtis. The dielectric properties of water-dielectric interphases. *J. Phys. Chem.*, 41(5):729–745, 1937.

C. Gabriel, S. Gabriel, E. H. Grant, B. S. J. Halstead, and D. M. P. Mingos. Dielectric parameters relevant to microwave dielectric heating. *Chemical Society Reviews*, 27: 213–224, 1998.

S. Gabriel, R. W. Lau, and C. Gabriel. The dielectric properties of biological tissues: Iii. parametric models for the dielectric spectrum of tissues. *Physics in Medicine and Biology*, 41(11):2271–2293, 1996.

Z. Ge, K. T. Schomacker, and N. S. Nishioka. Identification of colonic dysplasia and neoplasia by diffuse reflectance spectroscopy and pattern recognition techniques. *Applied Spectroscopy*, 52(6):833–839, 1998.

T. R. Globus, D. L. Woolard, A. C. Samuels, B. L. Gelmont, J. Hesler, T. W. Crowe, and M. Bykhovskaia. Submillimeter-wave fourier transform spectroscopy of biological macromolecules. *J. Appl. Phys.*, 92(9):6105–6113, 2002.

T. R. Globus, D. L. Woolard, T. Khromova, T. W. Crowe, M. Bykhovskaia, B. L. Gelmont, J. Hesler, and A. C. Samuels. Thz-spectroscopy of biological molecules. *Journal of Biological Physics*, 29(2-3):89–100, 2003.

N. Go, T. Noguti, and T. Nishikawa. Dynamics of a small globular protein in terms of low-frequency vibrational modes. *Proceedings of the National Academy of Sciences of the United States of America*, 80(12):3696–3700, 1983.

S. Godefroy, J. P. Korb, M. Fleury, and R. G. Bryant. Surface nuclear magnetic relaxation and dynamics of water and oil in macroporous media. *Phys. Rev. E*, 64(2): 021605, 2001.

S. Gorenflo, U. Tauer, I. Hinkov, A. Lambrecht, R. Buchner, and H. Helm. Dielectric properties of oilwater complexes using terahertz transmission spectroscopy. *Chemical Physics Letters*, 421:494–498, 2006.

E. H. Grant. Dielectric dispersion in bovine serum albumen. *Jounal of Molecular Biology*, 19:133–139, 1966.

E. H. Grant, V. E. R. McClean, N. R. V. Nightingale, R. J. Sheppard, and M. J. Chapman. Dielectric behavior of water in biological solutions: Studies on myoglobin, human low-density lipoprotein, and polyvinylpyrrolidone. *Bioelectromagnetics*, 7 (2):151–162, 1986.

I. S. Gregory, C. Baker, W. R. Tribe, I. V. Bradley, M. J. Evans, E. H. Linfield, A. G. Davies, and M. Missous. Optimization of photomixers and antennas for continuous-wave terahertz emission. *Quantum Electronics, IEEE Journal of*, 41(5):717–728, 2005.

I. S. Gregory, M. J. Evans, H. Page, S. Malik, I. Farrer, and H. E. Beere. Analysis of photomixer receivers for continuous-wave terahertz radiation. *Appl. Phys. Lett.*, 91 (15):154103–154103, 2007.

I. S. Gulyi and V. M. Klimovich. Model of the structure of sucrose solutions. *Journal of Structural Chemistry*, 32(5):675–679, 1990.

F. Gunstone. *Fatty acid and lipid chemistry*. Blackie Academic and Professional, Glasgow, 1996.

J. H. Guo, Y. Luo, A. Augustsson, S. Kashtanov, J. E. Rubensson, D. K. Shuh, H. Agren, and J. Nordgren. Molecular structure of alcohol-water mixtures. *Physical review letters*, 91(15):157401, 2003.

M. Gutman, E. Nachliel, and S. Kiryati. Dynamic studies of proton diffusion in mesoscopic heterogeneous matrix: I. concentrated solutions of sucrose. *Biophys. J.*, 63 (1):274–280, 1992.

H. P. Haber and M. Stern. Intestinal ultrasonography in children and young adults: bowel wall thickness is age dependent. *J Ultrasound Med*, 19(5):315–321, 2000.

J. B. Hasted. *Aqueous dielectrics*. Studies in chemical physics. Chapman and Hall, London, 1973.

M. Havenith, U. Heugen, A. Bergner, S. Ebbinghaus, E. Brundermann, E. Larios, D. M. Leitner, and M. Gruebele. Thz-biology: studying protein dynamics in solution. *Infrared and Millimeter Waves, 2004 and 12th International Conference on Terahertz Electronics, 2004. Conference Digest of the 2004 Joint 29th International Conference on*, pages 731–732, 2004.

S. Havriliak and S. Negami. A complex plane representation of dielectric and mechanical relaxation processes in some polymers. *Polymer*, 8:161–210, 1967.

U. Heugen, G. Schwaab, E. Brundermann, M. Heyden, X. Yu, D. M. Leitner, and M. Havenith. Solute-induced retardation of water dynamics probed directly by terahertz spectroscopy. *PNAS*, 103(33):12301–12306, 2006.

M. Heyden, E. Brndermann, U. Heugen, G. Niehues, D. M. Leitner, and M. Havenith. Long-range influence of carbohydrates on the solvation dynamics of water - answers from terahertz absorption measurements and molecular modeling simulations. *J. Am. Chem. Soc.*, 2008.

A. Hildebrandt, R. Blossey, S. Rjasanow, O. Kohlbacher, and H. P. Lenhof. Electrostatic potentials of proteins in water: a structured continuum approach. *Bioinformatics*, 23(2):e99–103, 2007.

K. Hinsen. Analysis of domain motions by approximate normal mode calculations. *Proteins: Structure, Function, and Genetics*, 33(3):417–429, 1998.

J. P. Hornak, A. C. Smith, and J. Szumowski. Spin-lattice relaxation time measurements using hybrid csi-phantom study. *Magnetic Resonance in Medicine*, 13(3):398–406, 1990.

R. Hornung, T. H. Pham, K. A. Keefe1, M. W. Berns, Y. Tadir, and B. J. Tromberg. Quantitative near-infrared spectroscopy of cervical dysplasia in vivo. *Hum. Reprod.*, 14(11):2908–2916, 1999.

B. B. Hu and M. C. Nuss. Imaging with terahertz waves. *Optics letters*, 20(16):1716–1718, 1995.

Y. Hu, L. Guo, X. Wang, and X. C. Zhang. Thz time-domain spectroscopy on plant oils and animal fats. *Proceedings of SPIE*, 5640(1):334–340, 2005.

S. Y. Huang, Y. X. J. Wang, D. K. W. Yeung, A. T. Ahuja, Y. T. Zhang, and E. Pickwell-MacPherson. Tissue characterization using terahertz pulsed imaging in reflection geometry. *Physics in Medicine and Biology*, 54(1):149–160, 2009.

D. P. Hurlstone, D. S. Sanders, A. J. Lobo, M. E. McAlindon, and S. S. Cross. Indigo carmine-assisted high-magnification chromoscopic colonoscopy for the detection and characterisation of intraepithelial neoplasia in ulcerative colitis: A prospective evaluation. *Endoscopy*, 37(12):1186–1192, 2005.

ICT. Dielectric constant and dielectric strength. *International Critical Tables of Numerical Data, Physics, Chemistry and Technology*, 6:82–101, 1933.

H. Inoue, J. Y. Cho, H. Satodate, M. Sakashita, E. Hidaka, S. Fukami, T. Kazawa, T. Yoshida, A. Shiokawa, and S. Kudo. Development of virtual histology and virtual biopsy using laser-scanning confocal microscopy. *Scandinavian Journal of Gastroenterology*, 38(5):37–39, 2003.

H. Ito, F. Nakajima, T. Furuta, and T. Ishibashi. Continuous thz-wave generation using antenna-integrated uni-travelling-carrier photodiodes. *Semiconductor Science and Technology*, 20(7):191–198, 2005.

I. Iwamoto, S. Nishizawa, M. W. Takeda, and M. Tani. Development of a new commercial thz-tds instrument. *Infrared and Millimeter Waves and 13th International Conference on Terahertz Electronics, 2005. IRMMW-THz 2005. The Joint 30th International Conference on*, 1:188–189, 2005.

B. Jacobson. Hydration structure of deoxyribonucleic acid and its physico-chemical properties. *Nature*, 172(4380):666–667, 1953.

P. Uhd Jepsen and S. J. Clark. Precise ab-initio prediction of terahertz vibrational modes in crystalline systems. *Chemical Physics Letters*, 442(4-6):275–280, 2007.

P. Uhd Jepsen, U. Mller, and H. Merbold. Investigation of aqueous alcohol and sugar solutions with reflection terahertz time-domain spectroscopy. *Optics Express*, 15 (22):14717–14737, 2007.

D. J. Jones. *ABC of colorectal diseases*. BMJ Books, London, 2 edition, 1999.

A. S. Karashima, H. Kataoka, H. Itoh, R. Maruyama, and M. Koono. Prognostic significance of alpha-1-antitrypsin in early stage of colorectal carcinomas. *International Journal of Cancer*, 45(2):244–250, 1990.

C. L. Kay, D. Kulling, R. H. Hawes, J. W. R. Young, and P. B. Cotton. Virtual endoscopy - comparison with colonoscopy in the detection of space-occupying lesions of the colon. *Endoscopy*, 32(03):226–232, 2000.

F. H. C. Kelly and M. Fong Keng. *The sucrose crystal and its solution*. Singapore University Press, 1975.

K. C. Kerby and J. T. Bernhard. Comparison of bend loss in terahertz waveguide and optical fiber. *Antennas and Propagation Society International Symposium, 2007 IEEE*, pages 4661–4664, 2007.

D. J. Kerr, A. M. Young, and F. D. R. Hobbs. *ABC of Colorectal Cancer*. BMJ Books, London, 1 edition, 2001.

R. Kiesslich and M. F. Neurath. Chromo- and magnifying endoscopy for colorectal lesions. *Europan Journal of Gastroenterology and Hepatology*, 17(8):793–801, 2005.

R. Kiesslich, J. Burg, M. Vieth, J. Gnaendiger, M. Enders, P. Delaney, A. Polglase, W. McLaren, D. Janell, S. Thomas, B. Nafe, P. R. Galle, and M. F. Neurath. Confocal laser endoscopy for diagnosing intraepithelial neoplasias and colorectal cancer in vivo. *Gastroenterology*, 127(3):706–713, 2004a.

R. Kiesslich, M. Jung, J. A. DiSario, P. R. Galle, and M. F. Neurath. Perspectives of chromo and magnifying endoscopy: How, how much, when, and whom should we stain? *Journal of Clinical Gastroenterology*, 38(1):7–13, 2004b.

J. T. Kindt and C. A. Schmuttenmaer. Far-infrared dielectric properties of polar liquids probed by femtosecond terahertz pulse spectroscopy. *Journal of Physics in Chemistry*, 100:10373–10379, 1996.

K. Kobayashi, J. A. Izatt, M. D. Kulkarni, J. Willis, and M. J. Sivak. High-resolution cross-sectional imaging of the gastrointestinal tract using optical coherence tomography: preliminary results, ,. *Gastrointestinal Endoscopy*, 47(6):515–523, 1998.

M. Koeberg, C. C. Wu, D. Kim, and M. Bonn. Thz dielectric relaxation of ionic liquid:water mixtures. *Chemical Physics Letters*, 439(1-3):60–64, 2007.

J. Kroll, J. Darmo, and K. Unterrainer. Terahertz optical activity of sucrose single-crystals. *Vibrational Spectroscopy*, 43(2):324–329, 2006.

S. Kudo, S. Hirota, T. Nakajima, S. Hosobe, H. Kusaka, T. Kobayashi, M. Himori, and A. Yagyuu. Colorectal tumours and pit pattern. *J Clin Pathol*, 47(10):880–885, 1994.

S. Kudo, S. Tamura, T. Nakajima, H. Yamano, H. Kusaka, and H. Watanabe. Diagnosis of colorectal tumorous lesions by magnifying endoscopy, , ,. *Gastrointestinal Endoscopy*, 44(1):8–14, 1996.

M. R. Kutteruf, C. M. Brown, L. K. Iwaki, B. M. Campbell, T. M. Orter, and E. J. Heilweil. Terahertz spectroscopy of short-chain polypeptides. *Chemical Physics Letters*, 375:337–343, 2003.

A. Laaksonen, P. G. Kusalik, and I. M. Svishchev. Three-dimensional structure in water-methanol mixtures. *J. Phys. Chem. A*, 101(33):5910–5918, 1997.

B. M. Ladanyi and M. S. Skaf. Wave vector-dependent dielectric relaxation of methanol-water mixtures. *J. Phys. Chem.*, 100(4):1368–1380, 1996.

M. Lazebnik, E. L. Madsen, G. R. Frank, and S. C. Hagness. Tissue-mimicking phantom materials for narrowband and ultrawideband microwave applications. *Physics in Medicine and Biology*, 50:4245–4258, 2005.

W. A. Lees and A. Burawoy. The effect of hydrogen bonding on the electronic spectra of organic molecules. *Tetrahedron*, 19(3):419–438, 1963.

A. Lerbret, P. Bordat, F. Affouard, M. Descamps, and F. Migliardo. How homogeneous are the trehalose, maltose, and sucrose water solutions? an insight from molecular dynamics simulations. *J. Phys. Chem. B*, 109(21):11046–11057, 2005.

C. MacAulay, P. Lane, and R. Richards-Kortum. In vivo pathology: microendoscopy as a new endoscopic imaging modality. *Gastrointestinal Endoscopy Clinics of North America*, 14(3):595–620, 2004.

E. L. Madsen, G. R. Frank, T. A. Krouskop, T. Varghese, F. Kallel, and J. Ophir. Tissue-mimicking oil-in-gelatin dispersions for use in heterogeneous elastography phantoms. *Ultrasonic Imaging*, 25:17–38, 2003.

Y. Maeda and H. Kitano. The structure of water in polymer systems as revealed by raman spectroscopy. *Spectrochimica Acta Part A: Molecular and Biomolecular Spectroscopy*, 51(14):2433–2446, 1995.

C. A. Makin, L. G. Bobrow, and W. F. Bodmer. Monoclonal antibody to cytokeratin for use in routine histopathology. *J Clin Pathol*, 37(9):975–983, 1984.

A. Markelz, A. Roitberg, and E. J. Heilweil. Pulsed terahertz spectroscopy of dna, bovine serum albumin and collagen between 0.1 and 2.0 thz. *Chemical Physics Letters*, 320:42–48, 2000.

A. Markelz, S. Whitmire, J. Hillebrecht, and R. Birge. Thz time domain spectroscopy of biomolecular conformational modes. *Physics in Medicine and Biology*, 47:3797–3805, 2002.

O. Markovitch and N. Agmon. Structure and energetics of the hydronium hydration shells. *The Journal of Physical Chemistry A*, 111(12):2253–2256, 2007.

M. Matsumoto and K. E. Gubbins. Hydrogen bonding in liquid methanol. *J. Chem. Phys.*, 93(3):1981–1994, 1990.

R. Mendis. Thz transmission characteristics of dielectric-filled parallel-plate waveguides. *J. Appl. Phys.*, 101(8):083115–4, 2007.

R. Mendis and D. Grischkowsky. Thz interconnect with low-loss and low-group velocity dispersion. *Microwave and Wireless Components Letters, IEEE*, 11(11):444–446, 2001.

S. P. Mickan, A. Menikh, H. Liu, C. A. Mannella, D. Abbott, J. Munch, and X. C. Zhang. Label-free bioaffinity detection using terahertz technology. *Physics in Medicine and Biology*, 47:3789–3795, 2002.

D. M. Mittleman, M. C. Nuss, and V. L. Colvin. Terahertz spectroscopy of water in inverse micelles. *Chemical Physics Letters*, 275(3-4):332–338, 1997.

V. Molinero, T. Cagin, and W. A. Goddard III. Sugar, water and free volume networks in concentrated sucrose solutions. *Chemical Physics Letters*, 377(3):469–474, 2003.

R. Moll, W. W. Franke, D. L. Schiller, B. Geiger, and R. Krepler. The catalog of human cytokeratins: Patterns of expression in normal epithelia, tumors and cultured cells. *Cell*, 31(1):11–24, 1982.

M. W. Mosesson. Fibrinogen and fibrin structure and functions. *Journal of Thrombosis and Haemostasis*, 3:1894–1904, 2005.

J. R. Mourant, I. J. Bigio, J. D. Boyer, T. M. Johnson, J. Lacey, A. G. Bohorfoush III, and M. H. Mellow. Elastic scattering spectroscopy as a diagnostic tool for differentiating pathologies in the gastrointestinal tract: preliminary testing. *J. Biomed. Opt.*, 1(2):192–199, 1996a.

J. R. Mourant, T. Fuselier, J. Boyer, T. M. Johnson, and I. J. Bigio. Predictions and measurements of scattering and absorption over broad wavelength ranges in tissue phantoms. *Applied Optics*, 36(4):949–957, 1996b.

M. Nagai, H. Yada, T. Arikawa, and K. Tanaka. Terahertz time-domain attenuated total reflection spectroscopy in water and biological solution. *International Journal of Infrared and Millimeter Waves*, 27(4):505–515, 2006.

A. Nahata, J. T. Yardley, and T. F. Heinz. Two-dimensional imaging of continuous-wave terahertz radiation using electro-optic detection. *Appl. Phys. Lett.*, 81(6):963–965, 2002.

M. Nakasako. Water-protein interactions from high-resolution protein crystallography. *Philosophical Transactions of the Royal Society B: Biological Sciences*, 359(1448): 1191–1206, 2004.

R. Nave. The interaction of radiation with matter. Personal Communication, 2007.

M. M. Nazarov, A. P. Shkurinov, E. A. Kuleshov, and V. V. Tuchin. Terahertz time-domain spectroscopy of biological tissues. *Quantum Electronics*, 38(7):647–654, 2008.

E. F. Nichols. A method for energy measurements in the infra-red spectrum and the properties of the ordinary ray in quartz for waves of great wave length. *Phys. Rev. (Series I)*, 4(4):297, 1897.

C. Nieto-Draghi, R. Hargreaves, and S. P. Bates. Structure and dynamics of water in aqueous methanol. *Journal of physics. Condensed matter*, 17(45):3265–3272, 2005.

A. Oka and K. Tominaga. Terahertz spectroscopy of polar solute molecules in non-polar solvents. *Journal of Non-Crystalline Solids*, 352(42-49):4606–4609, 2006.

K. S. Opstad, J. R. Griffiths, B. A. Bell, and F. A. Howe. Apparent t2 relaxation times of lipids and macromolecules: A study of high-grade tumor spectra. *Journal of Magnetic Resonance Imaging*, 27(1):178–184, 2008.

G. Palinkas, E. Hawlicka, and K. Heinzinger. Molecular dynamics simulations of water-methanol mixtures. *Chemical Physics*, 158(1):65–76, 1991.

J. E. Pedersen and S. R. Keiding. Thz time-domain spectroscopy of nonpolar liquids. *Quantum Electronics, IEEE Journal of*, 28(10):2518–2522, 1992.

R. Pethig. Protein-water interactions determined by dielectric methods. *Annual Review of Physical Chemistry*, 43:177–205, 1992.

E. Pickwell. *Biological Applications of terahertz pulsed imaging and spectroscopy*. PhD thesis, University of Cambridge, 2005.

E. Pickwell, B. E. Cole, A. J. Fitzgerald, M. Pepper, and V. P. Wallace. In vivo study of human skin using pulsed terahertz radiation. *Physics in Medicine and Biology*, 49: 1595–1607, 2004a.

E. Pickwell, B. E. Cole, A. J. Fitzgerald, V. P. Wallace, and M. Pepper. Simulation of terahertz pulse propagation in biological systems. *Appl. Phys. Lett.*, 84(12):21910–2192, 2004b.

E. Pickwell, A. J. Fitzgerald, B. E. Cole, P. Taday, R. J. Pye, T. Ha, M. Pepper, and V. P. Wallace. Simulating the response of terahertz radiation to basal cell carcinoma using ex vivo spectroscopy measuremen. *J. Biomed. Opt.*, 10(6):064021–1–064021–6, 2005.

A. B. Price and B. C. Morson. Inflammatory bowel disease: the surgical pathology of crohn's disease and ulcerative colitis. *Human Pathology*, 6(1):7–29, 1975.

E. K. Rofstad, E. Steinsland, O. Kaalhus, Y. B. Chang, B. Hovik, and H. Lyng. Magnetic resonance imaging of human melanoma xenografts in vivo: Proton spinlattice and spinspin relaxation times versus fractional tumour water content and fraction of necrotic tumour tissue. *International Journal of Radiation Biology*, 65(3):387–401, 1994.

A. M. Rollins, S. Yazdanfar, J. K. Barton, and J. A. Izatt. Real-time in vivo color doppler optical coherence tomography. *J. Biomed. Opt.*, 7(1):123–129, 2002.

C. Ronne, L. Thrane, P. O. Astrand, A. Wallqvist, K. V. Mikkelsen, and S. R. Keiding. Investigation of the temperature dependence of dielectric relaxation in liquid water by thz reflection spectroscopy and molecular dynamics simulation. *J. Chem. Phys.*, 107(14):5319–5331, 1997.

H. Rubens and F. Kurlbaum. On the heat radiation of long wave-length emitted by black bodies at different temperatures. *The astrophysical journal*, 14:335, 1901.

H Rubens and E. F. Nichols. Heat rays of great wave length. *Phys. Rev. (Series I)*, 4 (4):314, 1897.

G. Scalari, C. Walter, J. Faist, H. Beere, and D. Ritchie. Electrically switchable, two-color quantum cascade laser emitting at 1.39 and 2.3 thz. *Appl. Phys. Lett.*, 88(14): 141102–141103, 2006.

H. P. Schwan. Electrical properties of blood and its constitutents: Alternating current spectroscopy. *Annals of Hematology*, 46(4):185–197, 1983.

Y. Shi and L. Wang. Collective vibrational spectra of a- and g-glycine studied by terahertz and raman spectroscopy. *Journal of physics. D, applied physics*, 38(19): 3741, 2005.

C. Sirtori. Quantum cascade lasers: Breaking energy bands. *Nat Photon*, 3(1):13–15, 2009.

M. J. Sivak, K. Kobayashi, J. A. Izatt, A. M. Rollins, R. Ung-Runyawee, A. Chak, R. C. Wong, G. A. Isenberg, and J. Willis. High-resolution endoscopic imaging of the gi tract using optical coherence tomography. *Gastrointestinal Endoscopy*, 51(4): 512–516, 2000.

M. S. Skaf. Molecular dynamics study of dielectric properties of water-dimethyl sulfoxide mixtures. *J. Phys. Chem. A*, 103(50):10719–10729, 1999.

M. S. Skaf, T. Fonseca, and B. M. Ladanyi. Wave vector dependent dielectric relaxation in hydrogen-bonding liquids: A molecular dynamics study of methanol. *J. Chem. Phys.*, 98(11):8929–8945, 1993.

M. E. Smith and D. G. Morton. *The digestive system: basic science and clinical conditions*. Systems of the body. Churchill Livingstone, Edinburgh, 2001.

S. W. Smye, J. M. Chamberlain, A. J. Fitzgerald, and E. Berry. The interaction between terahertz radiation and biological tissue. *Physics in Medicine and Biology*, 46:R101–R112, 2001.

W. J. Stillman and M. S. Shur. Closing the gap: Plasma wave electronic terahertz detectors. *Journal of Nanoelectronics and Optoelectronics*, 2(3):209–221, 2007.

N. Stone, C. A. Kendall, N. Shepherd, P. Crow, and H. Barr. Near-infrared raman spectroscopy for the classification of epithelial pre-cancers and cancers. *Journal of Raman Spectroscopy*, 33(7):564–573, 2002.

N. Stone, C. A. Kendall, J. L. Smith, P. Crow, and H. Barr. Raman spectroscopy for identification of epithelial cancers. *Faraday Discuss. Y1 - 2009///*, 126:141–157, 2004.

M. R. Stringer, N. D. Lund, A. P. Foulds, A. Uddin, E. Berry, R. E. Miles, and A. G. Davies. The analysis of human cortical bone by terahertz time-domain spectroscopy. *Physics in Medicine and Biology*, 50:3211–3219, 2005.

A. Suggett. Molecular motion and interactions in aqueous carbohydrate solutions. iii. a combined nuclear magnetic and dielectric-relaxation strategy. *Journal of Solution Chemistry*, 5(1):33–46, 1976.

S. J. Suresh and V. M. Naik. Theory of dielectric constant of aqueous solutions. *J. Chem. Phys.*, 116(10):4212–4220, 2002.

M. Tachiki. Emission of terahertz electromagnetic waves driven by an external current in intrinsic josephson junctions. *Physica C: Superconductivity*, In Press, Accepted Manuscript, 2008.

E. Tahara, H. Ito, K. Taniyama, H. Yokozaki, and J. Hata. Alpha 1-antitrypsin, alpha 1-antichymotrypsin, and alpha 2-macroglobulin in human gastric carcinomas: a retrospective immunohistochemical study. *Human Pathology*, 15(10):957–964, 1984.

M. J. Tait, A. Suggett, F. Franks, S. Ablett, and P. A. Quickenden. Hydration of monosaccharides: A study by dielectric and nuclear magnetic relaxation. *Journal of Solution Chemistry*, 1(2):131–151, 1972.

J. C. Taylor, C. A. Kendall, N. Stone, and T. A. Cook. Optical adjuncts for enhanced colonoscopic diagnosis. *British Journal of Surgery*, 94(1):6–16, 2007.

G. J. Tearney, M. E. Brezinski, J. F. Southern, B. E. Bouma, S. A. Boppart, and J. G. Fujimoto. Optical biopsy in human gastrointestinal tissue using optical coherence tomography. *The American journal of gastroenterology*, 92(10):1800–1804, 1997.

F. Thompson. Permittivity measurements in solids, powders, and liquids. *American Journal of Physics*, 73(8):787–789, 2005.

P. Thueler, I. Charvet, F. Bevilacqua, M. S. Ghislain, G. Ory, P. Marquet, P. Meda, B. Vermeulen, and C. Depeursinge. In vivo endoscopic tissue diagnostics based on spectroscopic absorption, scattering, and phase function properties. *J. Biomed. Opt.*, 8(3):495–503, 2003.

H. Todt, G. Guthausen, W. Burk, D. Schmalbein, and A. Kamlowski. Water/moisture and fat analysis by time-domain nmr. *Food Chemistry*, 96(3):436–440, 2006.

M. Tonouchi. Cutting-edge terahertz technology. *Nat Photon*, 1(2):97–105, 2007.

B. J. Tromberg, N. Shah, R. Lanning, A. Cerussi, J. Espinoza, T. Pham, L. Svaasand, and J. Butler. Non-invasive in vivo characterization of breast tumors using photon migration spectroscopy. *Neoplasia*, 2(1-2):26–40, 2000.

S. Y. Tung, C. S. Wu, and M. Y. Su. Magnifying colonoscopy in differentiating neoplastic from nonneoplastic colorectal lesions. *American Journal of Gastroenterology*, 96 (9):2628–263, 2001.

Y. Ueno and K. Ajito. Analytical terahertz spectroscopy. *Analytical Sciences*, 24(2): 185–192, 2008.

P. C. Upadhya, Y. C. Shen, A. G. Davies, and E. H. Linfield. Terahertz time-domain spectroscopy of glucose and uric acid. *Journal of Biological Physics*, 29(2-3):117–121, 2003.

R. Usha and T. Ramasami. The effects of urea and n-propanol on collagen denaturation: using dsc, circular dicroism and viscosity. *Thermochimica Acta*, 409(2):201–206, 2004.

F. VacaChavez, E. Hellstrand, and B. Halle. Hydrogen exchange and hydration dynamics in gelatin gels. *J. Phys. Chem. B*, 110(43):21551–21559, 2006.

M. C. Vackier, B. P. Hills, and D. N. Rutledge. An nmr relaxation study of the state of water in gelatin gels. *Journal of Magnetic Resonance*, 138:36–42, 1999.

R. L. P. vanVeen, H. J. C. M. Sterenborg, A. Pifferi, A. Torricelli, and R. Cubeddu. Determination of vis- nir absorption coefficients of mammalian fat, with time- and spatially resolved diffuse reflectance and transmission spectroscopy. In *Biomedical Topical Meetings*. Optical Society of America, 2004.

D. S. Venables and C. A. Schmuttenmaer. Structure and dynamics of nonaqueous mixtures of dipolar liquids. ii. molecular dynamics simulations. *J. Chem. Phys.*, 113 (8):3249–3260, 2000a.

D. S. Venables and C. A. Schmuttenmaer. Spectroscopy and dynamics of mixtures of water with acetone, acetonitrile, and methanol. *J. Chem. Phys.*, 113(24):11222–11236, 2000b.

G. C. Walker, E. Berry, S. W. Smye, and D. S. Brettle. Materials for phantoms for terahertz pulsed imaging. *Physics in Medicine and Biology*, 49:N363–N369, 2004a.

G. C. Walker, E. Berry, S. W. Smye, N. N. Zinovev, A. J. Fitzgerald, R. E. Miles, J. M. Chamberlain, and M. A. Smith. Modelling the propagation of terahertz radiation through a tissue simulating phantom. *Physics in Medicine and Biology*, 49:1853–1864, 2004b.

V. P. Wallace, A. J. Fitzgerald, S. Shankar, N. Flanagan, R. J. Pye, J. Cluff, and D. D. Arnone. Terahertz pulsed imaging of basal cell carcinoma ex vivo and in vivo. *British Journal of Dermatology*, 151:424–432, 2004.

V. P. Wallace, A. J. Fitzgerald, B. Robertson, E. Pickwell, and B. Cole. Development of a hand-held tpi system for medical applications. *Microwave Symposium Digest, 2005 IEEE MTT-S International*, page 3, 2005.

M. Walther, B. M. Fischer, and P. Uhd Jepsen. Noncovalent intermolecular forces in polycrystalline and amorphous saccharides in the far infrared. *Chemical Physics*, 288(2-3):261–268, 2003.

M. Walther, M. R. Freeman, and F. A. Hegmann. Metal-wire terahertz time-domain spectroscopy. *Appl. Phys. Lett.*, 87(26):261107–3, 2005.

K. Wang and D. M. Mittleman. Metal wires for terahertz wave guiding. *Nature*, 432 (7015):376–379, 2004.

T. D. Wang, J. M. Crawford, M. S. Feld, Y. Wang, I. Itzkan, and J. Van Dam. In vivo identification of colonic dysplasia using fluorescence endoscopic imaging. *Gastrointestinal Endoscopy*, 49(4):447–455, 1999.

S. E. Whitmire, D. Wolpert, A. G. Markelz, J. R. Hillebrecht, J. Galan, and R. R. Birge. Protein flexibility and conformational state: A comparison of collective vibrational modes of wild-type and d96n bacteriorhodopsin. *Biophys. J.*, 85(2):1269–1277, 2003.

B. S. Williams. Terahertz quantum-cascade lasers. *Nat Photon*, 1(9):517–525, 2007.

C. Wohlfarth. *Static Dielectric Constants of Pure Liquids and Binary Liquid Mixtures. Supplement to IV/6*, volume 17 of *Numerical Data and Functional Relationships in Science and Technology - New Series Group 4 : Physical Chemistry*. Landolt-Bornstein, 2008.

K. N. Woods and H. Wiedemann. The influence of chain dynamics on the far-infrared spectrum of liquid methanol. *J. Chem. Phys.*, 123(13):134506–134507, 2005.

R. M. Woodward, B. E. Cole, V. P. Wallace, R. J. Pye, D. D. Arnone, E. H. Linfield, and M. Pepper. Terahertz pulse imaging in reflection geometry of human skin cancer and skin tissue. *Physics in Medicine and Biology*, 47:3853–3863, 2002.

R. M. Woodward, V. P. Wallace, R. J. Pye, B. E. Cole, D. D. Arnone, E. H. Linfield, and M. Pepper. Terahertz pulse imaging of ex vivo basal cell carcinoma. *Journal of Investigative Dermatology*, 120(1):72–78, 2003.

Q. Wu and X. C. Zhang. Ultrafast electro-optic field sensors. *Appl. Phys. Lett.*, 68(12): 1604–1606, 1996.

Q. Wu, T. D. Hewitt, and X. C. Zhang. Two-dimensional electro-optic imaging of thz beams. *Appl. Phys. Lett.*, 69(8):1026–1028, 1996.

J. Xu, K. W. Plaxco, and S. J. Allen. Probing the collective vibrational dynamics of a protein in liquid water by terahertz absorption spectroscopy. *Protein Sci*, 15(5): 1175–1181, 2006.

K. Yamamoto, K. Tominaga, H. Sasakawa, A. Tamura, H. Murakami, H. Ohtake, and N. Sarukura. Far-infrared absorption measurements of polypeptides and cytochrome c by thz radiation. *The Chemical Society of Japan*, 75:1083–1093, 2002.

V. X. D. Yang, N. Munce, J. Pekar, M. L. Gordon, S. Lo, N. E. Marcon, B. C. Wilson, and I. A. Vitkin. Micromachined array tip for multifocus fiber-based optical coherencetomography. *Optics letters*, 29(15):1754–1756, 2004.

T. Yokomizo, M. Nakasako, T. Yamazaki, H. Shindo, and J. Higo. Hydrogen-bond patterns in the hydration structure of a protein. *Chemical Physics Letters*, 401(4-6): 332–336, 2005.

S. Yoshioka, Y. Aso, T. Otsuka, and S. Kojima. Water mobility in poly(ethylene glycol) - , poly(vinylpyrrolidone) - , and gelatin - water systems, as indicated by dielectric relaxation time, spin - latice relaxation time, and water activity. *Journal of Pharmaceutical Sciences*, 84(9):1072–1077, 1995.

I. Zelvyte, T. Stevens, U. Westin, and S. Janciauskiene. alpha1-antitrypsin and its c-terminal fragment attenuate effects of degranulated neutrophil-conditioned medium on lung cancer hcc cells, in vitro. *Cancer Cell International*, 4(1):7, 2004.

C. F. Zhang and S. M. Durbin. Hydration-induced far-infrared absorption increase in myoglobin. *J. Phys. Chem. B*, 110(46):23607–23613, 2006.

X. C. Zhang. Terahertz wave imaging: horizons and hurdles. *Physics in Medicine and Biology*, 47(21):3667–3677, 2002.

Y. Zhong, G. L. Warren, and S. Patel. Thermodynamic and structural properties of methanol-water solutions using nonadditive interaction models. *Journal of Computational Chemistry*, 29(7):1142–1152, 2007.

G. Zonios, L. T. Perelman, V. Backman, R. Manoharan, M. Fitzmaurice, J. Van Dam, and M. Feld. Diffuse reflectance spectroscopy of human adenomatous colon polyps in vivo. *Applied Optics*, 38(31):6628–6637, 1999.

G. I. Zonios, R. M. Cothren, J. T. Arendt, Wu Jun, J. Van Dam, J. M. Crawford, R. Manoharan, and M. S. Feld. Morphological model of human colon tissue fluorescence. *Biomedical Engineering, IEEE Transactions on*, 43(2):113–122, 1996.

A. M. Zysk, F. T. Nguyen, A. L. Oldenburg, D. L. Marks, and S. A. Boppart. Optical coherence tomography: a review of clinical development from bench to bedside. *J. Biomed. Opt.*, 12(5):051403–051421, 2007.